ABSTRACT

Title of Dissertation: POPULATION STUDIES OF
TIDAL DISRUPTION EVENTS
AND THEIR HOSTS: UNDERSTANDING
HOST GALAXY PREFERENCES
AND THE ORIGIN OF THE
ULTRAVIOLET AND OPTICAL EMISSION
Erica Hammerstein
Doctor of Philosophy, 2024

Dissertation Directed by: Professor Sylvain Veilleux
Department of Astronomy
Dr. S. Bradley Cenko
NASA Goddard Space Flight Center

It is well-established that the majority of galaxies harbor a supermassive black hole (SMBH) in their nucleus. While some of these SMBHs are easily studied either through signatures of persistent gas-fueled accretion or direct observations of the SMBH's influence on stars and gas in its potential well, many more are elusive, providing no obvious evidence of their existence. One way to detect these dormant SMBHs is through the tidal disruption of a star that wanders too close and is torn apart under the tidal stress. These tidal disruption events (TDEs) illuminate otherwise difficult-to-study dim or distant galaxy nuclei, acting as cosmic signposts announcing the presence of the SMBH lurking there through luminous flares observed across the electromagnetic spectrum. These flares can, in principle, be used to extract information about the SMBH itself, and can therefore serve as important probes of SMBH growth and evolution. TDE host

galaxies can be used to study the connection between SMBHs and their environments, an important goal in understanding the origin of SMBHs, galaxy formation, and SMBH co-evolution. My dissertation addresses both of these important facets of TDEs, their light curves and their hosts, to understand not only the events themselves but how they can be used to study SMBHs.

First, I studied a sample of 30 optically selected TDEs from the Zwicky Transient Facility (ZTF), the largest sample of TDEs discovered from a single survey yet. After performing a careful light curve analysis, I uncovered several correlations between light curve parameters which indicate that the properties of the black hole are imprinted on the light curve. I also fit the light curves using tools that yield black hole mass estimates and I found no correlation between these estimates and the host galaxy stellar mass. I found no difference between the optical light curve properties, apart from the peak luminosity, of the X-ray bright and X-ray faint TDEs in this sample. This provides clues as to the origin of the optical emission and may support a scenario where the viewing angle is responsible for the observed emission. Lastly, I presented a new spectral class of TDE, TDE-featureless, which in contrast to other events, show no broad lines in their optical spectra. This new class may be connected to the rare class of jetted TDEs.

Next, I studied a subset of host galaxies in the ZTF sample of TDEs. I examined their optical colors, morphology, and star-formation histories. I found that TDE hosts can be classified as “green”, in a phase between red, inactive galaxies and blue, star-forming galaxies. Morphologically, the TDE hosts are centrally concentrated, more so than galaxies of similar mass and color. By looking at the optical spectra of the TDE hosts, which can be used to estimate the current star formation and the star formation history, I found that TDE host populations are dominated by the rare class of E+A, or post-starburst, galaxies. In tandem with the other peculiar photometric and morphological properties, this points to mergers as the likely origin for TDE hosts.

I extended this study of TDE hosts by using integral field spectroscopy to infer black hole masses via the $M_{\rm BH} - \sigma_{\star}$ relation and investigate large-scale stellar kinematics. I found that the black hole mass distribution for TDE hosts is consistent with the theoretical prediction that they should be dominated by lower mass SBMHs. Interestingly, one TDE-featureless object was found to have a black hole mass of $\log(M_{\rm BH}/M_{\odot}) = 8.01$, which is likely above the Hills mass for the disruption of a solar-type star and could necessitate a rapid spin for this particular black hole. If high spin is required to launch relativistic jets, this may further support the connection between featureless TDEs and jetted TDEs. The large-scale kinematics of a galaxy are strongly tied to its merger and star formation history. I found that TDE hosts share similar kinematic properties to E+A galaxies, which are thought to be post-merger.

Lastly, I presented further observations of the jetted TDE AT2022cmc. This event, discovered in the optical, presented an opportunity to place this rare class of TDE in the context of the larger TDE population. I performed a careful light curve analysis that accounts for both the thermal and non-thermal components in the light curve. I showed that the thermal component of AT2022cmc is similar to the TDE-featureless class of events and follows correlations presented for TDE light curve properties found in this thesis.

Population Studies of Tidal Disruption Events and Their Hosts: Understanding Host Galaxy Preferences and the Origin of the Ultraviolet and Optical Emission

by

Erica Hammerstein

Dissertation submitted to the Faculty of the Graduate School of the
University of Maryland, College Park in partial fulfillment
of the requirements for the degree of
Doctor of Philosophy
2024

Advisory Committee:
- Professor Sylvain Veilleux, Chair/Advisor
- Dr. S. Bradley Cenko, Co-Advisor
- Professor M. Coleman Miller
- Dr. Suvi Gezari (External Examiner)
- Professor Kara Hoffman (Dean's Representative)

Preface

Chapter 2 has been published in the *Astrophysical Journal* as "The Final Season Reimagined: 30 Tidal Disruptions Events from the ZTF Survey" (Hammerstein et al., 2023a). It is reproduced here with only changes to formatting and layout. Chapter 3 has been published in the *Astrophysical Journal Letters* as "Tidal Disruption Event Hosts Are Green and Centrally Concentrated: Signatures of a Post-merger System" (Hammerstein et al., 2021a). It is reproduced here with only changes to formatting and layout. Chapter 4 has been published in the *Astrophysical Journal* as "Integral Field Spectroscopy of 13 Tidal Disruption Event Hosts from the Zwicky Transient Facility Survey" (Hammerstein et al., 2023b). Additional figures not presented in the published manuscript have been added to the Appendix of this thesis. Chapter 5 is intended as part of a manuscript for submission to peer-reviewed journals this year.

Acknowledgments

I am endlessly grateful to be writing these acknowledgments. The journey to this dissertation has been a long one and includes more than just the six years I spent doing the work. This thesis is the product of all the support, friendship, and love that I have received throughout the years.

To my advisor, Brad Cenko: thank you for your support, advice, and encouragement. Despite being probably one of the busiest people I know, you always made sure that I had everything I needed to succeed and it has been an honor learning from you these past few years. I look forward to many more years of collaboration and science to come! To my campus advisor, Sylvain Veilleux: you have been an incredible source of encouragement and guidance. I am grateful for the times you had encouraging words to say about my work even if I wasn't so confident. To my first graduate school advisor, Suvi Gezari: thank you for introducing me to the wonders of time-domain astronomy. Your enthusiasm for your work is contagious and I aspire to be as full of ideas and excitement for science as you are.

To the friends I made in graduate school, Brendan, Joe, Rye, Ramsey, Harrison, Gabe, Alex, Liz, Julian, Milena, Sergio, Carrie, Tomás, Vicente, and Jegug: thank you for the wonderful times we had at parties, in DC, at conferences, at Town Hall, for conversations in the department, and for the opportunity to call you all friends. To Sara and Charlotte: thank you both for your collaboration, your guidance, your friendship, and all of the fun times we had observing and traveling for conferences together. To Giannina: thank you for always being someone I can talk to, for your advice, and for letting me spam you with memes. To Jordan: thank you for being a wonderful friend and fellow crafting enthusiast, for always going to get more yarn even when I definitely don't need it, and for your constant support and encouragement. To the C.O.O.K.S, a.k.a. Teal and Ben: our friendship will always hold a special place in my heart. Sharing an office with you both, playing video games, and forming the unofficial live-action Cat in the Hat fan club will be cherished memories. Here's to many more Victory Royales for the C.O.O.K.S.!

To some of my oldest friends: Maggie, thank you for being the best friend that I could hope to ask for all these years, for being someone I can always call or text no matter the hour, for letting me rant about anything, and for teaching me the cool way to color in kindergarten. I don't know if I would have made it without that. To Ben: thank you for the many hours spent in the Astro Undergrad Lounge, the road trips we took, the days spent at the coffee shop in Navy Yard, and for your quotes from books that you can seemingly conjure at will for any situation.

To my parents, Dave and Donita: thank you for everything that you have given me, all the ways in which you have helped me succeed, and all the ways in which you continue to help me succeed. To my brothers, Andrew, Collin, Matthew, and John: thank you for being my first friends, and for being a continual source of support, encouragement, and laughter. To my nephew, Lukey: thank you for being such a wonderful light in my life.

To David: thank you for all that you do, for the trips to Whole Foods to get me my favorite kombucha, for your kitchen experiments, and especially for your determination to cook the best steak ever. Thank you for staying up to keep me company on the nights I spent observing. Thank you for all the love, laughter, and support you have given me.

Thank you, each and every one of you. Your support means the world to me.

Table of Contents

Preface ii

Acknowledgements iii

Table of Contents v

List of Tables ix

List of Figures x

List of Abbreviations xiii

Chapter 1: Introduction 1
- 1.1 The Tidal Disruption of a Star by a Supermassive Black Hole 2
- 1.2 Observed Emission from TDEs 5
  - 1.2.1 The UV/Optical and X-ray Emission 5
  - 1.2.2 Non-thermal Emission and Jetted TDEs 7
- 1.3 TDE Environments 9
  - 1.3.1 Two-body Relaxation and the TDE Rate 9
  - 1.3.2 The Host Galaxies of TDEs 10
- 1.4 On the Optical Discovery of TDEs with ZTF 18
- 1.5 Scope of the Dissertation 22

Chapter 2: The Final Season Reimagined: 30 Tidal Disruption Events from the ZTF-I Survey 25
- 2.1 Introduction 25
- 2.2 The Search for TDEs in ZTF-I 27
  - 2.2.1 TDE Candidate Selection 27
  - 2.2.2 The ZTF-I TDE Sample 29
  - 2.2.3 Spectroscopic Classifications 29
- 2.3 Host Galaxy Properties 33
- 2.4 Observations 39
  - 2.4.1 ZTF Forced Photometry 39
  - 2.4.2 Swift (UVOT & XRT) 40
  - 2.4.3 ATLAS 42
- 2.5 Light Curve Analysis 43
  - 2.5.1 Model Fitting 43

2.5.2 Empirical Timescale Estimates . . . 45
2.6 Results . . . 47
2.6.1 Light Curve Property Correlations . . . 47
2.6.2 Spectral Class Correlations . . . 48
2.6.3 X-ray Correlations . . . 51
2.6.4 The Look-Elsewhere Effect . . . 53
2.6.5 Optical to X-ray Ratio . . . 54
2.7 Black Hole Mass Estimates . . . 56
2.7.1 `MOSFiT` . . . 56
2.7.2 `TDEmass` . . . 57
2.8 Discussion . . . 60
2.9 Conclusions . . . 67
2.10 Acknowledgements . . . 69

Chapter 3: TDE Hosts are Green and Centrally Concentrated: Signatures of a Post-Merger System 71
3.1 Introduction . . . 71
3.2 Sample & Data . . . 74
3.2.1 ZTF TDE Host Galaxies . . . 74
3.2.2 SDSS Comparison Sample . . . 76
3.3 Analysis & Results . . . 79
3.3.1 Photometry . . . 79
3.3.2 Spectral Measurements . . . 82
3.4 Discussion . . . 84
3.5 Conclusions . . . 91
3.6 Acknowledgements . . . 92

Chapter 4: Integral Field Spectroscopy of 13 Tidal Disruption Event Hosts from the ZTF Survey 95
4.1 Introduction . . . 95
4.2 Observations & Data Analysis . . . 98
4.2.1 Large Monolithic Imager and GALFIT . . . 103
4.2.2 Keck Cosmic Web Imager and GIST . . . 105
4.3 Results . . . 108
4.4 Black hole masses . . . 112
4.4.1 Comparisons to previous measurements . . . 117
4.4.2 Correlations with TDE light curve properties . . . 121
4.4.3 AT2020qhs and the TDE-featureless class . . . 123
4.5 Galaxy kinematics and stellar populations . . . 128
4.6 Conclusions . . . 134
4.7 Acknowledgements . . . 135

Chapter 5: The Jetted Tidal Disruption Event AT2022cmc in the Context of the Optical Tidal Disruption Event Population 137
5.1 Introduction . . . 137

5.2 Data & Observations . . . 142
5.3 Analysis . . . 145
    5.3.1 Spectrum Fitting . . . 145
    5.3.2 Light Curve Fitting . . . 146
5.4 Results . . . 149
    5.4.1 Spectrum Fitting . . . 149
    5.4.2 Light Curve Fitting . . . 152
5.5 Discussion . . . 153

Chapter 6: Summary and Future Work 159
6.1 Summary of the Thesis . . . 159
6.2 Future Work and Outlook . . . 161

Appendix A: Supplementary Materials for Chapter 2 165
A.1 Detailed Spectra . . . 165
    A.1.1 AT2018zr . . . 165
    A.1.2 AT2018bsi . . . 166
    A.1.3 AT2018hco . . . 166
    A.1.4 AT2018iih . . . 167
    A.1.5 AT2018hyz . . . 167
    A.1.6 AT2018lni . . . 168
    A.1.7 AT2018lna . . . 169
    A.1.8 AT2018jbv . . . 169
    A.1.9 AT2019cho . . . 169
    A.1.10 AT2019bhf . . . 170
    A.1.11 AT2019azh . . . 170
    A.1.12 AT2019dsg . . . 171
    A.1.13 AT2019ehz . . . 171
    A.1.14 AT2019mha . . . 171
    A.1.15 AT2019meg . . . 172
    A.1.16 AT2019lwu . . . 172
    A.1.17 AT2019qiz . . . 173
    A.1.18 AT2019teq . . . 173
    A.1.19 AT2020pj . . . 173
    A.1.20 AT2019vcb . . . 174
    A.1.21 AT2020ddv . . . 174
    A.1.22 AT2020ocn . . . 174
    A.1.23 AT2020opy . . . 175
    A.1.24 AT2020mot . . . 175
    A.1.25 AT2020mbq . . . 175
    A.1.26 AT2020qhs . . . 176
    A.1.27 AT2020riz . . . 176
    A.1.28 AT2020wey . . . 176
    A.1.29 AT2020zso . . . 177
    A.1.30 AT2020ysg . . . 177

A.2 Light Curves & Fits 182
A.3 Results from Statistical Tests 189

Appendix B: Supplementary Materials for Chapter 4 192
B.1 Fits with `GALFIT` 192
B.2 Bulge Spectrum Fits from `ppxf` 194

Appendix C: New Observations of AT2022cmc 196

Appendix D: Facilities and Software Used in this Thesis 199
D.1 Facilities 199
D.2 Software 200

Bibliography 202

List of Tables

2.1 Information on the 30 ZTF-I TDEs. 31
2.2 The properties of the ZTF-I TDE host galaxies, as estimated from the SED fitting. 38
2.3 XRT reduction parameters. 41
2.4 Free Parameters and Priors 45

3.1 ZTF TDE host galaxies. 77
3.2 E+A & QBS Overrepresentation. 91

4.1 Sample of TDE Host Galaxies. 102
4.2 Summary of LMI observations. 105
4.3 Summary of KCWI observations. 108
4.4 Results from photometric and kinematic analysis. 112

5.1 Summary of spectroscopic observations. 144
5.2 Free parameters and priors. 149
5.3 Results from power-law and blackbody continuum fits to optical spectra. 150
5.4 Results from fits to AT2022cmc optical light curve. 153

A.1 Spectroscopic observations. 178
A.2 The light curve fitting parameters from the 3 different light curve models used. . . 182
A.3 Black hole and disrupted star masses. 183
A.4 Kendall's tau coefficient and associated p-value comparing light curve and host galaxy properties. 190
A.5 Anderson-Darling p-value comparing the four TDE spectral classes. 191

C.1 New observations of AT2022cmc. 198

List of Figures

1.1 Tidal radius versus the size of the black hole for various black hole masses. . . . 3
1.2 Reported discoveries of TDEs by their discovery wavelength. 7
1.3 Schematic picture showing the unifying model for the observed emission from a TDE. 8
1.4 The Hα equivalent width versus Hδ absorption index. 12
1.5 The color-galaxy mass diagram for early-type and late-type galaxies. 14
1.6 Example Sérsic profiles. 16
1.7 Reported discoveries of TDEs by their discovery survey/telescope. 20
1.8 Rise timescales versus mean $g - r$ color for ZTF nuclear transients. 21
1.9 Rate of color change against mean $g - r$ color for ZTF nuclear transients. 21
1.10 Fade timescale versus rise timescale for ZTF nuclear transients. 22
1.11 Optical spectra of the three TDE spectral classes plus a composite QSO spectrum and a SNIa spectrum. 23

2.1 Spectral classifications for the ZTF-I TDE sample. 32
2.2 SDSS and Pan-STARRS gri images of the ZTF-I TDE hosts. 36
2.3 $u - r$ color – mass and $u - r$ color – magnitude diagrams for the ZTF-I sample of TDE hosts. 37
2.4 The r-band absolute magnitude, blackbody luminosity, blackbody radius, and blackbody temperature for the TDEs in the ZTF-I sample. 46
2.5 The peak blackbody luminosity and the rise time compared with the decay timescale. 49
2.6 Selected properties measured from the fits to the multi-band light curves compared to the host galaxy stellar mass, with the cumulative distributions of spectroscopic classes. 50
2.7 Cumulative distributions of selected properties of the TDE light curves for the X-ray bright and X-ray faint populations of TDEs in the ZTF-I sample. 52
2.8 The ratio of the blackbody luminosity, derived from the optical and UV light curves, to the 0.3–10 keV X-ray luminosity from *Swift*/XRT. 55
2.9 The black hole mass estimated from the `MOSFiT` fits to the optical/UV light curves vs. the total stellar mass of the host galaxies. 58
2.10 The disrupted star mass estimated from the `MOSFiT` fits to the optical/UV light curves for each of the TDE spectral types. 59
2.11 The black hole mass estimated from `TDEmass` vs. the total stellar mass of the host galaxies. 61
2.12 The disrupted star mass estimated from `TDEmass` split by the TDE spectral types. 62
2.13 The Hα and Hβ regions of the most extreme broad/flat-topped or double-peaked TDEs. 68

3.1 Rest-frame host galaxy spectra of the ZTF TDE sample. 78
3.2 The extinction-corrected, synthetic rest-frame $u-r$ color of the TDE host galaxies. 81
3.3 The total galaxy Sérsic index vs. the total stellar mass and the effective stellar mass surface density vs. the total stellar mass. 83
3.4 The H$\delta_{\rm A}$ absorption index vs. the Hα emission equivalent width. 85
3.5 BPT diagram for the 7 TDE hosts that show prominent nebular emission lines. . . 86

4.1 SDSS and Pan-STARRS *gri* images of the thirteen TDE host galaxies. 99
4.2 The distribution of redshifts for the TDE host galaxies in our sample. 100
4.3 The rest-frame, extinction corrected $u-r$ color as a function of host galaxy mass for the TDE host galaxies and a sample of 955 galaxies from the SAMI survey. . 101
4.4 A $29''\times29''$ cutout of the LMI observations of the host galaxy of AT2018bsi, shown with the `GALFIT` model and residuals. 104
4.5 An example output from `GIST` of the host galaxy of AT2019azh. 110
4.6 Example `ppxf` fits to the host galaxy of AT2019azh output from `GIST`. 111
4.7 Distribution of black hole masses for the host galaxies in our sample. 114
4.8 The black hole mass as a function of the velocity dispersion. 115
4.9 The black hole mass as a function of the host galaxy stellar mass. 116
4.10 The black hole mass derived from `MOSFiT` and `TDEmass` as a function of the black hole mass we derive from host kinematics. 120
4.11 The peak blackbody luminosity as a function of the Eddington luminosity implied by the black hole mass. 124
4.12 The Eddington ratio as a function of black hole mass. 125
4.13 The ratio between stellar ordered rotation and random orbital motion of the TDE host galaxies. 130

5.1 UV, optical, and near infrared light curve of AT2022cmc. 143
5.2 Optical spectra of AT2022cmc and featureless TDEs. 144
5.3 Power-law and blackbody fits to the optical spectra of AT2022cmc and featureless TDEs. 151
5.4 Model 1 fit to the AT2022cmc light curve. 154
5.5 Evolution of the SED for AT2022cmc light curve fits. 155
5.6 Light curve parameters as a function of host galaxy stellar mass. 158

A.1 Subset of optical spectra for the events in ZTF-I TDE sample. 179
A.2 Subset of optical spectra for the events in ZTF-I TDE sample. 180
A.3 Subset of optical spectra for the events in ZTF-I TDE sample. 181
A.4 Optical/UV light curves from ZTF, *Swift*/UVOT, and ATLAS photometry for a subset of ZTF-I TDEs. 184
A.5 Optical/UV light curves from ZTF, *Swift*/UVOT, and ATLAS photometry for a subset of ZTF-I TDEs. 185
A.6 Gaussian rise and power-law decay fits to ZTF-I TDE light curves. 186
A.7 Gaussian rise and power-law decay fits to ZTF-I TDE light curves. 187
A.8 Gaussian rise and exponential decay fits with fixed temperature to ZTF-I TDE light curves. 188

A.9 Gaussian rise and exponential decay fits with fixed temperature to ZTF-I TDE light curves. 189

B.1 Subset of host galaxy morphological fits with `GALFIT`. 192
B.2 Subset of host galaxy morphological fits with `GALFIT`. 193
B.3 A subset of bulge spectrum fits from `ppxf`. 194
B.4 A subset of bulge spectrum fits from `ppxf`. 195

List of Abbreviations

AGN	Active galactic nucleus (nuclei)
ALFOSC	Alhambra Faint Object Spectrograph and Camera
ASAS-SN	All-Sky Automated Survey for Supernovae
ATLAS	Asteroid Terrestrial-impact Last Alert System
BAT	Burst alert telescope
CNM	Circumnuclear medium
DEIMOS	DEep Imaging Multi-Object Spectrograph
EW	Equivalent width
GALEX	Galaxy Evolution Explorer
GIM2D	Galaxy IMage 2D
GIST	Galaxy IFU Spectroscopy Tool
GIT	GROWTH India Telescope
GMOS	Gemini Multi-Object Spectrograph
HST	Hubble Space Telescope
IFS	Integral field spectroscopy
IMF	Initial mass function
iPTF	Intermediate Palomar Transient Factory
JWST	James Webb Space Telescope
KCWI	Keck Cosmic Web Image
LBC	Large Binocular Camera
LBT	Large Binocular Telescope
LDT	Lowell Discovery Telescope
LMI	Large Monolithic Imager
LRIS	Low Resolution Imaging Spectrometer
LT	Liverpool Telescope
MBH	Massive black hole
MCMC	Markov chain Monte Carlo
MOSFiT	Modular Open-source FItter for Transients
NOT	Nordic Optical Telescope
Pan-STARRS	Panoramic Survey Telescope and Rapid Response System
PSF	Point spread function
QBS	Quiscent Balmer-strong
ROSAT	ROentgen SATellite
SDSS	Sloan Digital Sky Survey

SED	Spectral energy distribution
SFH	Star formation history
SLSN	Superluminous supernova
SMBH	Supermassive black hole
SNe	Supernovae
SRG	Spectrum-Roentgen-Gamma
TDE	Tidal disruption event
VLT	Very Large Telescope
WISE	Wide-field Infrared Survey Explorer
ZTF	Zwicky Transient Facility

Chapter 1: Introduction

It is generally accepted that most, if not all, massive galaxies host a supermassive black hole (SMBH) in their nucleus. These SMBHs, anywhere from millions to billions of times more massive than the Sun, likely play important roles in the formation and evolution of their hosts (Fabian, 2012; Gültekin et al., 2009; Ho, 2008; Kormendy & Ho, 2013; Kormendy & Richstone, 1995; Magorrian & Tremaine, 1999; Veilleux et al., 2005, 2020). This is clearly evidenced by scaling relations between SMBH masses and the properties of their host galaxies, such as the bulge velocity dispersion (e.g., Ferrarese & Merritt, 2000; Gebhardt et al., 2000), bulge luminosity (e.g., Dressler, 1989; Magorrian et al., 1998), or total stellar mass (e.g., Reines & Volonteri, 2015).

These objects can be readily studied in the nearby universe (within a few hundred Mpc), where kinematics of stars and gas in the sphere of influence provide dynamical measurements of the SMBH mass (e.g., Kormendy & Ho, 2013; McConnell & Ma, 2013). These objects can also make their presence known most prominently through sustained accretion of nuclear gas and dust as active galactic nuclei (AGN), which can be seen out to redshifts of $z > 8$ (e.g., Larson et al., 2023; Maiolino et al., 2023) with current observatories such as JWST. However, many more of these objects are dormant at the centers of their hosts, giving no indication of their presence and being too distant to perform direct studies. Every so often, however, a star will wander too close to a SMBH lying in wait and be torn apart under the tidal stress in what is called a tidal disruption event (TDE), creating a luminous flare visible from Earth and providing a unique way to gain insights into the population of distant and quiescent SMBHs.

1.1 The Tidal Disruption of a Star by a Supermassive Black Hole

The tidal disruption of a star by a SMBH was conceptualized in the late 1970s as a possible power source of Seyfert galaxies and quasars (Hills, 1975; Lidskii & Ozernoi, 1979). A star will be tidally disrupted by a SMBH if the star's orbital pericenter radius R_{P} is less than the tidal radius R_{T}, defined as the radius at which the tidal forces exceed the self-gravity of the star

$$\frac{GMR_\star}{r^3} > G\frac{M_\star}{R_\star^2}. \tag{1.1}$$

This results in a tidal radius of

$$R_{\mathrm{T}} = R_\star \left(\frac{M_{\mathrm{BH}}}{M_\star}\right)^{1/3}, \tag{1.2}$$

which depends weakly on the structure of the star (Evans & Kochanek, 1989; Phinney, 1989). Since the event horizon grows linearly with black hole mass and $R_{\mathrm{T}} \propto M_{\mathrm{BH}}^{1/3}$, above a critical black hole mass the event horizon will eventually exceed the tidal radius. This critical mass is often referred to as the "Hills mass", and depends on the type and structure of the star that is disrupted. For a solar-type star, this critical mass is $M_{\mathrm{BH}} \gtrsim 10^8 M_\odot$. In Figure 1.1, I show the tidal radius versus the black hole radius for various black hole masses. Because both the event horizon radius and the tidal radius depend on the spin of the black hole, with the dependence of $R_{\mathrm{EH}} = (1+\sqrt{1-a^2})\frac{GM_{\mathrm{BH}}}{c^2}$ for the event horizon radius of a black hole with spin parameter a,

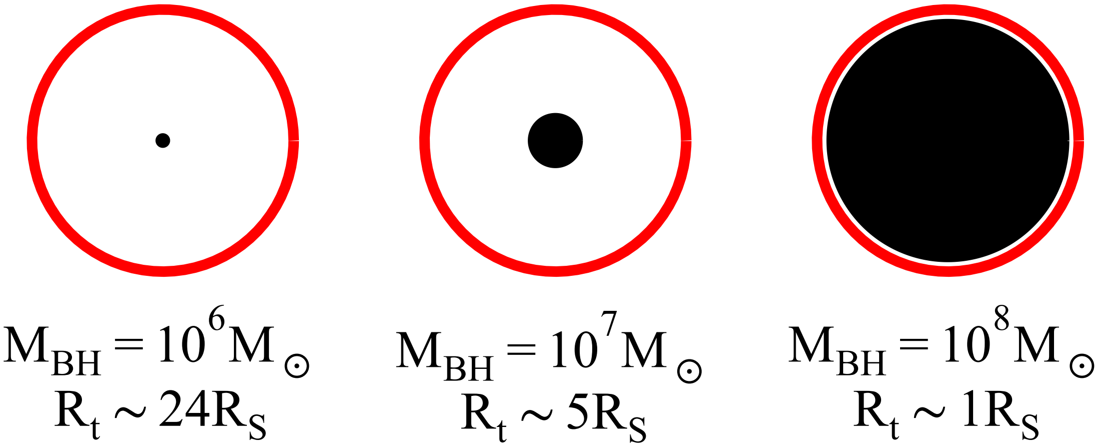

Figure 1.1: Tidal radius (red circle) from Equation 1.2 versus the size of the black hole (black circle) for various (non-spinning) black hole masses and the disruption of a solar-type star. Above $\sim 10^8 M_\odot$, the Hills mass, the tidal radius will be within the black hole and will not produce an observable tidal disruption flare. Spin will increase the Hills mass up to $\sim 7 \times 10^8 M_\odot$ for a maximally spinning black hole (Kesden, 2012).

the Hills mass will increase with increasing spin up to $\sim 7 \times 10^8 M_\odot$ for a maximally spinning black hole (Kesden, 2012). Estimates of black hole masses of TDEs have indeed shown that there is a dearth of events above $10^8 M_\odot$, with most distributions centered around $10^6 M_\odot$ (e.g., Hammerstein et al., 2023b; van Velzen, 2018; Wevers et al., 2017, 2019; Yao et al., 2023).

After disruption, the stellar debris has a spread of specific binding energy due to the change in the potential across the stellar radius

$$\Delta\epsilon = \pm \frac{G M_{\rm BH}}{R_{\rm T}^2} R_\star = \frac{G M_\star}{R_\star} \left(\frac{M_{\rm BH}}{M_\star} \right)^{1/3}, \tag{1.3}$$

which implies that half of the stellar debris will be bound to the black hole ($\Delta\epsilon < 0$) and become available for accretion and half ($\Delta\epsilon > 0$) will be ejected into circumnuclear medium (Evans & Kochanek, 1989; Lacy et al., 1982; Rees, 1988). This bound debris is expected to settle into highly eccentric elliptical orbits with the orbital period of the most bound material defined as the fallback timescale:

$$t_{\mathrm{fb}} = \frac{2\pi G M_{\mathrm{BH}}}{(2\Delta\epsilon)^{3/2}} = 0.11 \text{ year} \left(\frac{R_\star}{R_\odot}\right)^{3/2} \left(\frac{M_{\mathrm{BH}}}{10^6 M_\odot}\right)^{1/2} \left(\frac{M_\star}{M_\odot}\right)^{-1}. \tag{1.4}$$

The debris will continue to return to pericenter at a mass fallback rate of

$$\dot{M}_{\mathrm{fb}} = \frac{dm}{d\epsilon}\frac{d\epsilon}{dt} = \frac{dm}{d\epsilon}\frac{1}{3}(2\pi G M_{\mathrm{BH}})^{2/3} t^{-5/3}. \tag{1.5}$$

Because the fallback timescale and mass fallback rate scale with the black hole mass, the timing of TDE light curves should in principle allow for the SMBH mass to be obtained if the luminosity traces the fallback rate. Interestingly, the characteristic $t^{-5/3}$ power-law and correlations between the light curve timescales, such as the rise and decay rate, and the black hole mass (or host galaxy stellar mass) have been observed in optically selected samples of TDEs (e.g., van Velzen et al., 2021, and Chapter 2 of this thesis). This is not necessarily consistent with theory as a shallower power-law decay might be expected in the optical due to the cooling of the accretion disk with a decreasing accretion rate since $T_{\mathrm{disk}} \propto \dot{M}^{1/4}$. Additionally, as described in Section 1.2, the origin of this optical emission remains unclear and may not be related to the accretion flow at all.

While the light curves potentially allow for the investigation of the SMBH properties, TDEs can also offer further insights into phases of SMBH accretion, jet launching, and outflows. Because the peak fallback rate, $\dot{M}_{\mathrm{peak}} \sim \frac{1}{3}\frac{M_\star}{t_{\mathrm{fb}}}$, is dependent on black hole mass, the peak fallback and accretion of tidal debris will cover a range of Eddington ratios for different events, and evolve dramatically for a single event. The dependence ($\propto M_{\mathrm{BH}}^{-1/2}$) is such that TDEs around black holes less than $\sim 3 \times 10^7 M_\odot$ will have fallback rates in the super-Eddington regime and those above that limit in the sub-Eddington regime (Lodato & Rossi, 2011; Metzger & Stone, 2016; Stone et al., 2013; Strubbe & Quataert, 2009). Super-Eddington accretion is defined as the accretion rate at which the luminosity derived from accretion exceeds the luminosity at which radiation pressure is balanced by gravity. This theoretical limit makes several assumptions about the accretion geometry and efficiency but is an important reference point for accretion onto SMBHs. Because super-Eddington accretion rates imply that the radiation force is greater than the gravitational force, they may therefore be conducive to launching jets (e.g., Giannios & Metzger, 2011) or radiation-pressure-driven outflows (e.g., Strubbe & Quataert, 2011) and the short timescales at which the accretion rates evolve in TDEs provide insights not accessible by studying "normal" AGN alone.

1.2 Observed Emission from TDEs

1.2.1 The UV/Optical and X-ray Emission

Initially, the emission produced from TDEs was thought to be powered primarily by accretion, resulting in a soft thermal X-ray flare. Indeed, the first TDE candidates were discovered as soft X-ray outbursts by the ROSAT all-sky survey and were characterized by a soft X-ray spectrum (Bade et al., 1996; Greiner et al., 2000; Grupe et al., 1999; Komossa & Bade, 1999; Komossa & Greiner, 1999). However, with the advent of all-sky optical surveys, many more TDE candidates have now been discovered at optical wavelengths (Figure 1.2) and often without an accompanying X-ray flare. These UV-optically bright TDEs are well-described by a thermal blackbody with characteristic temperatures between 10^4 K $\lesssim T_{\mathrm{BB}} \lesssim 10^5$ K. This is in stark contrast to X-ray selected TDE candidates, which show significantly higher thermal blackbody temperatures. The discovery of optically selected TDEs with a corresponding X-ray component perhaps further complicates the problem, as the two components show distinct temperatures, implying that the optical and the X-ray radiation arise from two physically distinct components (see Gezari, 2021, for a review on candidates). There is also a range of different behaviors for the X-ray component in optically selected TDEs, such as late-time brightening, rebrightening, and rapid flaring (e.g. Guolo et al., 2023; Hammerstein et al., 2023a; van Velzen et al., 2021). Furthermore, the inferred blackbody radii for the optically selected TDEs are much larger than the expected size for a circularized debris disk (e.g., Wevers et al., 2019). The blackbody radii are more similar to the expected radius at which the tidal debris streams self-intersect. It is therefore not clear where the UV/optical emission arises from, though several models have been proposed to explain the peculiar nature of the emission and the occasional appearance of X-ray emission in optically selected TDEs.

In one family of models, X-ray emission is reprocessed to the optical by a disk wind or outflow launched after material begins to accrete onto the SMBH (Guillochon et al., 2014; Loeb & Ulmer, 1997). This scenario has been further modified by Dai et al. (2018) to suggest that viewing angle may play a large role in the observed emission, and TDEs viewed closer to the pole are X-ray dominated, while TDEs viewed along the accretion disk direction are dominated by UV/optical emission resulting from an outflow reprocessing the X-rays (Figure 1.3). Other models rely on the shocks and subsequent outflows created by intersecting stellar debris streams to explain observed TDE emission, in which case either shock-driven outflows reprocess X-rays into optical emission or the shocks themselves power the optical emission (Jiang et al., 2016; Lu & Bonnerot, 2020; Piran et al., 2015). Which of these models is at play and in what capacity

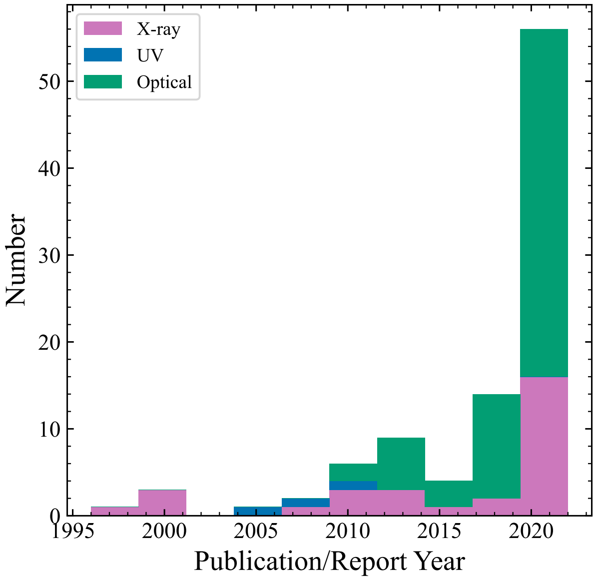

Figure 1.2: Reported discoveries of TDEs by their discovery wavelength from 1996 until the publication of the events presented in this thesis (January 2023), including those presented as part of this thesis. Data from before 2020 is from Gezari (2021).

remains an outstanding question in the study of TDEs today.

1.2.2 Non-thermal Emission and Jetted TDEs

While the majority of TDEs discoveries are made through the observation of their characteristic thermal emission, there are a few objects that have been discovered through non-thermal emission from an on-axis, collimated, relativistic jet. Three of these "jetted" TDEs have been discovered with the hard X-ray Burst Alert Telescope (BAT) aboard *Swift* and include Sw J1644+57 (Bloom et al., 2011; Burrows et al., 2011; Levan et al., 2011; Zauderer et al., 2011), Sw J2058+05 (Cenko et al., 2012; Pasham et al., 2015), and Sw J1112-82 (Brown et al., 2015, 2017). These objects are characterized by rapidly variable early-time X-ray emission and bright and long-lived radio emission (for a review, see De Colle & Lu, 2020). Jetted TDEs, though rare (inferred rates ~ 0.03 Gpc^{-3} yr^{-1}; Andreoni et al., 2022), provide an important opportunity to study the

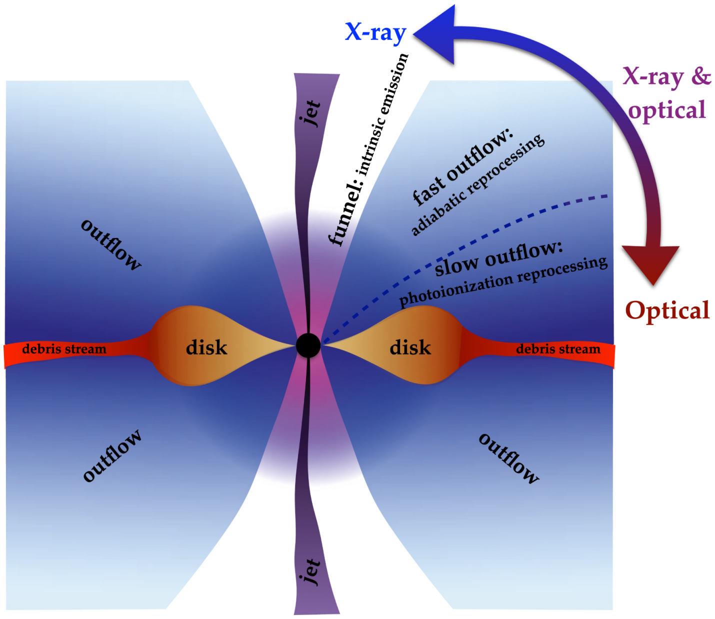

Figure 1.3: A schematic picture showing the unifying model for the observed emission from a TDE. Viewing angles through the optically thick outflow produce only optical emission (reprocessed X-ray emission from the disk) while viewing angles through the optically thin funnel yield X-ray and EUV radiation from the inner accretion disk. Figure is from Dai et al. (2018).

launching of relativistic jets by SMBHs, the jet emission mechanism, and the jet composition.

Among the best-studied of these jetted TDEs is Sw J1644+57, which has extensive multi-wavelength follow-up observations covering over a decade after the initial event. The millimeter and radio evolution of Sw J1644+57 is consistent with synchrotron emission from an outgoing forward shock as the jet interacts with the circumnuclear medium (CNM) (Berger et al., 2012; Cendes et al., 2021; Eftekhari et al., 2018; Generozov et al., 2017; Mimica et al., 2015; Zauderer et al., 2013, 2011). The bright X-ray emission seen in this and other jetted TDEs, however, is not as well understood. The early X-ray light curve is characterized by repeated high-amplitude flares. While the light curve began to decline after several days, it remained highly variable on timescales as short as ~ 100 s. The origin and emission mechanics of this X-ray emission have been a topic of debate, with some studies finding it consistent with synchrotron emission from the jet (Burrows et al., 2011) and others suggesting it arises from synchrotron self-Compton scattering or external inverse Compton scattering (Bloom et al., 2011; Crumley et al., 2016).

Recently, another jetted TDE candidate was reported: AT2022cmc (ZTF22aaajecp; Andreoni et al., 2022). Unlike the previous three jetted TDEs discovered more than a decade ago, AT2022cmc was discovered in the optical. AT2022cmc shows remarkable similarity to the previous jetted TDE Sw J1644+57, with rapid X-ray variability and radio emission indicating a newly formed relativistic jet. Unlike previous jetted TDEs, AT2022cmc is the first to exhibit a *bright* UV/optical counterpart, making it ideal for comparisons with populations of non-jetted TDEs discovered in the optical. In this thesis, I present further observations of AT2022cmc and draw comparisons between its optical light curve and the light curves of non-jetted TDEs.

1.3 TDE Environments

1.3.1 Two-body Relaxation and the TDE Rate

The phase-space for which $R_{\rm P} < R_{\rm T}$ (i.e., orbits for which stars will be tidally disrupted) is referred to as the "loss cone" (Frank & Rees, 1976), and is defined in terms of specific angular momentum such that stars with

$$L < L_{\rm T} = \sqrt{2GM_{\rm BH}R_{\rm T}}, \tag{1.6}$$

will be disrupted. The loss cone is thought to be replenished primarily through two-body interactions (Magorrian & Tremaine, 1999; Wang & Merritt, 2004). Therefore, the rate at which the loss cone is refilled and the resulting TDE rate are dependent on the properties of the stellar population, such as the stellar density profile, in the vicinity of the black hole. In general, calculations of the TDE rate from stars scattering into the loss cone as a result of two-body interactions are in agreement for a rate of TDEs that corresponds to $\sim 10^{-4} - 10^{-5}\ \mathrm{year}^{-1}\ \mathrm{galaxy}^{-1}$ (Magorrian & Tremaine, 1999; Stone & Metzger, 2016; Wang & Merritt, 2004). This rate changes with the nuclear density profile such that galaxies with steeper profiles, such as post-starburst galaxies, can reach rates as high as $10^{-3}\ \mathrm{year}^{-1}\ \mathrm{galaxy}^{-1}$ and has been used to explain the apparent overrepresentation of TDEs in such galaxies (e.g., Stone & van Velzen, 2016, see Section 1.3.2).

Comparisons between rates of TDEs from stellar dynamics and loss cone theory have revealed a rate discrepancy, with fewer TDEs detected than are predicted from theory (Stone & Metzger, 2016). While the rate in post-starburst galaxies is high (discussed more in the next section), the rate in “normal” galaxies is low and there is a lack of clear mechanisms that can decrease the dynamically predicted TDE rates to match the observed rates in normal galaxies (Stone & Metzger, 2016). One solution to this problem includes a steep TDE luminosity function, which suggests that current surveys are only seeing a small fraction of the total number of TDEs due to their flux-limited nature (van Velzen, 2018). The TDE luminosity function requires further investigation which future time-domain surveys can help address.

1.3.2 The Host Galaxies of TDEs

The factors in a galaxy nucleus that directly affect the TDE rate, such as the nuclear stellar density profile, can be difficult to measure, save for the few galaxies that are close enough to resolve the inner regions of their nuclei. Large-scale galaxy properties, however, are much more readily observed than the properties of stars and gas in the vicinity of the SMBH. Both the large-scale properties and nuclear properties will be affected by a galaxy's merger and star-formation history. As such, studying the large-scale properties of TDE hosts can provide insights into the connections that SMBHs have within their hosts and the processes that affect the TDE rate.

Arcavi et al. (2014) was the first to examine a sample of UV/optical bright TDE host galaxies. They found that the majority of the hosts show strong Balmer absorption features indicative of young A star populations superimposed on K star, or early-type galaxy stellar populations. These galaxies are called E+A, K+A, or more loosely, post-starburst or quiescent Balmer-strong (QBS) galaxies. E+A galaxies show no signs of active star formation: the A star populations formed possibly during a merger-induced starburst (Zabludoff et al., 1996) indicate that any activity subsided likely ∼1 Gyr ago (Dressler & Gunn, 1983). Spectroscopically, this manifests in strong Balmer absorption lines characteristic of A stars and very weak or no [O II] and Hα emission that would indicate ongoing star formation. Interestingly, E+A galaxies are rare, making up only $\lesssim 1\%$ of the general galaxy population[1].

French et al. (2016) further explored the unusual host preference of TDEs by quantifying the post-starburst overrepresentation in TDE host populations compared to a general galaxy sample from SDSS. Post-starburst galaxies can be selected from a galaxy population by using the Lick Hδ absorption index (Worthey & Ottaviani, 1997) and Hα emission equivalent width (EW) (Figure 1.4). Stronger Hδ absorption, which is optimized for stellar absorption from A stars, indicates a more "bursty" star formation history (SFH), or a greater stellar mass produced in a shorter amount of time. The lack of Hα emission is used as evidence for the lack of ongoing star formation. Using cuts on these parameters, French et al. (2016) found that QBS galaxies are

---

[1] The exact fraction of post-starburst/E+A galaxies in the general galaxy population depends on the spectroscopic classification cuts placed on the galaxy sample.

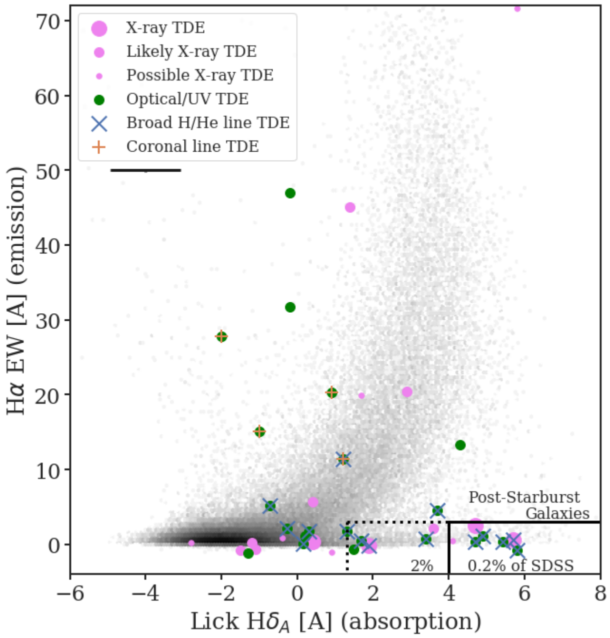

Figure 1.4: The Hα equivalent width versus Hδ absorption index for TDE hosts and a sample of SDSS galaxies. Hα is sensitive to current star formation while the Lick Hδ absorption index traces past star formation. Post-starburst galaxies occupy the lower right corner of the plot. Figure is from French et al. (2020b).

over-represented among the TDE hosts by a factor of 33$-$190. This overrepresentation has now been further observed by several other studies, with the preference persisting in TDE samples selected from optical to X-ray (Graur et al., 2018; Law-Smith et al., 2017; Sazonov et al., 2021). Law-Smith et al. (2017) attempted to explain this preference by accounting for possible selection effects due to SMBH mass, redshift completeness, strong AGN presence, bulge colors, and surface brightness. While they found that controlling for these factors (i.e., limiting the general galaxy comparison sample to values of these properties similar to the TDE hosts) can reduce the apparent post-starburst/E+A overrepresentation from $\sim \times 100 - 190$ to $\sim \times 25 - 48$, it cannot fully explain the preference.

Photometrically, this post-starburst preference can manifest as “green” optical colors measured from the rest-frame $u - r$ color (e.g., Law-Smith et al., 2017, and Chapter 3 of this thesis).

In the color-galaxy mass parameter space, shown in Figure 1.5, the "green valley" of galaxies resides between the "red sequence" of red, passive galaxies (typically elliptical/early-type galaxies) and the "blue cloud" of blue, star-forming galaxies (typically spiral/late-type galaxies). The mechanisms that lead to the evolution from the blue cloud to the green valley are varied, although mergers are one key pathway (e.g., Schawinski et al., 2010, 2014). Schawinski et al. (2010) found that green valley galaxies consistent with this merger scenario showed significantly more centrally concentrated galaxies with post-starburst stellar populations.

Interestingly, the post-starburst/green valley preference has not been observed in samples of TDEs recently discovered in the infrared (Masterson et al., 2024). The IR-selected host sample from Masterson et al. (2024) appears to be dominated by late-type galaxies, with several disturbed or merging galaxies. The IR host sample also tends to have more massive galaxies, though the authors suggest this is due to their relatively high limiting flux cut during sample selection. Compared to both optically selected and X-ray selected samples, the IR TDE hosts seem to prefer red galaxies, which may be due to either dust reddening or the age of the stellar population. Further modeling will be required to disentangle these effects. While the optical colors and star-formation histories of the IR TDE hosts may differ from other TDE host samples, other factors that may be more important for boosting the TDE rate could be similar. The red color of the IR TDE hosts suggests that they could be among the population of more bulge-dominated spiral galaxies and thus be more centrally concentrated than their disk-dominated counterparts. Additionally, many of the hosts in the IR sample appear to be barred spirals, a feature that has been noted among optically selected TDEs in spiral galaxies (Hammerstein et al., 2021a, 2023a; van Velzen et al., 2021). This may simply trace the fraction of barred spiral galaxies in the general galaxy population or it may hint at dynamical mechanisms that might boost the TDE

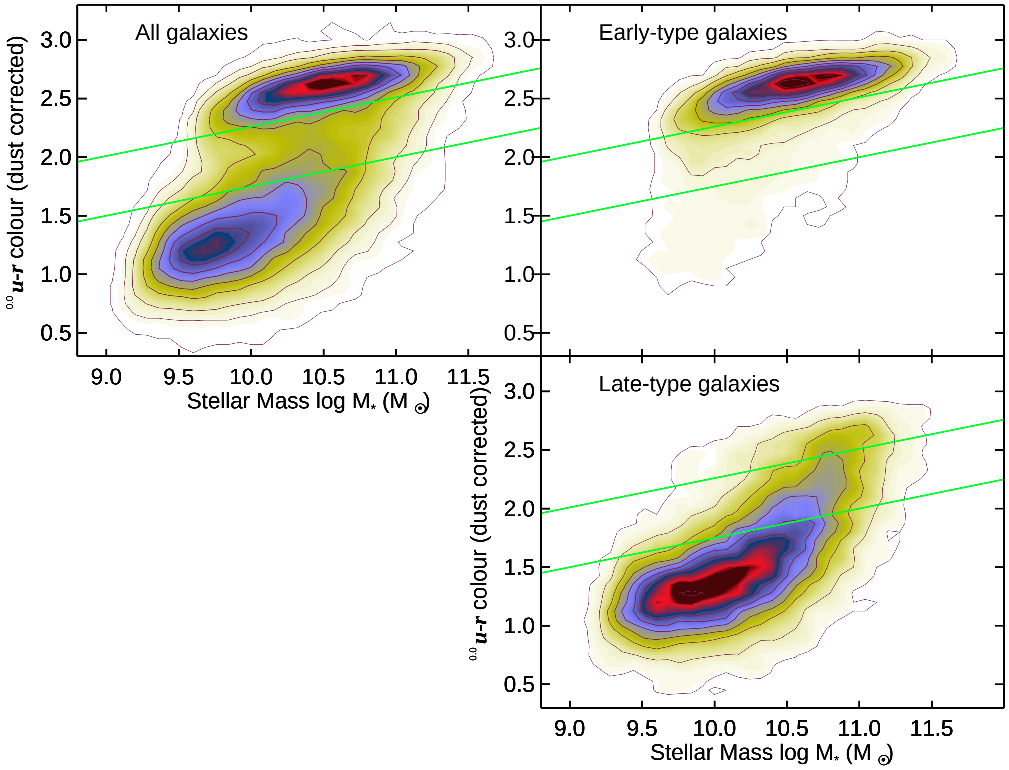

Figure 1.5: The reddening-corrected color-galaxy mass diagram from Schawinski et al. (2014). The top left panel shows all galaxies in their sample, while the right panels show the sample split by morphological type (early-type on top right, late-type on bottom right). The right panels illustrate that the red sequence is dominated by early-type galaxies while the blue cloud is dominated by late-type galaxies. The green valley, marked by the solid green lines, is made up of both early- and late-type galaxies.

rate in barred spirals. The discovery of this sample of IR TDEs implies that X-ray and optical surveys likely miss a significant fraction of TDEs in dusty galaxies. This is not surprising, given previous work has shown that accounting for dust significantly impacts the number of observed TDEs and the types of hosts they are observed in (Roth et al., 2021). Further work will be needed to determine whether other global properties, such as the central concentration of the galaxy light profile, show similarities to TDE host populations from optical and X-ray samples.

The central concentration of a galaxy light profile can quantified by the Sérsic profile (Sérsic, 1963), defined by:

$$I(R) = I_e \exp\left\{-b_n\left[\left(\frac{R}{R_e}\right)^{1/n} - 1\right]\right\}, \tag{1.7}$$

where R_e is the half-light radius or the radius that contains approximately half the total galaxy light, I_e is the intensity at that radius, n is the Sérsic index, and b_n is a function of the Sérsic index. A higher Sérsic index implies a steeper light profile, or more centrally concentrated, while a lower Sérsic index implies a shallower light profile (Figure 1.6). Elliptical galaxies are typically well-described by a Sérsic profile with $n = 4$, otherwise known as the de Vaucouleurs profile (de Vaucouleurs, 1948), whereas disk galaxies can be described by a Sérsic profile with $n = 1$, an exponential profile.

The global properties of a galaxy are unlikely to *directly* affect the TDE rate, as most TDEs are thought to be sourced from stars within the $0.1-10$ pc sphere of influence (Stone & Metzger, 2016, calculated for $10^{6-8} M_{\rm BH}/M_\odot$ SMBHs). Nonetheless, Graur et al. (2018) and Law-Smith et al. (2017) have both found significant trends in global galaxy properties which suggests that there must be a connection between these large-scale properties and nuclear properties that affect

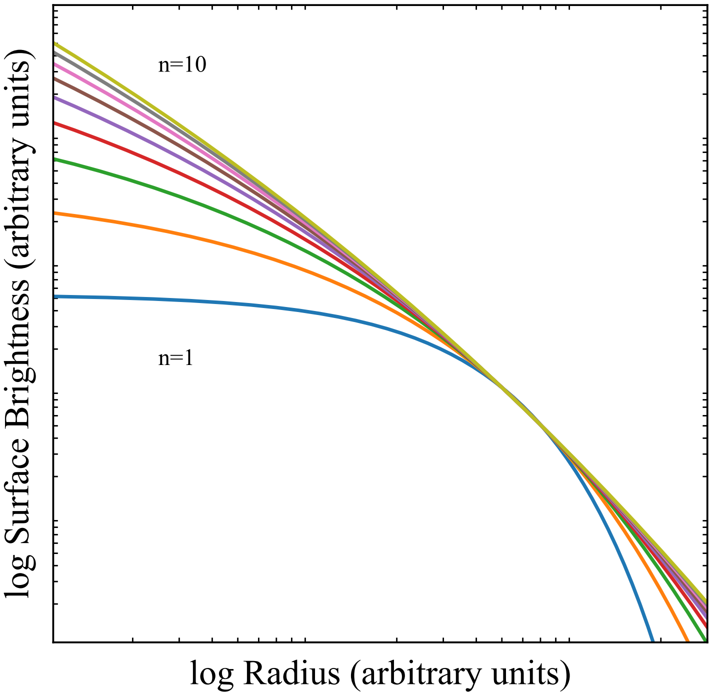

Figure 1.6: Example Sérsic profiles from $n = 1$ to $n = 10$. Elliptical galaxies can be described by a Sérsic profile with $n = 4$ (red line) while disk galaxies can be described by a Sérsic profile with $n = 1$ (blue line).

the TDE rate. Specifically, Graur et al. (2018) found that TDE hosts have, on average, a higher stellar mass surface density and marginally lower velocity dispersions than a control sample of galaxies. Law-Smith et al. (2017) found that TDE hosts, regardless of E+A classification, have higher Sérsic indices and higher bulge-to-total light ratios than galaxies of similar masses. This trend in concentration extends to higher-resolution studies with HST that can investigate properties on scales of 30−100 pc for the nearest TDE hosts. French et al. (2020a) indeed found that TDE hosts have higher central surface brightnesses and stellar mass surface densities on these scales, regardless of host galaxy type. The question remains how these large-scale properties connect to nuclear factors that boost the TDE rate in these galaxies.

Several studies have attempted to explain the connection between these large-scale properties, particularly the preference for post-starburst galaxies, and the TDE rate. E+A galaxies are known to have high Sérsic indices, large bulge-to-total light ratios, and high concentration indices (Yang et al., 2008). These properties are also common among TDE host populations, regardless of whether the host can be classified as E+A (e.g., French et al., 2020a; Graur et al., 2018; Law-Smith et al., 2017). The proposed merger-induced starburst which creates these stellar populations and global morphological properties could very well affect the nuclear regions in such a way as to boost the TDE rate in these galaxies. For example, the nuclear stellar overdensities created by the merger may lead to a greater number of stars that are available for disruption (French et al., 2020a; Stone & Metzger, 2016; Stone & van Velzen, 2016). This is seen in simulations where the merger-induced stellar overdensity results in a higher TDE rate at early times in the merger before the coalescence of the two SMBHs (Pfister et al., 2019). Additional merger-driven effects indeed include the possibility of a black hole binary. Other possible drivers for an enhanced TDE rate in post-starburst or post-merger systems include a circumnuclear gas disk, which has been predicted to enhance the TDE rate by a factor of up to 10 (Kennedy et al., 2016). This could work in tandem with other effects boosting the TDE rate, especially when merger-driven AGN activity is taken into account (e.g., Treister et al., 2012). However, as discussed in Section 1.4, many TDE searches exclude galaxies with pre-existing nuclear activity from consideration, likely creating a bias against discovering TDEs in galaxies with pre-existing circumnuclear gas disks.

In this thesis, I investigate the properties of a sample of TDE hosts selected from a single survey for the first time, to better understand the host galaxy preferences and drivers behind these preferences. I also perform the first population study of TDE hosts using integral field spectroscopy (IFS) to investigate their kinematic and stellar population properties on varying scales.

1.4 On the Optical Discovery of TDEs with ZTF

While early theoretical work predicted that TDEs would emit primarily in the X-ray regime, the advent of all-sky optical surveys has led to the discovery of dozens of optically bright TDEs, with many of them having no corresponding X-ray counterpart. These surveys have become so successful at discovering TDEs, that the majority of these events are now discovered in the optical[2], as shown in Figure 1.2. Of the most successful of these surveys is the Zwicky Transient Facility (ZTF, Figure 1.7).

The success of ZTF in discovering TDEs is largely due to the survey design and the efficient filtering and scanning methods applied to the ZTF transient alert stream, which allows TDE candidates to be selected even before peak. The main TDE search in ZTF is limited to transients within $0\farcs4$ of a known galaxy nucleus but places no requirements on host galaxy type or color, apart from filtering out known AGN using the Million Quasars Catalog (Flesch, 2015, v. 5.2) and constructed neoWISE (Mainzer et al., 2011) light curves to reject any galaxy with significant variability or a mean W1−W2 color consistent with the AGN threshold of Stern et al. (2012). The advantage of ZTF is that it regularly surveys the night sky in two primary optical filters: g and r. The color information provided by these filters ensures that TDE candidates can be differentiated from TDE "imposters" like nuclear SNe and AGN more easily. The three-night cadence of ZTF allows for the color change (or cooling) and rise and fade timescales of nuclear transients to be investigated.

In general, TDEs can be differentiated from nuclear SNe and even AGN pre-peak by the

---

[2] It should be noted that the large number of TDEs discovered in the optical compared to other wavelengths is a bias resulting from the current prevalence of optical surveys and should not necessarily be interpreted as a natural overabundance of TDEs in the optical.

mean pre-peak $g - r$ color and rise timescales (Figure 1.8). SNe typically rise at rates faster than TDEs and span a much larger range in mean color, with TDEs having a mean $g - r \lesssim 0.0$. AGN span a wide range of mean $g - r$ colors, but generally rise much slower than TDEs or SNe. TDE candidate selection becomes even clearer post-peak, where the rate of color change and rise and fade timescales provide further information to differentiate TDEs from AGN and SNe. While TDEs and AGN show similar rates of color change, SNe exhibit much faster rates of color change, typically becoming much cooler post-peak (Figure 1.9). Figure 1.10 demonstrates that the rise and fade timescales can differentiate TDEs from SNe and AGN, with SNe having the shortest rise and fade timescales and AGN having the longest. As compared to SNe, TDEs have slightly longer rise and fade timescales. These filtering methods narrow down the number of TDE candidates to a more reasonable size for optical spectroscopic follow-up and confident classification.

Once interesting TDE candidates have been identified from the photometric filtering, follow-up spectroscopy is required to confidently classify a transient as a TDE. In general, TDE classification is made upon the observation of a strong blue continuum with broad lines of hydrogen, helium, and occasionally Bowen fluorescence lines in the optical spectra. van Velzen et al. (2021) put forth three spectral classes of TDEs:

i. *TDE-H*: broad Hα and Hβ emission lines.

ii. *TDE-H+He*: broad Hα and Hβ emission lines and a broad complex of emission lines around He II λ4686. The majority of the sources in this class also show N III λ4640 and emission at λ4100 (identified as N III λ4100 instead of Hδ), and in some cases also O III λ3760.

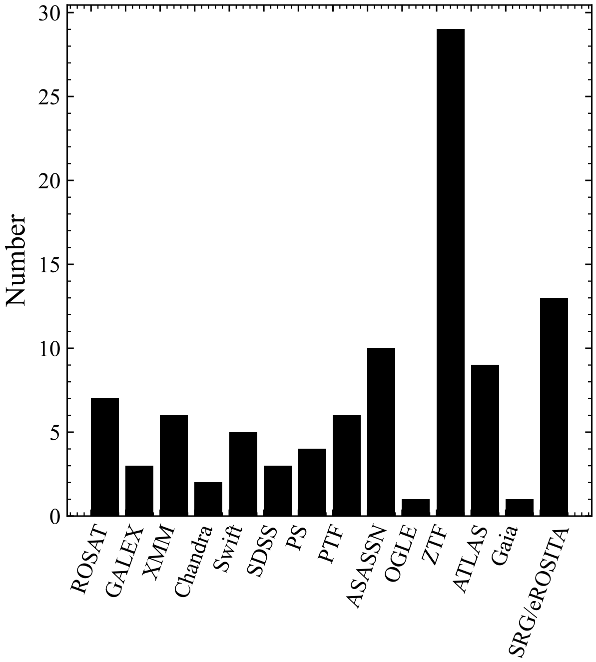

Figure 1.7: Reported discoveries of TDEs by their discovery survey/telescope, from 1996 until the publication of the events presented in this thesis (January 2023), including those presented as part of this thesis. Data from before 2020 is from Gezari (2021).

iii. *TDE-He*: no broad Balmer emission lines, a broad emission line near He II $\lambda4686$ only.

As part of this thesis, I present a fourth spectral class of TDE, described further in Chapter 2 (Hammerstein et al., 2023a):

iv. *TDE-featureless*: no discernible emission lines or spectroscopic features present in the three classes above, although host galaxy absorption lines can be observed.

In Figure 1.11, I show example spectra of the three main classes. These targeted discovery and classification methods have led to ZTF's discovery of over 38% of the optical TDEs from 2011 to 2022 (Figure 1.7), despite only having begun operations in 2018. 30 of the TDEs discovered in the first three years of ZTF are presented as part of this thesis.

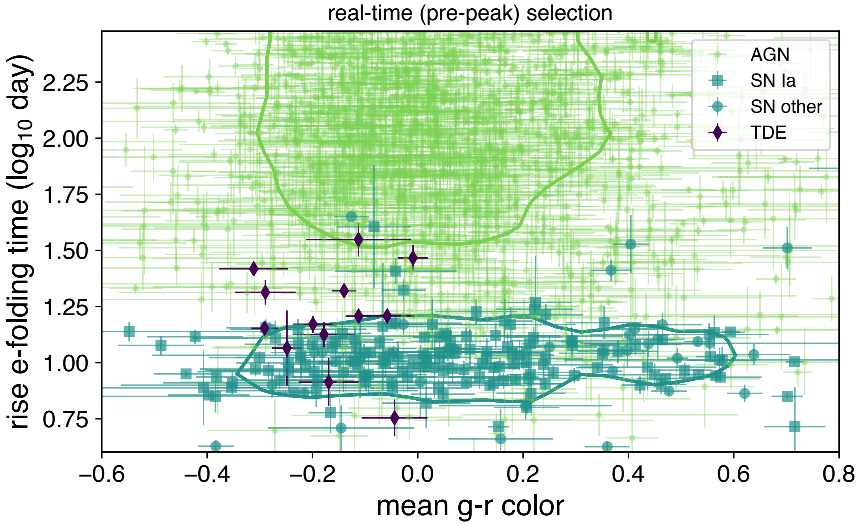

Figure 1.8: Rise timescale versus mean $g-r$ color for ZTF nuclear transients, used for pre-peak candidate selection. SNe generally rise to peak faster than TDEs and AGN and span a larger range in mean color compared to TDEs, which are bluer with a mean $g-r \lesssim 0.0$. Figure is from van Velzen et al. (2021).

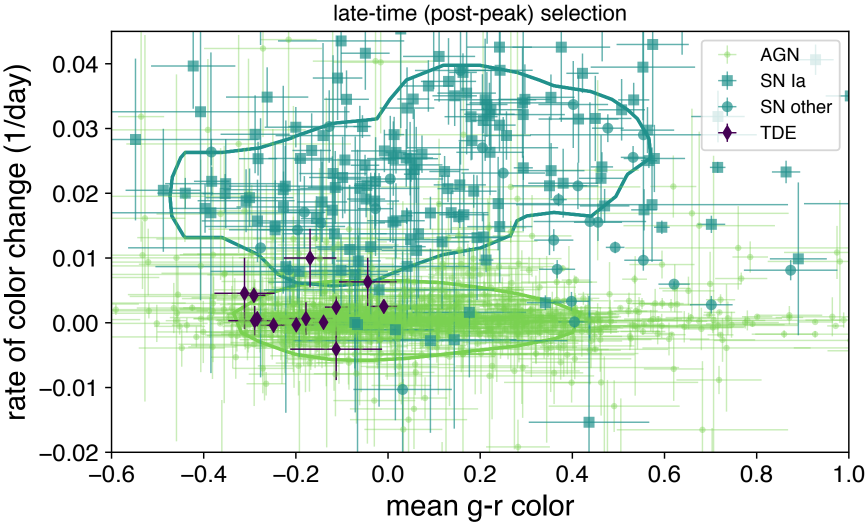

Figure 1.9: Rate of color change versus mean $g-r$ color for ZTF nuclear transients, used for post-peak candidate selection. SNe cool at much faster rates than TDEs or AGN and have a broader range of mean colors. Figure is from van Velzen et al. (2021).

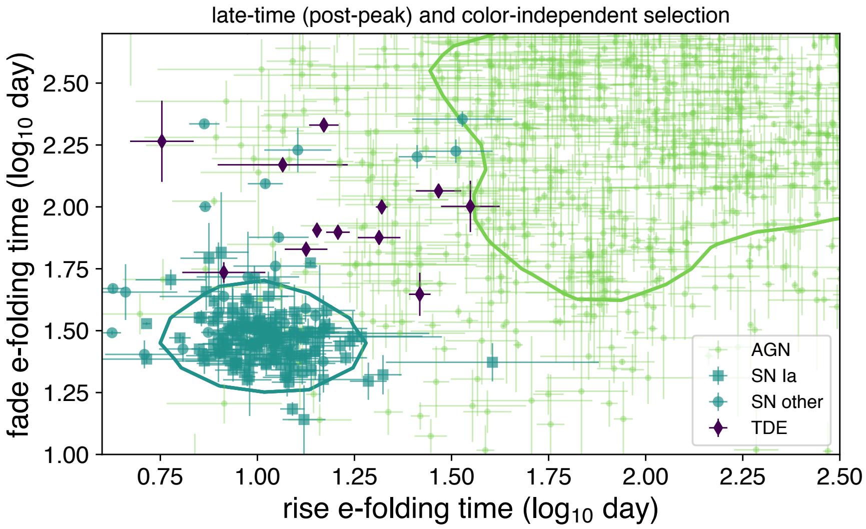

Figure 1.10: Fade timescale versus rise timescale for ZTF nuclear transients, used for post-peak candidate selection. SNe generally rise to peak and fade faster than TDEs and AGN. Figure is from van Velzen et al. (2021).

1.5 Scope of the Dissertation

The research performed as part of this thesis aims to address three main, open questions surrounding TDEs:

1. Where does the optical/UV emission in TDEs come from?
2. How are TDE host properties connected to the galaxy nucleus and TDE rate?
3. Can we use TDEs to measure the properties of SMBHs?

By answering these three questions, we can begin to answer broader questions regarding the nature of SMBH accretion and outflows, how SMBHs grow and evolve with their host galaxies, and how we can use future time-domain surveys to study the properties and evolution of SMBHs throughout cosmic history.

In Chapter 2, I present the discovery and characterization of 30 TDEs from the ZTF survey.

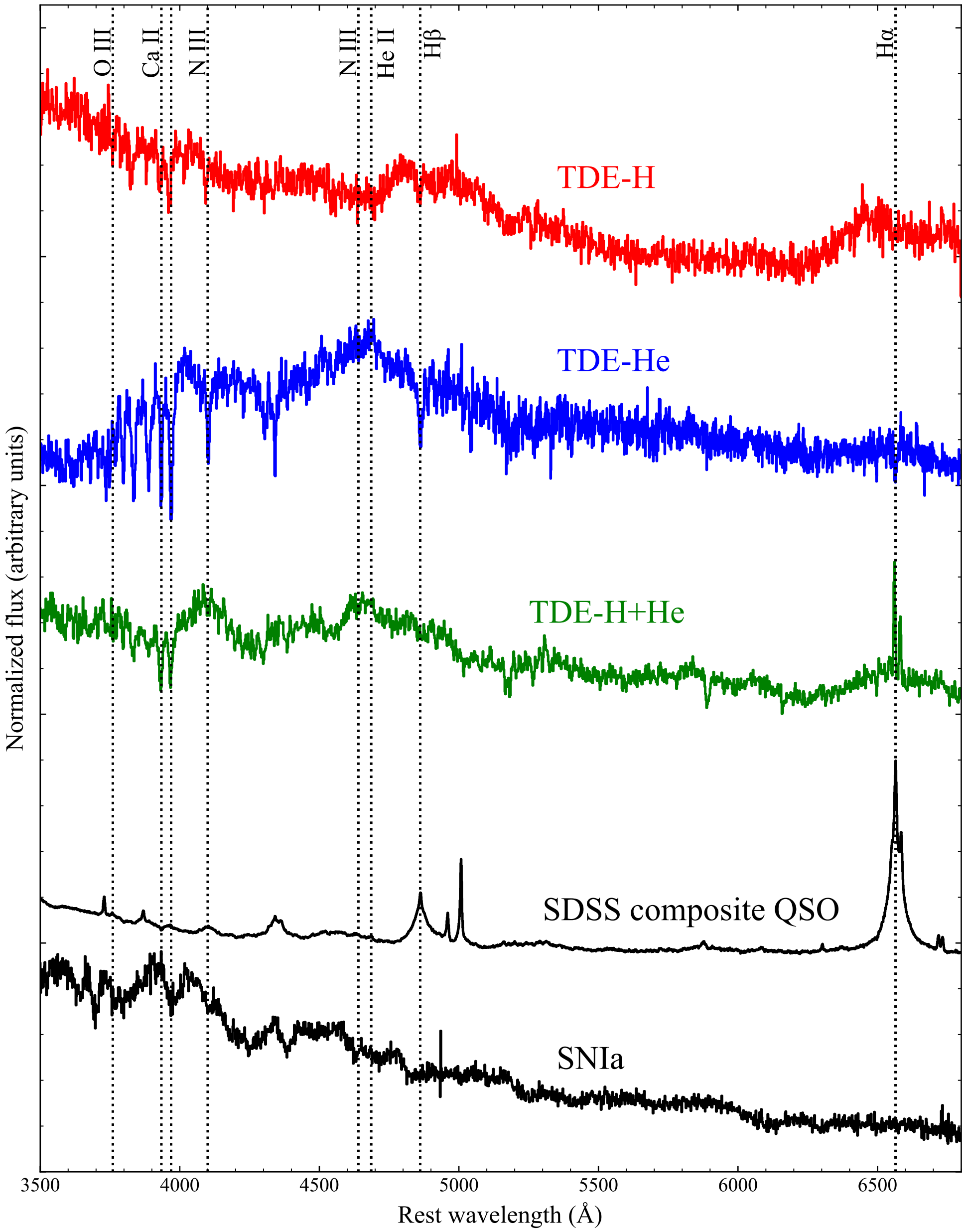

Figure 1.11: Optical spectra of the three TDE spectral classes plus a composite QSO spectrum and a SNIa spectrum for comparison. Optical TDE spectra are typically characterized by broad lines of hydrogen, helium, and occasionally N III and O III.

In Chapters 3 and 4, I present two studies on the nature of TDE host galaxies. I also present a study of the SMBHs at the centers of TDEs in Chapter 4. In Chapter 5, I present a study of the light curve and spectroscopic properties of the optically discovered jetted TDE AT2022cmc and place them in the context of other optically selected TDEs. I end with a summary of conclusions and a discussion on future directions in Chapter 6.

Chapter 2: The Final Season Reimagined: 30 Tidal Disruption Events from the ZTF-I Survey

2.1 Introduction

A tidal disruption event (TDE) occurs when a star passes close enough to a massive black hole (MBH), such that the tidal forces are stronger than the star's self-gravity and the star is ripped apart, causing a luminous flare of radiation from ∼half of the stellar debris that circularizes into an accretion disk and is accreted (Evans & Kochanek, 1989; Rees, 1988; Ulmer, 1999). While these events were first predicted theoretically almost 50 years ago (e.g., Hills, 1975; Lidskii & Ozernoi, 1979), the advent of all-sky surveys across the electromagnetic spectrum in the past several decades has been a catalyst for the discovery of these transients.

TDEs have now been observed from the radio to the X-rays, with wide-field optical surveys at the forefront of these discoveries, including iPTF (Blagorodnova et al., 2017, 2019; Hung et al., 2017), ASAS-SN (Hinkle et al., 2021; Holoien et al., 2014a, 2016a,b, 2019a; Wevers et al., 2019), Pan-STARRS (Chornock et al., 2014; Gezari et al., 2012; Holoien et al., 2019b; Nicholl et al., 2019), SDSS (van Velzen et al., 2011), and ZTF (van Velzen et al., 2019d, 2021), and now X-ray surveys, such as SRG/eROSITA (Sazonov et al., 2021). The growing number of TDEs discovered through these surveys is making their use as probes of MBH demographics, accretion, jet formation, and shock physics a reality. However, the origin of the strong optical and UV emission seen in these transients is still under debate and a resolution is required before these transients can be used to robustly study the properties of the MBHs behind these events (i.e., Mockler et al., 2019).

While the soft X-ray emission seen in some optically selected TDEs can be explained by thermal emission from the inner portions of the accretion disk (e.g., Saxton et al., 2021; Ulmer, 1999), the origin of the UV and optical emission is more puzzling. The blackbody radii measured from the UV/optical light curves are much larger than expected for the newly formed accretion disk (for a review, see Gezari, 2021), which has spurred several theories as to the nature of this larger structure. Outflows and winds have been proposed as the origin of this emission (Dai et al., 2018; Metzger & Stone, 2016), as well as shocks from the intersecting debris streams (Jiang et al., 2016; Piran et al., 2015). To further complicate the picture of TDE emission, the lack of an X-ray component in most optically selected TDEs is also not well understood. The most common explanations for this lack of X-ray emission are the absorption of the X-ray photons from the disk and subsequent reprocessing into optical/UV wavelengths (Auchettl et al., 2017; Guillochon et al., 2014), and the delayed onset of accretion and therefore X-ray emission due to the time it takes for the tidal debris to circularize and form an accretion disk (Gezari et al., 2017; Krolik et al., 2016; Piran et al., 2015). The model of Dai et al. (2018) proposes instead that viewing angle is responsible for the lack of X-rays in some optical TDEs and the detection of X-rays in others. The characterization of both the optical/UV and X-ray light curves is thus crucial to determining which of these models is at play.

The features observed in the optical spectra of TDEs are varied, with some having shown only He II emission (Gezari et al., 2012) and others showing evidence for Bowen fluorescence lines (Blagorodnova et al., 2019; Leloudas et al., 2019). Building on the classification scheme of Arcavi et al. (2014), van Velzen et al. (2021) presented a scheme for classifying the optical spectra into three categories with varying strengths of hydrogen and helium emission lines. Explanations for this observed diversity in spectroscopic features include the composition of the disrupted star due to stellar evolution (Kochanek, 2016a), details in the physics of photoionization (Gaskell & Rojas Lobos, 2014; Guillochon et al., 2014; Roth et al., 2016), and viewing angle effects (Holoien et al., 2019b; Hung et al., 2020). Here, we investigate whether the spectroscopic classes of TDEs show differences in their light curve and host galaxy properties.

In this paper, we present a sample of 30 spectroscopically classified TDEs from the ZTF survey, the largest systematically selected sample of TDEs from a single survey yet. We present our method for candidate selection and details on the sample in Section 2.2. We briefly discuss the host galaxy properties in Section 2.3 and describe the follow-up observations for each TDE in Section 2.4. We describe our methods for the analysis of the optical/UV light curves in Section 2.5 and we present our results in Section 2.6, an estimation of the MBH mass in Section 2.7, and a discussion in Section 2.8. We conclude with a summary in Section 2.9. Throughout this paper, we adopt a flat cosmology with $\Omega_\Lambda = 0.7$ and $H_0 = 70\ \mathrm{km\ s^{-1}\ Mpc^{-1}}$. All magnitudes are reported in the AB system.

2.2 The Search for TDEs in ZTF-I

2.2.1 TDE Candidate Selection

The first phase of the ZTF survey (hereafter ZTF-I; Bellm et al., 2019a; Graham et al., 2019) completed operations in October 2020. Over the course of the 2.6 year survey (March

2018 – October 2020), we conducted a systematic search for TDEs almost entirely within the public MSIP data (Bellm et al., 2019b), which observed the entire visible Northern sky every 3 nights in both g- and r-bands. The multi-band observations were key to the efficient filtering of the ZTF alert stream (Patterson et al., 2019), as they allowed us to narrow our search for TDEs to a specific subset of photometric properties that aid in the discrimination between TDEs and other nuclear transients, such as active galactic nuclei (AGN) and nuclear supernovae (SNe).

We will summarize the key aspects of our ZTF-I TDE search here, but we point the reader to van Velzen et al. (2021), where our filtering of the ZTF-I alert stream is described in more detail. Our filtering techniques included rejecting galaxies classified as broad-line AGN, but otherwise was not restricted to host galaxy type. We filtered known AGN using the Million quasar catalog (Flesch, 2015, v. 5.2) and constructed neoWISE (Mainzer et al., 2011) light curves to reject any galaxy with significant variability or a mean W1$-$W2 color consistent with the AGN threshold of Stern et al. (2012). We used the ZTF observations to filter on photometric properties which can discriminate TDEs from AGN and nuclear supernovae. These properties included $g - r$ color and rate of color change, in addition to rise and fade timescales. Specifically, our filters included rejecting transients that are significantly offset from the known galaxy host (mean offset $> 0\farcs4$), have significant $g - r$ color evolution ($d(g - r)/dt > 0.015$ day^{-1}), or show only a modest flux increase in the difference flux compared to the PSF flux in the ZTF reference image ($m_{\rm diff} - m_{\rm ref} > -1.5$ mag). This filtering allowed for a more focused spectroscopic follow-up effort, which allowed for further filtering of AGN and nuclear SNe based on features present in follow-up spectra. To manage data for the candidates, including photometry and spectra, we made use of the GROWTH Marshal (Kasliwal et al., 2019) and Fritz (Duev et al., 2019; van der Walt et al., 2019).

2.2.2 The ZTF-I TDE Sample

We present the entire sample of 30 TDEs classified during ZTF-I in Table 2.1, along with the IAU name, ZTF name, our internal nickname, names given by other surveys, and reference to the first classification as a TDE. The bolded names credit the first detection of the transient reported to the Transient Name Server (TNS). ZTF was the first to report 22/30 of the TDEs in this sample, with ATLAS providing 4 discoveries, ASAS-SN providing 2 discoveries, and PS1 and Gaia each providing 1 discovery.

Sixteen of these TDEs were originally presented as part of a ZTF-I sample in van Velzen et al. (2021). We note the exclusion of AT2019eve, which was included in van Velzen et al. (2021), but is not included here as the properties and evolution of the light curve and spectra of the source give rise to uncertainty in this classification.[1] We note that this issue is unlikely to affect other objects in our sample, which have much better spectral coverage post-peak.

2.2.3 Spectroscopic Classifications

We classify the TDEs into four spectroscopic classes, largely following the spectroscopic classification scheme given in van Velzen et al. (2021), which divides TDEs into three spectroscopic classes:

i. TDE-H: broad Hα and Hβ emission lines.

---

[1] AT2019eve was a sole outlier in light curve properties as compared to the rest of the sample in van Velzen et al. (2021), which led to the reconsideration of its classification. In addition to a fast rise and some reddening in the post-peak light curve, the source has only faint UV detections, all of which make the TDE classification less favorable. The Hα emission in the spectra that was originally used to classify the transient as a TDE persists over one year post peak, making association with the transient less likely. van Velzen et al. (2021) do not list a TDE spectral classification for this object.

ii. *TDE-H+He*: broad Hα and Hβ emission lines and a broad complex of emission lines around He II λ4686. The majority of the sources in this class also show N III λ4640 and emission at λ4100 (identified as N III λ4100 instead of Hδ), and in some cases also O III λ3760.

iii. *TDE-He*: no broad Balmer emission lines, a broad emission line near He II λ4686 only.

In addition to these three classes, we present a fourth spectroscopic class for TDEs:

iv. *TDE-featureless*: no discernible emission lines or spectroscopic features present in the three classes above, although host galaxy absorption lines can be observed.

Despite the lack of observed features in the optical spectra of these transients, they are nonetheless classified as TDEs due to their coincidence with galaxy nuclei, persistent blue optical colors, and other light curve properties consistent with the TDEs of other spectroscopic classes. We discuss the properties of this class of TDEs further in Section 2.8.

Our sample of TDEs contains 6 TDE-H, 3 TDE-He, 17 TDE-H+He, and 4 TDE-featureless, which we show in Figure 2.1. We note that the spectra used to classify these events have not been host galaxy subtracted, as host galaxy spectra are not yet available for all objects. We discuss the individual spectroscopic classifications and provide early- and late-time spectra for each object, when available, in Appendix A. While the four spectroscopic classes illustrate a clean division among spectroscopic features, there are still subtle differences among the spectra even within a particular class. TDEs in the TDE-H class all show strong, broad Hα and Hβ emission and lack He II, N III, and O III emission lines, but some also show evidence for Hγ emission. Furthermore, there is evidence for He I λ5876 in several TDE-H TDEs, such as AT2018zr and AT2018hco. The TDE-H+He shows similar variety in the lines that appear, with some showing hydrogen lines bluer than Hβ, some showing O III and N III, and He I λ5876. A more detailed analysis of the spectral features, including temporal evolution, present in this sample of TDEs will be presented in a forthcoming publication. For the purposes of this work we will only consider the spectroscopic class assigned to each TDE according to Table 2.1.

IAU Name	ZTF Name	GoT Name	Other/Discovery Name	First TDE Classification	Spectroscopic Class	Redshift
AT2018zr	ZTF18aabtxvd	Ned	**PS18kh**	ATel #11444	TDE-H	0.075
AT2018bsi	**ZTF18aahqkbt**	Jon		ATel #12035	TDE-H+He	0.051
AT2018hco	ZTF18abxftqm	Sansa	**ATLAS18way**	ATel #12263	TDE-H	0.088
AT2018iih	ZTF18acaqdaa	Jorah	**ATLAS18yzs**, Gaia18dpo	van Velzen et al. (2021)	TDE-He	0.212
AT2018hyz	ZTF18acpdvos	Gendry	**ASASSN-18zj**, ATLAS18bafs	ATel #12198	TDE-H+He	0.046
AT2018lni	**ZTF18actaqdw**	Arya		van Velzen et al. (2021)	TDE-H+He	0.138
AT2018lna	**ZTF19aabbnzo**	Cersei		ATel #12509	TDE-H+He	0.091
AT2018jbv	**ZTF18acnbpmd**	Samwell	ATLAS19acl, PS19aoz	This paper	TDE-featureless	0.340
AT2019cho	**ZTF19aakiwze**	Petyr		van Velzen et al. (2021)	TDE-H+He	0.193
AT2019bhf	**ZTF19aakswrb**	Varys		van Velzen et al. (2021)	TDE-H+He	0.121
AT2019azh	ZTF17aaazdba	Jaime	**ASASSN-19dj**, Gaia19bvo	ATel #12568[2]	TDE-H+He	0.022
AT2019dsg	**ZTF19aapreis**	Bran	ATLAS19kl	ATel #12752	TDE-H+He	0.051
AT2019ehz	ZTF19aarioci	Brienne	**Gaia19bpt**	ATel #12789	TDE-H	0.074
AT2019mha	ZTF19abhejal	Bronn	**ATLAS19qqu**	van Velzen et al. (2021)	TDE-H+He	0.148
AT2019meg	**ZTF19abhhjcc**	Margaery	Gaia19dhd	AN-2019-88	TDE-H	0.152
AT2019lwu	**ZTF19abidbya**	Robb	ATLAS19rnz, PS19ega	van Velzen et al. (2021)	TDE-H	0.117
AT2019qiz	**ZTF19abzrhgq**	Melisandre	ATLAS19vfr, Gaia19eks, PS19gdd	ATel #13131	TDE-H+He	0.015
AT2019teq	**ZTF19accmaxo**	Missandei		TNSCR #7482	TDE-H+He	0.087
AT2020pj	**ZTF20aabqihu**	Gilly	ATLAS20cab	TNSCR #7481	TDE-H+He	0.068
AT2019vcb	**ZTF19acspeuw**	Tormund	Gaia19feb, ATLAS19bcyz	TNSCR #7078	TDE-H+He	0.088
AT2020ddv	ZTF20aamqmfk	Shae	**ATLAS20gee**	ATel #13655	TDE-He	0.160
AT2020ocn	**ZTF18aakelin**	Podrick		ATel #13859	TDE-He	0.070
AT2020opy	**ZTF20abjwvae**	High Sparrow	PS20fxm	ATel #13944	TDE-H+He	0.159
AT2020mot	**ZTF20abfcszi**	Pycelle	Gaia20ead	ATel #13944	TDE-H+He	0.070
AT2020mbq	**ZTF20abefeab**	Yara	ATLAS20pfz, PS20grv	This paper	TDE-H	0.093
AT2020qhs	**ZTF20abowque**	Loras	ATLAS20upw, PS20krl	This paper	TDE-featureless	0.345
AT2020riz	**ZTF20abrnwfc**	Talisa	PS20jop	This paper	TDE-featureless	0.435
AT2020wey	**ZTF20acitpfz**	Roose	ATLAS20belb, Gaia20fck	TNSCR #7769	TDE-H+He	0.027
AT2020zso	**ZTF20acqoiyt**	Hodor	ATLAS20bfok	TNSCR #8025	TDE-H+He	0.057
AT2020ysg	**ZTF20abnorit**	Osha	ATLAS20bjqp, PS21cru	This paper	TDE-featureless	0.277

Table 2.1: The names of each of the 30 TDEs detected in ZTF-I, with boldface indicating the discovery name, i.e., the first survey to report photometry of the transient detection to the TNS, and the GoT name is the ZTF TDE Working Group nickname which references characters from the popular television show *Game of Thrones*. We also include the first TDE classification report, with abbreviations ATel corresponding to the Astronomer's Telegram[3], AN corresponding to AstroNotes [4], and TNSCR corresponding to TNS classification reports. The last two columns contain the TDE spectral class, as described in Section 2.2.3, and the redshift. Redshifts were determined using host galaxy stellar absorption lines or narrow emission lines associated with star formation, namely Ca II H and K or narrow Hα emission.

---

[2] See also Hinkle et al. (2021).

[3] `https://astronomerstelegram.org/`

[4] `https://www.wis-tns.org/astronotes`

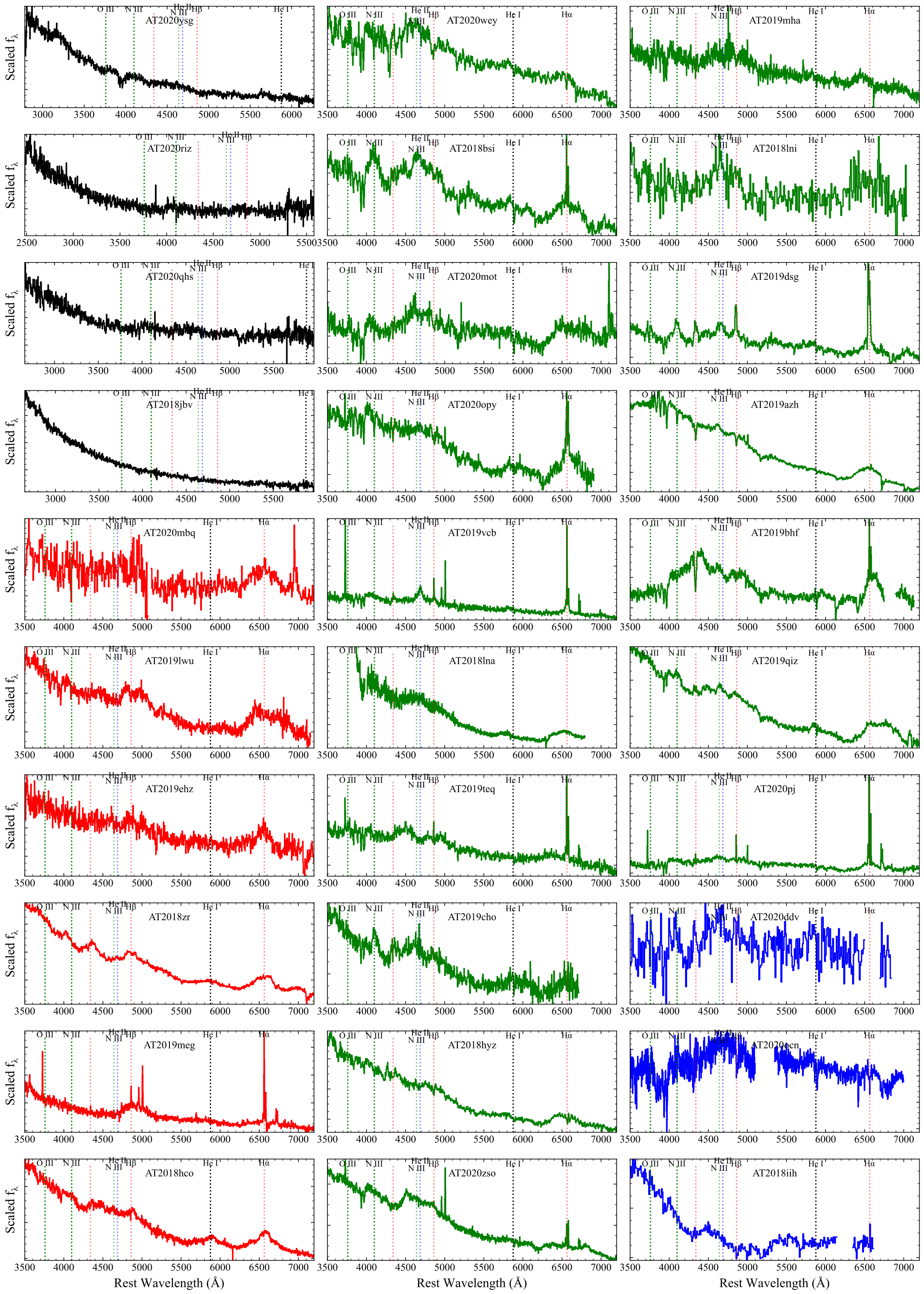

Figure 2.1: Spectral classifications for the ZTF-I TDE sample, which can also be found in Table 2.1, with black being TDE-featureless, red being TDE-H, green is TDE-H+He, and blue is TDE-He. Spectra have not been host galaxy subtracted. Details regarding the spectral classifications and more spectra are in Appendix A.

2.3 Host Galaxy Properties

In Figure 2.2 we show false-color gri cut-outs of the 30 TDE host galaxies from SDSS and Pan-STARRS, in order of increasing redshift. The majority of the hosts appear to be dominated by an elliptical component, with only the lowest redshift host galaxies showing a disk component accompanying a compact core. This may be an artifact of distance; in Figure 2.3 however, we show that very few of the TDE host galaxies fall in the blue cloud, a region where blue, disk-like galaxies are expected to reside. Additionally, Hammerstein et al. (2021a) found that many of the TDE hosts in this sample show morphological structure closer to that of red, elliptical galaxies despite falling in the green valley. Galaxies within the green valley, where a large number of TDE hosts fall, may still maintain a disk component, and better imaging is required to determine whether a disk component is present in these galaxies.

Using the pipeline of van Velzen et al. (2021), we fit SEDs of the TDE host galaxies constructed from pre-flare photometry in order to estimate the total stellar masses. This includes either SDSS model magnitudes or Pan-STARRS Kron magnitudes (if a source is outside the SDSS footprint), as well as GALEX NUV and FUV photometry. We use the Prospector software (Johnson et al., 2021) to run a Markov Chain Monte Carlo (MCMC) sampler (Foreman-Mackey et al., 2013), with 100 walkers and 1000 steps, to obtain the posterior distributions of the Flexible Stellar Population Synthesis models (Conroy et al., 2009). We discard the first 500 steps to ensure proper sampling of the posterior distribution. We follow the procedure of Mendel et al. (2014), adopting the same parameter choices for the 5 free parameters: stellar mass, Calzetti et al. (2000) dust model optical depth, stellar population age, metallicity, and the e-folding time of the star formation history. The results of this fitting are given in Table 2.2.

Figure 2.3 shows the extinction corrected, rest-frame $u-r$ color vs. total stellar mass of the TDE hosts estimated from the stellar population synthesis fits to the pre-flare photometry. Both panels in this figure show the same background sample of 30,000 SDSS galaxies taken from the Mendel et al. (2014) catalog of total stellar mass estimates, constructed in the same manner as in Hammerstein et al. (2021a), which corrects for the flux-limited nature of SDSS and produces a sample representative of the galaxies our search for TDEs is sensitive to. The top panel of Figure 2.3 also shows the limits of the green valley, the transition region between blue, star-forming galaxies and red, quiescent galaxies, originally defined by Schawinski et al. (2014).

Previous studies of TDE host galaxies have found that a majority of TDE hosts are green (Hammerstein et al., 2021a; Law-Smith et al., 2017). Most recently, Sazonov et al. (2021) found that a sample of X-ray bright TDE hosts discovered within the *SRG*/eROSITA survey were predominantly green. Hammerstein et al. (2021a) found that of the first 19 TDEs in this sample, 63% of them fell within the limits of the green valley. With an additional 11 TDE hosts, we find that 47% of the hosts fall within the green valley limits as defined in Hammerstein et al. (2021a) compared to only 13% of the background sample, with 9/30 TDE hosts in the red sequence and 7/30 in the blue cloud. However, 11/17 of the blue and red galaxies fall within 0.12 mag of the green valley limit, which can be difficult to define due to differences in sample selection and redshift cuts. We perform a binomial test to determine whether the number of TDE hosts within the green valley differs significantly from what is expected given the background sample of SDSS galaxies. We find that we can reject the null hypothesis that the TDE hosts are drawn uniformly from the sample of SDSS galaxies with a p-value $= 6.5 \times 10^{-6}$.

It is important to compare the properties of the TDE-featureless class to those of possible impostor transients and look-alikes. One such class of impostor are superluminous supernovae

(SLSN). The early-time light curves of TDEs and SLSN can be difficult to differentiate, and the optical spectra of SLSN can show features that can be mistaken for features characteristic of the 4 TDE spectroscopic classes described in Section 2.2.2 (Gal-Yam, 2012; Zabludoff et al., 2021). The early-time spectra of SLSN-II can even be featureless, making the classification of a transient as TDE-featureless more complicated. Figure 2.3 also shows the extinction corrected, rest-frame $u-r$ color vs. absolute r-band magnitude of the TDE hosts, along with a selection of SLSN host galaxies from TNS. SLSN hosts were chosen from those classified as SLSN-I and SLSN-II and were required to have SDSS observations for ease of data access. The distribution of SLSN hosts is not surprising, given previous studies of SLSN hosts (e.g. Hatsukade et al., 2018; Leloudas et al., 2015; Lunnan et al., 2014; Ørum et al., 2020; Perley et al., 2016; Schulze et al., 2018, 2021; Taggart & Perley, 2021). The majority of SLSN hosts shown in Figure 2.3 are blue, star-forming hosts, while all 4 TDE-featureless hosts are near or above the red edge of the green valley. This type of host color distinction, which has previously been discussed in French & Zabludoff (2018), will be important for distinguishing TDEs from impostors in the age of the Rubin Observatory. A more careful examination of the 30 TDE hosts in this sample, including spectroscopic $M_{\rm BH}-\sigma$ black hole mass estimates, will be presented in a forthcoming publication.

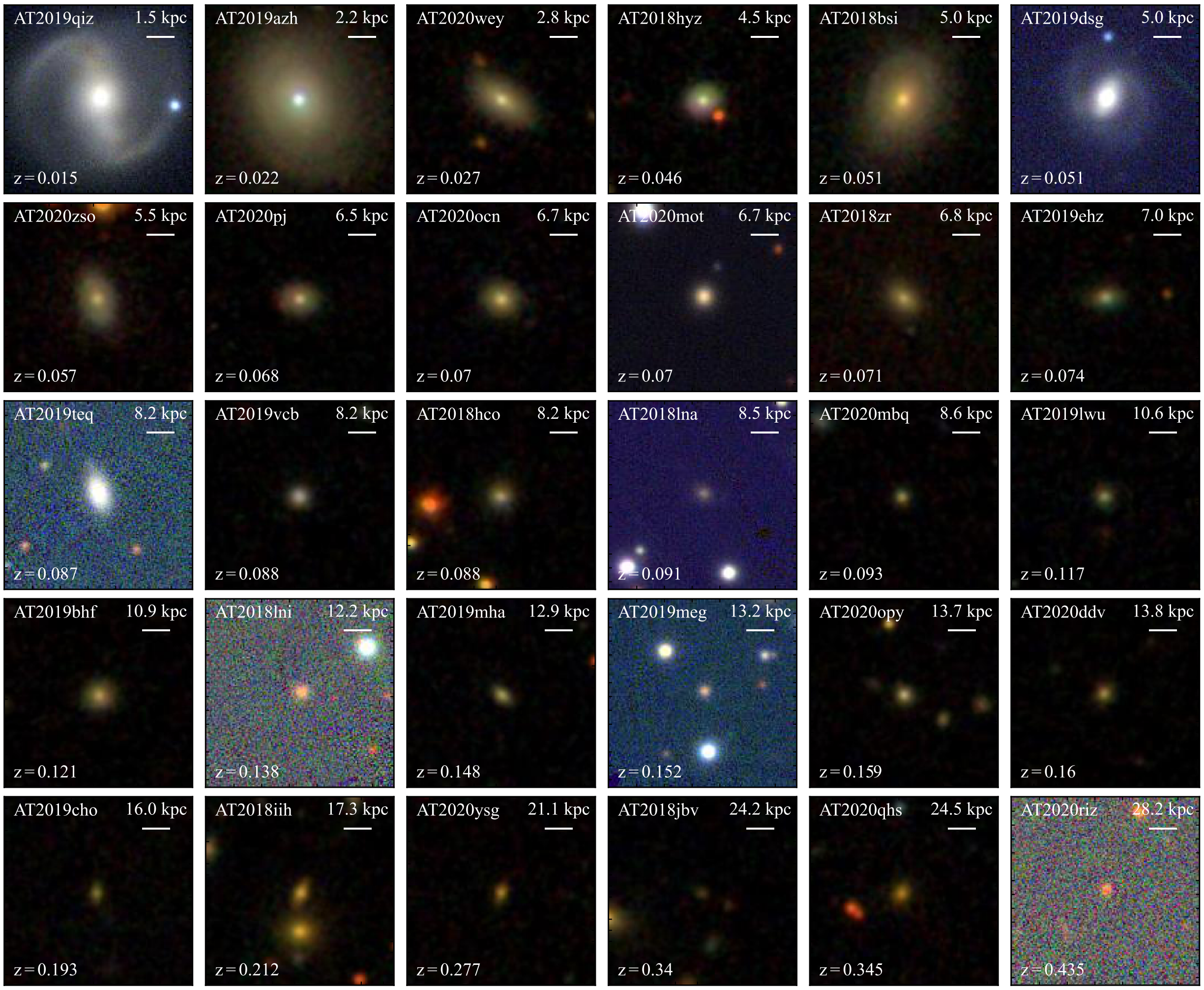

Figure 2.2: SDSS and Pan-STARRS gri images of the TDE host galaxies in order of increasing redshift. All images are $34'' \times 34''$. The morphology of the TDE hosts appears to be dominated by elliptical components, with only the lowest redshift TDEs showing discernible disk components.

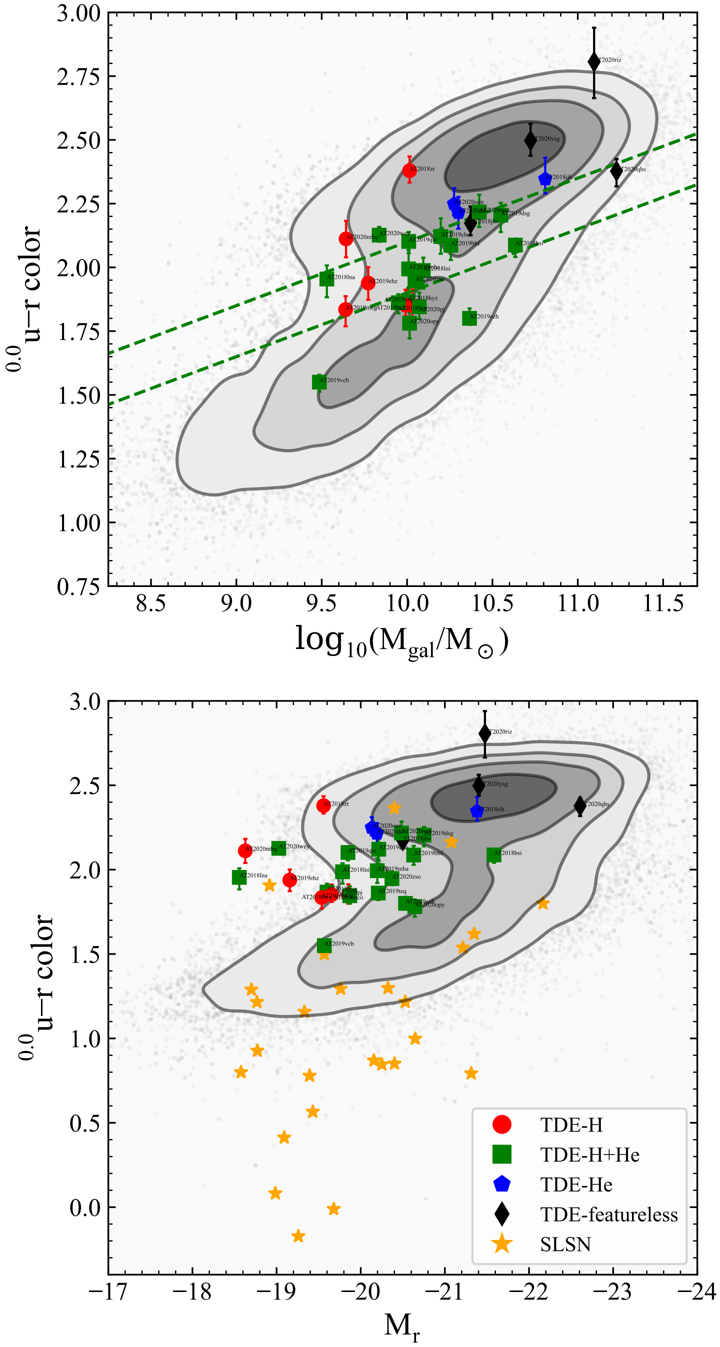

Figure 2.3: *Top*: The extinction-corrected, rest-frame $u - r$ color vs. total stellar mass of the TDE hosts, estimated from the stellar population synthesis fits to the pre-flare photometry. 47% of the TDE hosts are within the limits of the green valley, and 69% of the hosts outside of the green valley are within 0.12 mag of the boundary. Red circles are TDE-H; green squares are TDE-H+He; blue pentagons are TDE-He; and black diamonds are TDE-featureless. *Bottom*: The extinction-corrected, rest-frame $u - r$ color vs. absolute r-band magnitude of the TDE hosts, plus a selection of SLSN hosts from TNS with SDSS observations. The SLSN hosts are largely blue, star-forming galaxies, while the TDE hosts are dominated by green and red galaxies.

IAU Name	$\log M/M_\odot$	$^{0.0}u-r$	dust $E(B-V)$	age log **Gyr**	τ_{sfh} log **Gyr**	$\log Z/Z_\odot$
AT2018zr	$10.01^{+0.08}_{-0.14}$	$2.38^{+0.06}_{-0.05}$	$0.06^{+0.1}_{-0.04}$	$6.43^{+1.87}_{-2.67}$	$0.24^{+0.24}_{-0.11}$	$-0.09^{+0.17}_{-0.11}$
AT2018bsi	$10.62^{+0.05}_{-0.07}$	$2.09^{+0.03}_{-0.05}$	$0.76^{+0.17}_{-0.25}$	$3.08^{+0.63}_{-0.71}$	$0.8^{+0.14}_{-0.19}$	$-0.3^{+0.27}_{-0.4}$
AT2018hco	$10.03^{+0.12}_{-0.16}$	$1.85^{+0.06}_{-0.05}$	$0.2^{+0.13}_{-0.12}$	$7.44^{+3.42}_{-3.04}$	$0.31^{+0.32}_{-0.17}$	$-1.46^{+0.44}_{-0.37}$
AT2018iih	$10.81^{+0.11}_{-0.14}$	$2.35^{+0.08}_{-0.06}$	$0.38^{+0.31}_{-0.24}$	$7.2^{+3.39}_{-3.12}$	$0.27^{+0.34}_{-0.12}$	$-0.51^{+0.45}_{-0.44}$
AT2018hyz	$9.96^{+0.09}_{-0.16}$	$1.87^{+0.05}_{-0.04}$	$0.23^{+0.11}_{-0.14}$	$7.76^{+2.61}_{-2.9}$	$0.27^{+0.34}_{-0.14}$	$-1.48^{+0.52}_{-0.38}$
AT2018lni	$10.1^{+0.1}_{-0.13}$	$1.99^{+0.05}_{-0.07}$	$0.39^{+0.2}_{-0.22}$	$7.93^{+3.3}_{-2.86}$	$0.32^{+0.33}_{-0.17}$	$-1.5^{+0.44}_{-0.34}$
AT2018lna	$9.56^{+0.11}_{-0.14}$	$1.95^{+0.05}_{-0.07}$	$0.19^{+0.22}_{-0.14}$	$7.9^{+3.16}_{-2.98}$	$0.3^{+0.33}_{-0.16}$	$-1.23^{+0.32}_{-0.45}$
AT2018jbv	$10.34^{+0.14}_{-0.18}$	$2.17^{+0.07}_{-0.07}$	$0.44^{+0.49}_{-0.31}$	$5.83^{+4.09}_{-3.35}$	$0.43^{+0.74}_{-0.27}$	$-0.7^{+0.61}_{-0.55}$
AT2019cho	$10.2^{+0.14}_{-0.13}$	$2.12^{+0.07}_{-0.07}$	$0.33^{+0.31}_{-0.23}$	$5.95^{+3.74}_{-2.38}$	$0.37^{+0.39}_{-0.2}$	$-0.8^{+0.53}_{-0.55}$
AT2019bhf	$10.26^{+0.16}_{-0.15}$	$2.09^{+0.05}_{-0.06}$	$0.66^{+0.22}_{-0.39}$	$3.58^{+2.59}_{-1.46}$	$0.37^{+0.39}_{-0.21}$	$-1.04^{+0.56}_{-0.64}$
AT2019azh	$9.74^{+0.08}_{-0.05}$	$1.85^{+0.04}_{-0.03}$	$0.24^{+0.17}_{-0.17}$	$1.3^{+0.88}_{-0.29}$	$0.15^{+0.09}_{-0.03}$	$-0.27^{+0.22}_{-0.39}$
AT2019dsg	$10.55^{+0.09}_{-0.12}$	$2.2^{+0.05}_{-0.07}$	$0.31^{+0.25}_{-0.19}$	$8.82^{+2.42}_{-2.8}$	$0.34^{+0.38}_{-0.19}$	$-0.82^{+0.34}_{-0.38}$
AT2019ehz	$9.81^{+0.09}_{-0.12}$	$1.94^{+0.06}_{-0.07}$	$0.27^{+0.19}_{-0.18}$	$8.03^{+3.02}_{-2.73}$	$0.31^{+0.38}_{-0.16}$	$-1.33^{+0.42}_{-0.41}$
AT2019mha	$10.01^{+0.14}_{-0.18}$	$1.99^{+0.07}_{-0.07}$	$0.5^{+0.23}_{-0.23}$	$3.24^{+1.87}_{-1.61}$	$0.28^{+0.41}_{-0.13}$	$-1.07^{+0.79}_{-0.65}$
AT2019meg	$9.64^{+0.07}_{-0.08}$	$1.83^{+0.05}_{-0.07}$	$0.71^{+0.2}_{-0.27}$	$2.34^{+0.82}_{-0.63}$	$0.7^{+0.2}_{-0.2}$	$-0.61^{+0.57}_{-0.53}$
AT2019lwu	$9.99^{+0.09}_{-0.15}$	$1.85^{+0.06}_{-0.04}$	$0.15^{+0.13}_{-0.11}$	$8.66^{+2.55}_{-3.19}$	$0.26^{+0.29}_{-0.12}$	$-1.43^{+0.52}_{-0.39}$
AT2019qiz	$10.01^{+0.1}_{-0.12}$	$2.1^{+0.04}_{-0.05}$	$0.36^{+0.2}_{-0.24}$	$5.95^{+3.17}_{-1.94}$	$0.3^{+0.34}_{-0.15}$	$-0.97^{+0.25}_{-0.71}$
AT2019teq	$9.95^{+0.07}_{-0.11}$	$1.86^{+0.03}_{-0.04}$	$0.47^{+0.33}_{-0.34}$	$3.34^{+0.94}_{-1.27}$	$0.71^{+0.21}_{-0.31}$	$-0.79^{+0.39}_{-0.81}$
AT2020pj	$10.07^{+0.09}_{-0.13}$	$1.85^{+0.06}_{-0.05}$	$0.74^{+0.43}_{-0.47}$	$7.8^{+3.21}_{-3.64}$	$2.74^{+2.96}_{-1.94}$	$-1.44^{+0.63}_{-0.38}$
AT2019vcb	$9.49^{+0.06}_{-0.06}$	$1.55^{+0.03}_{-0.04}$	$0.67^{+0.2}_{-0.22}$	$1.74^{+0.54}_{-0.45}$	$0.69^{+0.18}_{-0.19}$	$-1.01^{+0.66}_{-0.37}$
AT2020ddv	$10.3^{+0.13}_{-0.16}$	$2.21^{+0.06}_{-0.06}$	$0.58^{+0.26}_{-0.35}$	$6.75^{+3.79}_{-2.86}$	$0.31^{+0.35}_{-0.15}$	$-1.03^{+0.62}_{-0.66}$
AT2020ocn	$10.28^{+0.13}_{-0.17}$	$2.25^{+0.06}_{-0.04}$	$0.76^{+0.14}_{-0.44}$	$6.7^{+4.09}_{-3.02}$	$0.27^{+0.31}_{-0.14}$	$-1.26^{+0.62}_{-0.55}$
AT2020opy	$10.01^{+0.13}_{-0.14}$	$1.78^{+0.04}_{-0.06}$	$0.45^{+0.21}_{-0.23}$	$2.25^{+1.51}_{-0.97}$	$0.29^{+0.38}_{-0.15}$	$-1.32^{+0.52}_{-0.47}$
AT2020mot	$10.42^{+0.07}_{-0.11}$	$2.22^{+0.07}_{-0.06}$	$0.13^{+0.23}_{-0.09}$	$9.12^{+2.32}_{-2.87}$	$0.29^{+0.34}_{-0.17}$	$-0.65^{+0.24}_{-0.35}$
AT2020mbq	$9.64^{+0.11}_{-0.15}$	$2.11^{+0.07}_{-0.07}$	$0.42^{+0.24}_{-0.26}$	$7.4^{+3.22}_{-3.05}$	$0.29^{+0.37}_{-0.15}$	$-1.11^{+0.44}_{-0.59}$
AT2020qhs	$11.23^{+0.07}_{-0.07}$	$2.38^{+0.05}_{-0.06}$	$0.09^{+0.12}_{-0.06}$	$5.81^{+1.96}_{-1.51}$	$0.45^{+0.38}_{-0.3}$	$0.0^{+0.05}_{-0.36}$
AT2020riz	$11.1^{+0.1}_{-0.13}$	$2.81^{+0.13}_{-0.14}$	$0.82^{+0.14}_{-0.22}$	$8.28^{+2.75}_{-3.13}$	$0.36^{+0.38}_{-0.21}$	$-0.19^{+0.29}_{-0.39}$
AT2020wey	$9.63^{+0.18}_{-0.22}$	$2.11^{+0.04}_{-0.07}$	$0.05^{+0.06}_{-0.04}$	$5.63^{+4.63}_{-3.42}$	$0.22^{+0.26}_{-0.1}$	$-0.25^{+0.37}_{-0.5}$
AT2020zso	$10.05^{+0.09}_{-0.12}$	$1.95^{+0.04}_{-0.04}$	$0.47^{+0.28}_{-0.26}$	$3.34^{+1.37}_{-1.36}$	$0.59^{+0.28}_{-0.3}$	$-0.96^{+0.52}_{-0.69}$
AT2020ysg	$10.72^{+0.11}_{-0.12}$	$2.5^{+0.07}_{-0.06}$	$0.45^{+0.33}_{-0.23}$	$3.62^{+2.27}_{-1.71}$	$0.17^{+0.16}_{-0.05}$	$0.12^{+0.05}_{-0.13}$

Table 2.2: The properties of the ZTF-I TDE host galaxies, as estimated from the SED fitting described in Section 2.3. We include the total stellar mass, the $u-r$ color, the color excess, age of the galaxy, the star formation e-folding timescale, and the metallicity. A rough star formation rate (SFR) can be calculated using the relation SFR $\propto e^{-t/\tau_{\mathrm{sfh}}}$.

2.4 Observations

2.4.1 ZTF Forced Photometry

We performed forced point spread function (PSF) photometry to extract precise flux measurements of each source through the ZTF forced-photometry service (Masci et al., 2019). The position of each source fed to the pipeline was taken as the median of the coordinates of all epochs in which the source was detected. The typical RMS scatter in R.A. and Dec. was $0\farcs19$ and $0\farcs14$ respectively. Photometry was gathered using ZTF DR12, including partnership data. Following the recommendations listed in Masci et al. (2019), we cleaned the resulting light curves by filtering out epochs that may have been impacted by bad pixels, and requiring thresholds for the signal-to-noise of the observations, seeing, the sigma-per-pixel in the input science image, and the 1-σ uncertainty on the difference image photometry measurement.

To correct for any systematic offsets in the forced photometric flux measurements, we define a temporal baseline for each ZTF field and filter combination. The baseline is defined using all observations up to 100 days prior to the peak of the flare (via visual inspection we confirm no pre-peak emission is included in the baseline window). For each field/filter combination, the median flux of the baseline is subtracted from all forced photometry flux measurements. We typically find small ($\sim$ 10 μJy), but significant offsets. In addition, we account for any systematic uncertainty by increasing the reported uncertainty with $\sqrt{\chi^2}/\mathrm{dof}$ of the observations in the baseline period.

We only accept photometry from ZTF field/filter combinations that have at least 5 observations in the baseline period. We also exclude fields for which the reference images were obtained after the baseline period (i.e., fields for which the transient is “caught in the reference frame”). An exception to the latter requirement is made for AT2018zr, AT2018bsi, and AT2018hyz. For these sources we allow a post-peak baseline using the last 180 days of observations in the light curve. The baseline corrections and the resulting ZTF forced photometry light curves will be available in machine-readable format at the journal website.

The forced-photometry light curves allow for detections over 800 days post-peak for some TDEs. The resulting forced-photometry light curves, which can be found in Appendix A, along with the follow-up observations described in the remainder of this section, are used in the analysis described below.

2.4.2 Swift (UVOT & XRT)

All 30 TDEs were followed up with observations from the *Neil Gehrels Swift Observatory* (Gehrels et al., 2004) in the UV with UVOT (Roming et al., 2005) and the X-ray with XRT (Burrows et al., 2005). We used the `uvotsource` package to analyze the *Swift* UVOT photometry, using an aperture of $5''$ for all sources except AT2019azh, AT2019bsi, AT2019qiz, and AT2019dsg, which required a larger aperture to capture the host galaxy light. We subtracted the host galaxy flux estimated from the population synthesis described in Section 2.3.

The 0.3–10 keV X-ray light curves for the 9/30 TDEs with XRT detections were produced using the UK Swift Data center online XRT data products tool, which uses the HEASOFT v6.22 software (Arnaud, 1996). We used a fixed aperture at the ZTF coordinate of the transient, and converted to flux using the best fit blackbody model to the stacked XRT spectrum. The XRT stacked spectra were processed by the XRT Products Page (Evans et al., 2009), with Galactic extinction fixed to values from the HI4PI survey (HI4PI Collaboration et al., 2016) shown in Table 2.3. The blackbody temperatures used to convert from counts/sec to flux using the online PIMMS tool[5] are also shown in Table 2.3.

Name	$N_{\rm H}/10^{20}$ cm^{-2}	kT/keV
AT2018zr	4.4	0.100
AT2018hyz	2.59	0.132
AT2019azh	4.16	0.053
AT2019dsg	6.46	0.071
AT2019ehz	1.42	0.101
AT2019teq	4.54	0.200
AT2019vcb	1.45	0.100
AT2020ddv	1.35	0.081
AT2020ocn	0.93	0.120

Table 2.3: Galactic extinction values and blackbody temperatures (for converting counts/sec to flux) used in the XRT reduction.

While all 30 TDEs have at least one epoch of simultaneous UVOT and XRT observations, it is difficult to define "X-ray bright" and "X-ray faint" classifications of the 30 TDEs, as there may be higher redshift TDEs which have X-ray emission that is below the flux limit for XRT and will thus go undetected. To account for this, we set a luminosity limit of $\log L_{\rm X} = 42$ ergs/s, and define a redshift cut-off, $z = 0.075$, beyond which that luminosity would no longer be detected by the typical XRT observation of 2.0 ks. We define "X-ray bright" to be any TDE with an XRT detection above the luminosity cutoff *and* a redshift below the redshift cutoff. We have therefore excluded one X-ray detected TDE from the "X-ray bright" group, AT2018zr, which has no detections above $\log L_{\rm X} = 42$ ergs/s, and moved it into the "X-ray faint" sample. We define "X-ray faint" (or dim) as any TDE below the redshift cut-off which has no XRT detections above the luminosity cutoff. This X-ray faint sample includes AT2018zr, AT2018bsi, AT2019qiz,

---

[5] `https://cxc.harvard.edu/toolkit/pimms.jsp`

AT2020pj, AT2020mot, AT2020wey, and AT2020zso.

2.4.3 ATLAS

We obtained additional forced photometry of all 30 TDEs from the Asteroid Terrestrial-impact Last Alert System (ATLAS) survey using the ATLAS forced photometry service[6] (Smith et al., 2020; Tonry et al., 2018). The ATLAS difference image forced photometry is less straightforward to clean in a similar manner to the ZTF forced photometry, as the metadata for each observation is not as comprehensive. We removed epochs with significantly negative flux measurements and large errors, as well as significant outliers.

The ATLAS forced photometry is included in the light curve fitting for the majority of the TDEs in this sample. For some TDEs, however, the reference image used for the difference image photometry changed partway through the event to a reference image that included the flare itself. This led to incorrect baselines for the difference image photometry, and without knowledge of which observations belong to which reference image, there is no straightforward way to perform robust baseline corrections as for the ZTF forced photometry. Therefore, we do not use the ATLAS forced photometry when fitting the light curves of the following 10 TDEs: AT2018bsi, AT2018iih, AT2018jbv, AT2019cho, AT2019dsg, AT2019ehz, AT2019mha, AT2019meg, AT2019lwu, and AT2020wey.

---

[6] `https://fallingstar-data.com/forcedphot/`

2.5 Light Curve Analysis

2.5.1 Model Fitting

Similar to van Velzen et al. (2021), we consider two models to describe the TDE light curve and fit the K-corrected multi-band data: an exponential decay and a power-law decay, both combined with a Gaussian rise. The Gaussian rise is chosen to be consistent with van Velzen et al. (2021) and avoids the addition of the power-law index as a free parameter in a rise characterized by a power-law. The first of these models, which is fit to only the first 100 days post-peak, is described by the following equation:

$$L_\nu(t) = L_{\nu_0\ \mathrm{peak}} \frac{B_\nu(T_0)}{B_{\nu_0}(T_0)} \times \begin{cases} e^{-(t-t_{\mathrm{peak}})^2/2\sigma^2} & t \leq t_{\mathrm{peak}} \\ e^{-(t-t_{\mathrm{peak}})/\tau} & t > t_{\mathrm{peak}} \end{cases} \tag{2.1}$$

In this equation, ν_0 refers to the reference frequency, which we have chosen to be the g-band (6.3×10^{14} Hz), and thus $L_{\nu_0\ \mathrm{peak}}$ is the luminosity at peak in this band. The g-band is chosen as the reference frequency to minimize the K-correction applied to the ZTF data. This model fits for only one temperature, T_0, which is used to predict the luminosity in the other bands at all times by assuming the spectrum follows a blackbody, $B_\nu(T_0)$.

We fit the long-term light curve ($\leq$350 days post-peak) with a Gaussian rise and power-law decay, to more accurately capture the deviation from exponential decay that most TDEs show (e.g. van Velzen et al., 2021). Fits to the photometry at times much longer than 400 days post-peak would require an additional constant component in the model to capture the plateaus that are seen in late-time TDE light curves (van Velzen et al., 2019c). This model is described by the following equation:

$$L(t,\nu) = L_{\mathrm{peak}} \frac{\pi B_\nu(T(t))}{\sigma_{\mathrm{SB}} T^4(t)} \times \begin{cases} e^{-(t-t_{\mathrm{peak}})^2/2\sigma^2} & t \leq t_{\mathrm{peak}} \\ [(t - t_{\mathrm{peak}} + t_0)/t_0]^p & t > t_{\mathrm{peak}} \end{cases} \tag{2.2}$$

We consider two types of temperature evolution with this model: linear and non-parametric evolution which allows for much more freedom in the way the temperature can evolve. In this more flexible, non-parametric temperature model, we fit the temperature at grid points spaced ±30 days apart beginning at peak and use a log-normal Gaussian prior at each grid point centered on the mean temperature obtained from Equation 2.1. The resolution of the temperature grid is chosen so that this method of fitting is applicable to all objects in our sample. While UV coverage at a resolution finer than 30 days is available for some objects, this is not the case for all objects in the sample.

To estimate the parameters of the models above we use the `emcee` sampler (Foreman-Mackey et al., 2013) using a Gaussian likelihood function that includes a "white noise" term, ln(f), that accounts for any variance in the data not captured by the reported uncertainties and flat priors for all parameters (except when employing the flexible temperature evolution as described above). We use 100 walkers and 2000 steps, discarding the first 1500 steps to ensure convergence. The free parameters of the models are listed in Table 2.4. We show the rest-frame absolute r-band magnitude, and derived blackbody luminosity, radius, and temperature with time in Figure 2.4.

Parameter	Description	Prior
$\log L_{\rm peak}$	Peak luminosity	$[L_{\rm max}/2, 2L_{\rm max}]$
$t_{\rm peak}$	Time of peak	[-20, 20] days
$\log T_0$	Mean temperature	[4, 5] Kelvin
$\log \sigma$	Gaussian rise time	[0, 1.5] days
$\log \tau$	Exponential decay time	[0, 3] days
p	Power-law index	[-5, 0]
$\log t_0$	Power-law normalization	[0, 3] days
dT/dt	Temperature change	[-200, 200] K day^{-1}
ln f	White noise factor	[-5, -1.8]

Table 2.4: The free parameters and corresponding priors for the light curve analysis described in Section 2.5.1. $L_{\rm max}$ is the observed maximum luminosity.

2.5.2 Empirical Timescale Estimates

To ensure that any correlations found between light curve properties, particularly the timescales, are not simply a product of the chosen model, we also measured the rise and peak timescales empirically. We calculate the time between the peak magnitude, $m_{\rm peak}$, and one magnitude fainter than peak, $m_{\rm peak} + 1$ mag, on both sides of the estimated peak of the light curve to measure the rise and decay timescales. The value $m_{\rm peak}+1$ mag often fell between two observed points on the light curve. We fit for $t_{m_{\rm peak}+1}$ on both sides of the peak in order to obtain the most likely value and uncertainties to accurately estimate the empirical rise and fade timescales, accounting for the uncertainties on the adjacent points and the uncertainty on the slope between them. These empirical rise and decay timescales are positively correlated with rise and decay timescales measured in Section 2.5, which implies that the light curve properties and resulting correlations found from our fits are not merely a product of our chosen model.

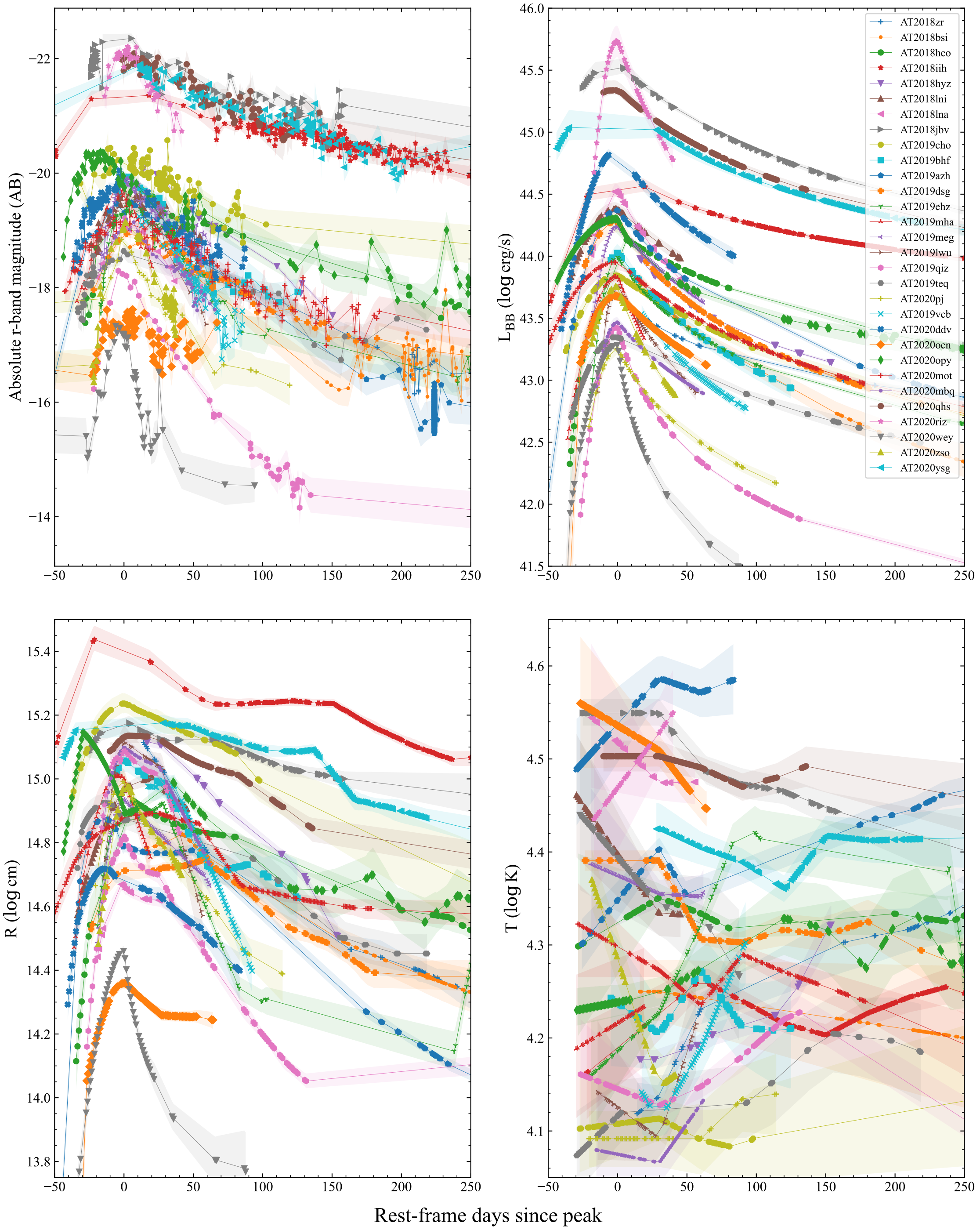

Figure 2.4: The r-band absolute magnitude, blackbody luminosity, blackbody radius, and blackbody temperature for the TDEs in our sample. The TDE-featureless class shows a distinct separation from the other classes in absolute magnitude and blackbody luminosity. All TDEs show a decrease in radius after peak and there is a spread in the change in temperature, with some events showing a modest decrease in temperature and some showing a modest increase in temperature.

2.6 Results

We present the results of the analysis described in Section 2.5. In the following sections, we will discuss our search for correlations between the light curve parameters and the host galaxy properties. We also investigate differences between the spectroscopic classes of TDEs and the light curve classes of TDEs, as well as the differences between the X-ray bright and X-ray faint events. We note the caveat that the results presented in this section, particularly the p-values, do not include a correction for the "look-elsewhere" effect. We discuss this in Section 2.6.4.

2.6.1 Light Curve Property Correlations

We searched for correlations between all of the parameters in the light curve fitting described in Section 2.5.1 using a Kendall's tau test (Kendall, 1938), the results of which are shown in Table A.4. We consider a correlation to be significant if we can reject the null hypothesis that the variables are uncorrelated at a significance level of $p < 0.05$.

We find significant correlations between the peak luminosity and the radius, as is expected from $L_{\rm BB} \propto R^2T^4$. In Figure 2.5, we show the peak blackbody luminosity and the rise timescale compared to the decay timescale. We find a significant, although shallow, positive correlation between the peak luminosity and the decay e-folding timescale (p-value $= 0.031$). We find that the rise timescale and the decay e-folding timescale are weakly positively correlated (p-value < 0.001), however, we find no significant correlation between the rise timescale and the luminosity.

We now turn to the correlations between the light curve properties and the host galaxy properties, particularly $M_{\rm gal}$. The properties of the light curve can be expected to be correlated with host galaxy mass, as the properties of the MBH should be imprinted on the TDE light curve and the host galaxy mass is correlated with the MBH mass. We show a selection of light curve properties vs. the host stellar mass in Figure 2.6. We find that the peak blackbody luminosity as well as the peak blackbody temperature are positively correlated with the mass of the host galaxy (p-value $= 0.005$ and $= 0.031$, respectively). We also find that the rise timescale and decay e-folding timescale is positively correlated with the mass of the host galaxy (p-value $= 0.019$ and $= 0.016$, respectively). We find no significant correlation with the fallback time-scale, defined as t_0 when $p = -5/3$. This may be due to late-time plateaus in the post-peak light curve.

2.6.2 Spectral Class Correlations

We used an Anderson-Darling test (Anderson & Darling, 1954) to assess whether the four spectroscopic classes of TDEs show differences in their light curve or host galaxy properties. The results of this test are shown in Table A.5. We consider a result to be significant if we can reject the null hypothesis that the two samples are drawn from the same parent population at a significance level of $p < 0.05$. We also show the cumulative distributions of the light curve properties and the cumulative distributions of the host galaxy mass in Figures 2.5 and 2.6.

We first examine the properties measured from the light curves. We do not find any significant (p-value < 0.05) differences in the rise timescales of the light curves for the four classes. We note that the spectral classifications in van Velzen et al. (2021) contained many more TDE-H objects, including events prior to ZTF-I, while three have been reclassified here as another class following more spectroscopic observations, which may explain why we no longer find a difference between the rise times of these two classes. We find that the TDE-featureless class has

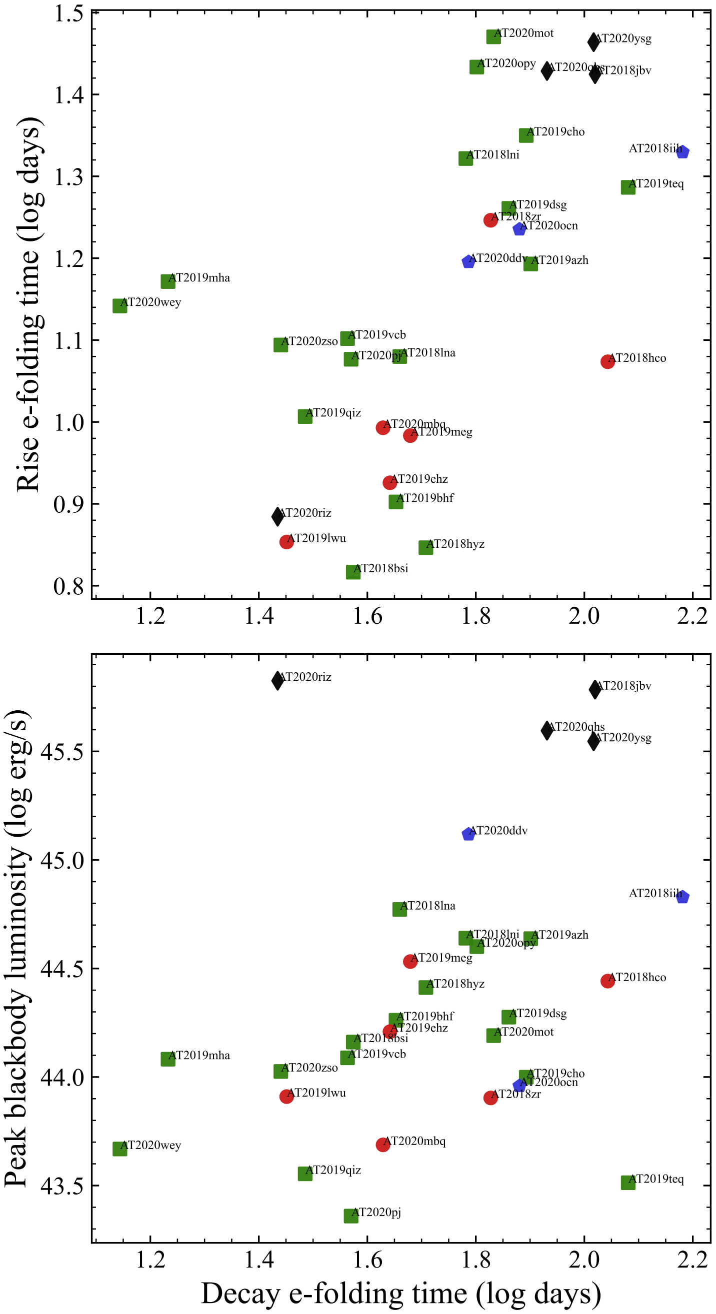

Figure 2.5: We show the peak blackbody luminosity and the rise time compared with the decay timescale. We find that both the blackbody luminosity and the rise timescale are positively correlated with the decay timescale. The colors and symbols are the same as in Figure 2.3.

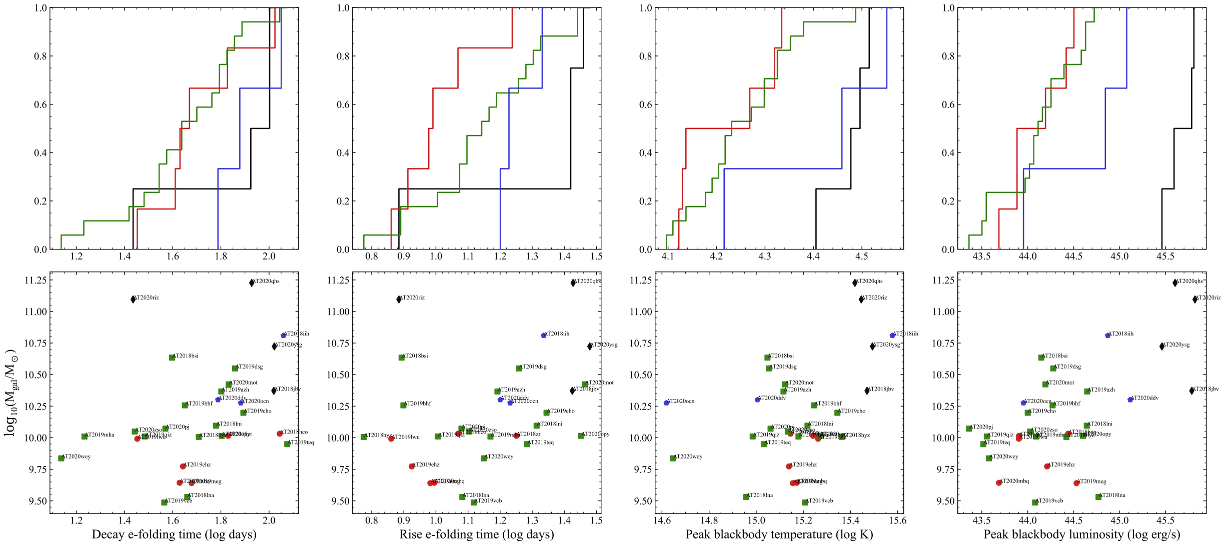

Figure 2.6: Selected properties measured from the fits to the multi-band light curves compared to the host galaxy stellar mass, with the cumulative distributions of spectroscopic classes. We find significant correlations between the host galaxy stellar mass and the properties shown, which include the decay e-folding timescale, the rise timescale, and the peak blackbody temperature and luminosity. We do not find that the spectroscopic classes show significant differences in their light curve decay or rise timescales, but the TDE-featureless class shows higher luminosities, temperatures, and radii than the other three classes. Both the TDE-He and TDE-featureless classes show significantly more massive host galaxies. The colors and symbols are the same as in Figure 2.3.

significantly hotter temperatures and larger radii when compared to the TDE-H and TDE-H+He classes, and higher peak blackbody and g-band luminosities when compared to all other classes.

Both TDE-He and TDE-featureless show significant differences in their host galaxy properties when compared to TDE-H and TDE-H+He. The TDE-featureless class shows a distribution favoring more massive and redder galaxies when compared to both TDE-H and TDE-H+He. The TDE-He possesses more massive galaxies as compared to the TDE-H class, with redder galaxies compared to the TDE-H+He class.

2.6.3 X-ray Correlations

We also employed an Anderson-Darling test to evaluate the differences in the X-ray bright and X-ray faint populations in this sample and test the null hypothesis that these two samples are drawn from the same parent population. As described in Section 2.4.2, we define X-ray bright to be a TDE with at least one detection of $\log L_{\rm X} \geq 42$ ergs/s and below a redshift of $z = 0.075$. We define X-ray faint to be any TDE below a redshift of $z = 0.075$ without an XRT detection. This gives an X-ray faint sample of 6 TDEs, compared to 8 X-ray bright TDEs. One TDE detected with XRT, AT2018zr, has no detections with $\log L_{\rm X} \geq 42$ ergs/s but is within the redshift cutoff, and so we include this object in the X-ray faint sample.

We find that the X-ray bright and X-ray faint TDEs differ only in their peak luminosities, with both the peak blackbody luminosity and peak g-band luminosity of the X-ray bright TDEs being more luminous (p-value $= 0.049$ and $= 0.045$, respectively). We show the results of the Anderson-Darling tests in Table A.5. We also show the cumulative distributions of the selected properties in Figure 2.7.

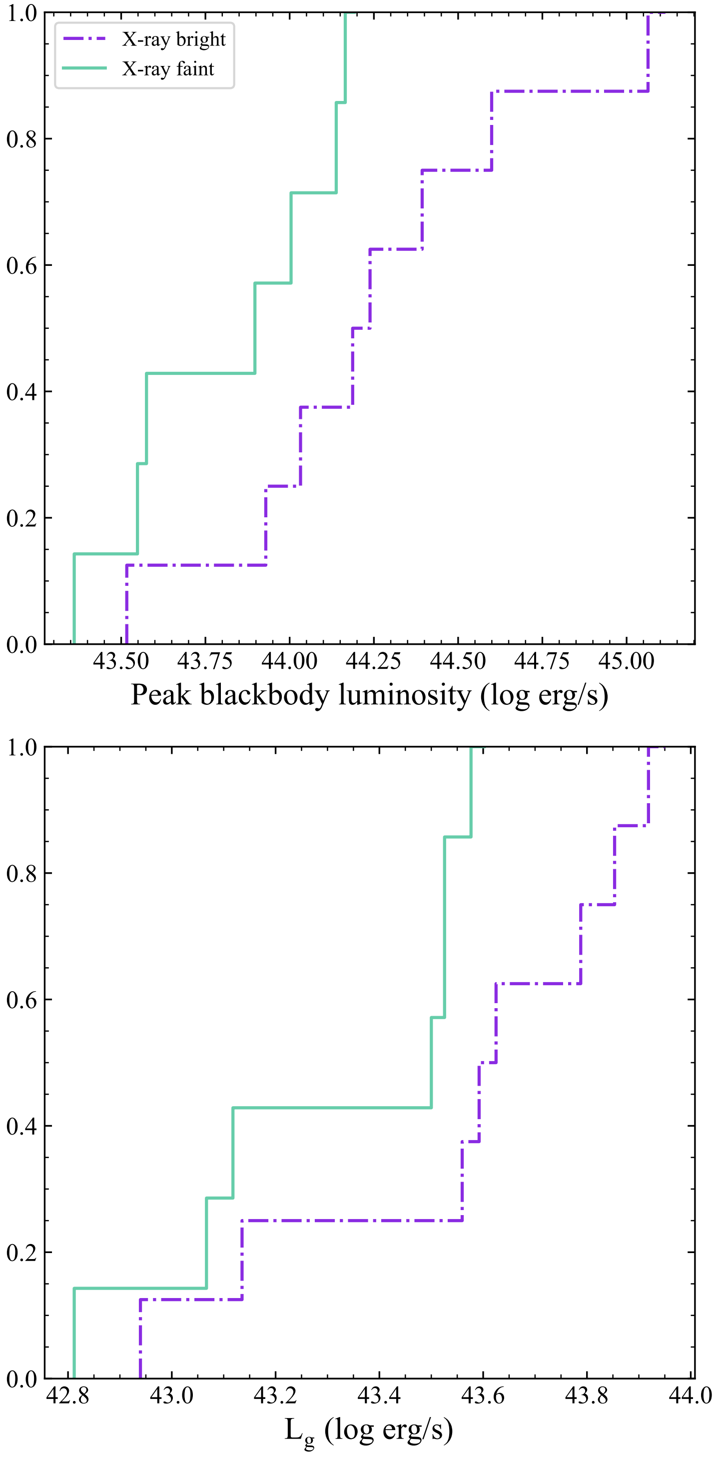

Figure 2.7: Cumulative distributions of selected properties of the TDE light curves for the X-ray bright (purple dot-dashed line) and X-ray faint (aqua, solid line) populations of TDEs in the ZTF-I sample. We find that the X-ray bright TDEs have significantly higher blackbody and g-band luminosities.

2.6.4 The Look-Elsewhere Effect

We search for correlations among the light curve properties and perform a total of 36 different Kendall's tau tests. Because of the size of this parameter space, it is important to address the "look-elsewhere" effect, which is a phenomenon in which statistically significant observations result by chance due to the large size of the parameter space being searched. If the parameters that are investigated are independent, for 36 Kendall's tau tests for correlations, we would expect a p-value of 0.05 to occur by chance once every 20 tests, or ≈2/36. The probability from a binomial distribution of having $\geq$1 significant ($p < 0.05$) outcome by chance is 84%. However, we have 12 significant outcomes. The probability of this happening by chance is $\approx 10^{-7}$. This low probability demonstrates that most of the significant correlations between parameters are not due to the look-elsewhere effect. We anticipate this happens because a large fraction of the parameters we investigate are not independent. However tracing the direction of causality (i.e., the fundamental relation which underpins the multiple correlations we observe here) is beyond the scope of this work.

We perform 70 different Anderson-Darling tests to assess whether there are differences in the properties of the spectral classes and the X-ray bright and X-ray faint samples. If all of the parameters that are tested are independent of each other, we expect a significant outcome to occur by chance every 20 tests, or ≈4/70. The probability from a binomial distribution of having $\geq$1 significant ($p < 0.05$) outcome by chance is 93%. We found 19 significant outcomes. The probability of this happening by chance is $\approx 10^{-9}$.

For both of these tests, we can account for the look-elsewhere effect by dividing our significance threshold by the number of degrees of freedom in the tests. If we take this to be the number of tests, this would reduce the threshold to $p < 0.001$ for the Kendall's tau tests and $p < 0.0007$ for the Anderson-Darling tests. However, our tests are not completely independent as we expect there to be some correlation between the parameters, such as between $L_{\rm peak}$, $T_{\rm peak}$, and $R_{\rm peak}$. We conclude that it is unlikely that the correlations we have found here are due to chance (i.e. the look-elsewhere effect), given the low probabilities for the number of significant outcomes we find occurring due to chance.

2.6.5 Optical to X-ray Ratio

In Figure 2.8, we show the ratio of blackbody luminosity derived from the fits to the UV/optical light curves to the 0.3–10 keV luminosity from the *Swift*/XRT observations, for 9 TDEs with *Swift* XRT detections. We also show the 0.3–10 keV light curves compared to the optical/UV blackbody light curves in the figures in Appendix A. Four of these TDEs were presented in van Velzen et al. (2021), including AT2018hyz, AT2019dsg, AT2019ehz, and AT2019azh. We present additional observations for each of these, in addition to 5 more TDEs not presented in that paper.

van Velzen et al. (2021) noted the large amplitude flaring of AT2019ehz, and the increase in luminosity over timescales of several months for other TDEs like AT2019azh. The 9 TDEs in Figure 2.8 show a similar long term increase in luminosity, and we note the general trend of $L_{\rm bb}/L_{\rm X}$ towards 1 at later times.

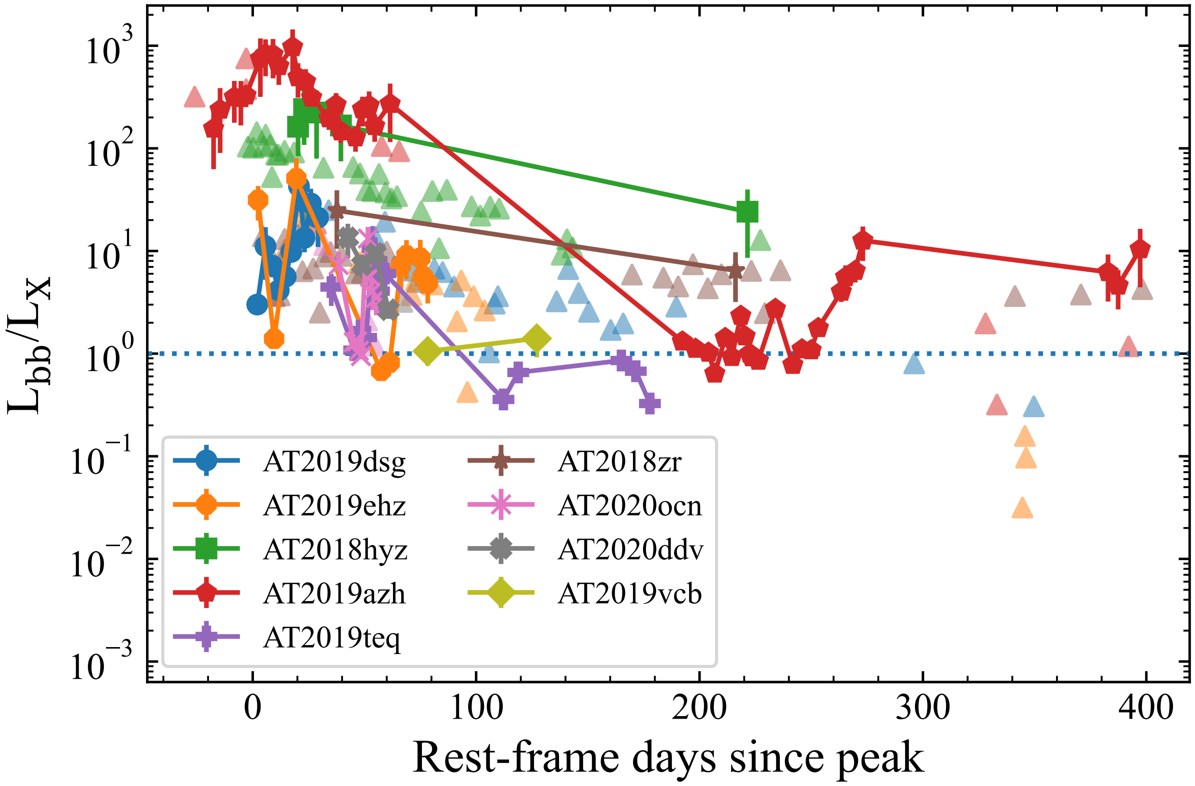

Figure 2.8: The ratio of the blackbody luminosity, derived from the optical and UV light curves, to the 0.3–10 keV X-ray luminosity from *Swift*/XRT. Triangles are 3σ lower limits.

2.7 Black Hole Mass Estimates

2.7.1 `MOSFiT`

In addition to the light curve fitting described in Section 2.5.1, we use the Modular Open-Source Fitter for Transients (`MOSFiT`; Guillochon et al., 2018; Mockler et al., 2019) to fit the light curves of the 30 TDEs in the ZTF-I sample. The TDE module in `MOSFiT` generates bolometric light curves via hydrodynamical simulations and passes them through viscosity and reprocessing transformation functions to create the single-band light curves. These single-band light curves are then used to fit the multi-band data to obtain the light curve properties and information on the physical parameters of the disrupted star, the tidal encounter, and the MBH. In this analysis, we are most interested in the properties of `MOSFiT`'s ability to estimate the parameters of the MBH and the disrupted star from the TDE light curve. `MOSFiT` is particularly sensitive to plateaus in the late-time data as well as the slope of the pre-peak rise. We therefore only fit our forced photometry data between $-10\ \mathrm{days} \leq t_{\mathrm{peak}} \leq +300\ \mathrm{days}$. We show the black hole mass estimated from this fitting compared to the host galaxy stellar mass in Figure 2.9 and the mass of the disrupted star in Figure 2.10.

We find that the MBH masses range from $\approx 6.0 \leq \log(M_{\mathrm{BH}}/M_{\odot}) \leq 7.9$. We evaluate the black hole masses vs. the galaxy stellar mass for correlation with a Kendall's tau test and find no significant correlation between the two parameters. This is surprising, given that one expects the mass of the galaxy to scale positively with the mass of its central MBH. Furthermore, this is in conflict with Mockler et al. (2019), who found that their estimates of the black hole mass are consistent with the estimates from the bulk galaxy properties. We point out that two joint papers which were released shortly before the submission of this manuscript, Nicholl et al. (2022) and Ramsden et al. (2022), find a positive correlation between black hole mass measured from `MOSFiT` and host galaxy bulge mass measured from stellar population synthesis fitting. Our use of total galaxy mass instead of bulge mass may be the source of the discrepancy. While Ramsden et al. (2022) derive the host galaxy masses in a similar manner to the one presented here and are generally consistent with those in Table 2.2, they perform bulge-disk decompositions on SDSS and PanSTARRS imaging of the TDE hosts. Hammerstein et al. (2021a) note that imaging from ground-based observatories may not provide the resolution required to study galaxy morphology at the redshifts of the TDE hosts. We therefore maintain our use of the total stellar mass instead of the bulge mass. Using an Anderson-Darling test, we find that the TDE-featureless events have significantly larger black holes (p-value $= 0.04$) as compared to the remainder of the sample. We also find that TDE-He events show larger disrupted star masses when compared to the rest of the sample (p-value $= 0.008$).

2.7.2 `TDEmass`

We also estimate the MBH mass from `TDEmass` (Ryu et al., 2020), which takes the peak luminosity and color temperature of the flare as input to calculate the masses of the MBH and the disrupted star. This method of estimating the MBH mass assumes that circularization happens slowly, and that the UV/optical emission arises from shocks in the intersecting debris streams instead of in an outflow or wind. We show the MBH mass estimated from `TDEmass` compared to the host galaxy stellar mass in Figure 2.11 and the mass of the disrupted star in Figure 2.12.

Using this method, we find MBH masses in the range $5.6 \leq \log M_{\rm BH} \leq 7.0$, which is

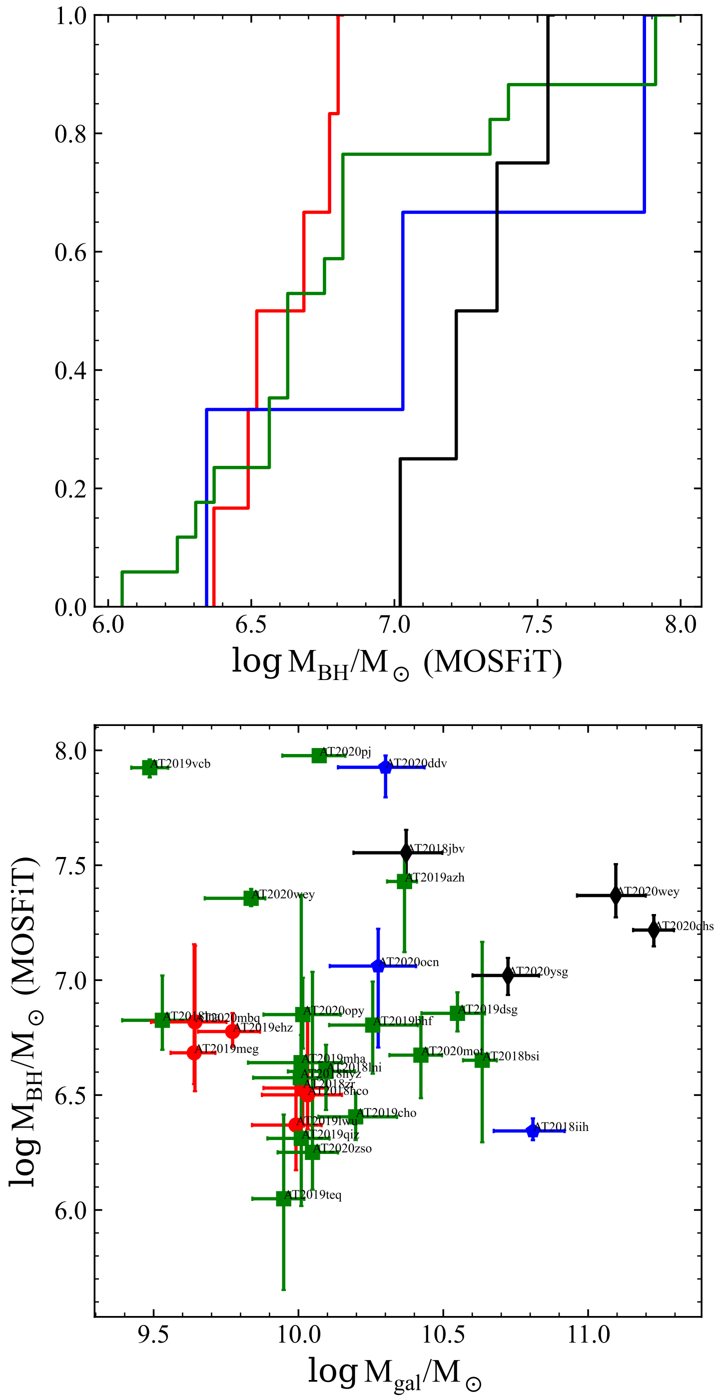

Figure 2.9: The black hole mass estimated from the `MOSFiT` fits to the optical/UV light curves vs. the total stellar mass of the host galaxies measured from the SED fits to the pre-flare photometry. We find no significant correlation between the black hole mass and the galaxy stellar mass. The TDE-featureless events are shown to have more massive black holes as compared to the remainder of the sample. Colors and symbols are the same as in Figure 2.3.

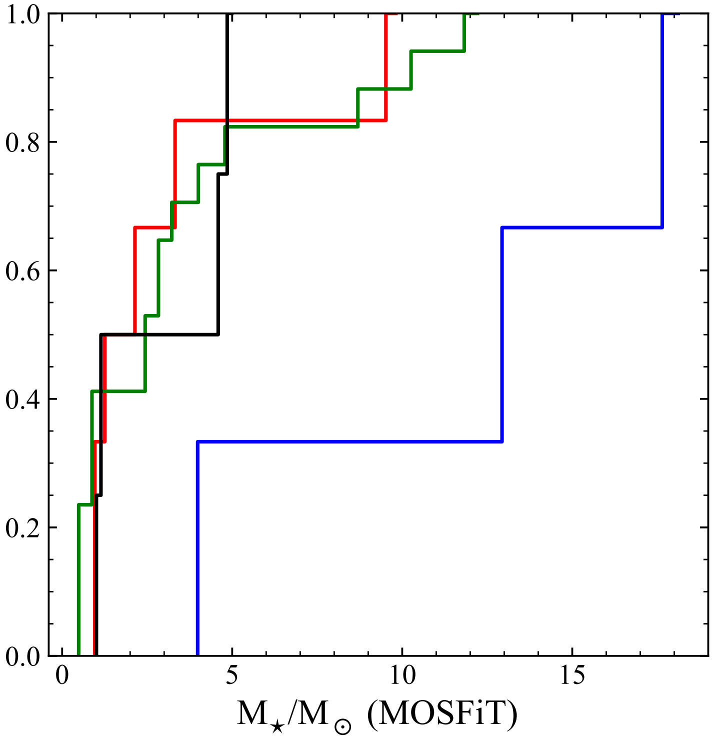

Figure 2.10: The disrupted star mass estimated from the `MOSFiT` fits to the optical/UV light curves for each of the TDE spectral types. We find that TDE-He events show significantly larger disrupted star masses as compared to the remainder of the sample. Colors are the same as in Figure 2.3.

less massive than found with `MOSFiT`. We point out that we were not able to obtain masses for the four featureless events with `TDEmass`, as the peak luminosities and temperatures are outside of the limits explored by the model. Again, we find no significant correlation with host galaxy stellar mass. Ryu et al. (2020) did, however, found that their estimates for the MBH mass were roughly consistent with the masses estimated from bulge properties. Again, we use the total stellar mass which may be the source for this discrepancy. Additionally, we find a negative correlation between the MBH mass estimated from `MOSFiT` and that estimated from `TDEmass`, with the `MOSFiT` estimates larger by factor of at least an order of magnitude in most cases. This large difference is perhaps not surprising, as the two methods for estimating the black hole mass employ completely different models for the origin of the UV/optical emission. Estimates of the black hole mass from other, light curve independent methods, such as via the $M_{\rm BH} - \sigma$ relation, will help to narrow down which of these mass estimates is more favorable. We find again that the TDE-He events show significantly larger disrupted star masses as compared to TDE-H and TDE-H+He events (p-value $=0.04$).

2.8 Discussion

We have investigated several correlations among the properties of the light curves presented in this paper, as well as the differences between sub-populations based on spectroscopic class, light curve shape, and X-ray detection. van Velzen et al. (2021), who analyzed the first 16 TDEs in this paper (plus an additional 22 from the literature) and whose light curve fitting methods we have reproduced here, found a correlation between the decay timescale and the host galaxy stellar mass. With an additional 15 events in our analysis, we find a similar correlation here, consistent

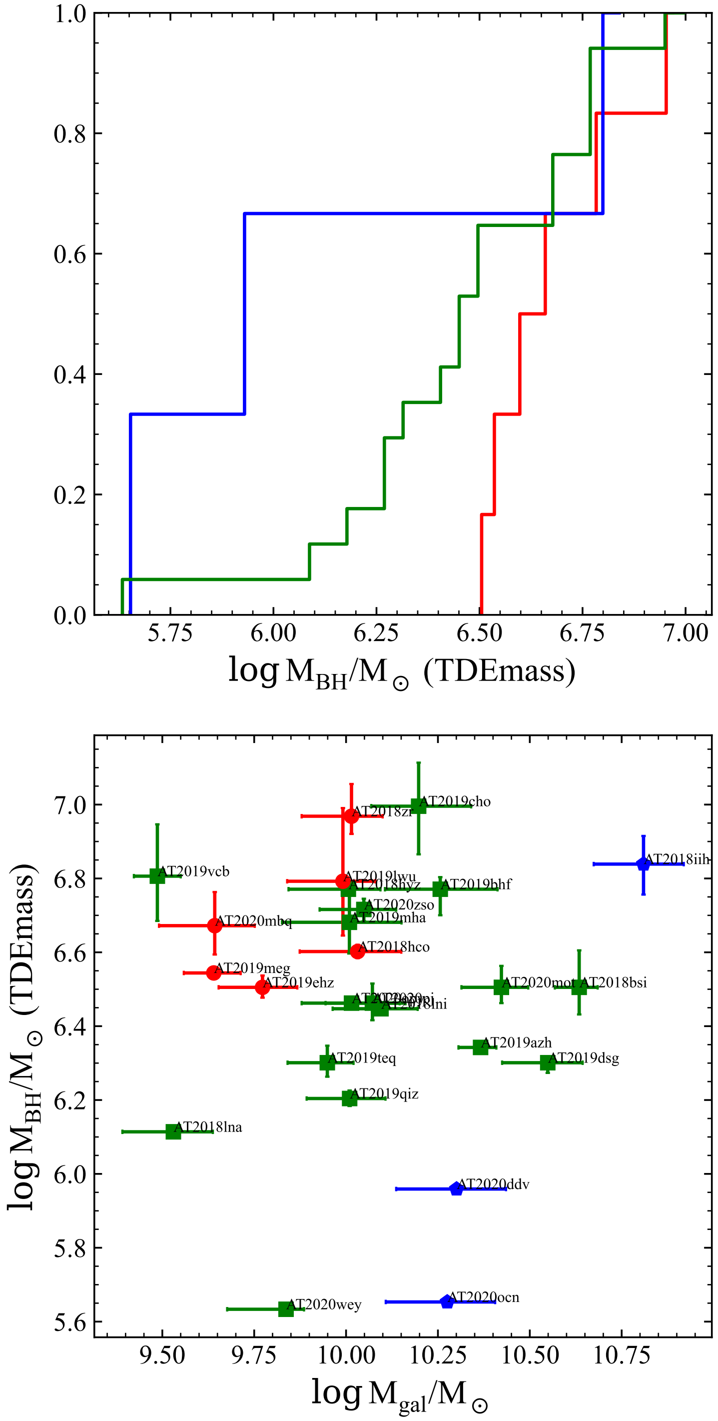

Figure 2.11: The black hole mass estimated from `TDEmass` vs. the total stellar mass of the host galaxies measured from the SED fits to the pre-flare photometry. We find no significant correlation between the black hole mass and the galaxy stellar mass. Colors and symbols are the same as in Figure 2.3.

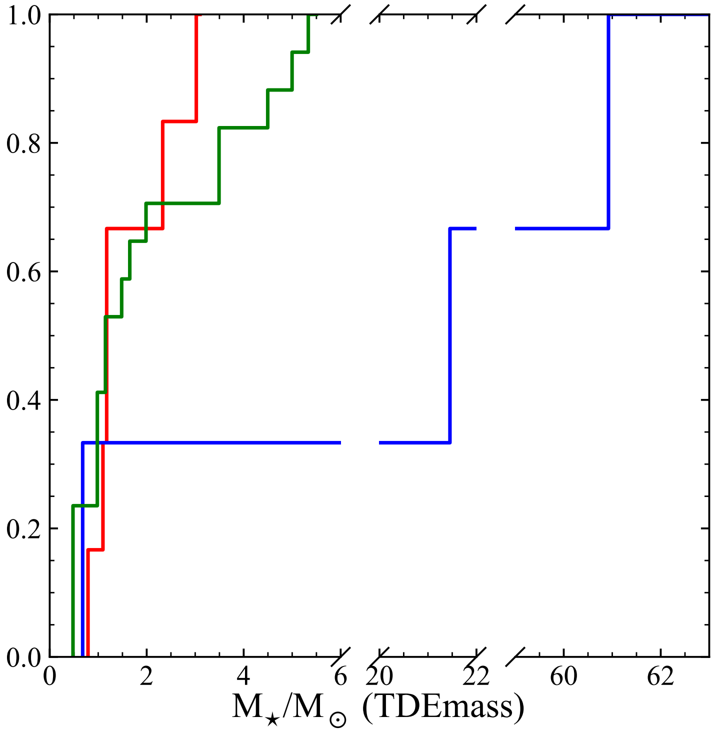

Figure 2.12: The disrupted star mass estimated from `TDEmass` split by the TDE spectral types. We find that TDE-He events have significantly larger disrupted star masses as compared to TDE-H and TDE-H+He events. We note the broken axis to accommodate the large star masses in the TDE-He class. Colors are the same as in Figure 2.3.

with van Velzen et al. (2021) and other previous studies (Blagorodnova et al., 2017; Wevers et al., 2017). Our results imply that the decay timescale of the optical/UV light curve follows the fallback rate, which is crucial for light curve fitting methods that produce an estimate of the black hole mass, such as `MOSFiT`. This has already been tested against a small sample of post-peak light curves (Mockler et al., 2019). They find evidence that the light curves fitted there are also consistent with tracing the fallback rate. We also recover a weak positive correlation between the peak blackbody luminosity and the decay timescale, which is consistent with a correlation found in Hinkle et al. (2020).

We do find a correlation, although shallow, between the rise timescale and the host galaxy stellar mass, which was not present in van Velzen et al. (2021). van Velzen et al. (2021) attributed this lack of correlation between rise timescale and host galaxy mass to two possible models, photon advection (Metzger & Stone, 2016) and diffusion (Piran et al., 2015). In the advection model, the optical radiation is advected through a wind until it reaches the trapping radius, which is the radius at which the radiative diffusion time through the debris is shorter than the outflow expansion time. One feature of this model is that for low mass black holes ($\lesssim 7 \times 10^6 M_\odot$), the correlation between the peak luminosity and the black hole mass is weak. However, we do find a correlation between the peak luminosity and the host galaxy stellar mass, which may weaken the plausibility of this model being at play here.

We find no differences between the TDE spectroscopic classes in terms of rise and decay timescales. van Velzen et al. (2021) found that the TDE-H+He class shows longer rise times and smaller blackbody radii than other spectroscopic classes. They attributed this to the idea that the Bowen fluorescence lines which are sometimes seen in the TDE-H+He class require high densities, which lead to longer diffusion timescales and can be reached at the smaller blackbody radii they found in the class.

A significant difference between blackbody radius and rise times for TDE-H and TDE-H+He was discovered by van Velzen et al. (2021) and confirmed by Nicholl et al. (2022). These works are based on a larger sample of TDEs compared to the ZTF-only collection presented in this work. van Velzen et al. (2021) contains 13 TDE-H, while our sample contains only 6 events in this spectral class. As such, our ZTF-only sample has less statistical power to uncover differences between the TDE-H and TDE-H+He populations. However, we can use the newly discovered TDEs in our sample to confirm the earlier conclusion that below a radius of $10^{15.1}$ cm, all TDEs between the two classes are classified as TDE-H+He. The same is true for the rise time, where above a rise time of $\sim$16 days, all TDEs between the two classes are TDE-H+He. Our work thus supports the idea that the TDE-H+He events require high density environments, and that the rise times of the light curves are governed not by the fallback timescale, but by the diffusion of photons through the tidal debris.

The TDE-featureless class is characterized by high luminosities, large blackbody radii, and high blackbody temperatures at peak, particularly when compared to the TDE-H and TDE-H+He classes. The spectra of TDE-featureless events are just that, lacking any discernible emission features present in the other three spectroscopic classes. While the four TDE-featureless events we present here are among the highest redshift events in this sample, this, supported by the high luminosities of this class, can be attributed to the rarity of these events, i.e., a larger volume is required to observe them. Additionally, the lack of spectral features is unlikely to be an artifact of their higher redshift, given that the observation of spectral features associated with the host galaxy stellar population, seen most prominently in the spectrum of AT2020ysg, is not uncommon. The host galaxies for the TDE-featureless class are generally more massive than TDE-H and TDE-H+He classes, in addition to being redder in color. We also point out the peculiar event AT2020riz, which shows a particularly fast rise and decay as compared to the other TDE-featureless events. A larger sample of TDE-featureless events is needed in order to understand the diversity of this class of TDEs.

We find that the X-ray bright and X-ray faint events differ in their peak blackbody and g-band luminosities. The lack of differences in other properties is surprising. In the reprocessing scenario for explaining the lack of X-rays in some optically selected TDEs, one might expect larger blackbody radii for the X-ray faint sample, as the blackbody radius is that of the larger reprocessing medium and not that of the smaller accretion disk. While it is not possible to entirely rule out the delayed onset of accretion due to circularization of the tidal debris to explain the lack of X-rays, the correlation we have found between the decay timescale and the host galaxy stellar mass makes this less likely as it appears the decay timescale closely follows the fallback rate. In the viewing angle model of Dai et al. (2018), the X-ray bright and X-ray faint TDEs differ only in whether or not X-rays are visible along the observer's line of sight. Thus, it is less likely that differences among other properties, such as the blackbody radius, will be as important. The lack of difference in host galaxy mass also favors the viewing angle model. One might expect a difference between the two populations in host galaxy mass (as a proxy for black hole mass) for several reasons, whether it be accretion disk temperature (e.g. Dai et al., 2015), rapid circularization (e.g. Guillochon & Ramirez-Ruiz, 2015), or the result of the Eddington ratio of the newly formed accretion disk (e.g. Mummery, 2021). While other studies, such as French et al. (2020b), have found a difference between the X-ray bright and X-ray faint populations in terms of host galaxy mass, we find no such difference in the sample presented here. However, a measurement of the black hole mass, as opposed to using the host galaxy mass as a proxy, will help to truly discern whether or not there are differences between the two populations.

While this work focuses largely on the light curve properties of these TDEs, the spectra play an important role in the follow-up and classification of candidates as TDEs. The classification of a candidate as a TDE and subsequent sub-classification as one of the spectral types presented in Section 2.2.3 and in van Velzen et al. (2021) is dependent on the appearance of broad hydrogen and helium emission lines in spectra. The profiles of these broad lines are varied, as seen in Figures A.1, A.2, and A.3, and the differences can give information on potential outflows and the geometry of the system. In particular, double-peaked emission lines, which are seen in some AGN, are thought to originate from the outer regions of an inclined accretion disk. Wevers et al. (2022) examined the line profiles of AT2020zso, a TDE we have included in our sample, and found that the emission lines after peak can be reproduced with a highly inclined, highly elliptical, and relatively compact accretion disk, further supporting the unification picture where viewing angle determines the observed properties of a TDE. In Figure 2.13, we show our spectrum of AT2020zso along with several other extreme broad and flat-topped/double-peaked TDEs in our sample. Of those shown, 2 are of the TDE-H class while the remaining 5 are of the TDE-H+He class. Two of these, AT2018zr and AT2018hyz, are also X-ray detected. The large fraction of X-ray dim TDE-H+He with extreme broad, flat-topped lines in this sample lends further support to the unification picture, but more work is needed to understand why these line profiles are not exclusive to X-ray brightness or spectral class.

Charalampopoulos et al. (2022) studied a larger sample of TDE spectra and quantified the evolution of prominent TDE lines with time, such as Hα, He II, and Bowen lines. They present a scheme for sub-classification of the spectral types of TDEs, with TDE-H and TDE-H+He having X-ray bright and X-ray dim sub-categories which show different spectroscopic features such as double-peaked lines, Fe lines, and N III lines. They conclude that the large spectroscopic diversity of TDEs, for which they have determined subcategories, can be attributed to viewing angle effects. Although a detailed study of the spectroscopic features of the TDEs is beyond the scope of this work, a cursory examination of the spectra reveals some agreement with these sub-classes. Specifically, AT2018zr and AT2018hyz show evidence for double-peaked Balmer lines accompanied with detected X-ray emission, which is in line with the sub-category of the TDE-H class presented by Charalampopoulos et al. (2022). A more thorough analysis of the spectra and investigation of emission lines will be necessary to understand these sub-categories further.

2.9 Conclusions

We have presented a sample of 30 systematically gathered TDEs with light curves from ZTF and *Swift* UVOT and XRT observations, the largest sample of TDEs from a single survey yet. We estimated the parameters of the UV/optical light curves by fitting the multi-band data with two models and examined correlations between the light curve parameters and host galaxy properties, as well as differences among the different sub-classes of TDEs. We summarize our main conclusions below.

- Our sample can be split into four spectroscopic classes, with 6 TDE-H, 3 TDE-He, 17 TDE-H+He, and 4 TDEs of the new TDE-featureless class, which we present here for the first time.
- Only 47% of the TDE host galaxies within this sample are in the green valley, although 11/17 of those outside the green valley are within 0.12 mag of its upper or lower bounds.
- Using `MOSFiT`, we find that the TDE-featureless events have significantly larger black

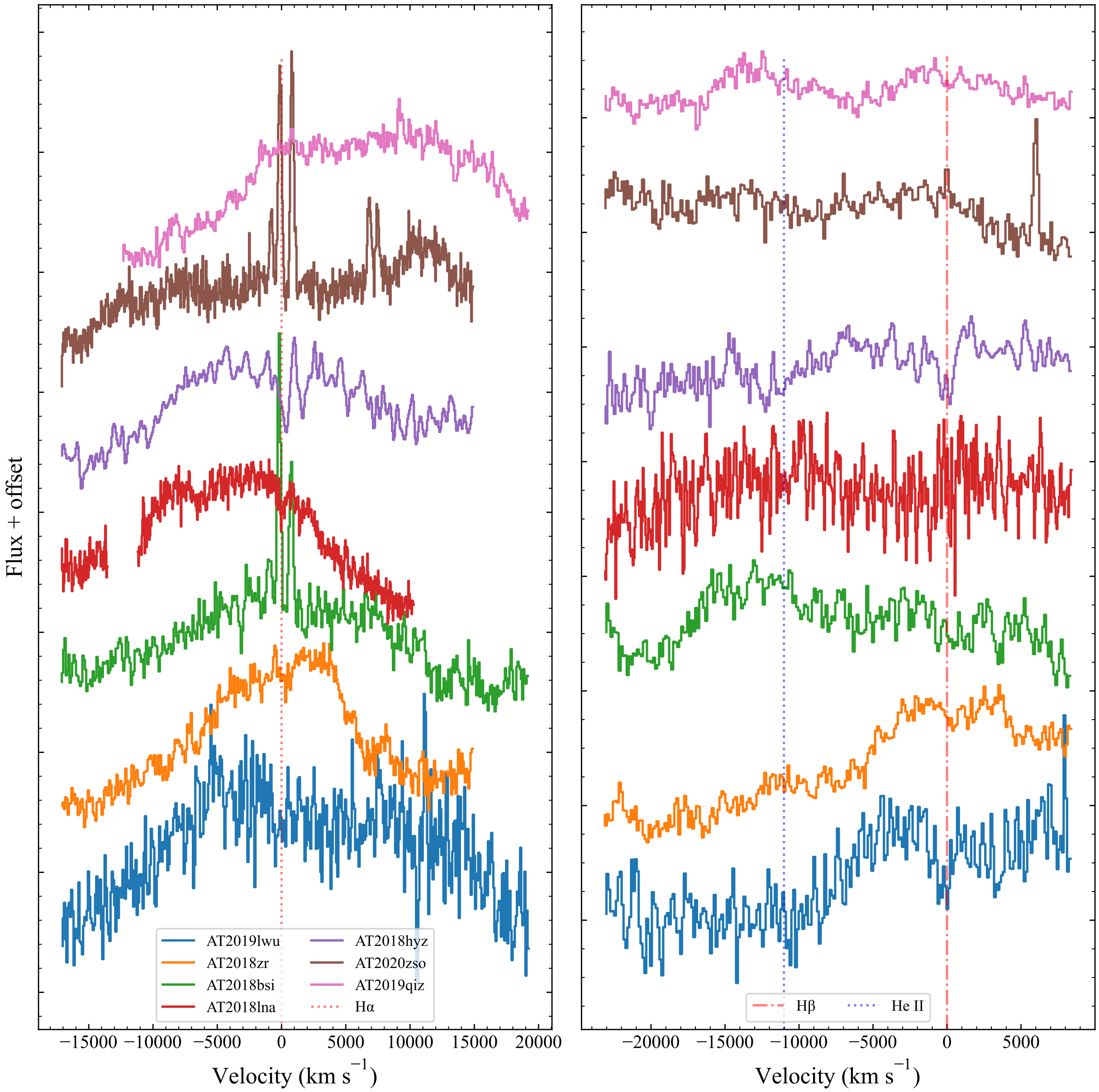

Figure 2.13: Left: The Hα regions of the most extreme broad/flat-topped or double-peaked TDEs in our sample. Hα is marked with a dotted red line. Right: The Hβ and He II region of the same objects shown in the left panel, with Hβ marked with a red dot-dashed line and He II marked with a blue dotted line.

hole masses as compared to the rest of the classes. We also find that both `MOSFiT` and `TDEmass` yield significantly higher disrupted star masses for the TDE-He class as compared to the rest of the spectral classes. This may hint at the reason for the different spectral classes of TDEs.

- We find a correlation between the decay timescale and the host galaxy stellar mass, which is consistent with previous findings from van Velzen et al. (2021), and is consistent with the picture where the post-peak TDE light curve follows the fallback rate.
- We recover a weak correlation between the peak luminosity and the decline rate, where more luminous TDEs decay more slowly, consistent with a correlation found in Hinkle et al. (2020).
- We find that the X-ray bright TDEs show significantly higher peak blackbody and g-band luminosities. The lack of differences among other properties such as blackbody radius and host galaxy mass makes the viewing angle model of Dai et al. (2018) for explaining the lack of X-rays in some TDEs more favorable.

2.10 Acknowledgements

We thank the anonymous referee for their helpful comments towards improving this manuscript. We also thank B. Mockler and M. Nicholl for their help with understanding and running the `MOSFiT` tool.

Based on observations obtained with the Samuel Oschin Telescope 48-inch and the 60-inch Telescope at the Palomar Observatory as part of the Zwicky Transient Facility project.

ZTF is supported by the National Science Foundation under Grant No. AST-1440341 and a collaboration including Caltech, IPAC, the Weizmann Institute for Science, the Oskar Klein Center at Stockholm University, the University of Maryland, the University of Washington, Deutsches Elektronen-Synchrotron and Humboldt University, Los Alamos National Laboratories, the TANGO Consortium of Taiwan, the University of Wisconsin at Milwaukee, and Lawrence Berkeley National Laboratories. Operations are conducted by COO, IPAC, and UW. SED Machine is based upon work supported by the National Science Foundation under Grant No. 1106171. The ZTF forced-photometry service was funded under the Heising-Simons Foundation grant #12540303 (PI: Graham). This work was supported by the GROWTH project funded by the National Science Foundation under Grant No 1545949.

The material is based upon work supported by NASA under award number 80GSFC21M0002. ECK acknowledges support from the G.R.E.A.T research environment funded by *Vetenskapsrådet*, the Swedish Research Council, under project number 2016-06012, and support from The Wenner-Gren Foundations.

Chapter 3: TDE Hosts are Green and Centrally Concentrated: Signatures of a Post-Merger System

3.1 Introduction

Supermassive black holes (SMBHs) are thought to reside at the center of every large galaxy, greatly influencing their environments, both in their galactic nuclei and on larger scales. However, unless a SMBH is close enough that we can precisely measure its gravitational pull on the stars and gas in its potential well or bright enough due to gas-fueled accretion, these objects are difficult to study. In distant galaxies with quiescent SMBHs, observations of tidal disruption events (TDEs) are one way to ascertain the presence and perhaps the properties of the central SMBH.

TDEs occur when a star is kicked into an orbit that brings it close enough to the SMBH to be tidally disrupted and accreted (e.g., Frank & Rees, 1976; Hills, 1975; Rees, 1988). These events are observed as bright, nuclear flares and have been discovered via observations from X-ray to optical wavelengths (Saxton et al., 2020; van Velzen et al., 2020). In order for these TDEs to be observable, the star's tidal disruption radius must be outside of the SMBH event horizon. The event horizon radius scales with black hole mass and thus, for a sun-like star, non-spinning SMBHs larger than $10^8 M_{\odot}$ will be too massive to host observable TDEs (Hills, 1975). This allows for the unique opportunity to find and study low-mass SMBHs, potentially including intermediate-mass black holes, and their host galaxies, as well as accretion physics and relativistic jet formation.

There is still much debate about what types of nuclear environments are most likely to host a TDE, particularly in the mechanisms that create the fatal stellar orbits that drive these events. The environments that are likely to produce TDEs can be linked to properties that reach far beyond the nucleus of a galaxy though. Graur et al. (2018) tested whether the TDE rate depends on kpc-scale global galaxy properties, including the stellar surface mass density and and the velocity dispersion, which are more easily observable than nuclear properties. They found that TDE hosts have, on average, a higher stellar mass surface density and marginally lower velocity dispersions than a control sample of galaxies. Multiple studies have shown that TDEs appear to be observed preferentially in post-starburst galaxies (otherwise known as K+A or E+A galaxies) (Arcavi et al., 2014; French et al., 2016; Law-Smith et al., 2017) whose spectra have deep Balmer absorption lines but no significant [O II] emission, indicating a burst of star-formation that occurred approximately a Gyr ago that has since subsided. Several mechanisms connecting the large scale properties of the host galaxy, in this the case star formation history and global stellar population, and the dynamics of the nuclear region have been proposed. In particular, E+A galaxies are known to have high Sérsic indices, large bulge-to-total light ratios, and high concentration indices (Yang et al., 2008). The nuclear stellar overdensities caused by merger-triggered bursts of star formation in these galaxies have been shown to greatly enhance the TDE rate, possibly because these overdensities lead to a greater number of stars able to fill the loss cone of stars that can be tidally disrupted (French et al., 2020a; Stone & Metzger, 2016; Stone & van Velzen, 2016).

Not all TDEs occur in post-starburst galaxies, however. Law-Smith et al. (2017) studied a sample of TDE host galaxies within the context of the local galaxy population, and while the sample they used was dominated by post-starburst galaxies (3/5 used in their analysis could be classified as quiescent, Balmer-strong), they found that the majority of the TDE hosts reside in the green valley, between star-forming and passive galaxies, have bluer bulge colors, higher Sérsic indices, and higher bulge-total-light ratios with respect to galaxies of similar masses, regardless of E+A classification. French et al. (2020a) studied four TDE host galaxies with high spatial resolution HST imaging: one post-starburst, two quiescent Balmer-strong galaxies, and one early type galaxy, classified by their spectra. They found that, compared to early type galaxies of similar stellar mass, the TDE host galaxies have higher central surface brightnesses and stellar mass surface densities on 30-100 pc scales, regardless of host galaxy type. Understanding the properties of not only E+A galaxies, but of the variety of galaxy types that produce TDEs is important for understanding the specific mechanisms that trigger TDEs both on large, galactic scales as well as in the nuclear environments surrounding the SMBH. In this paper, we investigate the properties of the latest Zwicky Transient Facility (ZTF; Bellm et al., 2019b; Graham et al., 2019; Masci et al., 2019) sample of TDE host galaxies and compare them with the properties of galaxies grouped by a variety of schema.

Previous studies that have aimed to understand TDE host galaxies have had to assemble samples from multiple surveys. This study is the first to use a systematically discovered sample of TDEs from a single survey, making the following analysis free from heterogeneous selection effects from multiple surveys. The ZTF sample selection criteria are also totally agnostic to host galaxy type, apart from rejecting galaxies that can be classified as broad-line AGN, and is therefore a prime sample for understanding properties of TDE host galaxies. See van Velzen et al. (2021) for a more detailed overview of the ZTF alert filtering and photometric selection criteria used to discover new TDEs. We then perform further follow-up of TDE candidates with spectroscopy to confirm the TDE classification and determine the TDE spectral class, discussed further in Section 3.2.1, as well as perform UV monitoring with *Swift*.

In this paper, we focus on the sample of 16 TDEs first presented in van Velzen et al. (2021) plus 3 new TDEs detected in ZTF thereafter. We study the properties of the galaxies hosting these ZTF TDEs using both photometry and spectroscopy in order to better understand the environments and mechanisms that produce them. We also compare the photometric and spectroscopic properties of these hosts to a sample of galaxies from the Sloan Digital Sky Survey (SDSS) in order to study them within the context of the local galaxy population. In Section 3.2 we present the TDE host galaxy sample with corresponding photometric and spectroscopic data, and the SDSS comparison sample used in the following analysis. In Section 3.3 we present the results and methods used to obtain them. We end with a discussion presented in Section 3.4 and conclusions and future work in Section 3.5.

3.2 Sample & Data

3.2.1 ZTF TDE Host Galaxies

ZTF has detected 19 spectroscopically confirmed TDEs, 16 of which were originally presented in van Velzen et al. (2021), and 3 of which that have been detected by ZTF but have not yet been reported in the literature. The light curves and spectra of these 3 new TDEs will be presented in Hammerstein et al. (2023a). The discovery history for the first 16 can be found in van Velzen et al. (2021). We present this sample in Table 3.1 with the redshift, host galaxy stellar mass, and TDE class. We give the IAU and ZTF names, as well as the internal name assigned to each TDE[1]. The ZTF TDE host galaxies have redshifts in the range $0.02 \lesssim z \lesssim 0.2$, which are obtained from the spectrum of the TDE as the majority of TDE hosts do not have a pre-flare spectrum.

The TDE hosts have total stellar masses in the range $9.31 \leq \log(M_\star/M_\odot) \leq 10.63$. Stellar population synthesis of the pre-flare photometry, obtained from SDSS, Pan-STARRS1 (PS1), and GALEX was used to estimate the total stellar mass of each galaxy as well as obtain extinction-corrected, synthetic rest-frame colors (see van Velzen et al., 2021). We adopt the same model choices as Mendel et al. (2014), a catalog we use for our comparison sample.

We have also listed the spectral class of the TDE in Table 3.1. The three different spectral classes correspond to emission features seen in the TDE spectrum. These classes are defined by van Velzen et al. (2021) as:

i. *TDE-H*: broad Hα and Hβ emission lines.

ii. *TDE-H+He*: broad Hα and Hβ emission lines and a broad complex of emission lines around He II λ4686. The majority of the sources in this class also show N III λ4640 and emission at λ4100 (identified as N III λ4100 instead of Hδ), plus and in some cases also O III λ3760.

iii. *TDE-He*: no broad Balmer emission lines, a broad emission line near He II λ4686 only.

To match the procedure used for the SDSS comparison sample, we use the SDSS and PS1 calibrated, sky-subtracted, corrected g- and r-band frames for photometric measurements performed in Section 3.3. The PSF at any pixel in a given SDSS frame is easily reconstructed using

---

[1] For ease of communication, we assigned each TDE a name of a character from the popular HBO television series *Game of Thrones* (GOT).

the corresponding psField file for that observation and the standalone code `readAtlasImages`[2]. For PS1 images, we use `PSFEx`[3] (Bertin, 2011) to model the PSF in each frame.

Spectra of the host galaxies are primarily used to measure the Hα flux and equivalent width and the Lick Hδ_{A} absorption index. In Table 3.1, we give the telescope/instrument used to obtain the spectrum and Δt of the observation, taken to be the time difference between the observation date and estimated peak date of the TDE flare. We used `PyRAF` to reduce the spectra with standard long-slit spectroscopy data reduction procedures, including bias subtraction, flat-fielding, aperture extraction, wavelength calibration, and flux calibration. These spectra are presented in Figure 3.1.

3.2.2 SDSS Comparison Sample

Throughout this paper, we compare the ZTF TDE host galaxy sample to a sample of SDSS galaxies to put the ZTF sample in the context of the local galaxy population. This comparison sample is based on the Mendel et al. (2014) value added catalog of bulge, disk, and total stellar mass estimates, which contains spectroscopically classified galaxies from the main SDSS galaxy sample (Strauss et al., 2002). Other values are taken from the Simard et al. (2011) value added catalog of bulge+disk decompositions as well as the MPA+JHU catalogs (Brinchmann et al., 2004). We remove galaxies with negative flux or continuum measurements and require a median signal-to-noise ratio per pixel of greater than 10 in the MPA+JHU catalog.

In order to correct for the flux-limited nature of the SDSS spectroscopic galaxy sample and to construct a sample representative of galaxies our TDE search is sensitive to, we further limit

---

[2] https://www.sdss.org/dr16/software/

[3] http://www.astromatic.net/software/psfex

ID	IAU Name	ZTF Name	GOT Name	Redshift	$\log(M_\star/M_\odot)$	TDE Class	Telescope/Inst.	$\mathrm{H}\alpha_{\mathrm{em}}$ EW	$\mathrm{H}\delta_{\mathrm{A}}$ EW	Δt (days)
1	AT2018zr	ZTF18aabtxvd	Ned	0.071	$10.02^{0.09}_{0.18}$	TDE-H	LDT/DeVeny	-0.15 ± 0.64	3.36	599
2	AT2018bsi	ZTF18aahqkbt	Jon	0.051	$10.60^{0.05}_{0.06}$	TDE-H+He	SDSS/BOSS	6.08 ± 0.06	1.53	-3031
3	AT2018hco	ZTF18abxftqm	Sansa	0.088	$9.93^{0.09}_{0.18}$	TDE-H	LDT/DeVeny	0.70 ± 0.34	2.00	376
4	AT2018iih	ZTF18acaqdaa	Jorah	0.212	$10.78^{0.09}_{0.15}$	TDE-He	LDT/DeVeny	1.89 ± 1.65	-0.28	566
5	AT2018hyz	ZTF18acpdvos	Gendry	0.0458	$9.77^{0.12}_{0.26}$	TDE-H	SDSS/BOSS	-0.29 ± 0.14	5.13	-6471
6	AT2018lni	ZTF18actaqdw	Arya	0.138	$9.96^{0.10}_{0.15}$	TDE-H+He	LDT/DeVeny	-1.82 ± 0.65	0.17	645
7	AT2018lna	ZTF19aabbnzo	Cersei	0.091	$9.49^{0.12}_{0.09}$	TDE-H+He	LDT/DeVeny	-0.36 ± 0.49	1.84	284
8	AT2019cho	ZTF19aakiwze	Petyr	0.193	$10.14^{0.17}_{0.16}$	TDE-H+He	LDT/DeVeny	0.98 ± 1.86	1.84	468
9	AT2019bhf	ZTF19aakswrb	Varys	0.1206	$10.23^{0.15}_{0.12}$	TDE-H	LDT/DeVeny	12.81 ± 1.35	5.63	473
10	AT2019azh	ZTF17aaazdba	Jaime	0.022	$9.84^{0.15}_{0.14}$	TDE-H+He	SDSS/BOSS	0.77 ± 0.08	7.65	-5615
11	AT2019dsg	ZTF19aapreis	Bran	0.0512	$10.37^{0.17}_{0.12}$	TDE-H+He	Lick/Kast	30.63 ± 0.46	1.28	182
12	AT2019ehz	ZTF19aarioci	Brienne	0.074	$9.69^{0.15}_{0.09}$	TDE-H	LDT/DeVeny	0.40 ± 1.06	3.58	403
13	AT2019mha	ZTF19abhejal	Bronn	0.148	$10.05^{0.15}_{0.11}$	TDE-H	LDT/DeVeny	-0.55 ± 0.87	3.66	311
14	AT2019meg	ZTF19abhhjcc	Margaery	0.152	$9.66^{0.05}_{0.05}$	TDE-H	LDT/DeVeny	23.69 ± 1.29	2.01	319
15	AT2019lwu	ZTF19abidbya	Robb	0.117	$9.86^{0.15}_{0.12}$	TDE-H	LDT/DeVeny	0.27 ± 0.63	3.73	324
16	AT2019qiz	ZTF19abzrhgq	Melisandre	0.0151	$10.04^{0.14}_{0.10}$	TDE-H+He	LDT/DeVeny	2.62 ± 0.12	0.57	317
17	AT2020pj[4]	ZTF20aabqihu	Gilly	0.068	$9.99^{0.17}_{0.09}$	TDE-H+He	LDT/DeVeny	18.45 ± 0.68	0.76	188
18	AT2019teq[5]	ZTF19accmaxo	Missandei	0.0874	$9.91^{0.06}_{0.07}$	TDE-He	LDT/DeVeny	17.28 ± 0.87	2.44	256
19	AT2020ocn[6]	ZTF18aakelin	Podrick	0.0705	$10.10^{0.17}_{0.16}$	TDE-He	SDSS/BOSS	-0.68 ± 0.14	0.98	-6183

Table 3.1: The names, redshifts, stellar masses, TDE spectroscopic classes, spectroscopic measurements of the ZTF sample of TDE host galaxies, and Δt ($t_{\mathrm{obs}} - t_{\mathrm{peak}}$) of the ZTF TDE hosts. Observations with negative Δt values are archival SDSS spectra which were taken several years pre-flare. Redshifts are measured from the spectrum of the TDE, as typically no pre-flare spectroscopy is available. We note that for Hα equivalent width (EW), a positive value indicates emission. Spectra are from the 4.3m Lowell Discovery Telescope DeVeny Spectrograph (LDT/DeVeny, PI: Gezari), the 3m Lick Kast Double Spectrograph (Lick/Kast, PI: Foley), and the SDSS BOSS spectrograph. For LDT observations, we used a slit width of $1\farcs5$ and a 300 g mm^{-1}. For Lick/Kast, a $2.0''$slit was used, with 452/3306 + 300/7500 grism/grating for the blue and red side respectively.

---

[4] TNS Classification Report #7481

[5] TNS Classification Report #7482

[6] ATel #13859

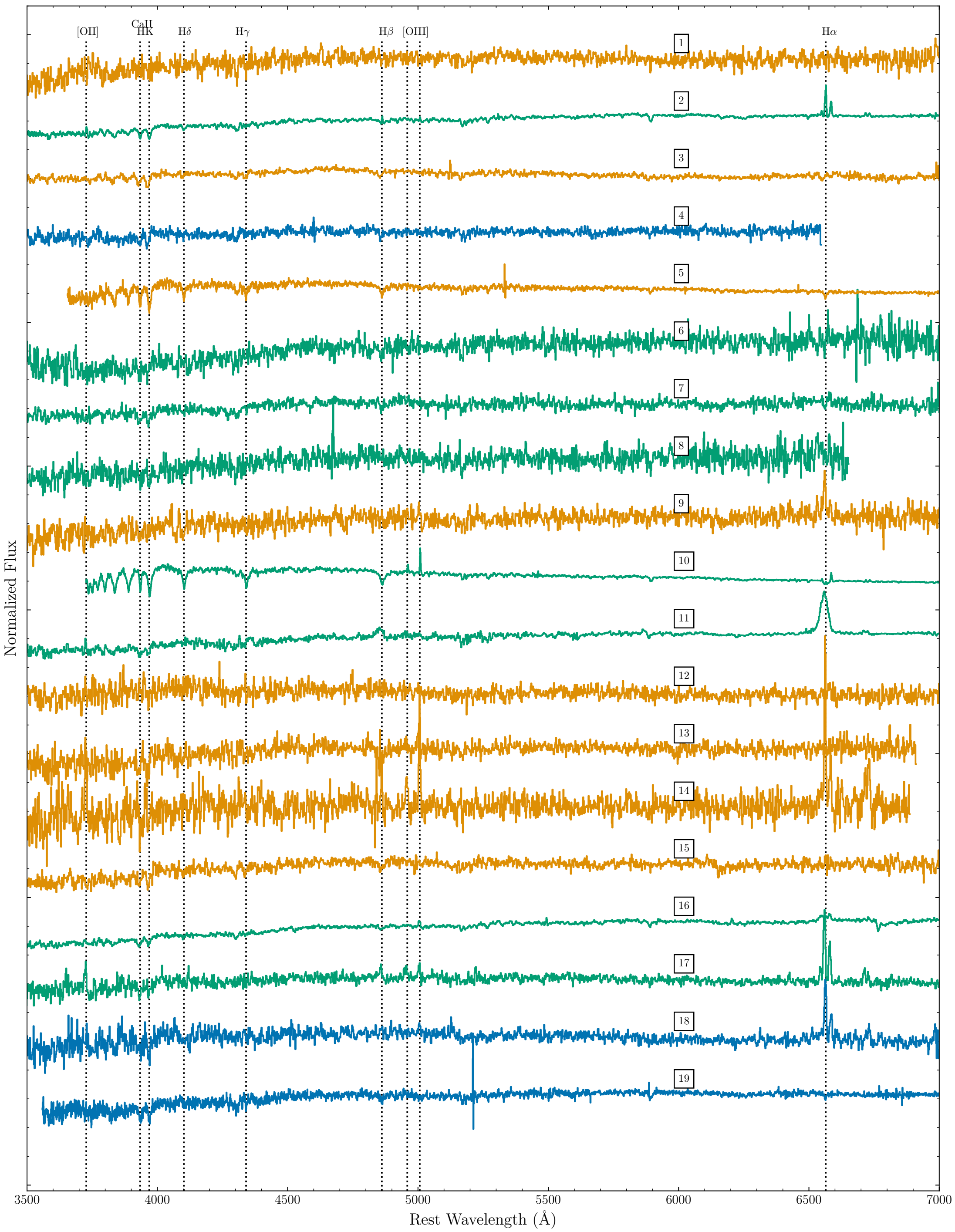

Figure 3.1: Rest-frame host galaxy spectra of the ZTF TDE sample. These spectra are not corrected for Galactic or internal extinction. The color of the spectrum corresponds to the TDE class from van Velzen et al. (2021), with orange being TDE-H, blue is TDE-He, and green being TDE-H+He.

the comparison sample by redshift. We give AT2018hco (ID 3) as an example. The absolute magnitude at peak of the AT2018hco flare light curve is ≈-20.1. If the ZTF detection limit is $m = 20$, ZTF can detect this flare out to a redshift of $z \approx 0.21$. If the ZTF reference image host galaxy detection limit is $m = 22$, ZTF is complete to $M \approx -18.1$ for this particular TDE. Finally, taking the SDSS spectroscopic magnitude limit to be $m = 18$, we create a comparison galaxy sub-sample with $z \leq 0.037$, which corresponds to galaxies with $M \approx -18.1$ and $m = 18$. We repeat this process for each TDE, ensuring that each TDE sub-sample has 1,000 galaxies by randomly sampling galaxies within the appropriate redshift range. Only one TDE requires oversampling of the galaxy catalog, as the redshift cut leaves less 1,000 galaxies. After applying all cuts to the comparison catalog, we are left with a sample of 19,000 galaxies. Each galaxy is weighted by 1/19 in the figures throughout this paper.

3.3 Analysis & Results

3.3.1 Photometry

We use the synthetic rest-frame and Galactic extinction corrected $u - r$ color from the stellar population synthesis of the pre-flare photometry (originally presented in van Velzen et al., 2021) to study where the ZTF TDE hosts fall within the red sequence, green valley, and blue cloud. Figure 3.2 shows this color vs. the total stellar mass of the TDE host galaxies against the sample of SDSS galaxies. The green valley is included on this figure, originally defined by Schawinski et al. (2014), but we redefine the upper limit here as our comparison sample has a different redshift cut:

$$^{0.0}u - r(M_{\text{gal}}) = -0.40 + 0.26 \times M_{\text{gal}}. \tag{3.1}$$

We have kept a similar width to the original Schawinski et al. (2014) green valley definition for the rest-frame $u - r$ color without internal dust corrections. The ZTF host galaxy sample is clearly dominated by green valley galaxies, with 63% of the TDE hosts falling within the limits of the green valley region compared to ∼13% of the SDSS comparison sample. We also include smoothed, normalized histograms of the galaxy stellar mass and $u - r$ color, for several groups of galaxies. The smoothed histograms show that the TDE hosts are typically more massive than E+A galaxies, but with similar colors characteristic of the green valley.

To study the light profile of each host galaxy, we perform two-dimensional Sérsic profile fits to the photometry using `GIM2D` (Simard et al., 2002). Following the procedure of Simard et al. (2011), we performed simultaneous g- and r-band fits on the calibrated, sky-subtracted corrected frames of each host galaxy to obtain the total galaxy Sérsic index. The top panel of Figure 3.3 shows the results of fitting the TDE hosts with a pure Sérsic model, along with the SDSS comparison sample. Many of ZTF TDE host galaxies have profiles between a de Vaucouleurs profile ($n_g = 4$) and a exponential disk profile ($n_g = 1$). We also show the smoothed histograms for the stellar mass and the Sérsic index for the TDE hosts as well as the green valley, blue cloud, red sequence, and E+A galaxies in the comparison sample. TDE hosts and E+A galaxies have steeper Sérsic indices than the green valley, more characteristic of the red sequence.

We calculate the effective stellar surface mass density, $\mu_\star$, of the TDE hosts and the comparison sample using the estimated half light radius, θ, from `GIM2D`. $\mu_\star$ is calculated using the following equation:

$$\mu_\star = M_\star/(2\pi\theta^2)\ [M_\odot \mathrm{kpc}^{-2}]. \tag{3.2}$$

The bottom panel of Figure 3.3 shows the effective stellar surface mass density vs. total stellar

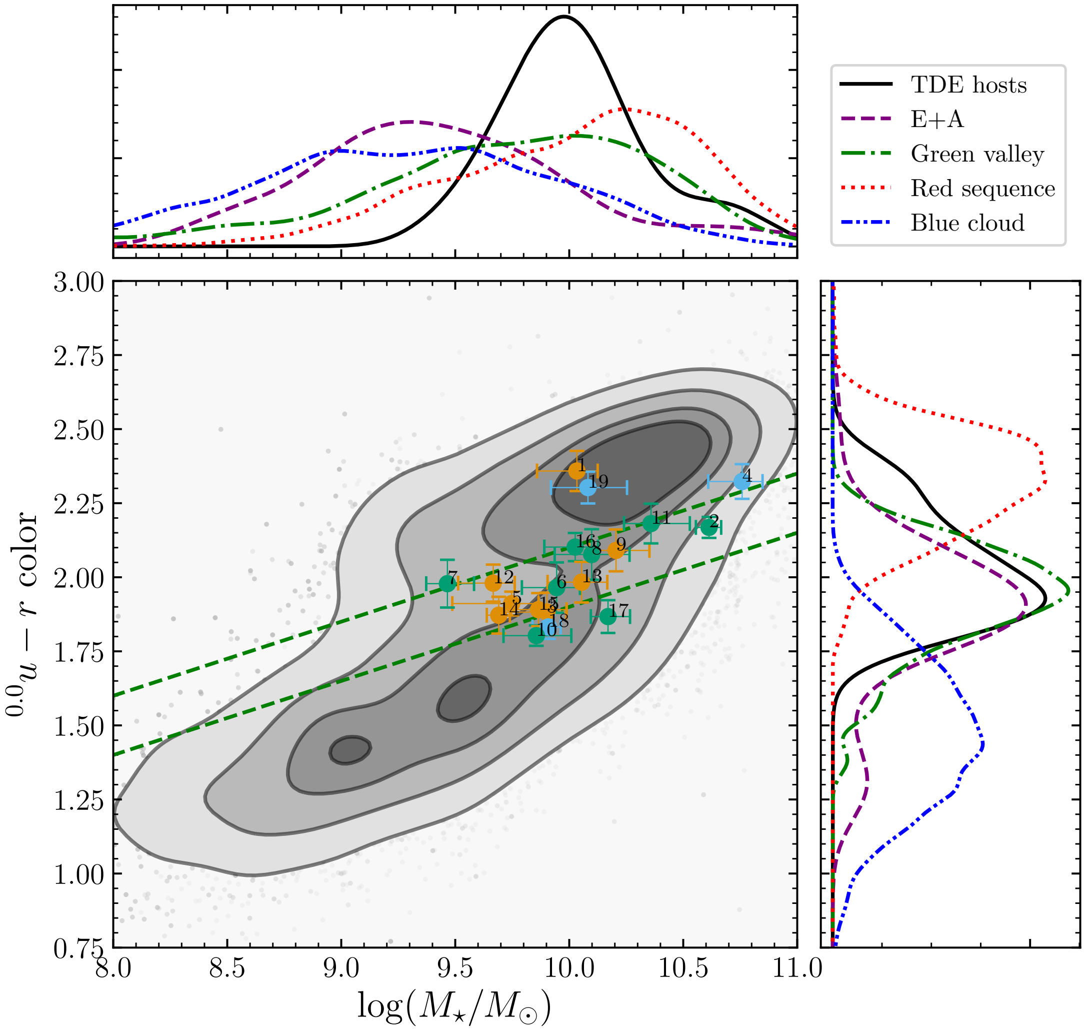

Figure 3.2: The extinction-corrected, synthetic rest-frame $u - r$ color of the TDE host galaxies. The green valley is denoted by the dashed green lines. TDE host galaxies are colored by their spectral type from van Velzen et al. (2021), where orange is TDE-H, green is TDE-H+He, and blue is TDE-He. They are also numbered by the ID column in Table 3.1. The contours enclose a volume-limited comparison sample of galaxies, matched to the depth of ZTF, from 0.5σ to 2σ in steps of 0.5σ. We also show the smoothed histograms for the stellar mass and the $u - r$ color for the TDE hosts as well as the green valley, blue cloud, and red sequence. We see that the TDE hosts are generally more massive than E+A galaxies, but with similar colors characteristic of the green valley.

mass for the TDE hosts as well as the comparison sample. The TDE hosts have surface mass densities similar to other galaxies in the green valley.

3.3.2 Spectral Measurements

The Hα emission equivalent width (EW) and the Lick H$\delta_{\rm A}$ absorption index can be used to explore the star formation history of a galaxy. TDE hosts in previous studies appear to be overrepresented in E+A or post-starburst galaxies, which occupy a specific region in the Hα EW vs. H$\delta_{\rm A}$ absorption index parameter space (French et al., 2016; Law-Smith et al., 2017). French et al. (2016) isolate E+A galaxies by requiring H$\delta_{\rm A} - \sigma({\rm H}\delta_{\rm A}) > 4.0$ and Hα EW < 3.0. These restrictions select galaxies that do not have any active star-formation, as seen from weak Hα emission, but strong H$\delta_{\rm A}$ absorption from A stars indicates star-formation in the past $\sim$ Gyr. Both French et al. (2016) and Law-Smith et al. (2017) also employ a looser cut, H$\delta_{\rm A} > 1.31$, allowing for host galaxies that have several possible star-formation histories. Here we make the distinction that E+A/post-starburst galaxies are identified with the stricter cut on both Hα and Hδ (hereafter E+A), while quiescent Balmer-strong galaxies are identified with the looser cut on these values (hereafter QBS). Both of these cuts are included in the following analysis.

We fit the spectra with stellar population models using `ppxf` (Cappellari, 2017) to fit the stellar continuum and emission lines, including Balmer lines, [O II], [S II], [O III], [O I], and [N II]. We use models from the MILES library of stellar spectra (Vazdekis et al., 2015), with the models based on a standard Salpeter IMF and Girardi et al. (2000) isochrones and covering the rest-frame range 3540–7410 Å. We measure the H$\delta_{\rm A}$ absorption index using the `ppxf` best-fit stellar continuum following the procedure and bandpasses given in Worthey & Ottaviani (1997).

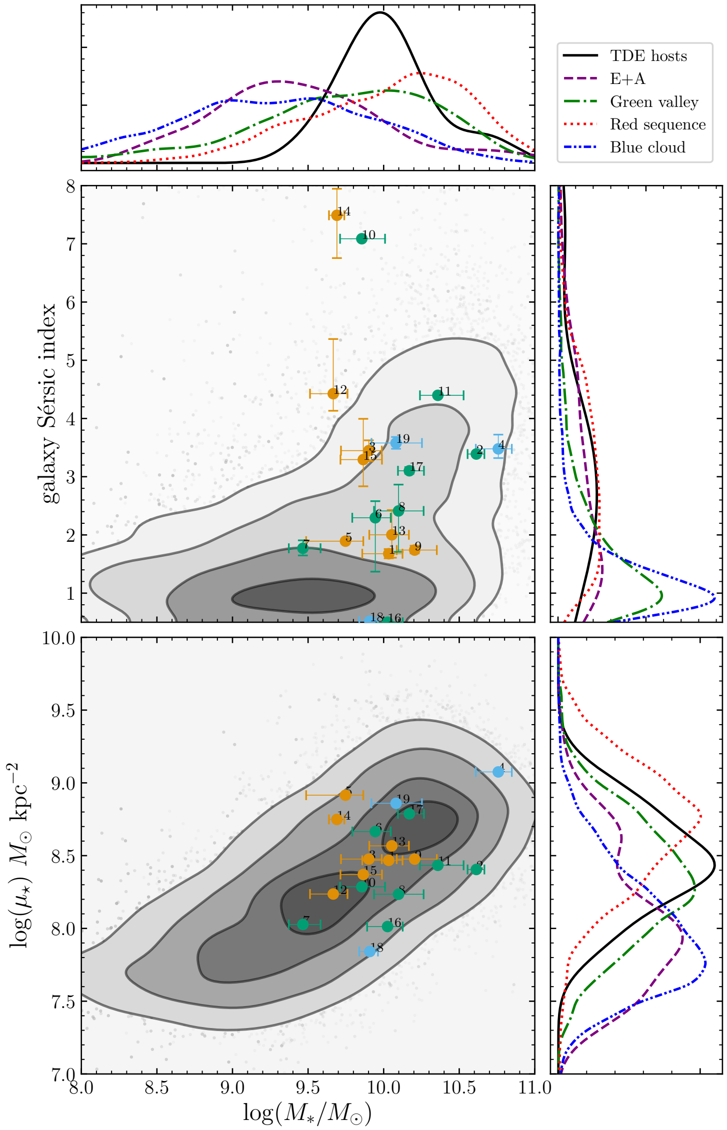

Figure 3.3: *Top panel*: The total galaxy Sérsic index vs. the total stellar mass. AT2019azh (ID 10) is an extreme post-starburst galaxy and high Sérsic index is expected. AT2019meg (ID 14) has a small angular size which likely affects the fit, resulting in the larger uncertainties and high Sérsic index. *Bottom panel*: The effective stellar mass surface density vs. the total stellar mass. Colors of points, labels, and contours are the same as previous figures. We also show the smoothed histograms for the stellar mass, the Sérsic index, and the effective stellar surface mass density for the TDE hosts as well as the green valley, blue cloud, and red sequence. We see that the TDE hosts have light profiles characteristic of red sequence galaxies.

The total Hα EW in Angstroms is measured from the host spectrum and is corrected for Balmer absorption by subtracting the equivalent width of the absorption line in the best-fit stellar continuum from the total EW of the line, leaving only the Hα emission EW. The Hα line for AT2018iih (ID 4) is redshifted out of the LDT bandpass. Thus, we measure the Hβ line, and take Hα to be $\approx$3 times Hβ, folding this into the uncertainties as well. Since the Balmer decrement (Hα/Hβ) will only increase in the presence of dust extinction, assuming a ratio of $\approx$3 is a conservative estimate. Figure 3.4 shows the Hδ_A absorption index vs. the Hα emission EW. Two TDE hosts are within the bounds of the E+A region defined by French et al. (2016).

For the TDE hosts with prominent emission lines (7/19), we plot the emission line ratios measured with `ppxf` on a BPT diagram (Baldwin et al., 1981) in Figure 3.5. 2 hosts (IDs 10 and 14) fall within the AGN region of the diagram, one host (ID 16) falls within the star-forming region of the diagram, while the remaining 4 (IDs 2, 9, 17, and 18) are between AGN and star-forming in the composite region. We discuss these results in Section 3.4. Note that we do not include AT2019dsg despite its prominent emission lines because Hα is rotationally broadened and we cannot resolve the [N II] doublet.

3.4 Discussion

Green valley galaxies dominate the ZTF TDE host galaxy sample. We find an overrepresentation of green valley galaxies of $\approx 5\times$, which is not accounted for by controlling for mass or Sérsic index. Law-Smith et al. (2017) used the definition of the green valley based on total star formation rate and found that their sample of TDE host galaxies may be transitioning from star-forming to quiescent, a time during which quenching of star formation causes galaxies to cross

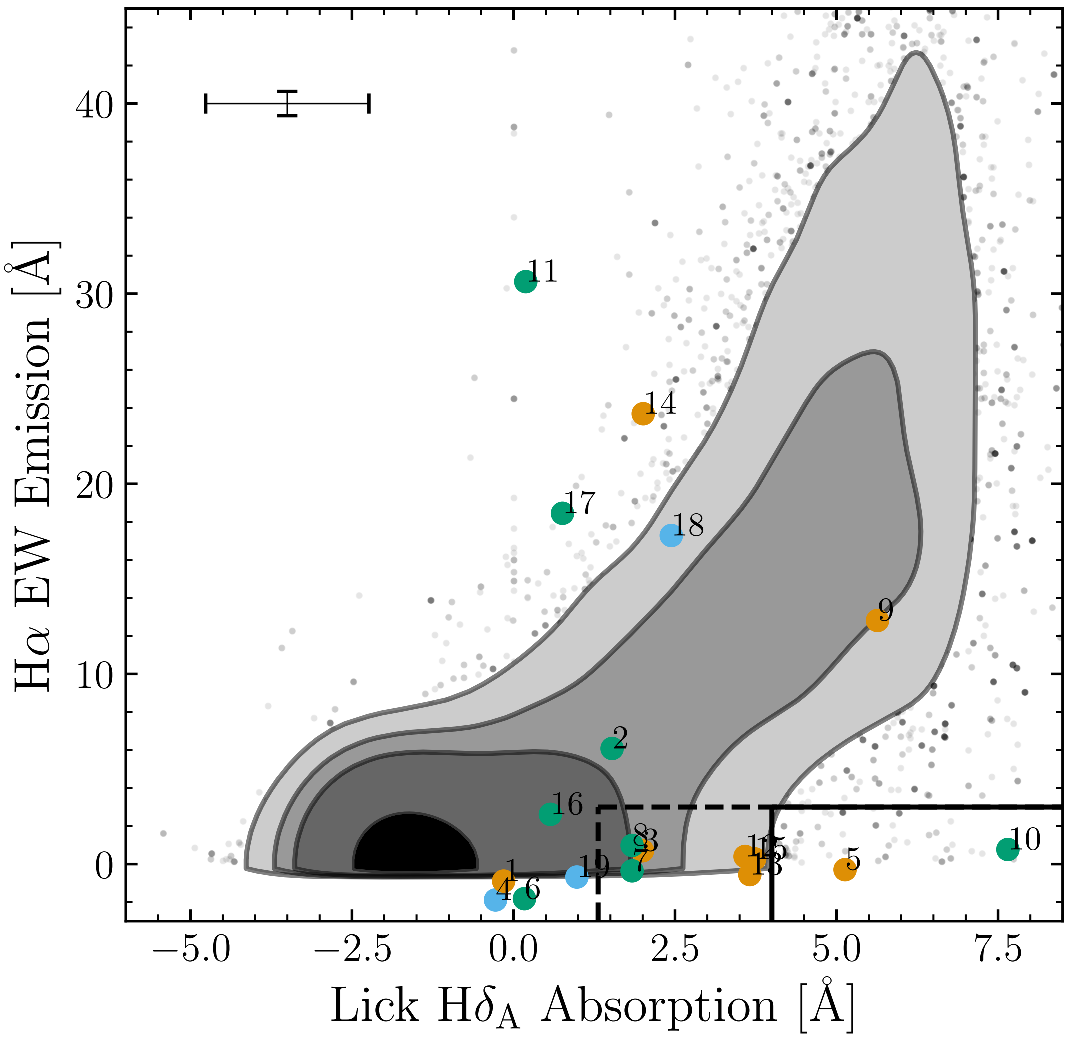

Figure 3.4: The $H\delta_A$ absorption index vs. the $H\alpha$ emission equivalent width. The median uncertainties for the TDE hosts are shown in the top left. The E+A region is the solid line while the QBS region is the dashed line. AT2019dsg (ID 11) is a star-forming galaxy. Two host galaxies fall within the strict E+A category: AT2018hyz (ID 5) and AT2019azh (ID 10). Colors of points, labels, and contours are the same as previous figures.

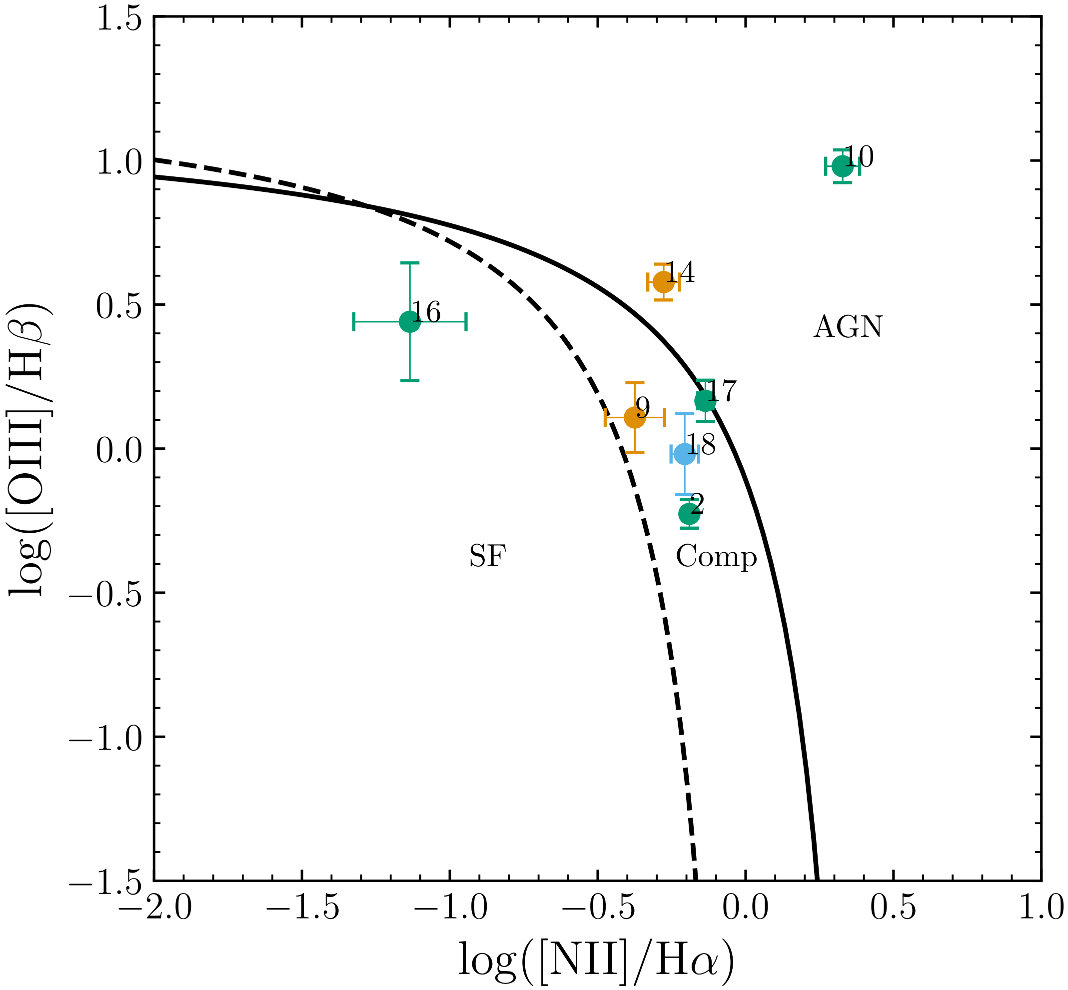

Figure 3.5: BPT diagram for the 7 TDE hosts that show prominent nebular emission lines. We show the separation lines of Kewley et al. (2001) and Kauffmann et al. (2003) as solid and dashed lines, respectively. The line ratios for the majority of the TDE hosts can be explained, at least in part, by star formation.

into the green valley (Schawinski et al., 2014). The green valley is also known to host a population of quiescent, Balmer-strong galaxies (including post-starburst or E+A galaxies), which previous studies observed to be overrepresented in TDE host galaxy samples (Arcavi et al., 2014; French et al., 2016; Law-Smith et al., 2017). Figure 3.4 reveals that two galaxies in this sample can be classified as E+A (AT2018hyz and AT2019azh, IDs 5 and 10 respectively) using the guidelines in Figure 3.4. AT2019azh is an extreme post-starburst galaxy, as noted by Hinkle et al. (2021). While 2 of 19 hosts fall within the E+A region, implying an E+A fraction of 10% with a binomial confidence interval of 1%–33%, this region makes up just 0.49% of the SDSS comparison sample, implying that E+A galaxies are overrepresented in the ZTF sample by a factor of ≈22. The overrepresentation is lower than previous studies have found by a factor of at least 4. This overrepresentation of E+A galaxies declines to a factor of ≈7 when selecting only on green valley galaxies. We also make a cut on "concentrated" galaxies ($n_g > 2.0$), and find that the E+A overrepresentation is a factor of ≈15. If we combine these two criteria, then the E+A overrepresentation is $\approx 3\times$.

To further test this result, we repeat these calculations by further limiting the comparison sample to the mass range of the TDE hosts, $9.47 \leq \log(M/M_{\odot}) \leq 10.76$. E+A galaxies are now overrepresented by a factor of ≈29. When considering only green valley galaxies in this mass limited sample, the overrepresentation declines to a factor of ≈8. The Sérsic index cut gives an E+A overrepresenation of $\approx 29\times$. After combining these two criteria, we find that the E+A overrepresentation can be completely accounted for. Note that E+A galaxies are predominantly in the green valley (see Figure 3.2), and thus the reduction in E+A overrepresentation among TDEs compared to green comparison galaxy sample is not surprising. However, this further supports the conclusion that green color is driving the E+A enhancement and not properties unique to the

E+A spectral class. These calculations can also be repeated to include the QBS region of the Hα-H$\delta_{\rm A}$ figure, in order to account for more ambiguous star-formation histories. These numbers are presented in Table 3.2.

E+A galaxies are also known to have nuclear stellar overdensities and thus have a higher Sérsic index (e.g. French et al., 2020a). Law-Smith et al. (2017) concluded that the Sérsic index is a stronger factor in enhancing the TDE rate in a galaxy than other properties that they measured. Figure 3.3 shows that galaxies in the ZTF sample have higher Sérsic indices than is typical for galaxies of similar stellar mass. Law-Smith et al. (2017) found a similar trend in Sérsic index for TDE host galaxies with Sérsic indices in the range $1 < n_g < 5$. We note, however, that the resolution of SDSS and PS1 is insufficient to fit the bulge Sérsic index independently of a disk that may be present. Thus, if a substantial disk component is present in a galaxy, the bulge component may actually have a higher Sérsic index. These fits should therefore be interpreted as lower limits on the bulge Sérsic index.

Despite the insufficient resolution of SDSS, Simard et al. (2011) found that galaxies fit with a free n_b bulge+disk model resulting in a bulge-to-total light ratio of $0.2 \leq (B/T) \leq 0.45$ required a bulge+disk model while a fit resulting in $(B/T) > 0.75$ did not require a bulge+disk model to fit the light profile. We performed free n_b bulge+disk decompositions on the sample of ZTF host galaxies in order to determine which galaxies may require a bulge+disk model to properly fit the light profile. Using the criteria from Simard et al. (2011), 6 of the TDE host galaxies require a bulge+disk model to properly fit the light profile and 5 require only a Sérsic profile, while the rest remain ambiguous. The ZTF TDE hosts may have steeper bulge profiles than Figure 3.3 demonstrates but higher resolution imaging is needed to separate the bulge and disk components.

French et al. (2017) constructed a BPT diagram for 5 TDE hosts, finding that the location of the TDE hosts in AGN region of the diagram is consistent with a sample of quiescent, Balmer-strong galaxies from SDSS. Figure 3.5 shows a BPT diagram for the TDE hosts with prominent nebular emission lines. One of the hosts (ID 16) has emission line ratios consistent with only star-formation. While previous studies, such as French et al. (2017), found that several TDE hosts had emission line ratios consistent with AGN or LINER-like activity, only 2 of the TDE hosts (IDs 10 and 16) have emission line ratios consistent with the AGN region of the BPT diagram. The remaining 4 hosts have emission line ratios that may, in part, be attributed to star formation. This BPT diagram is similar to the BPT diagram for X-ray selected TDEs in Wevers et al. (2019). For TDE hosts falling in the AGN region of the BPT diagram, French et al. (2017) mention several possible ionization mechanisms which may act to enhance the TDE rate in galaxies. These mechanisms include a low-luminosity AGN fueled by a circumnuclear gas reservoir and shocks resulting from a recent merger or starburst.

Figures 3.2 and 3.3 show smoothed histograms for the $u-r$, galaxy stellar mass, and Sérsic index. From Figure 3.2, we see that TDE hosts are typically more massive than E+A galaxies, which are on the low end of the green valley in terms of mass. We also see that TDE host galaxies are in the green valley in terms of color, with a distribution that matches that of E+A galaxies. Figure 3.3 shows that both E+A galaxies and TDE host galaxies have Sérsic indices different from other galaxies in the green valley, with a distributions closer to that of the red sequence.

Schawinski et al. (2010) found that the migration of low-mass, early-type galaxies from the blue cloud to the green valley is linked to mergers but the ability to link merger signatures to these galaxies over timescales longer than ∼500 Myr post-merger is limited. Subsequently, Schawinski et al. (2014) found that there are two main causes for galaxies to fall in the green valley. They found that morphologically late-type galaxies in the green valley are consistent with a scenario where the supply of gas fueling star-formation is shut off, leading to an exhaustion of the remaining gas over the next Gyr or so. Morphologically early-type galaxies are in the green valley as a result of a scenario where quenching of star formation happened rapidly and was accompanied by a change in morphology from disk to spheroid, likely as a consequence of a merger. E+A galaxies are thought to have undergone merger-triggered bursts of star-formation that place them in the green valley and that lead to centrally concentrated stellar distributions (Yang et al., 2008). Indeed, Schawinski et al. (2014) found that morphologically early-type galaxies in the green valley show classic post-starburst stellar populations.

Given that the TDE hosts show a distribution in Sérsic index more similar to red, early-type galaxies, it is possible that TDE host galaxies, E+A or not, are more likely to come from galaxies that have undergone some type of merger that produces centrally concentrated stellar distributions and which places them in the green valley. Prieto et al. (2016) found that the host galaxy of TDE ASASSN-14li (Holoien et al., 2016a), PGC 043234, possesses properties indicative of a recent merger, including AGN activity, post-starburst populations, and emission line filaments extending up to 10 kpc from the galaxy itself. This further supports the idea that E+A galaxies are the result of galaxy mergers that could enhance the TDE rate. The E+A phase of a post-merger system could also be a time when the TDE rate is greatly enhanced as compared to other phases of a post-merger system, which would explain the overrepresentation. Stone et al. (2018) showed the nuclear stellar overdensities created as the result of starbursts can reasonably match the TDE delay-time distribution and that the post-starburst TDE rate does indeed decline with time. This may be a reason why we find few red galaxies in the ZTF TDE sample. The majority of the ZTF TDE hosts are not E+A galaxies, but they do have more centrally concentrated stellar

	Overall	Green Valley	$n_g > 2.0$	Green Valley + $n_g > 2.0$
Full Sample (E+A)	22×	7×	15×	3×
$9.47 \leq \log(M_\star/M_\odot) \leq 10.76$ (E+A)	29×	8×	29×	1×
Full Sample (QBS)	16×	10×	13×	6×
$9.47 \leq \log(M_\star/M_\odot) \leq 10.76$ (QBS)	17×	9×	21×	3×

Table 3.2: The E+A overrepresentation in the ZTF TDE host galaxy sample calculated with respect to the full galaxy comparison sample and a mass-limited comparison sample, for the E+A criteria and the QBS criteria. We give the overall overrepresentation, the overrepresentation when considering only the green valley as well as considering only concentrated galaxies in the comparison sample, and the latter two combined.

distributions. We propose that, similar to Law-Smith et al. (2017), the overall stellar distribution in a galaxy is more important than the E+A classification and that E+A galaxies are only a subset of the larger population of galaxies that are likely to host TDEs.

3.5 Conclusions

We have studied a sample of galaxies hosting TDEs detected by ZTF in the first two-thirds of survey operations. Our main conclusions are:

- The ZTF TDE host galaxy sample is dominated by green valley galaxies, with 63% of the TDE hosts having $u - r$ colors corresponding to the green valley, compared to only 13% of the comparison sample of galaxies.

- E+A galaxies, which we define spectroscopically, are overrepresented in the ZTF TDE host galaxy sample by a factor of ≈22 compared to the SDSS comparison sample of galaxies. This overrepresentation reduces to a factor of ≈7 when selecting only on green valley galaxies (defined photometrically) and to a factor of ≈3 when selecting on green valley galaxies with concentrated stellar distributions. The apparent E+A preference for TDE host galaxies is completely accounted for when looking at galaxy populations with similar masses, colors, and Sérsic indices as the ZTF TDE hosts. However, we point the reader to a caveat on the correlated nature of E+A spectral type and green color in Section 3.4.

- The ZTF TDE hosts have higher Sérsic indices than galaxies of similar stellar masses and show a distribution of Sérsic indices similar to E+A galaxies and red sequence galaxies, rather than green valley galaxies.
- TDE hosts may be more likely to be found in the subset of galaxies that have undergone a more recent merger that produced centrally-concentrated stellar distributions, enhancing the TDE rate.

3.6 Acknowledgements

We thank the anonymous referee for their helpful comments. We thank S. Veilleux and R. Mushotzky for their valuable comments and discussion during the early stages of this paper. SG is funded in part by NSF CAREER grant 1454816, and NASA Swift grant 80NSSC20K0961. The UCSC team is supported in part by NSF grant AST-1518052; the Gordon & Betty Moore Foundation; the Heising-Simons Foundation; and by a fellowship from the David and Lucile Packard Foundation to R.J.F.

These results made use of the Lowell Discovery Telescope at Lowell Observatory. Lowell is a private, nonprofit institution dedicated to astrophysical research and public appreciation of astronomy and operates the LDT in partnership with Boston University, the University of Maryland, the University of Toledo, Northern Arizona University and Yale University. The upgrade of the DeVeny optical spectrograph has been funded by a generous grant from John and Ginger Giovale.

Based on observations obtained with the Samuel Oschin Telescope 48-inch and the 60-inch Telescope at the Palomar Observatory as part of the Zwicky Transient Facility project. ZTF is supported by the National Science Foundation under Grant No. AST-1440341 and a collaboration including Caltech, IPAC, the Weizmann Institute for Science, the Oskar Klein Center at Stockholm University, the University of Maryland, the University of Washington, Deutsches Elektronen-Synchrotron and Humboldt University, Los Alamos National Laboratories, the TANGO Consortium of Taiwan, the University of Wisconsin at Milwaukee, and Lawrence Berkeley National Laboratories. Operations are conducted by COO, IPAC, and UW. This work was supported by the GROWTH project funded by the National Science Foundation under Grant No 1545949.

Funding for the SDSS and SDSS-II has been provided by the Alfred P. Sloan Foundation, the Participating Institutions, the National Science Foundation, the U.S. Department of Energy, the National Aeronautics and Space Administration, the Japanese Monbukagakusho, the Max Planck Society, and the Higher Education Funding Council for England. The SDSS Web Site is `http://www.sdss.org/`. The SDSS is managed by the Astrophysical Research Consortium for the Participating Institutions. The Participating Institutions are the American Museum of Natural History, Astrophysical Institute Potsdam, University of Basel, University of Cambridge, Case Western Reserve University, University of Chicago, Drexel University, Fermilab, the Institute for Advanced Study, the Japan Participation Group, Johns Hopkins University, the Joint Institute for Nuclear Astrophysics, the Kavli Institute for Particle Astrophysics and Cosmology, the Korean Scientist Group, the Chinese Academy of Sciences (LAMOST), Los Alamos National Laboratory, the Max-Planck-Institute for Astronomy (MPIA), the Max-Planck-Institute for Astrophysics (MPA), New Mexico State University, Ohio State University, University of Pittsburgh, University of Portsmouth, Princeton University, the United States Naval Observatory, and the University of Washington.

The Pan-STARRS1 Surveys (PS1) and the PS1 public science archive have been made possible through contributions by the Institute for Astronomy, the University of Hawaii, the Pan-STARRS Project Office, the Max-Planck Society and its participating institutes, the Max Planck Institute for Astronomy, Heidelberg and the Max Planck Institute for Extraterrestrial Physics, Garching, The Johns Hopkins University, Durham University, the University of Edinburgh, the Queen's University Belfast, the Harvard-Smithsonian Center for Astrophysics, the Las Cumbres Observatory Global Telescope Network Incorporated, the National Central University of Taiwan, the Space Telescope Science Institute, the National Aeronautics and Space Administration under Grant No. NNX08AR22G issued through the Planetary Science Division of the NASA Science Mission Directorate, the National Science Foundation Grant No. AST-1238877, the University of Maryland, Eotvos Lorand University (ELTE), the Los Alamos National Laboratory, and the Gordon and Betty Moore Foundation.

Chapter 4: Integral Field Spectroscopy of 13 Tidal Disruption Event Hosts from the ZTF Survey

4.1 Introduction

It is generally accepted that most, if not all, massive galaxies host a supermassive black hole (SMBH) in their nucleus which play important roles in the evolution and properties of their host galaxies (e.g. Fabian, 2012; Gültekin et al., 2009; Ho, 2008; Kormendy & Ho, 2013; Kormendy & Richstone, 1995; Magorrian & Tremaine, 1999; Veilleux et al., 2005, 2020). This is evident from scaling relations between the SMBH mass and host galaxy properties such as the bulge velocity dispersion (e.g. Ferrarese & Merritt, 2000; Gebhardt et al., 2000) or bulge luminosity (e.g. Dressler, 1989; Magorrian et al., 1998). These objects can announce their presence most prominently through sustained accretion of nuclear gas and dust as active galactic nuclei (AGN), but many more SMBHs lie dormant, making the study of these objects more difficult. The tidal disruption of a star by the central SMBH, known as a tidal disruption event (TDE), provides a unique way to gain insights on the population of distant and mostly quiescent SMBHs.

A TDE occurs when a star passes sufficiently close (i.e., within the tidal radius) to a SMBH such that the tidal forces felt by the star are stronger than its own self-gravity, resulting in the star being torn apart and roughly half of that stellar debris being eventually accreted by the black hole, creating a luminous flare of radiation potentially visible from Earth (Evans & Kochanek, 1989; Rees, 1988; Ulmer, 1999). TDEs were only a theoretical prediction just ∼50 yrs ago (Hills, 1975; Lidskii & Ozernoi, 1979), and we now have observational evidence of these events from the radio to X-rays, with the largest samples of TDEs discovered in the optical using surveys such as iPTF (Blagorodnova et al., 2017, 2019; Hung et al., 2017), ASAS-SN (Hinkle et al., 2021; Holoien et al., 2014a, 2016a,b, 2019a; Wevers et al., 2019), Pan-STARRS (Chornock et al., 2014; Gezari et al., 2012; Holoien et al., 2019b; Nicholl et al., 2019), SDSS (van Velzen et al., 2011), and ZTF (Hammerstein et al., 2023a; van Velzen et al., 2019d, 2021; Yao et al., 2023). While the light curves and spectra of TDEs offer important clues to the formation of the accretion disk, winds, and jets, the host galaxies of these transients provide insights into SMBH–galaxy co-evolution, galaxy evolution and mergers, and the dynamics of galaxy nuclei. Understanding the environments that are most likely to host TDEs will even lead to more efficient discovery and follow-up during the era of the Vera Rubin Observatory, which is predicted to observe hundreds to even thousands of new TDEs a year (van Velzen et al., 2011).

TDEs have also been shown to be observed preferentially in E+A or post-starburst galaxies (Arcavi et al., 2014; French et al., 2016; Hammerstein et al., 2021a; Law-Smith et al., 2017), whose optical spectra are characterized by little to no Hα or [O II] emission and strong Balmer absorption, indicating the presence of stars formed within the past Gyr but no current star formation activity. Typical E+A overrepresentation (i.e., the ratio between the fraction of TDE hosts that are E+As to the fraction of all galaxies that are E+As) ranges widely depending on the study, with some population studies finding an overrepresentation of over 100× (Law-Smith et al., 2017) and others finding an overrepresentation of just 22× (Hammerstein et al., 2021a). E+A galaxies are also known to have large bulge-to-light ratios, high Sérsic indices, and high concentration indices (Yang et al., 2008), all of which have been shown to greatly enhance the TDE rate in these galaxies by making more stars available in the nuclear region to be tidally disrupted (French et al., 2020a; Stone & Metzger, 2016; Stone & van Velzen, 2016).

Several previous studies have aimed to characterize the environments that are most likely to host TDEs and have shown that certain large-scale galaxy properties are indeed linked with higher TDE rates. Graur et al. (2018) found that TDE host galaxies have higher stellar mass surface density and lower velocity dispersions as compared to a sample of galaxies not known to host recent TDEs. Law-Smith et al. (2017) examined a sample of TDE host galaxies in comparison to the local galaxy population and found that all of the TDE hosts in their sample reside below the star formation main sequence, have bluer bulge colors, high Sérsic indices and high bulge-to-light ratios compared to galaxies of similar masses. Hammerstein et al. (2021a) found that 61% of TDE host galaxies in their sample were in the green valley between the star-forming "blue cloud" and the passive "red sequence" of galaxies, compared to only 13% of SDSS galaxies. They also found that while most green valley galaxies have Sérsic indices comparable to blue cloud galaxies, the TDE hosts had higher Sérsic indices most similar to red, passive galaxies. All of these properties are indicative of systems which have undergone a merger that produce concentrated central stellar distributions and can indeed enhance the TDE rate (French et al., 2020a; Stone & Metzger, 2016; Stone & van Velzen, 2016).

In this paper, we present integral field spectroscopy (IFS) of a sample of 13 TDE host galaxies from the Zwicky Transient Facility (ZTF) survey in order to obtain their black hole masses and understand their large-scale kinematics and stellar populations, the latter of which we compare to several other galaxy populations, including E+A galaxies. Integral field spectroscopy provides spatially resolved spectra which gives a study such as this one an edge over long-slit spectroscopy when attempting to probe various size scales of the TDE host galaxies. In Section 4.2, we describe the observations of the 13 TDEs in our sample as well as the subsequent data reduction and analysis methods. We present the results of the kinematic and stellar population analysis and discuss these results in Section 4.3. We discuss the results pertaining to the black hole mass in Section 4.4 and those pertaining to the stellar kinematics and populations in Section 4.5. We close with our conclusions in Section 4.6.

4.2 Observations & Data Analysis

We selected our host galaxy sample from the ZTF-I TDEs published in van Velzen et al. (2021) and Hammerstein et al. (2023a), with the intention of constructing a sample which includes multiple TDE spectral classes and X-ray brightnesses. We point to van Velzen et al. (2021) for a full description of the ZTF TDE search, although we note that the method for discovering TDEs is agnostic to host galaxy type apart from filtering out known AGN. While this search is thus agnostic to host galaxy type, we do note that our selection of TDE hosts from the ZTF sample, designed to include TDEs from all classifications, will not follow the true observed rate of each type of TDE. However, this is likely not relevant for the study presented here as we do not make conclusions by comparing the TDE types. We show SDSS and Pan-STARRS images of each of the host galaxies in Figure 4.1. Our sample of thirteen TDEs includes all four TDE spectral classes (for a description of all classes, see Hammerstein et al., 2023a), with 2 TDE-H, 8 TDE-H+He, 2 TDE-He, and 1 TDE-featureless, 6 of which are also X-ray detected TDEs. The hosts span redshifts in the range $0.015 \leq z \leq 0.345$ and have stellar masses in the range $9.56 \leq \log(M_{\rm gal}/M_{\odot}) \leq 11.23$, both of which we take from the published values of van Velzen

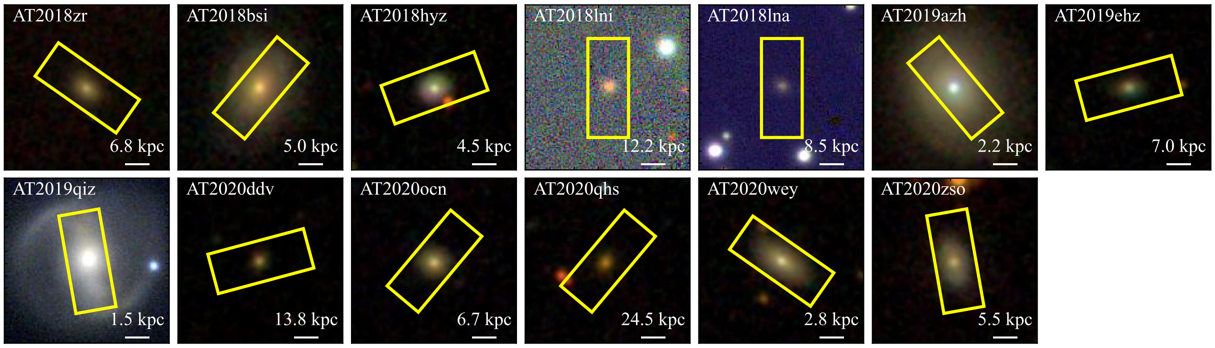

Figure 4.1: SDSS and Pan-STARRS *gri* images of the thirteen TDE host galaxies, with the yellow rectangle representing the positioning of the KCWI field of view. All images are $34'' \times 34''$ and the KCWI field of view is $8\farcs4 \times 20\farcs4$.

et al. (2021) and Hammerstein et al. (2023a). In Figure 4.2, we show the redshift distribution of the TDE hosts. In Sections 4.4 and 4.5, we separate and discuss our results based on resolution.

In Figure 4.3 we show the rest-frame, extinction corrected $u - r$ color from Hammerstein et al. (2023a) derived from fitting the host SED for the TDE host galaxies as a function of host galaxy stellar mass. We also include a background sample of 955 galaxies from the SAMI Galaxy Survey DR3 (Croom et al., 2021), which provides spatially resolved stellar kinematic and population information, discussed further in Section 4.5. The galaxies in the SAMI sample were selected to span the plane of mass and environments, with the redshifts spanning $0.004 \leq z \leq 0.095$, masses between $10^7 - 10^12M_{\odot}$, magnitudes with $r_{\rm pet} < 19.4$, and environments from isolated galaxies to groups and clusters (Bryant et al., 2015). ∼54% of the TDE hosts are in the green valley compared to just ∼20% of the background galaxies, in line with previous findings (e.g., Hammerstein et al., 2021a, 2023a; Sazonov et al., 2021; Yao et al., 2023). We summarize the properties of the host galaxies and include references to the first TDE classification in Table 4.1.

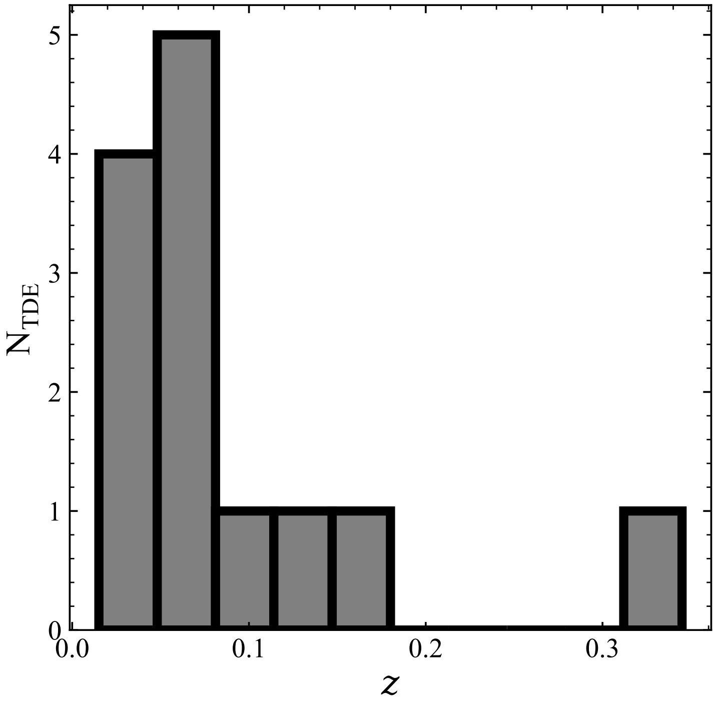

Figure 4.2: The distribution of redshifts for the TDE host galaxies in our sample. The distribution peaks below $z \sim 0.1$, with the highest redshift object, AT2020qhs, at $z = 0.345$. Values are taken from van Velzen et al. (2021) and Hammerstein et al. (2023a).

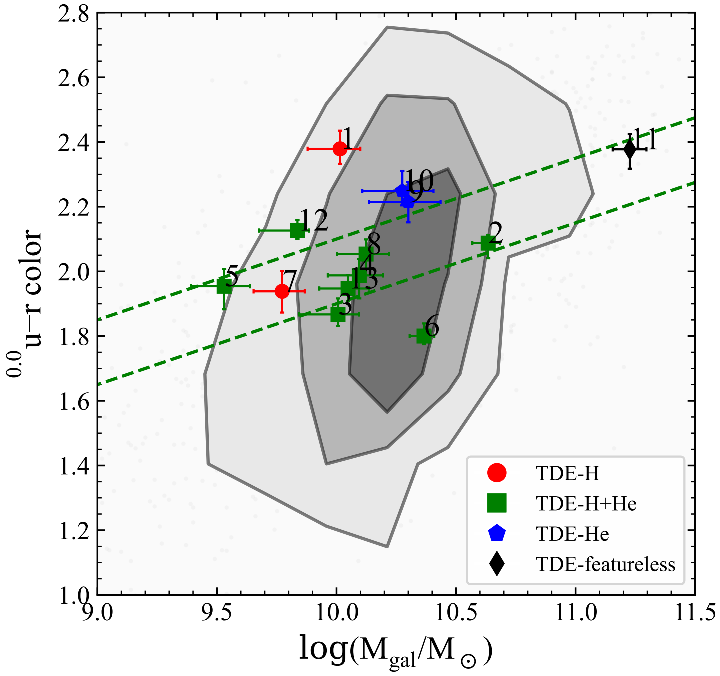

Figure 4.3: The rest-frame, extinction corrected $u - r$ color as a function of host galaxy mass for the TDE host galaxies and a sample of 955 galaxies from the SAMI survey. The dashed green lines indicate the location of the green valley, the location of which we take from Hammerstein et al. (2023a). The colors and shapes of the points indicate the spectral class of TDE for each event. IDs are listed in Table 4.1. The TDE hosts are typically less massive than the background sample and more often reside in the green valley compared to the background galaxies (∼54% vs. ∼20%).

ID	Name	RA	Dec.	First TDE Classification	Spectral Class	Redshift	$\log(M_{\rm gal}/M_{\odot})$	m_r	$\sigma_{\rm instr}$ (km s^{-1})
1	**AT2018zr**	07:56:54.55	+34:15:43.6	Tucker et al. (2018)	TDE-H	0.071	$10.01^{+0.08}_{-0.14}$	18.02	18.3
2	AT2018bsi	08:15:26.63	+45:35:32.0	Gezari et al. (2018)	TDE-H+He	0.051	$10.62^{+0.05}_{-0.07}$	15.50	18.8
3	**AT2018hyz**	10:06:50.88	+01:41:33.9	Dong et al. (2018)	TDE-H+He	0.046	$9.96^{+0.09}_{-0.16}$	16.96	16.3
4	AT2018lni	04:09:37.65	+73:53:41.7	van Velzen et al. (2021)	TDE-H+He	0.138	$10.10^{+0.10}_{-0.13}$	19.46	15.4
5	AT2018lna	07:03:18.65	+23:01:44.7	van Velzen et al. (2019e)	TDE-H+He	0.091	$9.56^{+0.11}_{-0.14}$	19.51	17.1
6	**AT2019azh**	08:13:16.95	+22:38:53.9	van Velzen et al. (2019a)[1]	TDE-H+He	0.022	$9.74^{+0.08}_{-0.05}$	14.39	22.1
7	**AT2019ehz**	14:09:41.91	+55:29:27.8	Gezari et al. (2019)	TDE-H	0.074	$9.81^{+0.09}_{-0.12}$	18.72	19.8
8	AT2019qiz	04:46:37.88	−10:13:34.9	Siebert et al. (2019)	TDE-H+He	0.015	$10.01^{+0.10}_{-0.12}$	14.17	18.6
9	**AT2020ddv**	09:58:33.42	+46:54:40.4	Gezari et al. (2020b)	TDE-He	0.160	$10.30^{+0.13}_{-0.16}$	19.37	14.9
10	**AT2020ocn**	13:53:53.80	+53:59:49.7	Gezari et al. (2020a)	TDE-He	0.070	$10.28^{+0.13}_{-0.17}$	17.57	18.3
11	AT2020qhs	02:17:53.95	−09:36:50.9	Hammerstein et al. (2023a)	TDE-featureless	0.345	$11.23^{+0.07}_{-0.07}$	19.40	13.0
12	AT2020wey	09:05:25.91	+61:48:09.1	Arcavi et al. (2020)	TDE-H+He	0.027	$9.63^{+0.18}_{-0.22}$	16.61	22.1
13	AT2020zso	22:22:17.13	−07:15:58.9	Ihanec et al. (2020)	TDE-H+He	0.057	$10.05^{+0.09}_{-0.12}$	17.03	21.4

Table 4.1: Labels used in figures, RA and Dec, TDE classification references, spectral classes, redshifts, host galaxy stellar masses, and host galaxy apparent r-band magnitudes for the thirteen objects in our sample. All spectral classifications, redshifts, and host galaxy stellar masses are based on those provided in van Velzen et al. (2021) and Hammerstein et al. (2023a). Host magnitudes are derived from Pan-STARRS. X-ray-detected events are bolded. We also provide the instrumental resolution, $\sigma_{\rm instr}$, measured from the FWHM of the arc spectrum at the observed wavelength of the Ca II H and K lines for each object.

---

[1] See also Hinkle et al. (2021).

4.2.1 Large Monolithic Imager and GALFIT

We obtained optical imaging of the host galaxies in our sample using the Large Monolithic Imager (LMI) mounted on the 4.3-m Lowell Discovery Telescope (LDT) in Happy Jack, AZ. Data were obtained on 2022-10-30, 2022-11-30, and 2023-02-13 (PIs: Hammerstein, O'Connor) under clear skies and good observing conditions (seeing $\sim 1''$). The targets were observed in the SDSS r-band filter with varying exposure times depending on the galaxy brightness, e.g., from 50 s for $r \approx 14$ AB mag to 200 s for $r \approx 19.5$ AB mag. The chosen exposure times lead to a high signal-to-noise ratio (SNR) for each galaxy, which when combined with the spatial resolution of LMI allow for an improved morphological analysis when compared to available archival data (e.g., SDSS). We were able to observe all thirteen host galaxies through this program. We reduced the LMI data using a custom `python` pipeline (see O'Connor et al., 2022; Toy et al., 2016) to perform bias subtraction, flat-fielding, and cosmic ray rejection. The observations for each galaxy, including observation date, exposure time, and seeing during each observation are described in Table 4.2. Given that the LMI observations were obtained several years after peak for all objects, we do not expect that the transient will contribute any appreciable flux to the photometry that may affect the fitting performed here.

We use `GALFIT` (Peng et al., 2002) to perform 2D fits to the host galaxy photometry and obtain morphological parameters such as the effective radius, ellipticity, and position angle of the host galaxies. Because we are interested in exploring galaxy properties at several different scales, we perform two fits with two different models. The first model includes a Sérsic component and exponential disk component which is used to obtain a bulge effective radius ($R_{\mathrm{e,bulge}}$). This radius is used to mask a region in the IFU data for obtaining the bulge velocity dispersion and

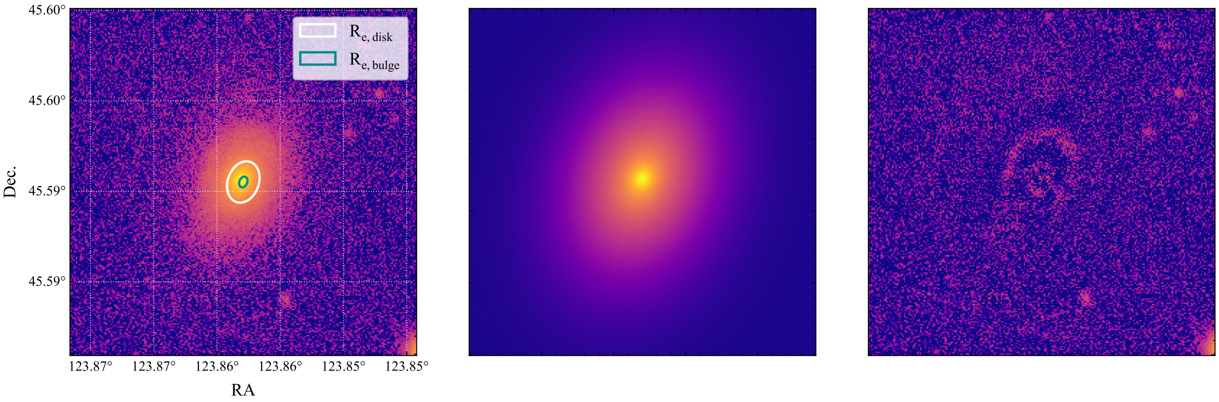

Figure 4.4: A 29″×29″ cutout of the LMI observations of the host galaxy of AT2018bsi, shown with the `GALFIT` model and residuals. All images are on the same scale. `GALFIT` is able to model the host galaxy reasonably well with the residuals showing potential dust lane or spiral arm features which are not as straightforward to model with `GALFIT` and for the purposes of the study presented here, are unimportant. In the left panel we show two ellipses representing the fitted bulge effective radius ($R_{\rm e,bulge}$, cyan) and the disk effective radius (where the relationship between the effective radius and the scale length of the disk is $R_{\rm e,disk} = 1.678 R_{\rm s,disk}$, white).

subsequently the black hole mass. The second fit includes a single Sérsic component, used to obtain the effective radius of the entire galaxy light profile ($R_{\rm e,gal}$). We use this radius to mask the region for general kinematic and stellar population analysis. We fit all galaxies using these two models with the exception of AT2019qiz. The prominent bar in AT2019qiz required the addition of another component in order to isolate the bulge of the galaxy. Instead, we used a model which includes an exponential disk and two Sérsic components, one for the bulge and one for the bar, which was sufficient to isolate the bulge and obtain the bulge effective radius. Some galaxies required additional components to mask out nearby stars or faint galaxies in the fitting window, which we included when necessary. We present the results of this fitting, namely the galaxy and bulge effective radii, in Table 4.4 and show an example fit and residuals in Figure 4.4.

Name	Obs. Date	Exp. Time (s)	Seeing ($''$)
AT2018zr	2022 Oct. 31	150	1.0
AT2018bsi	2022 Dec. 01	55	1.0
AT2018hyz	2022 Dec. 01	80	1.1
AT2018lni	2022 Dec. 01	200	1.1
AT2018lna	2022 Oct. 31	200	1.1
AT2019azh	2022 Oct. 31	70	1.0
AT2019ehz	2023 Feb. 13	120	1.9
AT2019qiz	2022 Dec. 01	50	1.1
AT2020ddv	2022 Oct. 31	200	1.3
AT2020ocn	2022 Dec. 01	100	1.1
AT2020qhs	2022 Dec. 01	200	1.0
AT2020wey	2022 Oct. 31	80	1.4
AT2020zso	2022 Dec. 01	60	1.2

Table 4.2: Summary of observations obtained with LMI, including the observation date, exposure time, and seeing measured from the PSF of the observation. All observations were performed using the SDSS r-band filter.

4.2.2 Keck Cosmic Web Imager and GIST

We present Keck Cosmic Web Imager (KCWI; Morrissey et al., 2018) observations of thirteen TDE host galaxies selected from the ZTF-I sample of TDEs. Integral field spectra were obtained on the night of 2021-12-25 under clear weather conditions (seeing $\sim 0.8''$) as part of program ID N096 (PI: Gezari). Observations for each object, described in Table 4.3, were obtained using the small ($8''.4 \times 20''.4$) slicer and 'BM' grating, which gives a nominal resolution of $R_0 = 8000$ and an average bandpass of 861 Å. In Table 4.3, we provide the instrumental resolution, $\sigma_{\rm instr}$, for each object measured from the FWHM of the arc spectrum at the observed wavelength of the Ca II H and K lines. We also provide the days since peak for each observation as well as the average seeing between coadded exposures in Table 4.3. Three different central wavelengths were used to ensure that important host galaxy stellar absorption lines were observed for each galaxy. The final configurations are as follows:

i. *C1*: Small slicer, ‘BM’ grating, central wavelength of 4200 Å.

ii. *C2*: Small slicer, ‘BM’ grating, central wavelength of 4800 Å.

iii. *C3*: Small slicer, ‘BM’ grating, central wavelength of 5200 Å.

In Figure 4.1, we overplot the KCWI pointing for each observed galaxy. Three host galaxies, AT2018bsi, AT2019azh, and AT2019qiz, have angular sizes larger than the KCWI field-of-view. For each of these galaxies we obtained sky exposures offset from the host galaxy in order to perform sky subtraction.

The observations were reduced using the standard procedure of the KCWI data reduction pipeline (Neill et al., 2023) which includes bias subtraction, flat fielding, cosmic ray removal, sky subtraction, wavelength calibration, heliocentric correction, and flux calibration. We used `CWITools` (O’Sullivan & Chen, 2020) to apply a WCS correction to the KCWI data in ‘src_fit’ mode, which fits 1D profiles to the spatial data to find the peak of the source and then applies a correction to the WCS such that the peak aligns with the input coordinates.

We use the Galaxy IFU Spectroscopy Tool (`GIST`; Bittner et al., 2019) modified to work with KCWI data to obtain the stellar kinematic and population information. The `GIST` pipeline performs all necessary steps to analyze the KCWI IFU spectra with `ppxf` (Cappellari, 2023), including spatial masking and binning, SNR determination and masking, stellar kinematic analysis, and stellar population analysis. The X-shooter library of simple stellar population models (XSL; Verro et al., 2022) offers the best spectral resolution ($\sigma \sim 13$ km s^{-1}, $R \sim 10000$) and wavelength coverage (3500 Å– 24800 Å) which matches our KCWI observations ($\lambda_{\rm obs,min} = 3768$ Å in configuration C1 and $\lambda_{\rm obs,max} = 5624$ Å in configuration C3), meaning we can fit the entire spectral range for each host galaxy. The XSL provides several options for initial mass functions

(IMF) and isochrones. We choose the set of models that utilizes the Salpeter IMF (Salpeter, 1955) and PARSEC/COLIBRI isochrones (Bressan et al., 2012; Marigo et al., 2013), which includes stellar populations with ages above 50 Myr and metallicities in the range $-2.2 <$ [Fe/H] $< +0.2$, normalized to obtain mass-weighted stellar population results.

We run the `GIST` pipeline three times for each host galaxy, each time using different binning and masking criteria, and using 1000 Monte-Carlo simulations to extract the uncertainties on the stellar kinematics. We spatially mask and bin the spaxels for the three different fits as follows:

i. *Bulge σ fit*: Mask all spaxels outside of $R_{\rm e,bulge}$ obtained from `GALFIT`; combine remaining spaxels into one bin to obtain σ, the bulge velocity dispersion.

ii. *Galaxy $(V/\sigma)_e$ fits*: Mask all spaxels outside of $R_{\rm e,gal}$ obtained from `GALFIT`; apply no binning to obtain the spatially resolved galaxy line-of-sight velocities (V) and velocity dispersions (σ), with $(V/\sigma)_e$ being the ratio of random to ordered motion within the galaxy effective radius.

iii. *Stellar population fit*: Mask all spaxels outside of $R_{\rm e,gal}$ obtained from `GALFIT`; combine remaining spaxels into one bin.

We are motivated to perform three different fits for several reasons. The first is so that our black hole masses are determined only from the bulge velocity dispersions, with the bulge effective radius determined from the two component `GALFIT` fit. The second is so that our determination of the large-scale kinematics and stellar population properties follows most closely the methods of van de Sande et al. (2018), who perform two fits within an ellipse that encloses half of the projected total galaxy light: one which is similar to our galaxy $(V/\sigma)_e$ fit and one which is similar

Name	Config.	Exp. Time (s)	$\Delta t_{\mathrm{obs-peak}}$ (days)	Seeing ($''$)
AT2018zr	C1	2×900	1372	0.72
AT2018bsi	C1	2×150	1362	0.65
AT2018hyz	C1	2×600	1150	0.61
AT2018lni	C2	2×1800	1097	0.69
AT2018lna	C1	2×1500	1067	0.82
AT2019azh	C1	2×100	1008	0.68
AT2019ehz	C1	2×1000	960	0.65
AT2019qiz	C1	2×500	807	0.95
AT2020ddv	C2	2×1500	655	0.71
AT2020ocn	C1	2×600	585	0.52
AT2020qhs	C3	1350, 500	511	0.75
AT2020wey	C1	2×200	418	0.74
AT2020zso	C1	300, 600	386	0.66

Table 4.3: Summary of observations obtained with KCWI, including the instrument configuration, exposure times, days post-peak from the tidal disruption flare, and the average seeing for the coadded observations. t_{peak} is taken from Hammerstein et al. (2023a). The configuration notation is described in Section 4.2.2.

to our stellar population fit. There are four cases in which the bulge effective radius is smaller than the seeing of the KCWI observations: AT2018lni, AT2020ddv, AT2020ocn, and AT2020qhs. For these objects, instead of simply using the bulge effective radius given by `GALFIT` to perform the bulge σ fit, we use the sum in quadrature of the bulge effective radius and the seeing given in Table 4.3. The galaxy effective radius for AT2018lni is also smaller than the seeing, and in this case, we use the sum in quadrature of the galaxy effective radius and the seeing to perform the galaxy $(V/\sigma)_e$ fits and the stellar population fit. We present and discuss the results of this analysis in the next sections.

4.3 Results

We present the results of our kinematic and stellar population analysis on the KCWI spectra of the 13 TDE host galaxies. We summarize our main results in Table 4.4. In Figure 4.5, we show a white light image of the host galaxy of AT2019azh and example output maps from `GIST`, including the line-of-sight velocity and velocity dispersion as well as the stellar population age and metallicity. In Figure 4.6, we show the bins constructed by `GIST`, as well as two example spectra and `ppxf` fits from different bins. The output we show in Figures 4.5 and 4.6 involves no spatial masking like that described in Section 4.2.2, but instead masks spaxels below the isophote level which has a mean SNR of 2.2. This particular fit is not used for any analysis and is for illustrative purposes only.

One important comparison to make for all results is that of the differing angular resolutions resulting from the range of redshifts for the TDE hosts. As such, we investigate whether angular resolution may influence the results we discuss in Sections 4.4 and 4.5. We split our sample into three different angular resolution bins:

i. $\sim$0.5 kpc/$''$: AT2019azh, AT2019qiz, AT2020wey

ii. $\sim$1.0 kpc/$''$: AT2018bsi, AT2018hyz, AT2020zso

iii. $\gtrsim$1.3 kpc/$''$: AT2018zr, AT2018lni, AT2018lna, AT2018ehz, AT2020ddv, AT2020ocn, AT2020qhs

We perform an Anderson-Darling test to compare these three subsamples and find that we cannot reject the null hypothesis that they are drawn from the same distribution of host galaxy stellar mass, velocity dispersion, black hole mass, or $(\mathrm{V}/\sigma)_e$ (p-value ≥ 0.25 for all tests). However, the sample sizes compared are small and may not provide a true measure of how angular resolution affects studies such as the one presented here. In the following sections, we discuss our results on obtaining the black hole masses and characterizing the host galaxy stellar kinematics and populations.

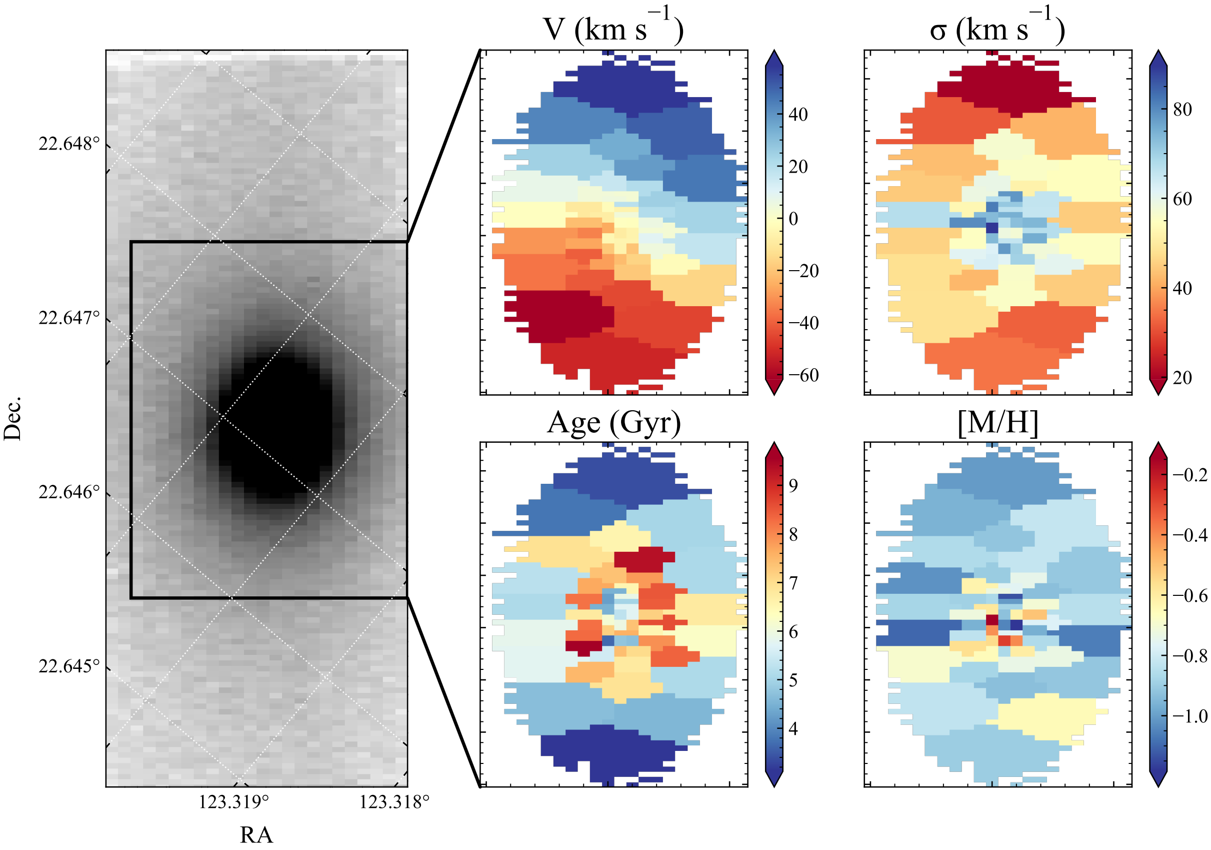

Figure 4.5: An example output from `GIST` of the host galaxy of AT2019azh. The left panel shows an unbinned white light image of the KCWI observation. The panels on the right depict the output maps from `GIST`, which show the `ppxf`-derived line-of-sight velocity, velocity dispersion, and stellar population ages and metallicities. The bins in this figure are constructed using the Voronoi binning method (Cappellari & Copin, 2003) to reach a threshold SNR for each bin, in this case SNR ~ 10. We note that Voronoi binning is not performed for the fits used in the analysis.

This fit involves no spatial masking like that described in Section 4.2.2, but instead masks spaxels below the isophote level which has a mean SNR of 2.2. This particular fit is not used for any analysis and is for illustrative purposes only.

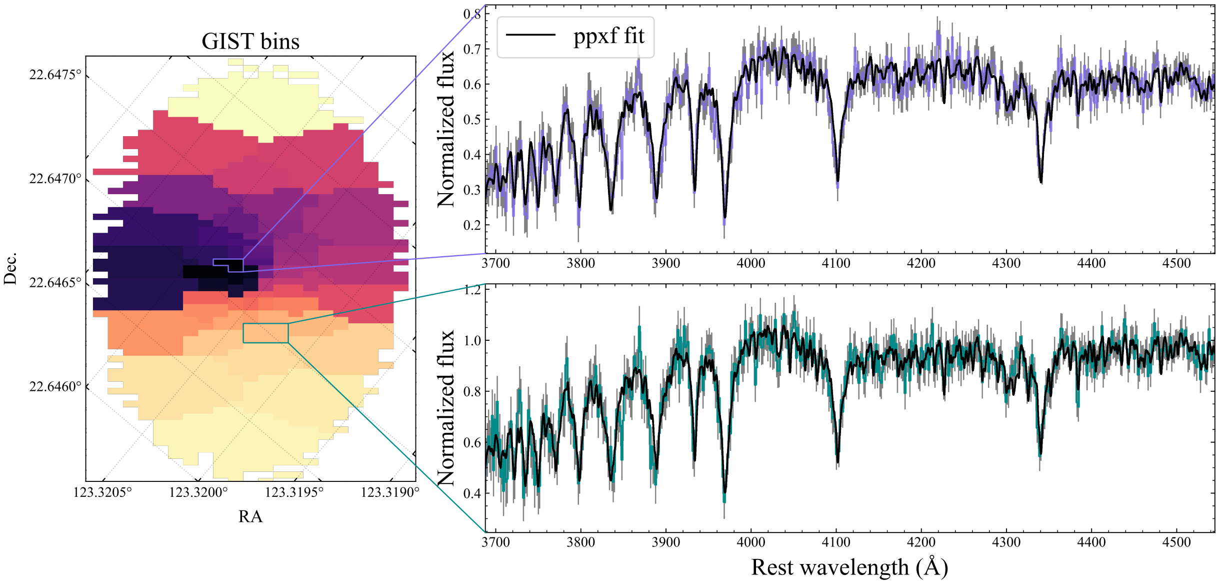

Figure 4.6: Example `ppxf` fits to the host galaxy of AT2019azh output from `GIST`. The left panel shows the bins constructed with `GIST` where the color represents the bin to which each spaxel belongs. Bins are constructed using the Voronoi binning method (Cappellari & Copin, 2003) to reach a threshold SNR for each bin, in this case SNR $\sim$ 10. We note that Voronoi binning is not performed for the fits used in the analysis. The two panels on the right show the spectra (purple and teal lines) and `ppxf` fits (black lines) from the outlined bins on the left. We show the uncertainties on the spectra in gray.

Name	kpc/$''$	$R_{\rm e,gal}$ ($''$)	$R_{\rm e,bulge}$ ($''$)	$\sigma_\star$ (km s^{-1})	$\log(M_{\rm BH}/M_\odot)$	(V/σ)$_e$	Age (Gyr)
AT2018zr	1.35	1.87	0.89	49.79 ±4.93	5.56 ± 0.76	0.52 ± 0.20	2.65
AT2018bsi	1.00	6.15	1.84	117.54 ±8.12	7.14 ± 0.62	0.93 ± 0.15	0.57
AT2018hyz	0.90	1.34	0.69	66.62 ±3.12	6.10 ± 0.67	0.12 ± 0.05	6.95
AT2018lni	2.44	0.56 (0.88)	0.34 (0.78)	59.47 ±3.78	5.89 ± 0.70	0.26 ± 0.09	8.65
AT2018lna	1.70	1.15	0.92	36.43 ±4.52	4.98 ± 0.83	0.78 ± 0.38	3.23
AT2019azh	0.45	9.75	2.52	68.01 ±2.02	6.13 ± 0.66	0.88 ± 0.11	8.68
AT2019ehz	1.41	1.76	1.15	46.65 ±11.83	5.44 ± 0.98	0.37 ± 0.20	6.03
AT2019qiz	0.31	8.85	2.27	71.85 ±1.93	6.23 ± 0.65	0.71 ± 0.08	2.15
AT2020ddv	2.76	0.88	0.47 (0.85)	73.44 ±10.06	6.28 ± 0.78	0.09 ± 1.11	6.12
AT2020ocn	1.34	1.40	0.28 (0.59)	90.15 ±4.46	6.65 ± 0.63	0.36 ± 0.14	8.09
AT2020qhs	4.89	2.05	0.72 (1.04)	188.69 ±37.86	8.01 ± 0.82	0.53 ± 0.15	1.98
AT2020wey	0.55	2.49	0.87	53.54 ±4.75	5.69 ± 0.74	0.40 ± 0.32	8.43
AT2020zso	1.10	2.57	1.08	61.80 ±4.93	5.96 ± 0.71	1.08 ± 0.27	6.32

Table 4.4: The results from our photometric and kinematic analysis of the LMI and KCWI data, including the galaxy and bulge half light radii measured from `GALFIT`, the bulge velocity dispersion and derived black hole mass, the ratio of ordered rotation to random stellar motion (V/σ)$_e$, and the stellar population age within the galaxy effective radius. For AT2018lni, AT2020ddv, AT2020ocn, and AT2020qhs, the values in parentheses are the values obtained from adding the `GALFIT` values and the KCWI seeing in quadrature, and are the values used to extract the bulge σ fits, and in the case of AT2018lni, the galaxy kinematics and stellar population fits.

4.4 Black hole masses

We derive the black hole masses through the $M_{\rm BH} - \sigma$ relation of Gültekin et al. (2009), assuming that this relation holds valid for all galaxies in this sample:

$$\log(M_{\rm BH}/M_\odot) = 8.12 + 4.24 \log\left(\frac{\sigma}{200\ \text{km s}^{-1}}\right) \tag{4.1}$$

We propagate the uncertainties on the velocity dispersion through this relation and add them linearly with the intrinsic scatter on the relation to obtain the uncertainty on the black hole mass.

In Figure 4.7, we show the distribution of black hole masses for the entire sample in addition to the subsamples of X-ray bright and X-ray faint events. We find that the distribution peaks at $\log(M_{\rm BH}/M_{\odot}) = 6.05$ with a range of masses $4.98 \leq \log(M_{\rm BH}/M_{\odot}) \leq 8.01$, which is consistent with previous studies performing a similar analysis (e.g., Wevers et al., 2017, 2019; Yao et al., 2023). We examine whether the populations of X-ray bright and X-ray faint events show any significant difference in their black hole mass distributions by performing an Anderson-Darling test and find that we cannot reject the null hypothesis that the X-ray bright and X-ray faint samples are drawn from the same distribution in black hole mass (p-value ≥ 0.25). This is consistent with several previous studies (e.g., French et al., 2020b; Hammerstein et al., 2023a; Wevers et al., 2019) which largely found no significant difference in the black hole, host galaxy, or even light curve properties between X-ray bright and X-ray faint TDEs. This lack of difference between X-ray bright and X-ray faint populations may be explained by the unifying theory of Dai et al. (2018), which posits that whether or not X-rays are observed in a particular TDE is a matter of viewing angle effects.

Figure 4.8 shows the black hole mass as a function of the velocity dispersion along with several derived relations from the literature, including Gültekin et al. (2009), Xiao et al. (2011), and Kormendy & Ho (2013). While values derived from the Kormendy & Ho (2013) relation would generally be higher than those derived from the Gültekin et al. (2009) relation, the Xiao et al. (2011) relation is flatter, with higher velocity dispersion values yielding lower black hole masses and lower velocity dispersion values yielding higher black hole masses. We discuss further implications of our choice of $M_{\rm BH} - \sigma$ relation used to derive black hole masses in Sections 4.4.2 and 4.4.3.

In Figure 4.9, we show the derived black hole masses as a function of host galaxy stellar mass along with several empirical relations from the literature. Reines & Volonteri (2015) derived the relations for AGN and inactive galaxies, while Greene et al. (2020) derived the relations for

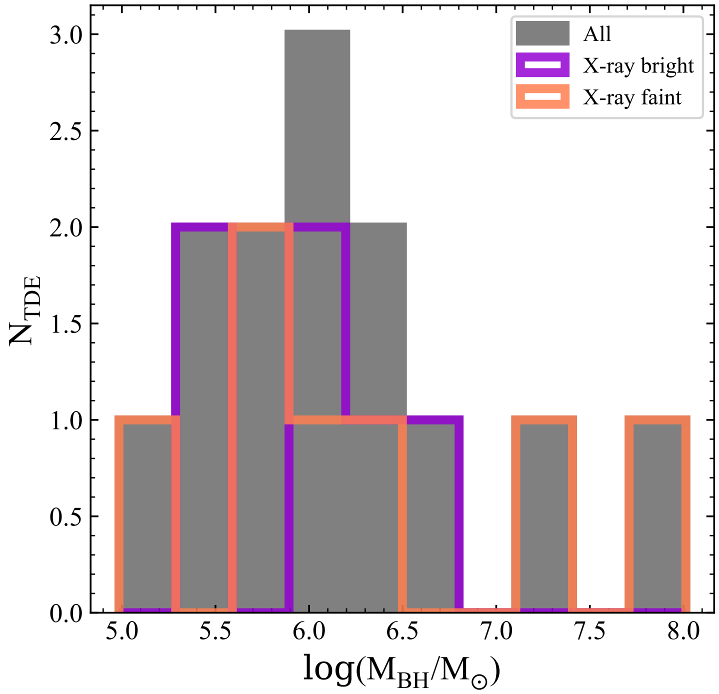

Figure 4.7: Distribution of black hole masses for the host galaxies in our sample. We show the entire sample in black, with the divisions on X-ray bright vs. X-ray faint in purple and orange, respectively. The distribution peaks at $\log(M_{\rm BH}/M_\odot) = 6.05$, consistent with previous results for similar analyses. We find no significant difference in black hole masses between the X-ray bright (6 total) and X-ray faint (7 total) events.

late, early, and all galaxy types. Importantly, Greene et al. (2020) used upper limits in their calculations which are crucial for including low-mass systems, such as the ones that host TDEs, in the relation. We also show the fitted relation from Yao et al. (2023), which was derived by fitting a linear relation between $M_{\rm gal}$ and $M_{\rm BH}$ for the TDE hosts in their sample. Rather interestingly, the TDE hosts most closely follow the relation for late-type galaxies, despite very few being classified as such. This could be explained by the very few low-mass early-type galaxies used in deriving the relations for early-type galaxies and all galaxy types. Alternatively, this may be caused by our choice in $M_{\rm BH} - \sigma$ relation, although each scaling will have its own resulting offset.

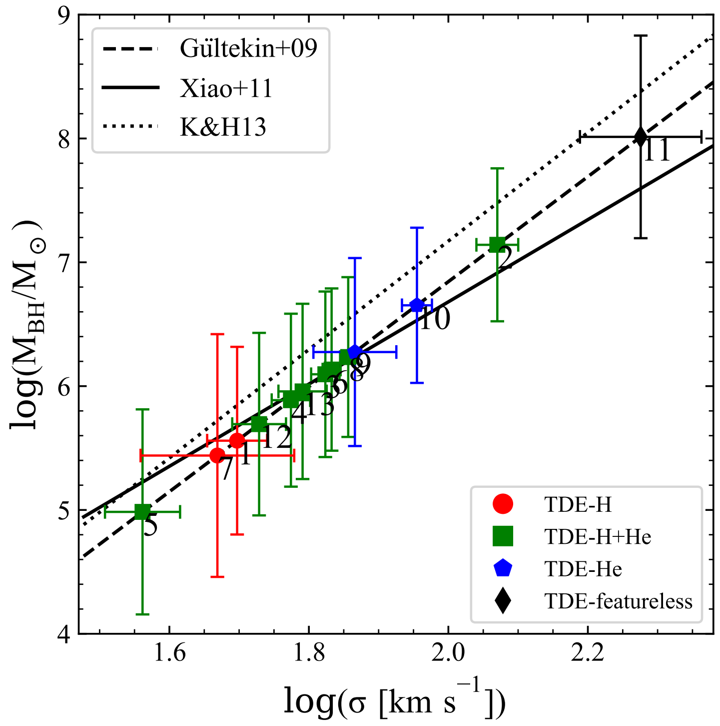

Figure 4.8: The black hole mass as a function of the velocity dispersion, along with several derived relations from the literature. We employ the relation of Gültekin et al. (2009) (Gültekin+09) to derive the black hole masses presented here. Black hole masses derived from Kormendy & Ho (2013) (K&H13) would generally be higher than those derived from Gültekin et al. (2009), while the Xiao et al. (2011) relation (Xiao+11) would yield lower masses at the higher velocity dispersion end of the relation and higher masses at the lower velocity dispersion end of the relation. Labels for each TDE are in Table 4.1.

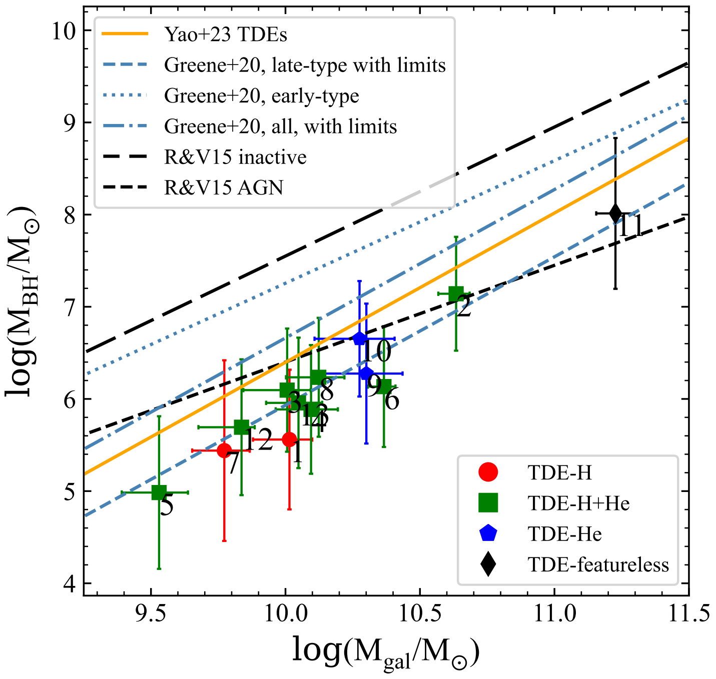

Figure 4.9: The black hole mass as a function of the host galaxy stellar mass. We show several derived $M_{\mathrm{BH}} - M_{\mathrm{gal}}$ relations. Black dashed and long-dashed lines show the relations from Reines & Volonteri (2015) derived from AGN host galaxies and inactive galaxies, respectively. The blue dashed, dotted, and dot-dashed lines show the relations from Greene et al. (2020) derived from late-type galaxies, early-type galaxies, and all galaxy types, respectively. We also showed the fitted relation from Yao et al. (2023), which was fit only for TDE hosts. Labels for each TDE are in Table 4.1.

4.4.1 Comparisons to previous measurements

All objects in our sample have previously measured black hole masses through a variety of methods, although only three have previously measured velocity dispersions. We compare our estimate of the black hole mass derived from the bulge velocity dispersion and $M_{\rm BH} - \sigma$ relation with previous estimates using the same method.

AT2019azh: Yao et al. (2023) derived the black hole mass for AT2019azh by fitting the optical ESI spectrum using `ppxf`. They found $\sigma_\star = 67.99 \pm 2.03$ km s^{-1}, corresponding to a black hole mass of $\log(M_{\rm BH}/M_\odot) = 6.44 \pm 0.33$ using the $M_{\rm BH} - \sigma$ relation of Kormendy & Ho (2013). Our value of $\sigma_\star = 68.01 \pm 2.02$ km s^{-1} is consistent with that of Yao et al. (2023).

AT2020wey: Yao et al. (2023) also measured the velocity dispersion of the host galaxy of AT2020wey in the same manner as AT2019azh, finding $\sigma_\star = 39.36 \pm 2.79$ km s^{-1}. We find a significantly higher value for the velocity dispersion of $\sigma_\star = 53.54 \pm 4.75$ km s^{-1}. It is possible that with the small effective radius of AT2020wey (see Table 4.4), the long-slit spectra used to derive the velocity dispersion in Yao et al. (2023) are inclusive of stars much farther from the bulge effective radius and thus have lower velocity dispersions. This may explain the discrepancy we see here. Indeed, a fit to the entire host galaxy of AT2020wey reveals that regions away from the nucleus have much lower velocity dispersions (~ 24 km s^{-1}) which may influence the resulting black hole mass derived from stellar kinematics.

AT2019qiz: Nicholl et al. (2020) fit the late time X-shooter spectrum of AT2019qiz using `ppxf` and found $\sigma_\star = 69.7 \pm 2.3$ km s^{-1}. Our value for the velocity dispersion is marginally higher, $\sigma_\star = 71.85 \pm 1.93$ km s^{-1}, but still consistent within the mutual uncertainties of the two measurements.

All objects in our sample also have at least one estimate of the black hole mass obtained from fitting the TDE light curve with the `MOSFiT` (Guillochon et al., 2018) TDE model (Mockler et al., 2019). The TDE model fits each TDE by generating bolometric light curves via hydrodynamical simulations and passing them through viscosity and reprocessing transformation functions to create the the single-band, observed light curves. `MOSFiT` then uses the single-band light curves to fit the multi-band input data to estimate the light-curve properties and information on the disrupted star in addition to the mass of the SMBH. Hammerstein et al. (2023a) used `MOSFiT` to fit the light curves of every object in our sample, but found no significant correlation with the host galaxy mass.

We now reexamine any potential correlation using the derived black hole mass instead. In Figure 4.10, we show the `MOSFiT` black hole mass as a function of the black hole mass we have derived here. The gray dashed line indicates a one-to-one relationship. While we do find a weak positive correlation between the `MOSFiT` masses and the masses we derive here using a Kendall's tau test ($\tau = 0.05$), it is not significant (p-value $= 0.9$). As our $M_{\rm BH} - \sigma$ derived black hole masses are so well correlated with the host galaxy masses from Hammerstein et al. (2023a), it is not surprising that we do not find a significant correlation between the `MOSFiT` masses and our masses. Given that the `MOSFiT` mass are typically orders of magnitude larger than those inferred through the $M_{\rm BH} - \sigma$ relation, it is possible that an underestimation of the black hole mass due to uncertainties of the relation at such low velocity dispersions is causing the discrepancy. Additional updates to the `MOSFiT` TDE model, which will be presented in Mockler & Nicholl et al. (2023, in prep), may also help to address the discrepancies.

Hammerstein et al. (2023a) also estimated the black hole mass using the `TDEmass` code (Ryu et al., 2020) which assumes that circularization happens slowly, and that the UV/optical emission arises from shocks in the intersecting debris streams instead of in an outflow or wind. Again, they found no significant correlation between the SMBH mass and the host galaxy mass. We show the `TDEmass` SMBH mass as a function of the SMBH mass derived from stellar kinematics in Figure 4.10, with gray dashed line indicates a one-to-one relationship. We note that the mass for AT2020qhs (ID 11) was not able to be determined with `TDEmass`. We find no significant correlation between the `TDEmass` values for the black hole mass and the ones we derive here (p-value $= 0.4$).

While it is not surprising that the `MOSFiT` and `TDEmass` values do not agree, as they derive the black hole mass using differing assumptions on the origin of the UV/optical emission, the lack of any correlation with host galaxy properties is puzzling. Previous studies (e.g., Mockler et al., 2019; Ramsden et al., 2022) which derive the black hole mass from `MOSFiT` have found weak correlations between the SMBH mass and properties such as the bulge mass and host galaxy stellar mass, but parameters such as the bulge mass can be difficult to determine for TDE host galaxies without sensitive imaging given their masses and redshifts. On the other hand, studies like Wevers et al. (2019) have confirmed a disparity between SMBH masses measured using `MOSFiT` and those from host scaling relations such as $M_{\rm BH} - \sigma$. The lack of correlation is not entirely discouraging, as there is indeed some correlation between light curve properties such as rise and fade timescale and the black hole mass (Hammerstein et al., 2023a; Nicholl et al., 2022; van Velzen et al., 2021; Yao et al., 2023), and perhaps indicates a need to revisit the exact ways in which the properties of the black hole are imprinted onto the observed TDE light curves.

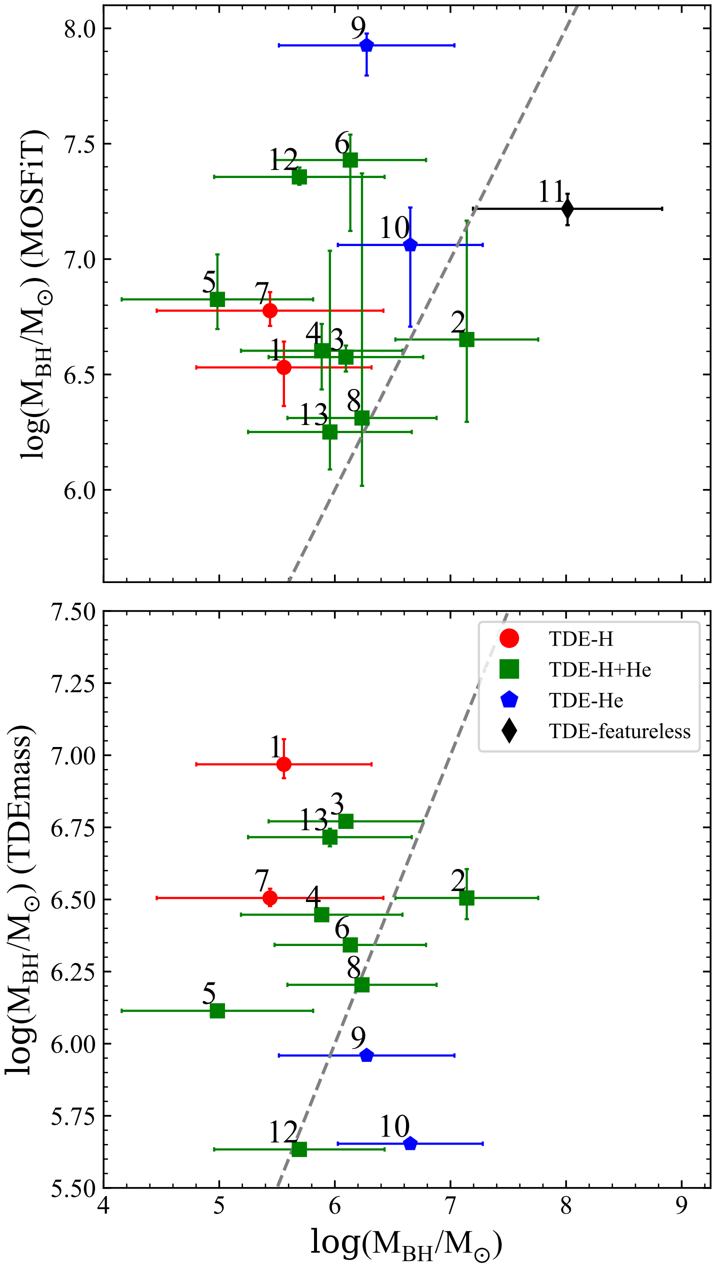

Figure 4.10: *Top panel*: The black hole mass derived from `MOSFiT` as a function of the black hole mass we derive from host kinematics. The gray dashed line indicates a one-to-one relationship. We do not find a significant correlation between the two measurements. *Bottom panel*: The black hole mass derived from `TDEmass` as a function of the black hole mass we derive from host kinematics. The gray dashed line indicates a one-to-one relationship. We note that the mass for AT2020qhs (ID 11) was not able to be determined with `TDEmass`. We do not find a significant correlation between the two measurements. Labels for each TDE are in Table 4.1.

4.4.2 Correlations with TDE light curve properties

Many previous studies have found significant correlations between the light curve properties of TDEs and the black hole mass or, more often, the host galaxy mass. van Velzen et al. (2021) found a correlation between the decay timescale and host galaxy stellar mass, which Hammerstein et al. (2023a) further confirmed with a larger sample. This is consistent with many previous results in the literature (e.g., Blagorodnova et al., 2017; Wevers et al., 2017). Hammerstein et al. (2023a) additionally found a weak correlation between the rise timescale and the host galaxy stellar mass as well as between the peak luminosity and the host galaxy stellar mass.

We now reexamine the correlations with host galaxy stellar mass presented in Hammerstein et al. (2023a). Between the SMBH mass and the decay rate for the 13 TDEs, we find a weak positive correlation with a Kendall's tau test, but the $\tau = 0.26$ correlation is not significant with p-value $= 0.25$. The Kendall's tau test between the SMBH mass and the rise results in $\tau = 0.41$, but again is not significant with a p-value $= 0.06$. We no longer find a correlation between the black hole mass and the peak blackbody luminosity. While we generally find the same trends as previous works, our smaller sample size weakens our ability to make significant conclusions and the disappearance of significant correlations here should be interpreted with caution.

The black hole mass now makes it possible to compare the peak blackbody luminosity of the TDE light curves with the Eddington luminosity implied by the black hole mass. We define the Eddington luminosity as $L_{\rm Edd} \equiv 1.25 \times 10^{38}(M_{\rm BH}/M_{\odot})$ and take values for the peak blackbody luminosity from Hammerstein et al. (2023a) measured using the peak UV/optical SED. In Figure 4.11, we show the peak blackbody luminosity as a function of the Eddington luminosity, with solid, dashed, and dotted curves representing lines of constant Eddington ratio.

All of our events are consistent with being at or below the Eddington luminosity (solid line), apart from AT2018lna (ID 5), with its blackbody luminosity significantly super-Eddington even at the maximum extent of its uncertainties. We note that this is also the lowest mass object in our sample with $\log(M_{\rm BH}/M_\odot) = 4.98 \pm 0.83$. The apparent significantly super-Eddington luminosity may be due to the large uncertainty on the calibration of $M_{\rm BH} - \sigma$ relation at such low velocity dispersions, although without larger samples of dynamically measured masses for intermediate mass black holes, this problem is hard to constrain (for a review on such measurements, see Greene et al., 2020). If we instead obtain the mass for AT2018lna using the relation from Xiao et al. (2011), derived from active galaxies with low black hole masses, we find that the resulting black hole mass is higher: $\log(M_{\rm BH}/M_\odot) = 5.22$. Although the peak luminosity is still super-Eddington. The mass for AT2018lna should thus be interpreted with caution. Super-Eddington mass fallback rates are not unexpected for black holes with such low masses, with duration of $\dot{M}/M_{\rm Edd} > 1$ longer for smaller black holes (De Colle et al., 2012). AT2018lna, the lowest mass black hole and the one with the largest Eddington ratio, does indeed follow this expected relation, its bolometric luminosity staying above Eddington for much longer than the other objects in this sample when examing the light curve fits of Hammerstein et al. (2023a).

AT2020qhs is an outlier in black hole mass, but not necessarily an outlier in its Eddington ratio. Wevers et al. (2019) found that the TDE candidate ASASSN-15lh possessed similar qualities and that the observed emission is consistent with the peak Eddington ratio and luminosity of a maximally spinning Kerr black hole. As we discuss in Section 4.4.3, a non-negligible spin may explain the properties of AT2020qhs.

Yao et al. (2023) found a correlation between the Eddington ratio ($\lambda_{\rm Edd} \equiv L_{\rm bb}/L_{\rm Edd}$) and the black hole mass which was inconsistent with the expected ratio between the peak fallback rate and Eddington accretion rate. Instead, they found a much shallower relation between $\dot{M}_{\rm fb}/\dot{M}_{\rm Edd}$ and the black hole mass, which they attribute to either Eddington-limited accretion or that the UV/optical luminosity only captures a fraction of the total bolometric luminosity. We report similar findings here, with a moderate negative correlation between $\lambda_{\rm Edd}$ and $M_{\rm BH}$ resulting from a Kendall's tau test ($\tau = -0.46$, p-value = 0.03). In Figure 4.12, we show $\log(\lambda_{\rm Edd})$ as a function of $M_{\rm BH}$, along with the fitted relations from Yao et al. (2023) (solid line, fitted for all 33 TDEs in their sample: $\dot{M}_{\rm fb}/\dot{M}_{\rm Edd} \propto M_{\rm BH}^{-0.49}$, dashed line, correcting for selection bias by only fitting objects with $z < 0.24$: $\dot{M}_{\rm fb}/\dot{M}_{\rm Edd} \propto M_{\rm BH}^{-0.72}$) and the expected relation $\dot{M}_{\rm fb}/\dot{M}_{\rm Edd} \propto M_{\rm BH}^{-3/2}$. Visual inspection shows that the relation for our sample may be steeper than that found by Yao et al. (2023).

4.4.3 AT2020qhs and the TDE-featureless class

We now turn our attention specifically to AT2020qhs (ID 11), which is a notable event for several reasons. AT2020qhs is a member of the new class of featureless TDEs put forth by Hammerstein et al. (2023a). These events are characterized by optical spectra showing a strong blue continuum but with no broad Balmer or He II emission typical of the optical spectra of TDEs. The peak flare luminosities of these events are several orders of magnitude larger than those of broad-line TDEs, but the rise and fade timescales are similar to the other spectral classes. The host galaxies of TDE-featureless events are typically more massive than broad-line TDEs, suggestive of a higher central black hole mass. Indeed, we find that AT2020qhs possesses the highest black hole mass in our sample, with $\log(M_{\rm BH}/M_{\odot}) = 8.01 \pm 0.82$. We caution, however, that AT2020qhs is also the highest redshift event in our sample, and as such has the lowest spatial

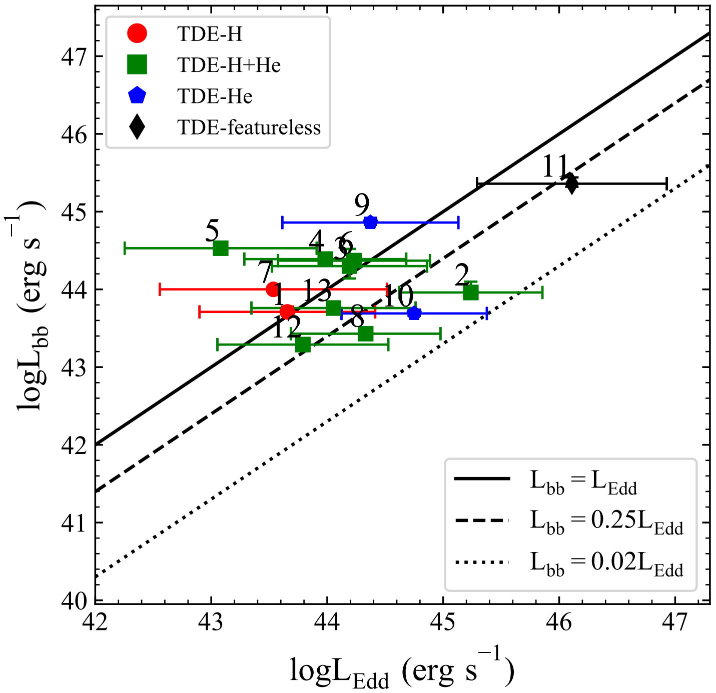

Figure 4.11: The peak blackbody luminosity as a function of the Eddington luminosity implied by the black hole mass. The solid, dashed, and dotted lines indicate constant Eddington ratios. We find that nearly all TDEs in our sample are consistent with being at or below the Eddington limit, with the exception of AT2018lna. This object has the lowest velocity dispersion in our sample and the black hole mass should be interpreted with caution. Labels for each TDE are in Table 4.1.

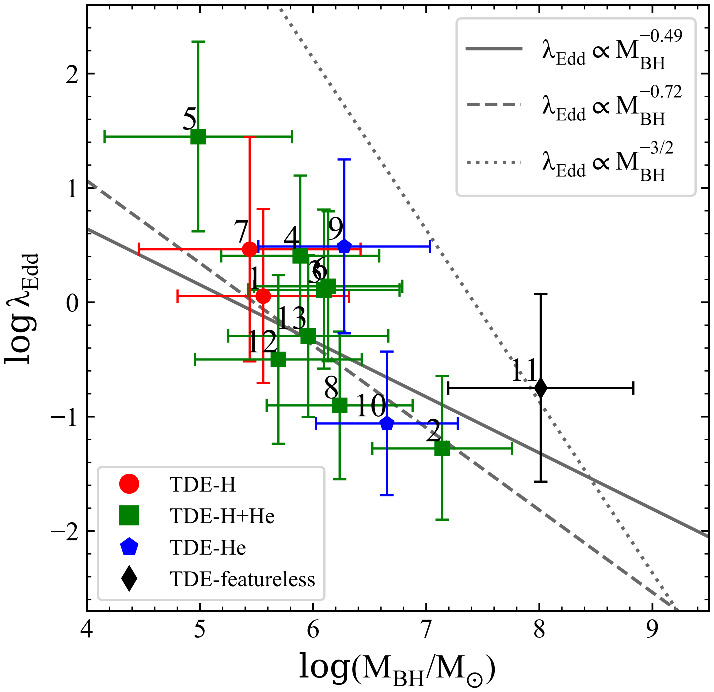

Figure 4.12: The Eddington ratio as a function of black hole mass. The dotted line is the expected Eddington ratio for the peak fallback accretion rate and the solid and dashed lines are the fitted relations from Yao et al. (2023) where $\dot{M}_{\rm fb}/\dot{M}_{\rm Edd} \propto M_{\rm BH}^{-0.49}$ and $\dot{M}_{\rm fb}/\dot{M}_{\rm Edd} \propto M_{\rm BH}^{-0.79}$, respectively. We find a moderate negative correlation between $\lambda_{\rm Edd}$ and the black hole mass, with the relation shallower than the expected $\lambda_{\rm Edd} \propto M_{\rm BH}^{-3/2}$, but likely steeper than that obtained by Yao et al. (2023). Labels for each TDE are in Table 4.1.

resolution of any event in our sample (4.89 kpc/″). Additionally, the choice of $M_{\rm BH} - \sigma$ relation can affect the derived black hole mass, which may have implications for the resulting conclusions made here.

Yao et al. (2023) measured the velocity dispersions for two additional TDE-featureless events, AT2020acka (Hammerstein et al., 2021b; Yao et al., 2023) and AT2021ehb (Gezari et al., 2021; Yao et al., 2022), and found corresponding black hole masses of $\log(M_{\rm BH/}/M_{\odot}) = 8.23 \pm 0.40$ and $\log(M_{\rm BH}/M_{\odot}) = 7.16 \pm 0.32$, respectively. If we use the Greene et al. (2020) $M_{\rm BH} - M_{\rm gal}$ relation for late-type galaxies to estimate the black hole masses for the remaining three featureless events in the Hammerstein et al. (2023a) sample, AT2018jbv, AT2020riz, and AT2020ysg, we obtain masses within the range $\log(M_{\rm BH}/M_{\odot}) =$ 6.48 – 7.70, which are still among the highest masses of those obtained here.

The dependence of the tidal radius and the Schwarzschild radius on the black hole mass is such that above $\sim 10^8 M_{\odot}$ (sometimes called the “Hills mass”; Hills, 1975), a solar-type star will typically pass beyond the black hole’s event horizon undisturbed, producing no visible flare. While the black hole mass for AT2020qhs is above this limit, it is still possible to produce an observable TDE around a SMBH of this size. The Hills mass may be exceeded through the disruption of giant stars, although the long timescales and lower luminosities of these events makes it less likely that they will be detected and noted by traditional TDE search methods (MacLeod et al., 2012; Syer & Ulmer, 1999). This explanation for such a high black hole mass seems unlikely, as the TDE-featureless class is shown to have the highest luminosities of any TDE class while the timescales for these events are comparable to other classes of TDEs (Hammerstein et al., 2023a).

A more favorable explanation is that the SMBH of AT2020qhs possesses a non-negligible spin which serves to increase the Hills mass (Kesden, 2012), as was similarly suggested for the TDE candidate ASASSN-15lh (Leloudas et al., 2016). It has been shown, however, that such SMBHs will contribute only marginally to the overall TDE rate (Stone & Metzger, 2016). The low predicted rates of spinning SMBHs amongst TDEs may not be a large concern, as Hammerstein et al. (2023a) noted that most of the TDE-featureless events occur at high redshifts, implying that a larger volume is needed to observe them and hinting at their rarity. Following the work of Kesden (2012) and under the assumption that the disrupted star was of solar type, we can place a lower limit on the spin of the AT2020qhs black hole of $a \gtrsim 0.16$. However, if we instead derive the black hole mass for AT2020qhs using the relation from Xiao et al. (2011), the black hole mass becomes $\log(M_{\mathrm{BH}/}/M_{\odot}) = 7.60$, which requires no spin for the disruption of a solar type star.

We note that the disruption of a higher mass star can also potentially explain the black hole mass of AT2020qhs. Leloudas et al. (2015) also addressed this for ASASSN-15lh, finding that only star masses greater than $\sim 3M_{\odot}$ can be disrupted by a non-rotating Schwarzschild black hole. These events are also rare (Kochanek, 2016b; Stone & Metzger, 2016), but may be a plausible explanation for AT2020qhs flare. Mockler et al. (2022) used measurements of the N III to C III ratio in UV spectra to infer the masses of the disrupted stars, finding that the observed ratios necessitate the disruption of more massive stars in the post-starburst hosts they targeted. Larger samples of UV spectra for all TDE types and black hole masses are needed to further investigate whether this is the case for TDE-featureless events such as AT2020qhs.

Spin has been invoked to explain other phenomena observed in TDEs, such as the launching of relativistic jets. Recently, Andreoni et al. (2022) reported the discovery of a jetted TDE in the ZTF survey, concluding that a high spin is likely required to produce such jets. They put a lower limit on the spin parameter of $a \gtrsim 0.3$. Andreoni et al. (2022) also noted the similarities between AT2022cmc and the TDE-featureless class, with the comparable peak flare luminosities and similar lack of broad emission lines in spectra suggesting a connection between the two classes of events. They propose that TDE-featureless events may be jetted TDEs observed off-axis, but further multi-wavelength follow-up of these events is needed to confirm this hypothesis. Nonetheless, the black hole masses AT2020qhs and AT2020acka imply SMBHs with rapid spins and further bolster the possible connection between jetted TDEs and the TDE-featureless class.

4.5 Galaxy kinematics and stellar populations

We now investigate the kinematic properties on the scale of the effective radius of the entire galaxy light profile ($R_{\mathrm{e,gal}}$). Our fits using `ppxf` yield velocities and velocity dispersions, which can be used to estimate the level of rotational support the TDE hosts possess, quantified by the ratio of ordered to random stellar motion $(V/\sigma)_e$, where lower values of $(V/\sigma)_e$ indicate a higher degree of random stellar motions. We adopt the formula of Cappellari et al. (2007), defined for integral field data:

$$\left(\frac{V}{\sigma}\right)_e^2 \equiv \frac{\langle V^2 \rangle}{\langle \sigma^2 \rangle} = \frac{\Sigma_{n=1}^{N} F_n V_n^2}{\Sigma_{n=1}^{N} F_n \sigma_n^2}, \tag{4.2}$$

where F_n is the flux contained within the nth bin, while V_n and σ_n are the mean measured velocity and velocity dispersion within that bin. In Figure 4.13 we show the $(V/\sigma)_e$ for the thirteen TDE host galaxies as a function of stellar population age. We also show the same comparison sample of galaxies as in Figure 4.3. The top and side panels of Figure 4.13 show the distribution of galaxies in the red sequence, which hosts largely quiescent, elliptical galaxies, the blue cloud, which hosts primarily star-forming galaxies, and the green valley, which hosts recently quenched galaxies, defined from Figure 4.3, E+A galaxies, and the TDE hosts. E+A galaxies from the SAMI survey were selected using the Hα equivalent width and Lick Hδ_{A} absorption index using values presented in the MPA+JHU catalogs (Brinchmann et al., 2004). We note that only a third of the galaxies in the SAMI survey have a counterpart in the MPA+JHU catalog. The Hα equivalent width is limited to < 4.0 Å and the Hδ_A index is limited to H$\delta_{\mathrm{A}} - \sigma(\mathrm{H}\delta_{\mathrm{A}}) > 4.0$ Å to isolate post-starburst galaxies.

van de Sande et al. (2018) found a strong correlation between the ratio of ordered rotation to random stellar motion and the stellar population age of a galaxy, such that younger stellar populations are predominantly rotationally supported as in late-type galaxies while older stellar populations are pressure supported by random stellar motions as in early-type galaxies. They also found that $(V/\sigma)_e$ is linked to the observed shape (quantified by the ellipticity ϵ). These correlations link a galaxy's star formation history with its merger history, as mergers will enhance the formation of bulges which in turn lowers a galaxy's $(V/\sigma)_e$ and ellipticity. We find that the TDE host galaxies largely follow this same relation between $(V/\sigma)_e$ and stellar population age, apart from two outliers AT2019azh and AT2020zso (IDs 6 and 13, respectively). AT2019azh is a known E+A galaxy, which have been shown to have varied central stellar population ages and young stellar populations not necessarily confined to the nucleus (Norton et al., 2001; Pracy et al., 2009). This may affect the measurement of the host galaxy stellar population age in the central regions in unforeseen ways.

The close link between the merger history, stellar population age, and stellar kinematics is very likely a driving factor behind post-starburst color (used as a proxy for stellar population age) and morphology, and may help explain the TDE preference for such environments. Even before van de Sande et al. (2018) noted the connection between stellar kinematics and stellar

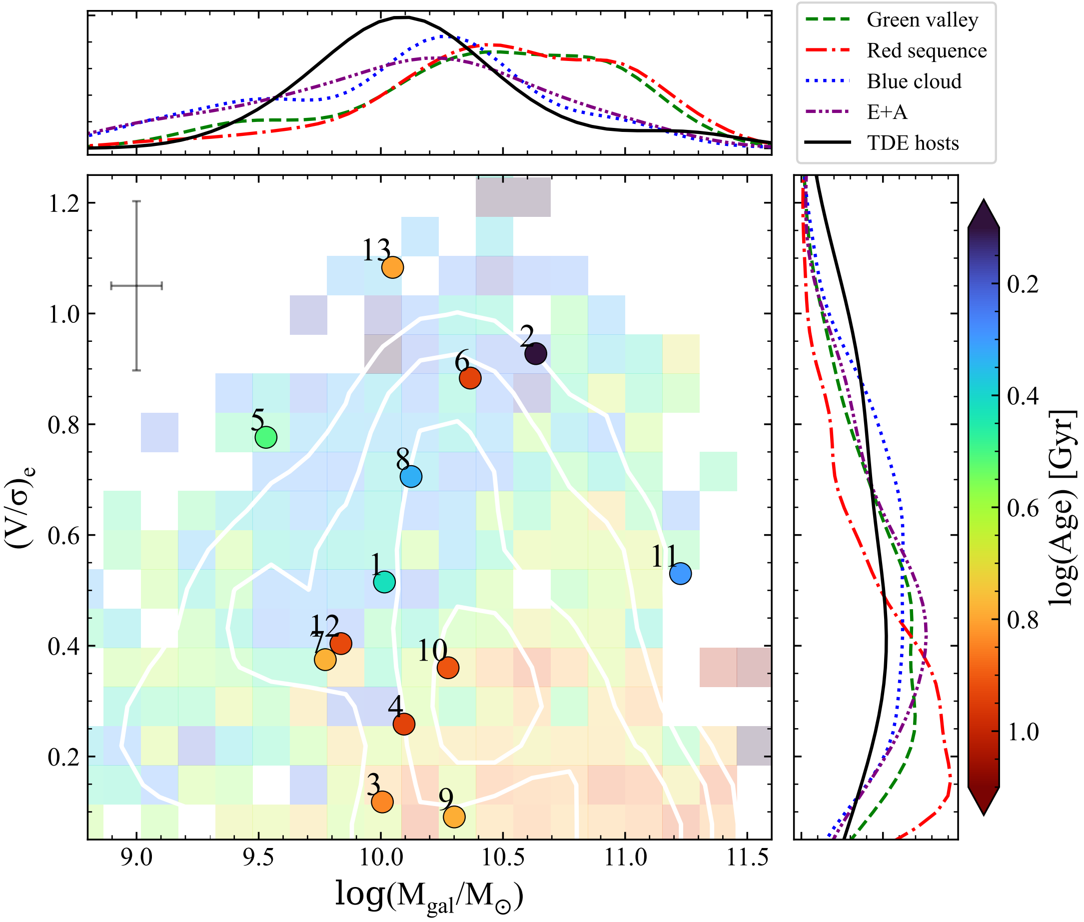

Figure 4.13: The ratio between stellar ordered rotation and random orbital motion of the TDE host galaxies, defined as $(V/\sigma)_e$, as a function of galaxy stellar mass, with the color of the points/pixels corresponding to the stellar population age. The median uncertainty on the TDE host galaxy values is shown in the top left. Galaxies from the SAMI galaxy survey are shown in the background, with the mean stellar population age of galaxies within a pixel used to determine the pixel color. White contours represent the number density of background galaxies. The top and side panels show the distribution of the TDE hosts and the red sequence, green valley, blue cloud, and E+A galaxies in the background sample obtained by kernel density estimation. We find that the TDE hosts are generally lower mass than most of the background sample, with a larger spread in $(V/\sigma)_e$ than green valley or red sequence galaxies but a distribution similar to E+A galaxies. Labels for each TDE are in Table 4.1.

population age, Schawinski et al. (2010) found that low-mass morphologically early type galaxies in the green valley, which is thought to contain more recently quenched galaxy populations, are linked to mergers which rapidly ushered their migration from the star-forming blue cloud to the green valley and which changed their shape from disk to spheroidal. Schawinski et al. (2014) subsequently found that these systems have classic post-starburst populations. However, the majority of galaxies migrate into the green valley through a slow decline in star formation rate likely as a result of gas supply shut off and retain hence their disk shape. The population of green, spiral-like galaxies is noted in Hammerstein et al. (2021a), who compared 19 TDE hosts to red sequence, green valley, and blue cloud galaxies, finding that the TDE hosts are inconsistent with the majority of green valley galaxies which maintained their disk-like morphology inferred through the Sérsic index.

Given the rate enhancement of TDEs in green valley (and E+A) galaxies, one could expect that TDE host galaxies also cluster in a specific region of $(V/\sigma)_e$. However, we observe a relatively large spread in $(V/\sigma)_e$. The TDE hosts are more evenly distributed in $(V/\sigma)_e$ with a median value of 0.52. We compare the distribution of the TDE host galaxies in $(V/\sigma)_e$ and mass to the red sequence, green valley, and blue cloud galaxies. We find that the TDE hosts, while predominantly green, are generally less massive than the majority of green valley galaxies. This is in agreement with the findings of Hammerstein et al. (2021a) for a larger sample of 19 TDE host galaxies from ZTF. The green valley and red sequence distributions in $(V/\sigma)_e$ peak around ~ 0.2, indicating that these galaxies are dominated by random stellar motions. In general, we expect a negligible contribution to the TDE rate from stars on circular orbits. This could lead one to conclude that at a fixed stellar mass, a low $(V/\sigma)_e$ might imply a higher TDE rate. However, we should note that the stars within the SMBH sphere of influence (radius ~ 1 parsec) contribute only a tiny fraction to the stellar light within the effective radius. Hence the large spread in the $(V/\sigma)_e$ that we observe for the TDE host galaxies cannot directly be translated into a spread in the TDE rate. We thus arrive at the somewhat puzzling observation that the TDE rate appears to be correlated more strongly with the global colors of the host galaxy than the $(V/\sigma)_e$ at its effective radius.

Galaxies that are most certainly dominated by random stellar motions and have stellar populations older than 10 Gyr (i.e., early-type galaxies), have a mean $(V/\sigma)_e = 0.22$. Although three TDE hosts have values around or below this level, they have stellar population ages younger than 10 Gyr at ~ 7.1 Gyr. The older, more massive galaxies which are dominated by random stellar motions may also host black holes which exceed the Hills mass, which could explain why the TDE hosts with lower $(V/\sigma)_e = 0.22$ have younger stellar populations than galaxies with similar kinematics. The difference in age between galaxies dominated by random stellar motions and the TDE hosts of similar $(V/\sigma)_e$ implies that the TDE rate likely declines as a galaxy ages despite the increase in the degree of random motion, although the precise reason, whether it be black hole growth beyond the Hills mass or otherwise, and the connection this has with nuclear dynamics is not yet clear given the indirect relationship that these global properties have with factors influencing the TDE rate in the nucleus.

The E+A distribution in $(V/\sigma)_e$ has a mean value of 0.49, similar to the TDE hosts' median value of 0.52. The E+A mass distribution also peaks at $\log(M_{\rm gal}/M_\odot) = 10.07$, while the median TDE host galaxy mass is $\log(M_{\rm gal}/M_\odot) = 10.09$. It is clear that the TDE host galaxies are likely consistent with the same population of galaxies as post-starburst galaxies, which has been suggested previously (e.g., Hammerstein et al., 2021a; Law-Smith et al., 2017). We can also rule out that the TDE hosts come from the same population as red sequence galaxies. An Anderson-

Darling test comparing the $(V/\sigma)_e$ of red sequence galaxies to the TDE hosts reveals that the null hypothesis that the two are drawn from the same parent population can be rejected (p-value = 0.02). The same cannot be said, however, when comparing green valley galaxies and blue cloud galaxies to the TDE hosts.

The TDE host galaxies also differ in age when compared to the E+A galaxies, with the former having a median stellar population age of 6.12 Gyr, while the E+A galaxies have a mean stellar population age of 2.82 Gyr. One possible conclusion from this is that the TDE host galaxies are post-merger, similar to E+As, but the younger stellar populations produced in the merger-induced starburst having subsided meaning the ages of the stellar populations are older but the other factors which enhance the TDE rate in E+A galaxies (e.g., nuclear star clusters, high central stellar concentrations) remain. Future observations which search for merger signatures, such as in French et al. (2020b), for larger samples of TDEs will be able to confirm the prevalence of post-merger galaxies among TDE host populations. The `GALFIT` residuals for several galaxies from the LMI data presented here do show remaining features, although differentiating normal dust lane features from true merger signatures like tidal features is difficult. Stone et al. (2018) examined factors which enhance TDE rates in post-starburst galaxies, such as SMBH binaries, nuclear stellar overdensities, radial orbit anisotropies, and delay between the initial starburst and the enhancement of the TDE rate due to these factors. This delay time between the initial post-merger starburst and the enhancement of the TDE rate could help to explain why the TDE hosts show older ages but similar global stellar dynamics to the younger post-starburst galaxies.

4.6 Conclusions

We have presented the first sample study of IFU observations of thirteen TDE host galaxies from the ZTF survey in order to investigate their kinematic properties and infer their black hole masses. Our main conclusions are as follows:

- The black hole mass distribution peaks at $\log(M_{\rm BH}/M_{\odot}) = 6.05$, consistent with theoretical predictions that TDE populations are dominated by lower mass SMBHs and past observational findings.

- There is no significant statistical difference between the X-ray bright and X-ray faint population of TDEs in our sample, which further supports the unifying theory of Dai et al. (2018) that proposes viewing angle effects as the factor which determines X-ray brightness in a TDE.

- We find no significant correlation between the black hole masses derived from $M_{\rm BH}-\sigma$ and the black hole masses derived from `MOSFiT` or `TDEmass`. This may indicate a need to revisit the way that the black hole mass is imprinted on the light curves of TDEs.

- The Eddington ratio is moderately correlated with the black hole mass, although the correlation is likely shallower than the expected relation between the peak fallback accretion rate and the black hole mass, similar to the findings of Yao et al. (2023).

- We find that the event AT2020qhs, a member of the TDE-featureless class, has the highest black hole mass of the sample: $\log(M_{\rm BH}/M_{\odot}) = 8.01 \pm 0.82$, above the Hills mass for the disruption of a solar type star. We suggest that the SMBH at the center of this event is rapidly spinning and, assuming that the disrupted star was of solar type, put a lower limit on the spin of $a \gtrsim 0.16$. This further supports the proposed connection between jetted TDEs and the TDE-featureless class put forth by Andreoni et al. (2022).

- We investigate the large-scale kinematics of the TDE host galaxies, particularly the ratio of ordered rotation to random stellar motions $(V/\sigma)_e$, and find that the TDE hosts show similar distributions in $(V/\sigma)_e$ to E+A galaxies but older stellar populations. This may indicate that TDE host galaxies, like E+A galaxies, are post-merger galaxies with the younger stellar populations produced in the merger-induced starburst having subsided, leaving only the older stellar populations. The delay time between post-merger starburst and TDE rate enhancement may also explain the discrepancy in age (e.g., Stone et al., 2018)

4.7 Acknowledgements

We thank the anonymous referee for their helpful comments towards improving this paper. EH acknowledges support by NASA under award number 80GSFC21M0002.

These results made use of the Lowell Discovery Telescope (LDT) at Lowell Observatory. Lowell is a private, non-profit institution dedicated to astrophysical research and public appreciation of astronomy and operates the LDT in partnership with Boston University, the University of Maryland, the University of Toledo, Northern Arizona University and Yale University. The Large Monolithic Imager was built by Lowell Observatory using funds provided by the National Science Foundation (AST-1005313).

The data presented here were obtained at the W. M. Keck Observatory, which is operated as a scientific partnership among the California Institute of Technology, the University of California and the National Aeronautics and Space Administration. The Observatory was made possible by the generous financial support of the W. M. Keck Foundation. The authors wish to recognize and acknowledge the very significant cultural role and reverence that the summit of Mauna Kea has always had within the indigenous Hawaiian community. We are most fortunate to have the opportunity to conduct observations from this mountain.

The SAMI Galaxy Survey is based on observations made at the Anglo-Australian Telescope. The Sydney-AAO Multi-object Integral field spectrograph (SAMI) was developed jointly by the University of Sydney and the Australian Astronomical Observatory. The SAMI input catalogue is based on data taken from the Sloan Digital Sky Survey, the GAMA Survey and the VST ATLAS Survey. The SAMI Galaxy Survey is supported by the Australian Research Council Centre of Excellence for All Sky Astrophysics in 3 Dimensions (ASTRO 3D), through project number CE170100013, the Australian Research Council Centre of Excellence for All-sky Astrophysics (CAASTRO), through project number CE110001020, and other participating institutions. The SAMI Galaxy Survey website is http://sami-survey.org.

The data analysis in this paper was performed on the Yorp and Astra clusters administered by the Center for Theory and Computation, part of the Department of Astronomy at the University of Maryland.

Chapter 5: The Jetted Tidal Disruption Event AT2022cmc in the Context of the Optical Tidal Disruption Event Population

5.1 Introduction

Every so often ($\sim 10^4$ years) in the nucleus of a galaxy, a star will wander too close to the supermassive black hole (SMBH) lurking there and will be subsequently torn apart by the tidal forces and accreted by the SMBH (Frank & Rees, 1976; Hills, 1975). These tidal disruption events (TDEs) create luminous flares of radiation visible from Earth. Samples of TDEs have now been discovered across the electromagnetic spectrum from X-ray (e.g., Sazonov et al., 2021) to optical (e.g., Hammerstein et al., 2023a; van Velzen et al., 2021; Yao et al., 2023), and even infrared (e.g., Masterson et al., 2024) and radio (e.g., Somalwar et al., 2023).

The advent of all-sky optical surveys, such as Pan-STARRS (Chornock et al., 2014; Gezari et al., 2012; Holoien et al., 2019b; Nicholl et al., 2019), ASAS-SN (Hinkle et al., 2021; Holoien et al., 2014b, 2016a,b, 2019a; Wevers et al., 2019), and the Zwicky Transient Facility (ZTF, Hammerstein et al., 2023a; van Velzen et al., 2021; Yao et al., 2023), in the last ~ 20 years has led to the majority of current TDE discoveries being made at these wavelengths. These optically selected TDEs are typically dominated by a hot (10^4–10^5 K), thermal continuum with rise timescales of ~ 30 days, peak absolute magnitudes of $M_r \sim -18$ to -20 mag, and fade timescales of 200–400 days (e.g., Hammerstein et al., 2023a; van Velzen et al., 2021). Optically selected TDEs show a broad range of emission at other wavelengths, including a variety of behaviors in the X-ray (e.g., Guolo et al., 2023; Hammerstein et al., 2023a; Saxton et al., 2021; van Velzen et al., 2021). The optical spectra of TDEs are most often characterized by broad emission features, with van Velzen et al. (2021) formalizing a classification scheme:

i. *TDE-H*: broad Hα and Hβ emission lines.

ii. *TDE-H+He*: broad Hα and Hβ emission lines and a broad complex of emission lines around He II λ4686. The majority of the sources in this class also show N III λ4640 and emission at λ4100 (identified as N III λ4100 instead of Hδ), and in some cases also O III λ3760.

iii. *TDE-He*: no broad Balmer emission lines, a broad emission line near He II λ4686 only.

Hammerstein et al. (2023a) put forth an additional class:

iv. *TDE-featureless*: no discernible emission lines or spectroscopic features present in the three classes above, although host galaxy absorption lines can be observed.

This featureless class of TDEs is characterized by higher peak luminosities ($M_r \sim -21$ mag), peak blackbody temperatures, and peak blackbody radii. Their host galaxies are often more massive, potentially implying more massive black holes, and redder than typical TDE hosts, which tend to favor "green" galaxies (e.g., Hammerstein et al., 2021a; Law-Smith et al., 2017).

TDEs discovered at other wavelengths, such as in the soft X-ray, are also characterized by thermal emission, though the thermal continuum in X-ray selected events is typically much hotter than their optically selected counterparts (see Gezari, 2021, for a review). A very small fraction of TDEs have been discovered through non-thermal emission from an on-axis, collimated, relativistic jet (hereafter "jetted TDE"). Three of these objects were discovered more than a decade ago by the hard X-ray Burst Alert Telescope (BAT) aboard *Swift*. These candidates include Sw J1644+57 (Bloom et al., 2011; Burrows et al., 2011; Levan et al., 2011; Zauderer et al., 2011), Sw J2058+05 (Cenko et al., 2012; Pasham et al., 2015), and Sw J1112-82 (Brown et al., 2015, 2017). Several of these jetted TDEs have shown faint or late-time optical counterparts, including Sw J1644+57, Sw J2058+05, and Sw J1112-82. Jetted TDEs provide an important opportunity to study the launching of relativistic jets by SMBHs, the jet emission mechanism, and the jet composition (for a review, see De Colle & Lu, 2020).

Recently, a fourth candidate jetted TDE was reported. In contrast to the previous three candidates, AT2022cmc (ZTF22aaajecp) was discovered by ZTF as an optical transient (Andreoni et al., 2022). The first detection in the optical on 2022 February 11 was shortly followed by detections in the radio (Perley, 2022), sub-millimeter (Perley et al., 2022), and X-ray (Pasham et al., 2022). The emission across wavelengths is exceptionally luminous, and the redshift ($z = 1.193$) provided by follow-up spectroscopy (Tanvir et al., 2022) implies an absolute optical luminosity of $M_i \approx -25$ mag at peak (Andreoni et al., 2022). The follow-up observations revealed remarkable similarities to the jetted TDE Sw J1644+47, including long-lived X-ray emission with short timescale variability and corresponding radio and infrared counterparts (Bloom et al., 2011; Burrows et al., 2011; Levan et al., 2011). Sw J1644+57 was not detected in the optical or ultraviolet until much later (Levan et al., 2016), although this is unsurprising due to the large inferred host galaxy extinction (Burrows et al., 2011). Because of these similarities, and after ruling out other possible transients such as a kilonova, a luminous fast blue optical transient (LFBOT), blazer, or a γ-ray burst (GRB), the interpretation of AT2022cmc as a jetted TDE is favored (Andreoni et al., 2022; Pasham et al., 2023; Rhodes et al., 2023).

Interestingly, AT2022cmc's UV, optical, and IR light curve is characterized by a red color which turns bluer after several days post-peak. This contrasts with the typical evolution of optical TDEs, which show little color evolution throughout their light curves (e.g., Hammerstein et al., 2023a; van Velzen et al., 2021; Yao et al., 2023). Andreoni et al. (2022) interpret this fast-fading red flare as synchrotron emission resulting from the jet interaction with the circumnuclear medium. The slower-evolving, blue, thermal optical/UV emission is thought to have origins similar to non-jetted TDEs, which may come from reprocessing of X-ray emission originating in the accretion disk to the UV and optical by a wind or outflow (Dai et al., 2018; Guillochon et al., 2014; Loeb & Ulmer, 1997), or shocks and subsequent outflows created by intersecting stellar debris streams (Jiang et al., 2016; Lu & Bonnerot, 2020; Piran et al., 2015). The blue component of AT2022cmc's optical/UV light curve indeed shows similar properties to non-jetted TDEs, with a high rest-frame UV luminosity of $\sim 10^{45}$ erg s^{-1} and a blackbody temperature $\sim 3 \times 10^4$ K (Andreoni et al., 2022).

The follow-up optical spectra of AT2022cmc, both in the red and blue phases, show a featureless continuum with evidence for host stellar absorption lines but no broad features typically associated with many TDEs. Sw J2058+05 showed a similar lack of features in its optical spectrum (Cenko et al., 2012; Pasham et al., 2015). Because of its featureless optical spectra and high peak optical luminosity, Andreoni et al. (2022) suggested there may be a connection between jetted TDEs and the featureless class of TDEs put forth by Hammerstein et al. (2023a), which show similar high optical luminosities ($M_r \sim -22$ mag). This possible connection was further bolstered by Hammerstein et al. (2023b), who found that the SMBH at the center of the featureless TDE AT2020qhs (Hammerstein et al., 2023a) has a mass of $\log(M_{\rm BH}/M_\odot) = 8.01 \pm 0.82$

obtained from stellar kinematics. The high black hole mass could require that the SMBH possesses a spin that would ensure that the tidal radius remains outside the event horizon radius and produces an observable TDE, however this would require the disruption of a solar-type star as lower density star such as a giant could still be disrupted outside of the event horizon (MacLeod et al., 2012). This may lend further support to the possible connection between jetted TDEs and featureless TDEs, if high spin is required to launch a relativistic jet (e.g., Tchekhovskoy et al., 2014). Andreoni et al. (2022) propose that TDE-featureless objects may be off-axis jetted TDEs, though deep radio observations of featureless TDEs are required to prove the presence of a jet at all viewing angles.

Despite extensive follow-up observations, the host galaxy of AT2022cmc has yet to be detected. Lower limits on the host magnitude were obtained from forced photometry to archival imaging in $u-$ and $r-$bands obtained with the MegaPrime camera on the 3.58-m Canada-France-Hawaii Telescope in 2015 and 2016. These limits are $m_u > 24.19$ mag and $m_r > 24.54$ mag. Andreoni et al. (2022) estimated the host properties by modeling the SED. The limits on the galaxy luminosity yielded limits on the host galaxy stellar mass of $\log M/M_{\odot} < 11.2$, which we use as the upper limit in this paper. Deep, late-time observations of AT2022cmc, such as with HST or JWST, are needed to constrain the host galaxy properties more strongly.

The discovery of AT2022cmc, a jetted TDE with a bright optical counterpart, presents an unprecedented opportunity to place this rare class of TDEs in the context of the non-jetted optical TDE population and study the potential connection between TDE-featureless objects and jetted TDEs. We therefore present an analysis of the optical/UV light curve and optical spectra of AT2022cmc and place it within the context of other optically selected TDEs. The paper is organized as follows. We describe the observations and data reduction in Section 5.2. In Section

5.3, we describe the optical spectra fitting methods and light curve fitting methods we employ. We present the results of both of these in Section 5.4 and end with a discussion and conclusions in Section 5.5.

5.2 Data & Observations

Here we present new observations of AT2022cmc taken since its discovery in Andreoni et al. (2022) (see Table C.1). In Figure 5.1, we show the UV/optical light curve including the observations presented in Andreoni et al. (2022) which cover up to $\sim$ 30 days from the first detection (observed frame). We point the reader to Section 12 of Andreoni et al. (2022) for details on the reduction of the discovery light curve data. The additional data which we present here extends the light curve to $\sim$ 180 days from the first detection (observed frame) and includes observations from the GROWTH India Telescope (GIT), Nordic Optical Telescope (NOT) Alhambra Faint Object Spectrograph and Camera (ALFOSC), Lowell Discovery Telescope (LDT) Large Monolithic Imager (LMI), Large Binocular Telescope (LBT Hill et al., 2008) Large Binocular Camera (LBC Speziali et al., 2008), and the Liverpool Telescope (LT) IO:O camera (Steele et al., 2004). Standard photometric reduction procedures such as bias subtraction, flat-fielding, and cosmic ray rejection were performed on all data.

Andreoni et al. (2022) also presented 6 optical spectra of AT2022cmc taken over $\sim$18 days, starting from $\sim$4 days after the first ZTF detection, which we reproduce here (Figure 5.2). The collection of optical data includes spectra taken with NOT+ALFOSC, Gemini+Gemini Multi-Object Spectrograph (GMOS), Keck+DEep Imaging Multi-Object Spectrograph (DEIMOS), and Keck+Low Resolution Imaging Spectrometer (LRIS). We point the reader to Andreoni et al.

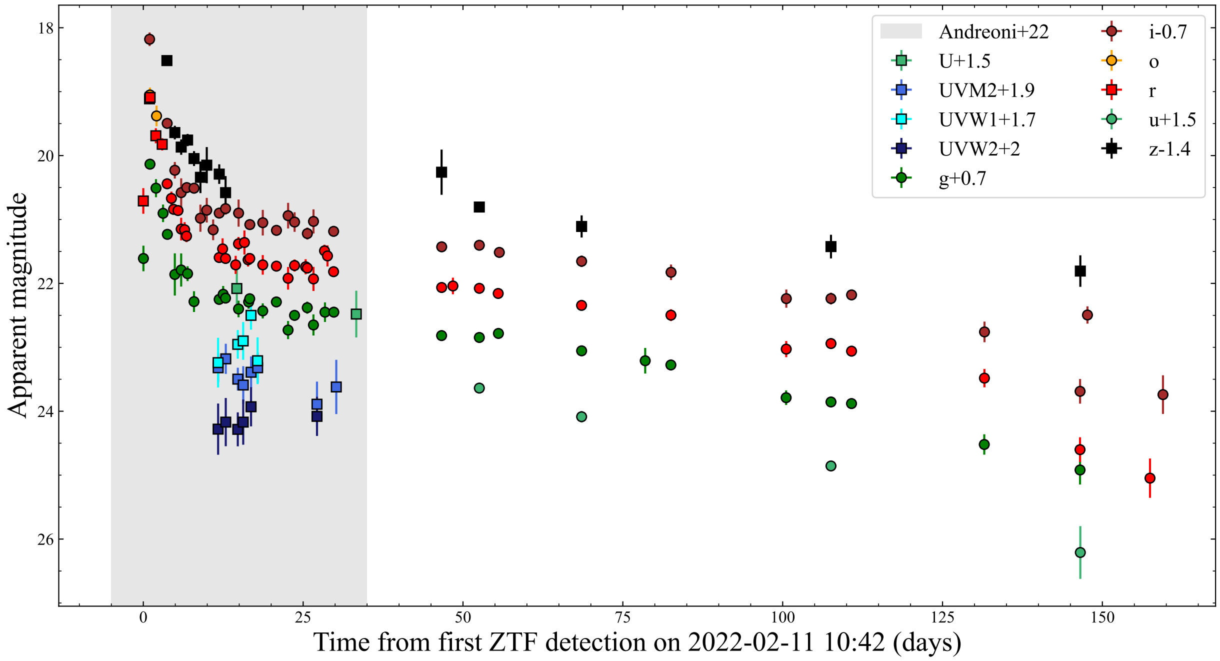

Figure 5.1: UV, optical, and near infrared light curve of AT2022cmc. The original discovery light curve published in Andreoni et al. (2022) covers the first ∼30 days since discovery (observed frame) and is indicated by the shading. Here we present additional observations that extend the light curve up to ∼160 days since first detection. Magnitudes are not corrected for Galactic extinction.

(2022) for details on the data reduction. Several absorption lines in the Very Large Telescope (VLT) + Xshooter spectrum were identified as Al III, Fe II, Mn II, Mg II, Mg I, and Ca II and used to obtain the source redshift of $z = 1.193$. The spectra cover both the red and blue phases of the optical light curve, and while the spectra remain featureless over all epochs, a clear evolution in the continuum is seen.

In Figure 5.2, we show the 6 available spectra of AT2022cmc presented in Andreoni et al. (2022). In Table 5.1, we summarize the spectroscopic observations of both AT2022cmc.

---

[1] We use time since first detection for AT2022cmc.

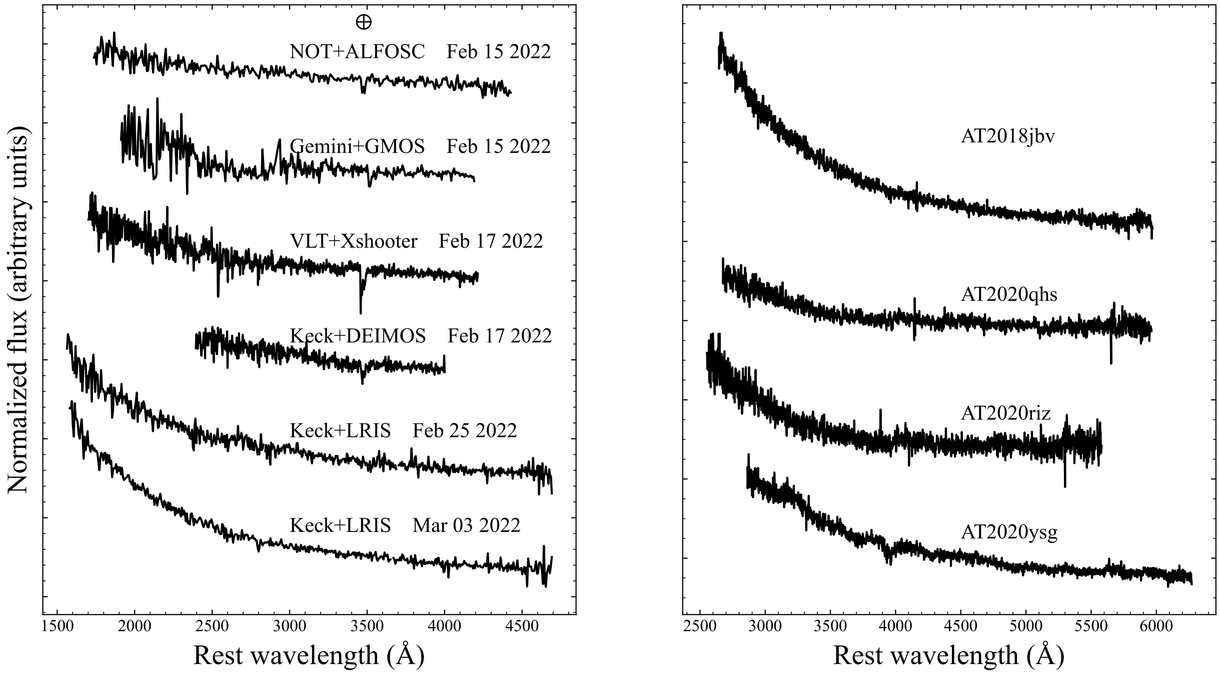

Figure 5.2: *Left*: Optical spectra of AT2022cmc from Andreoni et al. (2022). The light curves cover both the red and blue phases of the light curve but remain featureless despite the clear evolution in the continuum. The absorption line near 3500 Å in the AT2022cmc spectra is telluric (non-astrophysical). *Right*: Optical spectra of the four TDE-featureless objects in Hammerstein et al. (2023a), which show remarkable similarities to the later spectra of AT2022cmc. The absorption feature in the AT2020ysg spectrum around 4000 Å is the stellar absorption Ca II feature. All spectra have been corrected for Galactic extinction.

Name	Redshift	Telescope+Inst.	Date	Phase
AT2022cmc	1.193	NOT+ALFOSC	Feb 15 2022	4
		Gemini+GMOS	Feb 15 2022	4
		VLT+Xshooter	Feb 17 2022	6
		Keck+DEIMOS	Feb 17 2022	6
		Keck+LRIS	Feb 25 2022	14
		Keck+LRIS	Mar 03 2022	20
AT2018jbv	0.340	LDT+DeVeny	Mar 28 2019	101
AT2020qhs	0.345	LDT+DeVeny	Oct 11 2020	77
AT2020riz	0.435	LDT+DeVeny	Oct 15 2020	57
AT2020ysg	0.277	LDT+DeVeny	Dec 6 2020	50

Table 5.1: Summary of spectroscopic observations for AT2022cmc and the four TDE-featureless objects in Hammerstein et al. (2023a). We include here the redshift, telescope and instrument used, date the spectrum was taken, and phase (i.e., time since flare peak that the observation was taken[1]). Phase is approximate to within one day of when the spectrum was taken.

5.3 Analysis

Throughout this paper, we compare the light curve of AT2022cmc to the light curves of non-jetted TDEs. We draw our comparison sample and light curve data from Hammerstein et al. (2023a) and use the light curve fit parameters presented there. We also fit the spectra of the four TDE-featureless objects in the Hammerstein et al. (2023a) sample, using the spectra presented in the Appendix of that paper, all of which were observed with the DeVeny spectrograph on the LDT. The spectra were observed 50–101 days post-peak. In Figure 5.2, we show the optical spectra of the 4 TDE-featureless objects presented in Hammerstein et al. (2023a). We describe the methods used to fit the spectra and light curves in the follow sections.

5.3.1 Spectrum Fitting

Given the faintness of the host galaxy ($\gtrsim 24.5$ mag Andreoni et al., 2022) and the luminosity of the flare, we expect the optical spectra to be dominated by transient light. It is therefore of interest to characterize the properties of the optical spectra to gain information on the transient itself. While the optical spectra are primarily featureless, the continuum may provide information on the thermal and non-thermal emission.

We fit the continuum of all AT2022cmc spectra and the four featureless TDEs using two different models. We note that the spectra have not been host galaxy subtracted, though this is unlikely to be a concern given the phase of the light curve that the spectra were taken. The average difference image flare magnitude at the time of the spectroscopic observations is $g \sim 19.7$ mag versus the average host magnitude $g \sim 21.6$ mag. All spectra have been corrected for Galactic extinction prior to fitting. The spectra of the four featureless TDEs have been corrected for telluric absorption features, while only the Keck+LRIS spectra of AT2022cmc have been corrected for telluric features. The first model is a simple blackbody which allows us to obtain the blackbody temperature and inferred blackbody radius, with the temperature bounds of 10^{4-5} K, as is expected for TDEs (e.g., Hammerstein et al., 2023a; van Velzen et al., 2021). The second model is a power-law of the form:

$$F_\nu = F_{\rm pl} \left(\frac{\nu}{\nu_0} \right)^{\alpha} , \tag{5.1}$$

where F_ν is the spectral flux density in erg s^{-1} Hz^{-1}, $F_{\rm pl}$ is the reference spectral flux density at $\nu_0 = 10^{15}$ Hz, and α is the spectral index. We place no limits on the value of α and note that it should be interpreted with caution but may provide insights into the evolution of the red component present in the light curve of AT2022cmc. Despite the lack of emission and absorption lines in the spectra, apart from some host galaxy stellar absorption lines, we mask regions commonly associated with emission in TDEs (see Section 5.1) and host stellar absorption lines during the continuum fits in addition to any remaining telluric absorption lines. We describe the results and present the fits in Section 5.4.

5.3.2 Light Curve Fitting

To analyze the UV/optical light curve of AT2022cmc and to compare it to previous TDE light curves, we adopt fitting methods similar to van Velzen et al. (2021) and Hammerstein et al. (2023a). The rest-frame, multi-band data is fit with a Gaussian rise and an exponential decay. The Gaussian rise avoids the addition of the power-law index and power-law normalization as a free parameter in a rise characterized by a power-law. This model is described by:

$$L_\nu(t) = L_{\nu_0\ \mathrm{peak}} \frac{B_\nu(T_0)}{B_{\nu_0}(T_0)} \times \begin{cases} e^{-(t-t_{\mathrm{peak}})^2/2\sigma^2} & t \leq t_{\mathrm{peak}} \\ e^{-(t-t_{\mathrm{peak}})/\tau} & t > t_{\mathrm{peak}} \end{cases}, \tag{5.2}$$

where ν_0 refers to the reference frequency, which we have chosen to be 10^{15} Hz, and thus $L_{\nu_0\ \mathrm{peak}}$ is the luminosity at peak at this frequency. This model fits for only one temperature, T_0, which is used to predict the luminosity in the other bands.

While this model assumes the emission is well-described by a blackbody, and in many TDEs it is, the presence of the red (presumed non-thermal) component in the light curve of AT2022cmc requires the addition of a spectral power-law component. We therefore modify that model to include an additional component, such that the light curve can be described by:

$$\begin{aligned} L_\nu(t) =& L_{\mathrm{pl}} \times \begin{cases} 10^{\beta_{\mathrm{rise}}(t-t_{\mathrm{peak}})} & t \leq t_{\mathrm{peak}} \\ 10^{\beta_{\mathrm{decay}}(t-t_{\mathrm{peak}})} & t > t_{\mathrm{peak}} \end{cases} \\ &+ L_{\mathrm{BB}} \times \begin{cases} e^{-(t-t_{\mathrm{peak}})^2/2\sigma^2} & t \leq t_{\mathrm{peak}} \\ e^{-(t-t_{\mathrm{peak}})/\tau} & t > t_{\mathrm{peak}} \end{cases}, \end{aligned} \tag{5.3}$$

where L_{pl} describes the power-law component luminosity and is a function of the power-law spectral flux density described by Equation 5.1 and L_{BB} is the blackbody contribution which is described by $L_{\nu_0\ \mathrm{peak}} \frac{B_\nu(T_0)}{B_{\nu_0}(T_0)}$.

For consistency with Andreoni et al. (2022), we also fit the AT2022cmc light curve with a time-evolving power-law component and *static* blackbody component. However, this model is unlikely to be able to reproduce the light curve at later times once the power-law component has faded. Equation 5.3 then becomes:

$$L_\nu(t) = L_{\mathrm{BB}} + L_{\mathrm{pl}} \times \begin{cases} 10^{\beta_{\mathrm{rise}}(t-t_{\mathrm{peak}})} & t \leq t_{\mathrm{peak}} \\ 10^{\beta_{\mathrm{decay}}(t-t_{\mathrm{peak}})} & t > t_{\mathrm{peak}} \end{cases} . \tag{5.4}$$

Because Andreoni et al. (2022) find little evolution of the power-law spectral index with time, and because we are primarily interested in the properties of the thermal component, we forgo performing a fit with a time-variable power-law spectral index.

To estimate the parameters of the models above we use the `emcee` sampler (Foreman-Mackey et al., 2013) using a Gaussian likelihood function that includes a “white noise” term, ln(f), which accounts for any variance in the data not captured by the reported uncertainties and flat priors for all parameters. We use 100 walkers and 2000 steps, discarding the first 1500 steps to ensure convergence. The free parameters of the models are listed in Table 5.2. We have chosen the priors for the power-law component to be consistent with Andreoni et al. (2022) but have modified several priors from Hammerstein et al. (2023a) for the blackbody component light curve timescales as we expect them to differ slightly. In summary, we perform the following fits to the AT2022cmc UV/optical light curve:

Model 1. A fit with time-dependent power-law and time-dependent blackbody (with constant temperature) components described by Equation 5.3.

Model 2. A fit with a time-dependent power-law component and a static blackbody component described by 5.4.

Parameter	Description	Prior
$\log L_{\mathrm{BB},\nu_0}$	Peak blackbody luminosity	$[L_{\max}/2, 2L_{\max}]$
$\log T_0$	Mean temperature	[4, 5] Kelvin
$t_{\mathrm{peak,BB}}$	Time of peak	$[-2, 20]$ days
$\log \sigma_{\mathrm{BB}}$	Gaussian rise time	[0, 1.5] days
$\log \tau_{\mathrm{BB}}$	Exponential decay time	[0, 3] days
$\log F_{\mathrm{peak,pl}}$	Peak power-law flux density	[10, 80] erg s^{-1} Hz^{-1}
α	Power-law spectral index	$[-10, 0]$
$t_{\mathrm{peak,pl}}$	Time of peak	$[-2, 2]$ days
β_{rise}	Power-law rise time	[0, 100] days
β_{decay}	Power-law decay time	$[-100, 0]$ days
$\ln f$	White noise factor	$[-5, -1.8]$

Table 5.2: The free parameters and corresponding priors for the light curve analysis described in Section 5.3.2. $L_{\max}$ is the observed maximum luminosity. Note that the table is split into blackbody parameters (top section) and power-law parameters (middle section).

We present the results of this light curve analysis in Section 5.4.

5.4 Results

5.4.1 Spectrum Fitting

In Figure 5.3, we show the results of the spectrum fitting described in 5.3.1. For each spectrum, the power-law and blackbody fits to the continuum are shown, along with the fit parameters. We summarize these in Table 5.3. The early-time spectra of AT2022cmc are not well-fit by the blackbody continuum model and in some cases produce temperatures lower and inferred radii larger than the sample of optically discovered thermal TDEs. The early-time emission is described much better by the power-law fits to the continuum which is unsurprising given that the red component dominates the light curve until ~ 12 days from the first detection (Andreoni et al., 2022).

The Gemini+GMOS spectrum (taken on 2022 Feb 15, $t - t_{\mathrm{peak}} = 4$ days) is consistent

Name	Telescope/Inst.	Date	$\log(F_{\rm pl}/{\rm erg\ s^{-1}\ Hz^{-1}})$	α	$\log(T_{\rm BB}/{\rm K})$	$\log(R_{\rm BB}/{\rm cm})$
AT2022cmc	NOT+ALFOSC	Feb 15 2022	28.520 ± 0.004	-0.830 ± 0.038	4.174 ± 0.006	15.210 ± 0.012
	Gemini+GMOS	Feb 15 2022	31.103 ± 0.005	-1.080 ± 0.056	4.182 ± 0.012	16.480 ± 0.024
	VLT+Xshooter	Feb 17 2022	28.974 ± 0.003	-0.470 ± 0.026	4.271 ± 0.005	15.270 ± 0.010
	Keck+DEIMOS	Feb 17 2022	28.270 ± 0.003	-0.210 ± 0.046	4.196 ± 0.008	15.040 ± 0.013
	Keck+LRIS	Feb 25 2022	28.069 ± 0.004	0.170 ± 0.027	4.399 ± 0.006	14.650 ± 0.010
	Keck+LRIS	Mar 03 2022	27.859 ± 0.004	0.460 ± 0.025	4.464 ± 0.005	14.480 ± 0.007
AT2018jbv	LDT+DeVeny	Mar 28 2019	28.170 ± 0.002	1.000 ± 0.009	4.555 ± 0.009	14.670 ± 0.008
AT2020qhs	LDT+DeVeny	Oct 11 2020	27.805 ± 0.004	-1.090 ± 0.018	4.089 ± 0.005	15.130 ± 0.010
AT2020riz	LDT+DeVeny	Oct 15 202	27.705 ± 0.004	-0.600 ± 0.026	4.269 ± 0.011	14.760 ± 0.015
AT2020ysg	LDT+DeVeny	Dec 6 2020	28.075 ± 0.002	0.270 ± 0.011	4.251 ± 0.005	14.980 ± 0.007

Table 5.3: Results from power-law and blackbody continuum fits to optical spectra.

with the power-law spectral index found by Andreoni et al. (2022) from the light curve fit within mutual uncertainties. However, the power-law spectral index implied by the NOT+ALFOSC spectrum is also inconsistent with the Gemini+GMOS spectrum taken within the same day. This is also the case for the VLT+Xshooter and Keck+DEIMOS spectra, both taken on 2022 Feb 17. The cause is very likely inaccurate relative flux calibration between the observations. By comparing the $g-$ or $r-$band flux implied by the light curve at the time that the spectrum was taken to the flux implied by the spectra in those bands, we conclude that the NOT+ALFOSC, Gemini+GMOS, and VLT+Xshooter spectra all suffer from flux calibration issues that lead to at least an order of magnitude difference between the light curve flux values and the spectrum flux values.

The blackbody continuum fits to the spectra taken on 2022 Feb 25 and 2022 Mar 03, both taken with Keck+LRIS, produce more reasonable results with regard to blackbody temperature and inferred radius, with the 2022 Mar 03 LRIS spectrum implying a blackbody temperature consistent with Andreoni et al. (2022) within mutual uncertainties. The spectra show remarkable similarity to the featureless TDEs (shown in the bottom 4 panels of Figure 5.3).

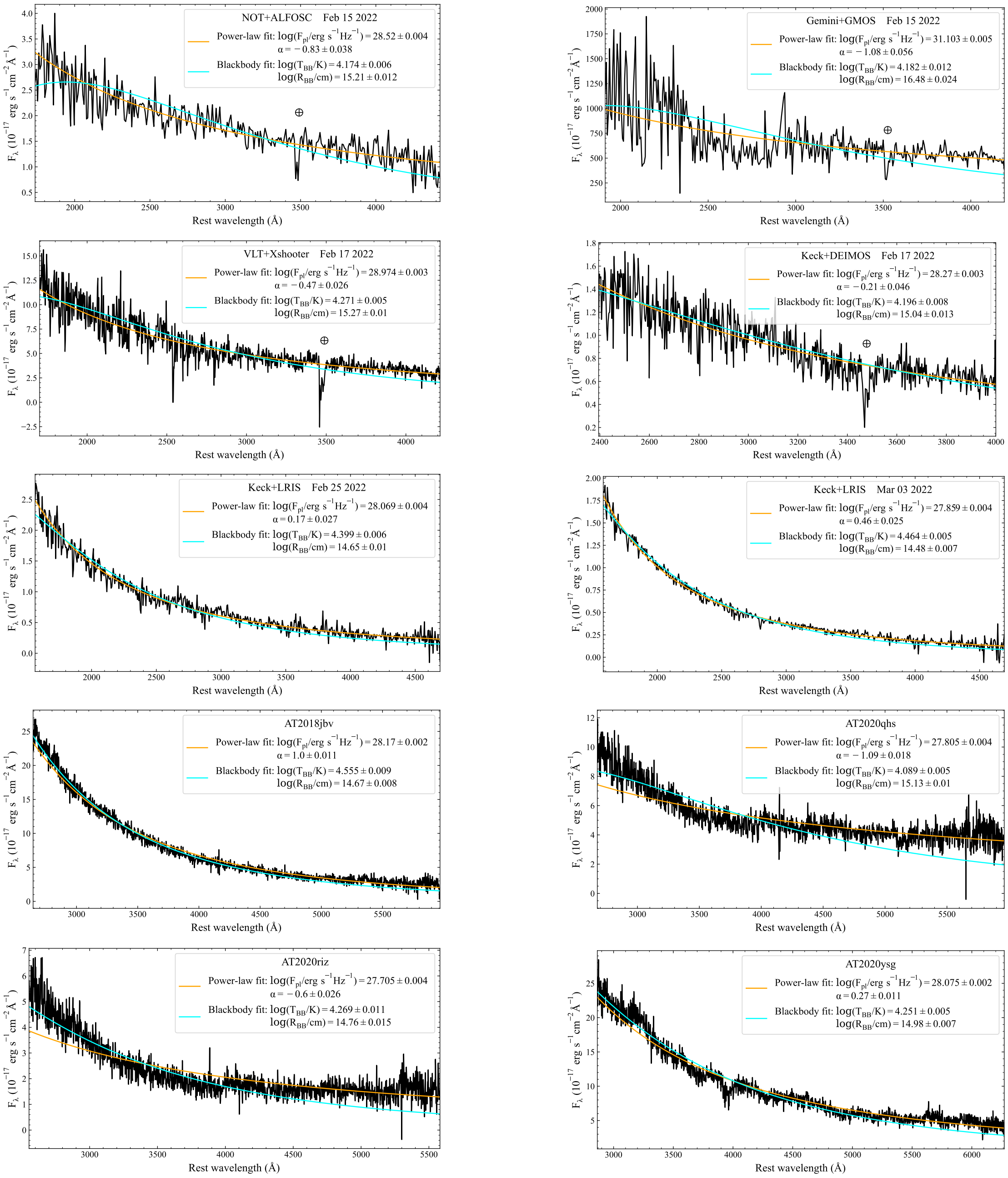

Figure 5.3: The blackbody and power-law fits described in Section 5.3.1. While most of the featureless TDEs can be well-described by a blackbody, the early-time AT2022cmc spectra are not, although a power-law may reasonably describe the data. The late-time spectra of AT2022cmc produce more reasonable results in temperature and inferred radius with a simple blackbody when compared to the non-jetted TDEs. The absorption features near 3500 Å in the AT2022cmc spectra are telluric features which are masked during fitting. The absorption feature in the AT2020ysg spectrum around 4000 Å is the stellar absorption Ca II feature.

5.4.2 Light Curve Fitting

In Table 5.4, we show the results from fitting the two models described in Section 5.3.2 to the UV/optical light curve of AT2022cmc. For the time-dependent power-law and static blackbody fit, we find results consistent with the light curve fit performed by Andreoni et al. (2022). While the blackbody luminosity we find is lower ($L_{\rm BB} = 10^{44.22}$ erg s^{-1} compared to $L_{\rm BB} = 10^{45.53}$ erg s^{-1}) and blackbody temperature is higher ($T_{\rm BB} = 10^{4.61}$ K compared to $T_{\rm BB} = 10^{4.48}$ K), our results are nonetheless consistent with typical values for TDEs. The blackbody radius implied by the temperature and bolometric blackbody luminosity is $R_{\rm BB} = 15.15$ cm is comparable to the value implied by Andreoni et al. (2022), $R_{\rm BB} = 15.30$ cm. The time-dependent power-law component is consistent within uncertainties with the findings of Andreoni et al. (2022), with the reference spectral flux density $F_{\rm peak,pl} = 10^{30.61}$ compared to their $F_{\rm peak,pl} = 10^{30.51}$, and the spectral index $\alpha = -1.19$ compared to their $\alpha = -1.32$[2]. When we allow the blackbody luminosity to vary with time, our results for both the power-law and blackbody components are consistent within mutual uncertainties. We show the light curve fit to only the r-band light curve (for clarity) in Figure 5.4.

In Figure 5.5, we show the SED derived from both fits, starting from the peak of the light curve until the ∼last epoch of observations (rest-frame). There is a clear evolution in the shape of the SED in both cases, with the early-time SED dominated by the power-law component until $\sim$ 11 days post-peak. This is consistent with Andreoni et al. (2022). In the case of the time-dependent power-law and blackbody fit, the blackbody component is found to peak $\sim$ 5 days after the power-law component. Similar behavior is observed in the continuum in the optical

---

[2] Note that Andreoni et al. (2022) label the power-law spectral index as β.

Model Fit	L_{BB,ν_0} log erg s^{-1}	$t_{\mathrm{peak,BB}}$ MJD	σ_{BB} log day	τ_{BB} log day	T_0 log K	$F_{\mathrm{peak,pl}}$ log erg s^{-1} Hz^{-1}	$t_{\mathrm{peak,PL}}$ MJD	β_{rise} day	β_{decay} day	α
1.	$44.44^{+0.12}_{-0.13}$	59627.34	$1.14^{+0.26}_{-0.52}$	$1.44^{+0.36}_{-0.44}$	$4.53^{+0.08}_{-0.08}$	$30.59^{+0.07}_{-0.09}$	59621.98	$35.30^{+44.06}_{-29.48}$	$-0.46^{+0.07}_{-0.07}$	$-1.19^{+0.46}_{-0.45}$
2.	$44.22^{+0.10}_{-0.12}$	–	–	–	$4.61^{+0.10}_{-0.08}$	$30.61^{+0.08}_{-0.07}$	59621.94	$39.76^{+40.05}_{-30.84}$	$-0.43^{+0.05}_{-0.06}$	$-1.19^{+0.39}_{-0.43}$

Table 5.4: Results from fits to AT2022cmc optical light curve. The fit numbers correspond to those in Section 5.3.2. For fit 1, L_{BB,ν_0} corresponds to the peak luminosity at the reference frequency.

spectra. In general, the evolution is slower for the blackbody component. In the next section, we compare the blackbody component of the fit to other TDEs discovered in the optical.

5.5 Discussion

Several correlations have been found between properties of the optical light curve as well as between these properties and the SMBH mass (or host galaxy mass as a proxy). van Velzen et al. (2021) found that the rise time of the flare (σ) is correlated with the peak bolometric luminosity. This correlation was not found by Hammerstein et al. (2023a), but their smaller sample size may affect this. Hammerstein et al. (2023a) did, however, find a weak correlation between the decay timescale and the peak luminosity, which has also been found by Hinkle et al. (2020). van Velzen et al. (2021) also reported a correlation between the decay timescale (τ) for their sample of TDEs and the host galaxy stellar mass. This correlation was also found in the Hammerstein et al. (2023a) sample, in addition to a correlation with the rise time, and a similar correlation was confirmed by Yao et al. (2023). In this Section, we compare the properties of the UV/optical emission in AT2022cmc to those of non-jetted optically selected TDEs, focusing on properties for which significant correlations have been reported. We use the sample of 30 TDEs from ZTF for comparison (Hammerstein et al., 2023a).

In Figure 5.6, we show the light curve parameters σ_{BB}, τ_{BB}, peak bolometric blackbody

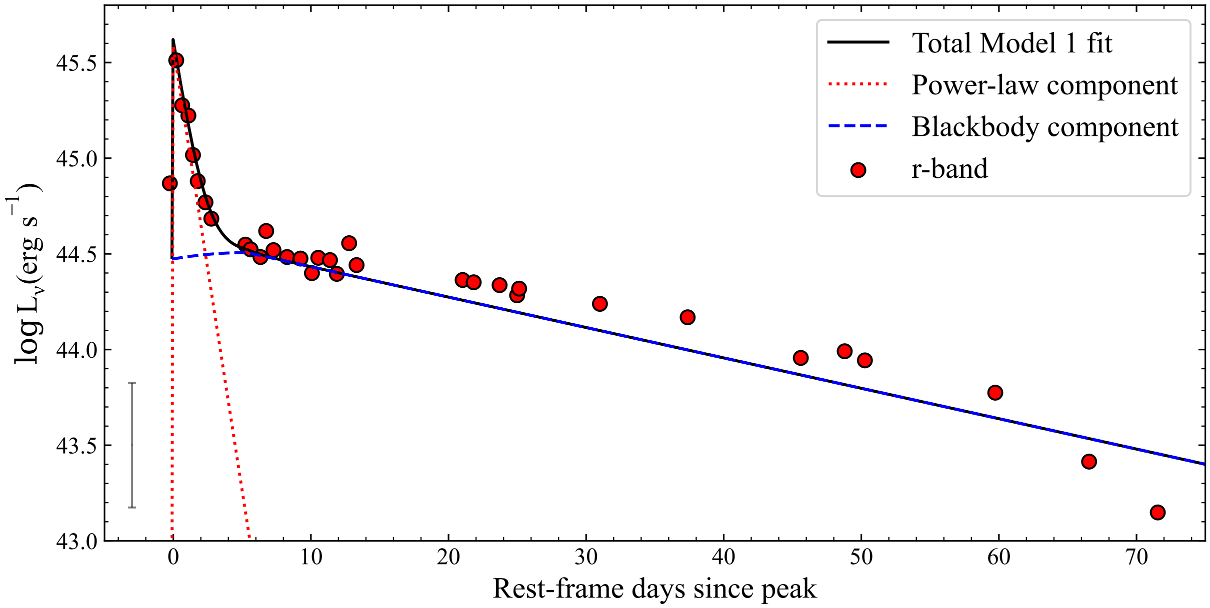

Figure 5.4: Model 1 fit to the AT2022cmc light curve, showing only the r-band for clarity. We show the two components, the power-law and the blackbody as red dotted and blue dashed lines, respectively. The rise times for the two components, σ_{BB} and β_{rise}, are derived from the red and blue curves. We note that the rise times, particularly for the power-law component, are not well-constrained. Additionally, we show the median uncertainties on the light curve data points in the bottom left corner.

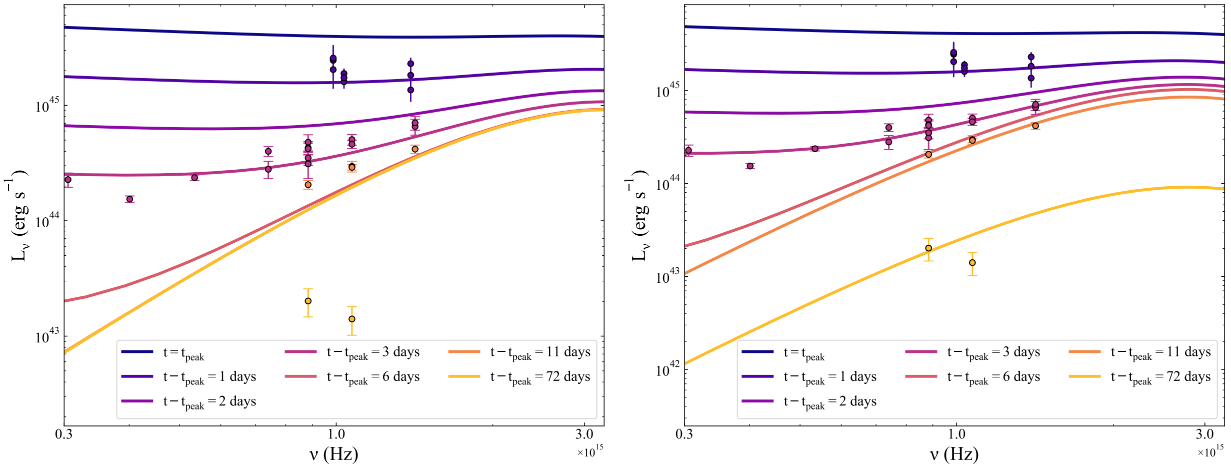

Figure 5.5: Evolution of the SED starting from peak ($t = t_{\rm peak}$) until the ∼last epoch of observations (rest-frame). Horizontal axis is limited to frequencies included in the fit. For each panel, we show light curve data points for $t - t_{\rm peak} \approx 1, 3, 11, 72$ days. *Left*: SEDs from the time-dependent power-law + static blackbody fit to the AT2022cmc light curve. After ~ 11 days, the blackbody component dominates the SED, but the static blackbody is unable to accurately represent the evolution of the light curve. *Right*: SEDs from the time-dependent power-law + fixed temperature blackbody fit to the AT2022cmc light curve. Once again after ~ 11 days, the blackbody component dominates the SED. This is consistent with findings from Andreoni et al. (2022).

luminosity $L_{\rm peak,BB}$ calculated using the mean blackbody temperature T_0 as a function of the host galaxy stellar mass for the 30 TDEs and AT2022cmc obtained from Model 1 (Section 5.3.2). While black hole mass estimates are available for some objects in the comparison sample (e.g., Hammerstein et al., 2023b; Yao et al., 2023), we choose the host galaxy stellar mass for consistency across all objects. Additionally, Hammerstein et al. (2023b) and Yao et al. (2023) find that the host galaxy stellar mass is strongly correlated with the black hole mass derived from stellar kinematics. We adopt the estimate from Andreoni et al. (2022) for the upper limit on the host stellar mass of $\log(M_{\rm gal}/M_\odot) < 11.2$. We emphasize that this is only an upper limit on the host galaxy mass and may change significantly once better constraints are placed on the host galaxy properties in future observations.

While both the rise and decay timescales for AT2022cmc are faster than would normally be expected for a TDE and do not follow the correlation with host mass, this may not be surprising given the light curve. Both the rise and decay timescales are still comparable to other TDE light curves, albeit for much lower host galaxy masses. The values for the other parameters (peak bolometric luminosity, and blackbody temperature) are more consistent with previously found correlations.

Interestingly, the values for the peak bolometric luminosity and blackbody temperature show remarkable similarity to the TDE-featureless class. Andreoni et al. (2022) noted the potential connection between AT2022cmc and the TDE-featureless class due to similarities in photometric and spectroscopic properties, such as peak luminosity and lack of broad lines in the optical spectra. They suggest that the TDE-featureless class may represent the off-axis jetted TDE scenario. This connection is potentially further supported due to the high black hole masses observed for TDE-featureless objects, which could necessitate a non-negligible spin for the black holes in these events so that the stars are disrupted outside of the event horizon, depending on the type of star that is disrupted. Hammerstein et al. (2023b) reported a mass of $\log(M_{\rm BH}/M_{\odot}) = 8.01{\pm}0.82$ obtained from stellar kinematics for AT2020qhs. Additional measurements made by Yao et al. (2023) for featureless events yielded masses $\log(M_{\rm BH}/M_{\odot}) = 7.16 - 8.23$. If high spin is required to launch a relativistic jet (e.g., Andreoni et al., 2022; Tchekhovskoy et al., 2014), then the TDE-featureless class may be capable of launching relativistic jets. This should be interpreted cautiously, however, as TDEs around SMBHs with masses lower than $\sim 10^8 M_{\odot}$ (the “Hills mass”) may still have large spins.

Two other jetted TDE candidates exhibited faint optical counterparts: Sw J2058+05 (Cenko et al., 2012; Pasham et al., 2015) and Sw J1112-82 (Brown et al., 2015, 2017). Pasham et al. (2015) fit the UV/optical observations of Sw J2058+05 with a single blackbody model, yielding a mean temperature over several epochs of $T_{\rm BB} = 10^{4.43}$ K. This is comparable to AT2022cmc and the TDE-featureless objects. The peak bolometric luminosity implied by the UV/optical observations is also comparable to AT2022cmc and the TDE-featureless class at $L_{\rm BB} = 10^{45.03}$ erg s^{-1}. Black hole mass estimates from host galaxy properties for both of these events are significantly lower than estimates for the mass in AT2022cmc (Andreoni et al., 2022; Brown et al., 2017; Pasham et al., 2015). As more jetted TDEs are discovered and their host galaxies are characterized, we can further explore the similarities and differences between the optical components in jetted TDEs and the TDE-featureless class.

Unfortunately, there have yet to be published observations of TDE-featureless objects that may indicate the presence of a jet, such as late-time radio emission. Cendes et al. (2023) found that $\sim 40\%$ of optical TDEs are detected at late times in the radio, but concluded that this emission is likely due to outflows instead of off-axis relativistic jets. It is clear that future and long-term follow-up observations of TDE-featureless events are needed to further explore this possible connection.

We have now shown here that the thermal component present in the UV/optical light curve of AT2022cmc is indeed similar to the light curves of other TDEs which are dominated by almost exclusively thermal emission. Moreover, we have shown that the properties of this component are similar to the class of featureless TDEs put forth by Hammerstein et al. (2023a). Future studies will need to investigate the presence of emission that might indicate that these TDE-featureless objects are indeed off-axis analogs to jetted TDEs. One key piece of information that is still missing is an observation of the host galaxy of AT2022cmc. Observations that can confirm the coincidence of the event in the nucleus of a galaxy and accurately measure the host galaxy mass will be crucial to making further comparisons with the general TDE population.

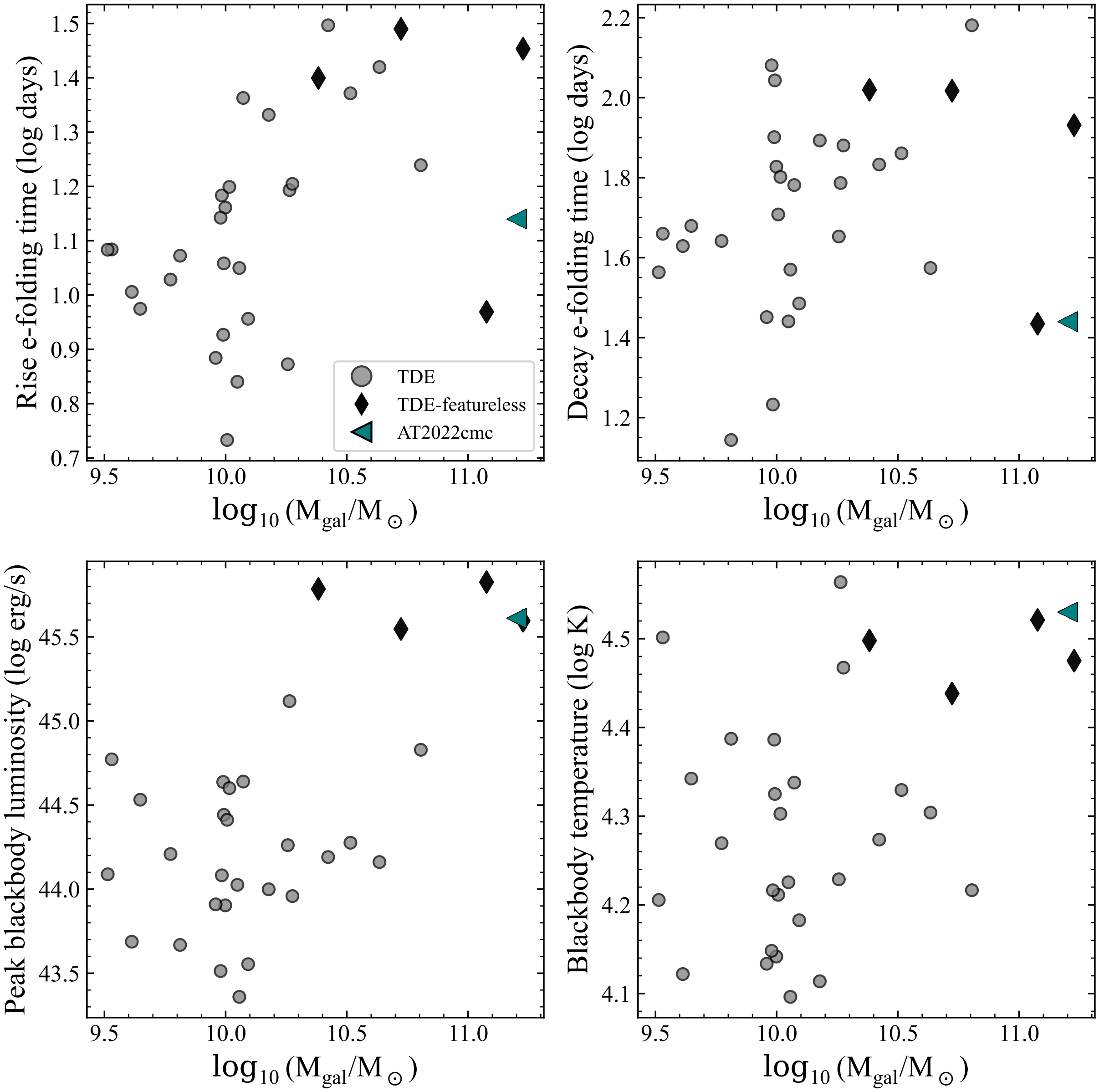

Figure 5.6: Selected light curve parameters from Model 1 for the 30 TDEs from ZTF (gray circles, black diamonds indicate TDE-featureless Hammerstein et al., 2023a) and AT2022cmc (blue triangle). The rise and decay times for the blackbody component are much shorter for AT2022cmc than the other TDEs. The other parameters, peak bolometric blackbody luminosity and mean blackbody temperature, are more consistent with expected values from TDEs and show remarkable similarity to the TDE-featureless class.

Chapter 6: Summary and Future Work

6.1 Summary of the Thesis

This thesis has explored the properties of optically selected TDEs and their host galaxies. In Chapter 2, I presented the sample of 30 TDEs from the ZTF-I survey, the largest sample discovered from a single survey yet. I found several correlations between light curve parameters, such as the peak luminosity and decline rate, which have been reported in the literature before (e.g., Hinkle et al., 2020; Yao et al., 2023). By fitting the light curves with tools that yield black hole mass estimates, I found no correlation between these estimates and the host galaxy stellar masses as one might expect if the current tools can accurately predict black hole mass from TDE light curves. However, the correlation I uncovered between the rise timescale and decay timescale and host galaxy stellar mass indicates that the properties of the SMBH are indeed imprinted on the light curve and motivates future work in this area. Lastly, by comparing the properties of the X-ray bright TDEs in this sample to the X-ray faint TDEs in this sample, I found no significant difference in their host galaxy or optical light curve properties apart from the peak luminosity. This may further support the idea that the viewing angle is responsible for the differences in observed emission in TDEs (Dai et al., 2018). I also put forth a new class of TDE, TDE-featureless, which may be connected to the rare class of jetted TDEs.

In Chapter 3, I studied a subset of host galaxies of the 30 TDEs presented in Chapter 2. By examining their optical colors, I found that 64% of the hosts reside in the green valley between red, inactive galaxies and blue, star-forming ones. Using optical imaging, I modeled the morphology of the hosts, which showed that TDE host galaxies are more centrally concentrated than galaxies of similar mass and color. I investigated the star formation histories and stellar populations of the host galaxies, finding that E+A (or post-starburst) galaxies are overrepresented among the TDE host population by a factor of ~ 22 when compared to the general galaxy population. These properties point to mergers as a likely origin for TDE hosts, but future work will need to connect these large-scale properties to factors in the nucleus that directly affect the TDE rate.

I extended this study of TDE hosts in Chapter 4, where I used integral field spectroscopy to infer black hole masses via the $M_{\rm BH} - \sigma_\star$ relation and investigate large-scale stellar kinematics to further understand the origins of peculiar TDE host properties. I found that the black hole mass distribution for TDE hosts is consistent with theoretical predictions that TDE populations are dominated by lower mass SMBHs. Once again, I found that there is no significant difference between X-ray bright and X-ray faint TDEs, lending further support to the viewing angle unification theory for TDE emission. One object in this study, AT2020qhs which is part of the TDE-featureless class, was found to have a black hole mass of $\log(M_{\rm BH}/M_\odot) = 8.01$, which is likely above the Hills mass for the disruption of a solar-type star and could necessitate a rapid spin for this particular black hole. This may further support the connection to jetted TDEs if high spin is required to launch relativistic jets.

In the final chapter, I presented further observations of a jetted TDE discovered in the optical, AT2022cmc. This event presented an opportunity to place this rare class of TDE in the context of the larger TDE population. By performing a careful light curve analysis which accounts for the non-thermal component visible at early times in the light curve, I was able to show that the slowly-evolving thermal component shows properties similar to the TDE-featureless class of events and indeed follows correlations for TDE light curve properties found in the literature. Future studies will need to investigate the presence of late-time emission in TDE-featureless events that would indicate the presence of a relativistic jet.

6.2 Future Work and Outlook

This thesis has demonstrated that TDEs have unique host galaxy preferences likely connected to galaxy mergers (Chapters 3 and 4). However, the large-scale galaxy properties studied here (e.g., stellar populations, kinematics) are unlikely to directly affect the TDE rate. Nonetheless, their ubiquity among TDE host populations implies that the same mechanisms that produce these particular properties likely impact the nuclear properties that do affect the TDE rate. High-resolution imaging of nearby TDE hosts that can resolve scales of tens of parsecs, for example with HST (e.g., French et al., 2020b), may be able to help investigate this connection. Previous studies have found that radial velocity anisotropies in nuclear star clusters created during a starburst event could explain the post-starburst galaxy preference of TDEs (Stone et al., 2018; Stone & van Velzen, 2016). Studying the properties of resolved nuclear star clusters in nearby galaxies and investigating whether they are correlated with large-scale properties can also shed further light on the connection between these scales.

While much work has been done in recent years to grow the number of TDEs discovered at all wavelengths, future time-domain surveys will drastically expand the number of TDE discoveries that can be made. Some of these endeavors include the High Latitude Time Domain Survey with the *Nancy Grace Roman Space Telescope* (Roman, infrared), the Legacy Survey of

Space and Time (LSST) at the Vera C. Rubin Observatory (Rubin, optical), ULTRASAT (UV), UVEX (UltraViolet EXplorer, UV), and Einstein Probe (X-ray). These new surveys will discover hundreds to thousands of new TDEs per year at redshifts higher than ever before (Gomez et al., 2023; van Velzen et al., 2011; Yuan et al., 2016). These numbers will enable more statistically robust and multi-wavelength population studies of TDEs, their light curves, and their host galaxies, but will also necessitate the use of more efficient TDE candidate selection and classification tools. Some work has already been done to explore the application of machine learning to the photometric classification of TDEs (Gomez et al., 2023; Stein et al., 2023), which may allow for more targeted follow-up initiatives. The work presented in this thesis on host galaxy characterization may also offer a way to select TDE candidates in future surveys (e.g., French & Zabludoff, 2018).

The higher redshift TDEs discovered by surveys such as Rubin will be observed in the rest-frame UV. It is therefore of great interest to further our understanding of these transients in the UV. The UV spectra of TDEs in particular can provide key information on the velocity, temperature, composition, and density of the gas involved in TDEs in a way that optical photometry alone cannot. The early accretion rate of tidal debris in a TDE is likely above the Eddington limit and one might therefore expect large-scale outflows from these systems during this phase which would be detectable via broad absorption lines in the UV spectra. These outflows are thought to play a role in determining the visibility of X-ray and optical emission in TDEs (Guillochon et al., 2014; Metzger & Stone, 2016; Miller et al., 2015; Roth et al., 2016), and UV spectra can help to test the viability of models for TDE optical emission. Therefore, further work in this area is of the utmost importance.

Lastly, the ability to use the light curves to infer the properties of SMBHs will be crucial to fully utilizing the large samples of TDEs that future time-domain surveys will provide. The high redshift TDEs observed with surveys such as Roman and Rubin will probe the populations of SMBHs at these redshifts which will help to distinguish between SMBH formation mechanisms. This thesis has demonstrated that our current methods of using TDE light curves to infer the properties of SMBHs need further modification. However, the correlations found between light curve timescales and SMBH mass reported in this thesis have demonstrated that the properties of the SMBH are indeed imprinted on the light curve. The disconnect likely lies in our understanding of the origin of the UV and optical emission in TDEs and determining where this emission comes from is crucial.

The current models for this emission make disparate predictions for how the observed emission (primarily X-ray, primarily optical, or some combination) in TDEs should depend on the black hole mass. Therefore, by measuring the SMBH masses of events showing emission at various wavelengths, we can test the viability of these models. In the viewing angle model of Dai et al. (2018), which relies on reprocessing of X-ray emission from the accretion disk to the UV and optical through a wind, the type of emission observed depends primarily on the angle at which the observer views the system and there should therefore be little dependence on black hole mass. Other models to explain the UV and optical emission rely on the shocks and subsequent outflows created by intersecting stellar debris streams to explain observed TDE emission. In the case where shock-driven outflows reprocess X-rays into optical emission, the visibility of X-rays will be viewing angle dependent at higher SMBH masses, but below $M \sim 10^{5-6}\,M_{\odot}$ no outflow is launched and no optical emission is produced (Lu & Bonnerot, 2020). Thus, lower mass SMBHs would produce primarily X-ray dominated events. In the case where the shocks themselves produce the optical emission (Jiang et al., 2016; Piran et al., 2015), optical flares become extremely faint at lower SMBH masses. Therefore, by measuring black hole masses for events that show either primarily X-ray emission or primarily optical emission, we can begin to test the validity of these models.

Unfortunately, many TDE host galaxies are much too distant to resolve the 0.1–10 pc sphere of influence for SMBHs in the expected mass regime of $10^6 - 10^8 M_\odot$ and obtain dynamical measurements of the SMBH mass. Scaling relations which most often relate the SMBH mass to the properties of a galaxy's bulge or spheroid component can be used to obtain estimates of these more distant TDE hosts. The $M_{\rm BH} - \sigma_\star$ relation (e.g. Ferrarese & Merritt, 2000; Gebhardt et al., 2000; Gültekin et al., 2009), which relates the SMBH mass to the velocity dispersion of a galaxy's bulge or spheroidal component is often used as it has the smallest scatter compared to other relations. There is, however, much debate as to whether the $M_{\rm BH} - \sigma_\star$ relation still holds at lower black hole masses (see Greene et al., 2020, for a review). Nonetheless, future studies that expand upon the work presented in Chapter 4 and measure the black hole masses for TDEs discovered across the electromagnetic spectrum can test models that predict how the type of observed emission in TDEs depends on black hole mass.

Appendix A: Supplementary Materials for Chapter 2

A.1 Detailed Spectra

We describe the spectra for each event presented in this sample and justify our TDE spectral type classification. For each event, we provide an early-time spectrum and a late-time spectrum when available. We detail any evolution which may appear from the early to late time spectra provided. We note that some events do not have pre-peak or even near peak spectra, with the first medium-to-high resolution spectra available over 2 months post-peak. However, this is likely not a problem when investigating spectral class evolution, as most evolution from one class to another for a single object occurs from pre- or near peak to post-peak. All spectra presented here will be made publicly available upon publication.

For the objects that show evolution in their spectra or are unclear in their classification, namely AT2018hyz, AT2019bhf, and AT2019mha, we re-investigate the significance of the spectral class differences after changing their spectral type from what is presented in Table 2.1.

A.1.1 AT2018zr

We classify AT2018zr as a TDE-H. This is consistent with the original classification given by Tucker et al. (2018), which reports broad Balmer emission lines 18 days after first detection.

We provide an early-time spectrum of this source from the Lowell Discovery Telescope (LDT) DeVeny spectrograph on 2018 Apr 4, which shows broad Hα, Hβ, and Hγ emission lines and evidence for He I λ5876. We provide a late-time spectrum from LDT/DeVeny on 2018 May 19, which again shows broad Hα, Hβ, and Hγ emission lines and evidence for He I λ5876.

A.1.2 AT2018bsi

We classify AT2018bsi as a TDE-H+He. This classification is consistent with Gezari et al. (2018), which reports broad hydrogen and helium lines 8 days after first detection. We present an early-time low resolution spectrum from the Palomar P60 SED machine (SEDM; Blagorodnova et al., 2018; Rigault et al., 2019) on 2018 Apr 18 which shows broad Balmer lines and broad He II λ4686. We provide a late-time spectrum from LDT/DeVeny on 2018 May 19, which additionally shows N III λ4100. We do not interpret this as evolution given that the SEDM spectrum is very low resolution.

A.1.3 AT2018hco

We classify AT2018hco as TDE-H. This is consistent with the classification given in van Velzen et al. (2018), which classifies AT2018hco as a TDE-H object with broad Hα emission and evidence for He I emission. We present an early-time low resolution spectrum from SEDM on 2018 Oct 26 which shows a blue continuum. We also provide a spectrum from the Keck Low Resolution Imaging Spectrograph (LRIS) 2018 Dec 1, which shows broad Hα and He I emission. Reynolds et al. (2018) reported a weak He II λ4686 emission line on 2018 Dec 5 in a spectrum from the Nordic Optical Telescope (NOT) Alhambra Faint Object Spectrograph and

Camera (ALFOSC). The LRIS spectrum from 4 days prior does indeed show weak emission closer to N III λ4640 than He II λ4686. However, when comparing this host+transient spectra to the host spectrum in Hammerstein et al. (2021a), we find there is a persistent feature near N III λ4640. We therefore keep the original classification of TDE-H.

A.1.4 AT2018iih

We classify AT2018iih as a TDE-He, consistent with the classification presented in van Velzen et al. (2021). We provide a spectrum from LDT/DeVeny on 2019 Mar 10, which shows a steep blue continuum and emission near λ4500 that we interpret as broad, blueshifted He II. While the redshift of the source places Hα nearly out of the wavelength range of the spectrograph, we do not observe broad Hβ, which typically accompanies broad Hα emission in TDEs. We provide a late-time spectrum from the Palomar P200 Double Spectrograph (DBSP) on 2019 Oct 3, which shows a flattening in the continuum, although still blue, and does indeed cover the wavelength range of Hα. The telluric-corrected DBSP spectrum shows the He II emission detected at early times, but no evidence for broad Hα emission.

A.1.5 AT2018hyz

We classify AT2018hyz as a TDE-H+He. AT2018hyz is one event where evolution of the spectral features has been noted. Dong et al. (2018) found broad Hα and weaker broad Hβ emission, but no He II emission in a Lick/Kast spectrum from 2018 Nov 9. Arcavi (2018) noted similar features in a spectrum from the Faulkes Telescope North (FTN) Floyds on 2018 Nov 9, which we provide here as an early-time spectrum. van Velzen et al. (2021) classified AT2018hyz as a TDE-H and performed their analysis with this classification. However, Hung et al. (2020) and Short et al. (2020) presented a suite of spectra which showed evolution in He II and N III. We show a spectrum from Short et al. (2020) from the Magellan-Baade Inamori Magellan Areal Camera and Spectrograph (IMACS) from 2019 Jun 6 as an example of a late-time spectrum of AT2018hyz. Because of this evolution, we perform our investigation into differences among the spectral class properties again, with AT2018hyz classified as TDE-H but keeping all other classifications as shown in Table 2.1.

If we change the classification of AT2018hyz to TDE-H, as it was in van Velzen et al. (2021), the difference in rise time between TDE-H and TDE-H+He events is now significant with p-value $= 0.012$, which is consistent with the result from van Velzen et al. (2021). We also find that the difference in rise time between TDE-H and TDE-He events are significant with $p = 0.044$. The difference in t_0 between the TDE-H+He and TDE-He class is no longer significant. There are no changes to the other comparisons between light curve classes which would make an insignificant correlation now significant or vice versa.

A.1.6 AT2018lni

We classify AT2018lni as a TDE-H+He. This is consistent with the classification given by Frederick et al. (2019) which details the detection of broad Hα and He II emission. We provide a spectrum from Palomar/DBSP on 2019 Jan 7, which is detailed in Frederick et al. (2019) and shows broad Hα and He II emission. We provide a spectrum from LDT/DeVeny on 2019 Mar 1, which also shows evidence for broad Hα and He II emission.

A.1.7 AT2018lna

We classify AT2018lna as a TDE-H+He event. van Velzen et al. (2019e) did not note any He II in the spectrum from DBSP on 2019 Jan 26 that was used to classify AT2018lna as a TDE, although we provide this observation as an example of an early-time spectrum and now note that there is evidence for He II emission. We present a late-time spectrum from LDT/DeVeny on 2019 Mar 28, which shows further evidence for strong Balmer, He II, and N III emission.

A.1.8 AT2018jbv

We classify AT2018jbv as a TDE-featureless event. We provide a spectrum from LDT/DeVeny on 2019 Mar 28 as an early-time spectrum. The early-time spectroscopic follow-up of AT2018jbv with medium-to-high resolution spectrographs is limited. This is likely because there were no ZTF g-band observations pre-peak, which resulted in AT2018jbv not being flagged in our TDE search until g-band observations were performed post-peak. While this spectrum does not cover Hα, there is no evidence for broad emission near Hβ.

A.1.9 AT2019cho

We classify AT2019cho as a TDE-H+He, consistent with the classification in van Velzen et al. (2021). We provide an early-time spectrum from SEDM on 2019 Mar 4, which shows a blue continuum and evidence for broad Hα emission. Due to the low resolution obtained by SEDM, it is difficult to determine whether there is broad He II present in this spectrum. The late-time spectrum we provide was obtained on 2019 May 2 with LDT/DeVeny. This spectrum shows broad Balmer emission accompanied by broad He II and N III emission.

A.1.10 AT2019bhf

We classify AT2019bhf as a TDE-H+He. This object was originally classified as TDE-H in van Velzen et al. (2021), however, further examination of the available spectra revealed broad bumps near He II and N III $\lambda4640$. This has led to the reclassification of this object as TDE-H+He. We provide one early-time spectrum from SEDM on 2019 Mar 30, which shows broad Hα emission, and a broad bump in the Hβ, He II, N III region. The late-time spectrum we provide is from LDT/DeVeny on 2019 Jun 29, which again shows broad Hα and a broad bump near Hβ, He II, and N III. We perform our search for correlations among light curve and host properties again, with AT2019bhf classified as TDE-H.

After performing our investigation into the spectral class differences with AT2019bhf classified as TDE-H, we find several differences. The difference between TDE-H and TDE-H+He rise times (σ) is now significant with a p-value $= 0.021$. The difference between the TDE-H and TDE-He rise times is also significant with p-value $= 0.044$. The difference in t_0 between the TDE-H+He and TDE-He classes is no longer significant. The remaining comparisons are unchanged.

A.1.11 AT2019azh

We classify AT2019azh as a TDE-H+He. van Velzen et al. (2021) classified this object as TDE-H+He based on follow-up spectra, which evolved from featureless to show broad Balmer emission and evidence for He II and N III emission. We provide a spectrum near peak from LDT/DeVeny on 2019 Mar 10, which shows evidence for broad Balmer emission and a steep blue continuum, although there is Balmer absorption from the host galaxy. Our late-time spectrum from LDT/DeVeny on 2019 May 2 shows strong broad Hα, a broad bump near Hβ, and emission near He II and N III. Hinkle et al. (2020) also examined spectra of AT2019azh and found that there are Bowen fluorescence lines that appear post-peak in addition to the broad Balmer emission, although the spectra are dominated by Balmer emission at early times.

A.1.12 AT2019dsg

We classify AT2019dsg as TDE-H+He, consistent with the classification in van Velzen et al. (2021). We include an early-time spectrum from New Technology Telescope (NTT) ESO Faint Object Spectrograph and Camera v.2 (EFOSC2) on 2019 May 13, which shows broad Balmer emission, broad He II, and broad N III emission (Short et al., 2019). We provide a late-time spectrum from LDT/DeVeny on 2019 Jun 29, which shows a flattening in the continuum, but persistent broad Balmer, He II, and N III emission.

A.1.13 AT2019ehz

We classify AT2019ehz as a TDE-H object. The early-time spectrum we present is from the Liverpool Telescope (LT) SPectrograph for the Rapid Acquisition of Transients (SPRAT) on 2019 May 10. This spectrum is blue and mostly featureless. Our late-time spectrum from LDT/DeVeny on 2019 Jun 29 shows broad Hα emission and possible broad Hβ emission.

A.1.14 AT2019mha

We classify AT2019mha as TDE-H+He. We have only one early-time spectrum for this source from DBSP on 2019 Aug 27, which shows host galaxy lines at $z = 0.148$ but broad

Balmer emission, and He II and N III emission blueshifted by $\sim$5000 km s^{-1} with respect to the host galaxy lines. Because this source was reclassified from van Velzen et al. (2021), we have performed the investigation into spectral class differences again, with AT2019mha classified as TDE-H while keeping all other classifications in Table 2.1 the same. We find that changing the classification of AT2019mha to TDE-H does not affect any comparisons between spectral classes.

A.1.15 AT2019meg

We classify AT2019meg as TDE-H. This is consistent with the classification given by van Velzen et al. (2019b). We provide one early time spectrum from SEDM on 2019 Jul 31, which shows a blue continuum and broad Hα and Hβ emission lines. The late-time spectra of this object are limited, but we provide a later time spectrum from DBSP on 2019 Aug 10, which also shows a blue continuum, but the broad Hβ emission is now more prominent.

A.1.16 AT2019lwu

We classify AT2019lwu as TDE-H, consistent with the classification given in van Velzen et al. (2021). We provide an early-time spectrum from SEDM on 2019 Aug 8, which shows a blue continuum, however no discernible broad emission features are seen in the low-resolution spectrum. The late-time spectra of AT2019lwu are limited, but we provide another spectrum from LDT/DeVeny on 2019 Aug 27 which shows a blue continuum and now broad Hα and Hβ emission lines.

A.1.17 AT2019qiz

We classify AT2019qiz as a TDE-H+He object. We provide an early-time spectrum from SEDM on 2019 Sept 24, which shows a blue continuum and potential for broad emission lines near Hα, Hβ, He II, and N III. A late-time spectrum from LDT/DeVeny on 2019 Nov 5 confirms that the existence of broad Balmer emission, as well as broad He II and N III emission.

A.1.18 AT2019teq

We classify AT2019teq as a TDE-H+He object. We provide one early-time spectrum of this object from LDT/DeVeny on 2019 Oct 23, which shows broad Balmer emission that is potentially blueshifted by $\sim$8000 km s^{-1}. The He II and N III emission is also blueshifted by this same amount. The classification report for this object (Hammerstein, 2020) notes the possibility for the presence of Fe II narrow line complex near He II. We provide a later-time spectrum from LDT/DeVeny on 2019 Nov 5, which shows stronger evidence for blueshifted TDE-like lines.

A.1.19 AT2020pj

We classify AT2020pj as a TDE-H+He object. We provide an early-time spectrum from LT/SPRAT on 2020 Jan 15, which shows a blue continuum and a broad bump near Hβ and He II. We note a peculiar absorption line near Hα which is due to an error in the telluric absorption correction. We also note that this galaxy is a star-forming galaxy and possesses narrow Hα emission. The late-time spectrum that we provide is from LDT/DeVeny on 2020 Feb 26. This spectrum shows a blue continuum and a broad base to the narrow Hα emission. It also shows a broad base to the Hβ emission and broad He II and N III.

A.1.20 AT2019vcb

We classify AT2019vcb as TDE-H+He. We provide an early-time low-resolution spectrum from LT/SPRAT on 2019 Dec 28, which shows a strong blue continuum and a broad base to the narrow Hα from the host galaxy. There are also potential broad bumps near Hβ and He II. We provide a late-time spectrum from Keck/LRIS on 2020 Feb 18, which additionally shows broad He II and N III emission.

A.1.21 AT2020ddv

We classify AT2020ddv as a TDE-He object. The follow-up spectra of this object are unfortunately limited, but we provide an early-time spectrum from DBSP on 2020 Feb 27, which shows a blue continuum and lack of obvious broad Balmer emission. There is, however, a broad bump near He II, which points towards the classification of this object as TDE-He. We provide a late-time spectrum of this object from LDT/DeVeny on 2020 Jun 9, which shows a flattening in the continuum and broad emission near He II, but again no obvious broad Balmer emission lines.

A.1.22 AT2020ocn

We classify AT2020ocn as a TDE-He object. We provide an early-time spectrum of AT2020ocn from DBSP on 2020 Jun 17, which shows a blue continuum a broad emission near He II and potentially N III. There is no obvious broad Balmer emission. We provide a later time spectrum from DBSP on 2020 Jul 16, which shows flattening in the continuum but the broad emission near He II remains. Again, there is no obvious broad Balmer emission.

A.1.23 AT2020opy

We classify AT2020opy as a TDE-H+He object. We provide an early-time spectrum from LDT/DeVeny on 2020 Aug 19, which shows a blue continuum, a broad base to the narrow Hα from the host galaxy, and broad emission near He II and Hβ. We provide a late-time spectrum from LDT/DeVeny on 2020 Oct 11. The continuum has now flattened, but the broad emission near He II and N III is now more apparent, accompanied by the broad Balmer emission.

A.1.24 AT2020mot

We classify AT2020mot as a TDE-H+He object. The spectra of this object are unfortunately limited. We provide a low-resolution spectrum from LT/SPRAT on 2020 Jul 29, which shows a broad emission feature near He II and Hβ. There is also a potential broad emission feature near Hα. We provide a spectrum from LDT/DeVeny on 2020 Aug 19 as a late-time spectrum. This spectrum shows a broad emission feature near Hα and Hβ, as well as broad emission from He II and N III.

A.1.25 AT2020mbq

We classify AT2020mbq as a TDE-H object. The available spectra for this source are unfortunately very limited. We provide one spectrum from DBSP on 2020 Aug 14, which shows a blue continuum and broad Hα and Hβ emission.

A.1.26 AT2020qhs

We classify AT2020qhs as a TDE-featureless object. Similar to AT2018jbv, we were unable to classify this object close to peak as the ZTF survey did not observe this object until it had already started to decline. We did not obtain a first spectrum of this object until roughly 77 days post-peak. We provide this spectrum from LDT/DeVeny on 2020 Oct 11 as the earliest-time spectrum available. The spectrum shows a steep blue continuum with no obvious emission lines. Although Hα is not within the wavelength range observed by DeVeny, there is no broad Hβ emission, which typically accompanies any broad Hα. We provide a late-time spectrum from Keck/LRIS on 2020 Nov 20, which also shows a steep blue continuum and no obvious broad emission lines. This spectrum does cover Hα, and no obvious broad emission is present.

A.1.27 AT2020riz

We classify AT2020riz as a TDE-featureless object. The follow-up spectra for this object are unfortunately very limited. We show one spectrum from LDT/DeVeny on 2020 Oct 15, which shows a steep blue continuum and no obvious broad emission features. While some TDEs do evolve from featureless to having broad emission features, this typically occurs pre-peak to post-peak, as we have discussed above. The spectrum we provide here is sufficiently post-peak that this is likely not what is occurring in this spectrum.

A.1.28 AT2020wey

We classify AT2020wey as a TDE-H+He object. This object was originally classified by Arcavi et al. (2020) as a TDE-H+He object. We provide the spectrum used in this classification as an example of an early-time spectrum. This spectrum is from FTN/Floyds on 2020 Oct 22. We provide one additional spectrum from DBSP on 2020 Nov 12, which shows a similar blue continuum, and more prominent Hα emission. The broad He II emission is still present.

A.1.29 AT2020zso

We classify AT2020zso as a TDE-H+He object. The available spectra for this event are not spread over a large span of time, but we provide one earlier-time spectrum from SEDM on 2020 Nov 25, which shows a blue continuum and evidence for broad Balmer, He II, and N III emission. The later-time spectrum we provide is from Keck/LRIS on 2020 Dec 12, which now shows the broad Hα and Hβ emission more prominently, and confirms the presence of broad He II and N III.

A.1.30 AT2020ysg

We classify AT2020ysg as a TDE-featureless object. We provide one early-time spectrum from LDT/DeVeny on 2020 Dec 6, which shows a steep blue continuum and no apparent broad emission features. We provide another spectrum from LDT/DeVeny on 2021 Jan 11, which still shows the steep blue continuum and lack of broad emission features. We note that these spectra are over 50 days post-peak. AT2020ysg suffers from a similar predicament as AT2018jbv, where the peak was missed by the ZTF survey and no color information was available pre-peak. This delayed the classification of this object and subsequent follow-up efforts until sufficiently post-peak that the classification was secure. We note that the first spectrum was taken approximately 50 days after post-peak color information became available. Additionally, any evolution from featureless to the emergence of broad lines that we have noted in the spectra presented in this Appendix typically occurs from pre-peak to post-peak. These spectra are sufficiently post-peak that evolution would likely have already taken place.

IAU Name	Date	Phase	Telescope/Inst.	Date	Phase	Telescope/Inst.
AT2018zr	2018 Apr 04	7	LDT/DeVeny	2018 May 19	52	LDT/DeVeny
AT2018bsi	2018 Apr 18	1	P60/SEDM	2018 May 19	32	LDT/DeVeny
AT2018hco	2018 Oct 26	12	P60/SEDM	2018 Dec 01	48	Keck/LRIS
AT2018iih	2019 Mar 10	90	LDT/DeVeny	2019 Oct 03	297	P200/DBSP
AT2018hyz	2018 Nov 9	3	FTN/Floyds[1]	2019 Jun 06	213	Magellan-Baade/IMACS[2]
AT2018lni	2019 Jan 07	23	P200/DBSP	2019 Mar 01	76	LDT/DeVeny
AT2018lna	2019 Jan 26	0	P200/DBSP	2019 Mar 28	61	LDT/DeVeny
AT2018jbv	2019 Mar 28	101	LDT/DeVeny			
AT2019cho	2019 Mar 04	0	P60/SEDM	2019 May 02	58	LDT/DeVeny
AT2019bhf	2019 Mar 30	28	P60/SEDM	2019 Jun 29	119	LDT/DeVeny
AT2019azh	2019 Mar 10	−6	LDT/DeVeny	2019 May 02	46	LDT/DeVeny
AT2019dsg	2019 May 13	12	NTT/EFOSC2[3]	2019 Jun 29	59	LDT/DeVeny
AT2019ehz	2019 May 10	0	LT/SPRAT	2019 Jun 29	50	LDT/DeVeny
AT2019mha	2019 Aug 27	18	P200/DBSP			
AT2019meg	2019 Jul 31	−1	P60/SEDM	2019 Aug 10	8	P200/DBSP
AT2019lwu	2019 Aug 08	11	P60/SEDM	2019 Aug 27	30	LDT/DeVeny
AT2019qiz	2019 Sep 24	−13	P60/SEDM	2019 Nov 05	28	LDT/DeVeny
AT2019teq	2019 Oct 23	−15	LDT/DeVeny	2019 Nov 05	−2	LDT/DeVeny
AT2020pj	2020 Jan 15	1	LT/SPRAT	2020 Feb 26	43	LDT/DeVeny
AT2019vcb	2019 Dec 28	16	LT/SPRAT	2020 Feb 18	68	Keck/LRIS
AT2020ddv	2020 Feb 27	−9	P200/DBSP	2020 Jun 09	93	LDT/DeVeny
AT2020ocn	2020 Jun 17	30	P200/DBSP	2020 Jul 16	59	P200/DBSP
AT2020opy	2020 Aug 19	−9	LDT/DeVeny	2020 Oct 11	43	LDT/DeVeny
AT2020mot	2020 Jul 29	7	LT/SPRAT	2020 Aug 19	13	LDT/DeVeny
AT2020mbq	2020 Aug 14	55	P200/DBSP			
AT2020qhs	2020 Oct 11	77	LDT/DeVeny	2020 Nov 20	117	Keck/LRIS
AT2020riz	2020 Oct 15	57	LDT/DeVeny			
AT2020wey	2020 Oct 22	-5	FTN/Floyds[4]	2020 Nov 12	15	P200/DBSP
AT2020zso	2020 Nov 25	−14	P60/SEDM	2020 Dec 12	2	Keck/LRIS
AT2020ysg	2020 Dec 06	50	LDT/Deveny	2021 Jan 11	86	LDT/DeVeny

Table A.1: Information for all spectra shown in Figures A.1, A.2, and A.3. We include the date the spectrum was observed, the approximate phase from estimated peak the spectrum was observed in days, and the telescope and instrument. The phase is approximate to within one day of when the spectrum was observed.

---

[1] Arcavi (2018)

[2] Short et al. (2020)

[3] Short et al. (2019)

[4] Arcavi et al. (2020)

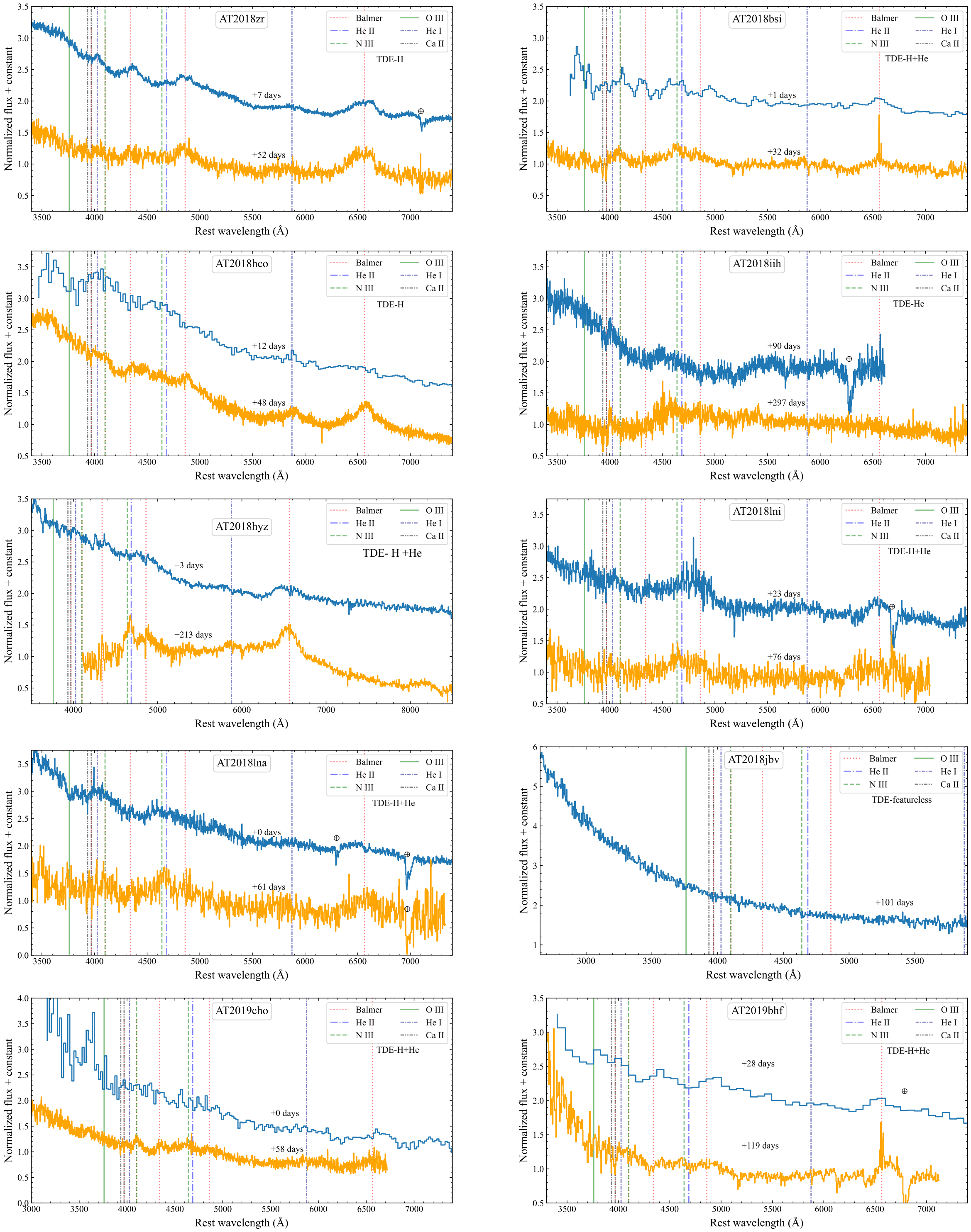

Figure A.1: Optical spectra for the events in this sample. We provide an early and late time spectrum for each event when available and provide the approximate phase relative to peak that the spectrum was taken. We label common TDE emission lines and galaxy absorption lines. Spectra have not been host subtracted. Some spectra still contain telluric absorption lines, which have been labeled.

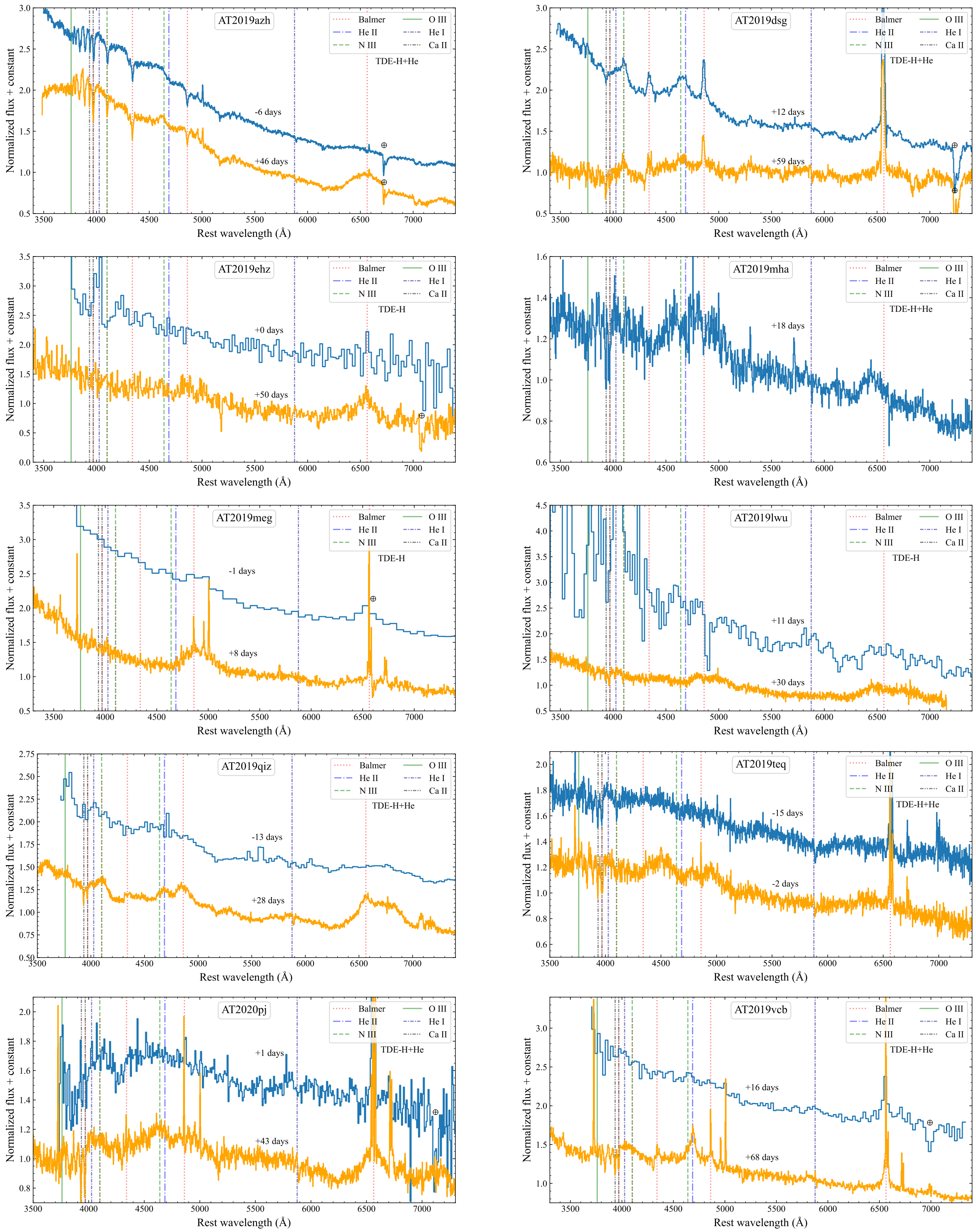

Figure A.2: Optical spectra for the events in this sample. We provide an early and late time spectrum for each event when available and provide the approximate phase relative to peak that the spectrum was taken. We label common TDE emission lines and galaxy absorption lines. Spectra have not been host subtracted. Some spectra still contain telluric absorption lines, which have been labeled.

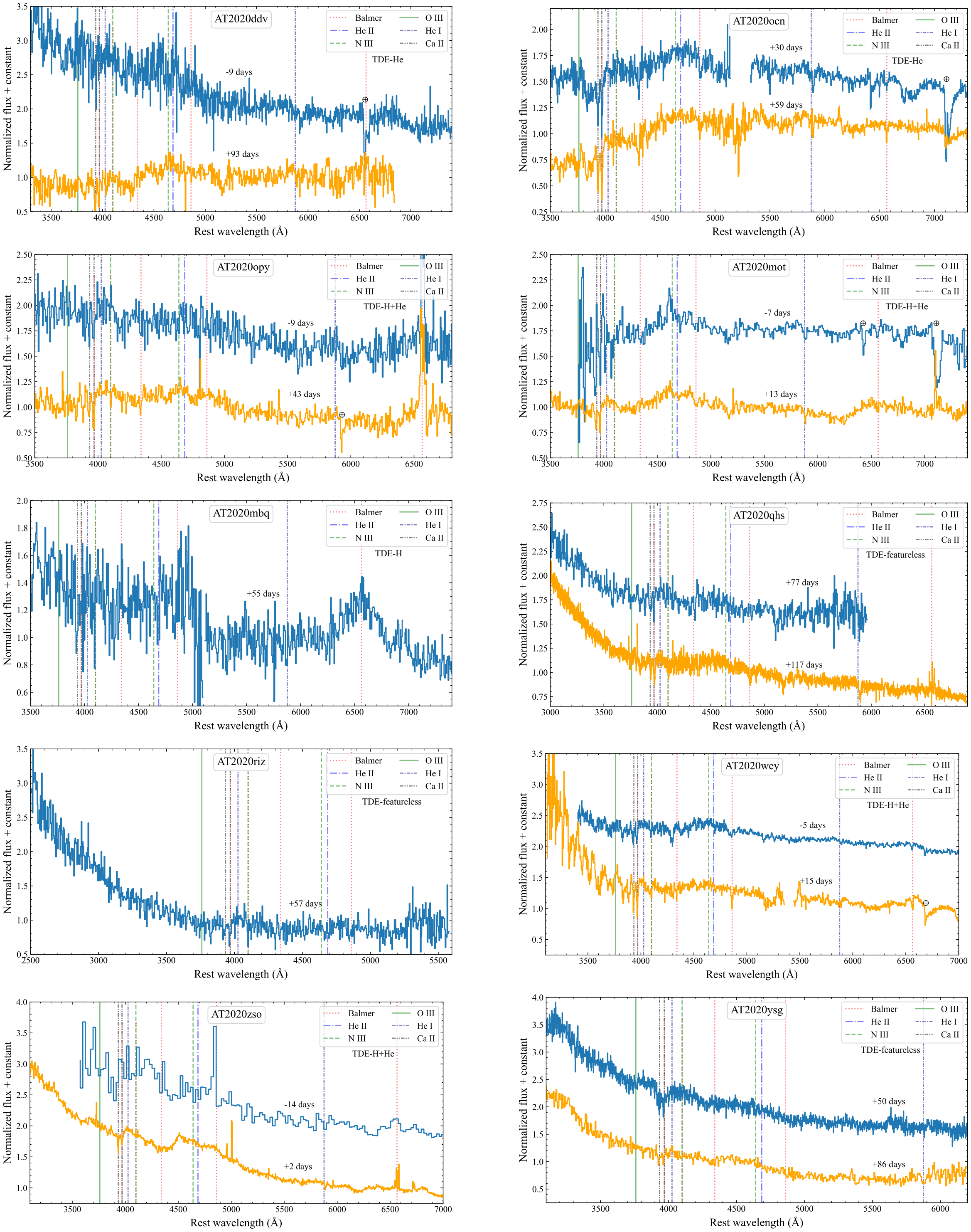

Figure A.3: Optical spectra for the events in this sample. We provide an early and late time spectrum for each event when available and provide the approximate phase relative to peak that the spectrum was taken. We label common TDE emission lines and galaxy absorption lines. Spectra have not been host subtracted. Some spectra still contain telluric absorption lines, which have been labeled.

A.2 Light Curves & Fits

IAU Name	σ log day	τ log day	$T_{\rm peak}$ log K	$L_{\rm BB}$ log erg/s	t_0 log day	t_0 ($p=5/3$) log day	p	$L_{\rm g}$ log erg/s	dT/dt 10^2 K/day	$t_{\rm peak}$ MJD
AT2018zr	$1.16^{+0.04}_{-0.04}$	$1.83^{+0.03}_{-0.03}$	$4.14^{+0.01}_{-0.01}$	$43.71^{+0.07}_{-0.04}$	$1.36^{+0.15}_{-0.19}$	$2.04^{+0.03}_{-0.03}$	$-0.78^{+0.09}_{-0.12}$	$43.55^{+0.02}_{-0.02}$	$0.56^{+0.05}_{-0.04}$	$58202.06^{+1.88}_{-4.24}$
AT2018bsi	$1.40^{+0.07}_{-0.35}$	$1.60^{+0.26}_{-0.14}$	$4.30^{+0.03}_{-0.03}$	$43.96^{+0.14}_{-0.08}$	$1.97^{+0.19}_{-0.29}$	$1.72^{+0.09}_{-0.10}$	$-2.92^{+0.93}_{-0.86}$	$43.51^{+0.05}_{-0.05}$	$-0.76^{+0.66}_{-0.15}$	$58212.63^{+7.92}_{-5.33}$
AT2018hco	$1.06^{+0.02}_{-0.02}$	$2.04^{+0.02}_{-0.02}$	$4.32^{+0.01}_{-0.01}$	$44.18^{+0.06}_{-0.03}$	$1.98^{+0.11}_{-0.14}$	$2.06^{+0.02}_{-0.02}$	$-1.68^{+0.27}_{-0.26}$	$43.75^{+0.01}_{-0.01}$	$-0.12^{+0.05}_{-0.04}$	$58409.75^{+2.12}_{-2.07}$
AT2018iih	$1.36^{+0.01}_{-0.01}$	$2.06^{+0.03}_{-0.03}$	$4.22^{+0.02}_{-0.02}$	$44.71^{+0.08}_{-0.07}$	$1.62^{+0.19}_{-0.19}$	$2.20^{+0.04}_{-0.04}$	$-0.88^{+0.14}_{-0.15}$	$44.39^{+0.02}_{-0.02}$	$0.09^{+0.04}_{-0.07}$	$58459.66^{+2.14}_{-2.38}$
AT2018hyz	$0.73^{+0.55}_{-0.50}$	$1.71^{+0.01}_{-0.01}$	$4.21^{+0.01}_{-0.01}$	$44.30^{+0.22}_{-0.16}$	$1.29^{+0.10}_{-0.19}$	$1.54^{+0.09}_{-0.09}$	$-1.20^{+0.08}_{-0.09}$	$43.95^{+0.07}_{-0.08}$	$0.13^{+0.04}_{-0.04}$	$58424.96^{+7.90}_{-6.63}$
AT2018lni	$1.36^{+0.02}_{-0.02}$	$1.78^{+0.02}_{-0.02}$	$4.34^{+0.03}_{-0.03}$	$44.39^{+0.07}_{-0.04}$	$2.00^{+0.17}_{-0.17}$	$1.96^{+0.07}_{-0.06}$	$-2.51^{+0.50}_{-0.71}$	$43.92^{+0.02}_{-0.02}$	$-0.20^{+0.17}_{-0.13}$	$58477.08^{+2.16}_{-2.81}$
AT2018lna	$1.08^{+0.04}_{-0.04}$	$1.66^{+0.02}_{-0.02}$	$4.50^{+0.02}_{-0.01}$	$44.53^{+0.07}_{-0.04}$	$1.62^{+0.13}_{-0.16}$	$1.70^{+0.05}_{-0.04}$	$-2.20^{+0.38}_{-0.40}$	$43.67^{+0.01}_{-0.01}$	$-0.36^{+0.20}_{-0.16}$	$58507.58^{+1.59}_{-2.49}$
AT2018jbv	$1.40^{+0.07}_{-0.10}$	$2.02^{+0.03}_{-0.03}$	$4.50^{+0.01}_{-0.01}$	$45.57^{+0.09}_{-0.06}$	$1.82^{+0.13}_{-0.15}$	$1.91^{+0.02}_{-0.02}$	$-1.78^{+0.22}_{-0.24}$	$44.69^{+0.02}_{-0.02}$	$-0.46^{+0.05}_{-0.05}$	$58469.19^{+2.47}_{-2.40}$
AT2019cho	$1.33^{+0.06}_{-0.07}$	$1.89^{+0.04}_{-0.03}$	$4.11^{+0.02}_{-0.02}$	$43.85^{+0.05}_{-0.04}$	$2.22^{+0.15}_{-0.18}$	$2.32^{+0.23}_{-0.14}$	$-3.00^{+0.72}_{-0.72}$	$43.69^{+0.03}_{-0.03}$	$0.47^{+0.28}_{-0.31}$	$58552.00^{+2.44}_{-2.32}$
AT2019bhf	$0.87^{+0.07}_{-0.22}$	$1.65^{+0.03}_{-0.03}$	$4.23^{+0.04}_{-0.04}$	$44.03^{+0.08}_{-0.05}$	$1.76^{+0.21}_{-0.25}$	$1.68^{+0.06}_{-0.06}$	$-2.23^{+0.61}_{-0.69}$	$43.76^{+0.04}_{-0.04}$	$-0.09^{+0.20}_{-0.21}$	$58543.90^{+1.47}_{-1.87}$
AT2019azh	$1.13^{+0.01}_{-0.01}$	$1.80^{+0.02}_{-0.02}$	$4.39^{+0.01}_{-0.01}$	$44.37^{+0.03}_{-0.02}$	$1.77^{+0.08}_{-0.09}$	$1.77^{+0.02}_{-0.02}$	$-2.10^{+0.19}_{-0.18}$	$43.81^{+0.01}_{-0.01}$	$0.09^{+0.03}_{-0.03}$	$58566.78^{+1.16}_{-1.75}$
AT2019dsg	$1.37^{+0.08}_{-0.08}$	$1.86^{+0.02}_{-0.02}$	$4.33^{+0.01}_{-0.01}$	$44.29^{+0.10}_{-0.08}$	$1.61^{+0.12}_{-0.13}$	$1.75^{+0.02}_{-0.02}$	$-1.84^{+0.17}_{-0.18}$	$43.57^{+0.02}_{-0.02}$	$-0.23^{+0.04}_{-0.04}$	$58605.38^{+2.48}_{-2.38}$
AT2019ehz	$1.03^{+0.02}_{-0.02}$	$1.64^{+0.01}_{-0.01}$	$4.27^{+0.01}_{-0.01}$	$44.00^{+0.04}_{-0.03}$	$1.51^{+0.09}_{-0.10}$	$1.56^{+0.02}_{-0.03}$	$-1.44^{+0.11}_{-0.11}$	$43.63^{+0.01}_{-0.01}$	$-0.39^{+0.03}_{-0.02}$	$58614.21^{+0.54}_{-0.62}$
AT2019mha	$1.18^{+0.03}_{-0.03}$	$1.23^{+0.03}_{-0.03}$	$4.22^{+0.05}_{-0.04}$	$43.84^{+0.06}_{-0.04}$	$1.64^{+0.16}_{-0.17}$	$1.38^{+0.07}_{-0.07}$	$-3.26^{+0.76}_{-1.03}$	$43.60^{+0.04}_{-0.04}$	$0.95^{+0.70}_{-0.81}$	$58705.23^{+0.98}_{-1.01}$
AT2019meg	$0.98^{+0.02}_{-0.03}$	$1.68^{+0.02}_{-0.02}$	$4.34^{+0.01}_{-0.01}$	$44.24^{+0.02}_{-0.01}$	$1.85^{+0.17}_{-0.17}$	$1.77^{+0.04}_{-0.04}$	$-2.28^{+0.57}_{-0.73}$	$43.80^{+0.01}_{-0.01}$	$-0.06^{+0.21}_{-0.19}$	$58697.91^{+0.73}_{-0.89}$
AT2019lwu	$0.88^{+0.05}_{-0.06}$	$1.45^{+0.03}_{-0.03}$	$4.13^{+0.02}_{-0.02}$	$43.76^{+0.08}_{-0.07}$	$1.90^{+0.13}_{-0.17}$	$1.60^{+0.07}_{-0.07}$	$-3.80^{+0.93}_{-0.84}$	$43.56^{+0.03}_{-0.03}$	$0.47^{+0.32}_{-0.36}$	$58694.28^{+1.17}_{-1.04}$
AT2019qiz	$0.96^{+0.01}_{-0.01}$	$1.48^{+0.01}_{-0.01}$	$4.18^{+0.01}_{-0.01}$	$43.43^{+0.03}_{-0.03}$	$1.20^{+0.05}_{-0.05}$	$1.19^{+0.02}_{-0.02}$	$-1.61^{+0.07}_{-0.06}$	$43.13^{+0.01}_{-0.01}$	$-0.21^{+0.02}_{-0.02}$	$58767.61^{+0.60}_{-0.61}$
AT2019teq	$1.14^{+0.04}_{-0.04}$	$2.08^{+0.06}_{-0.06}$	$4.15^{+0.01}_{-0.01}$	$43.35^{+0.05}_{-0.04}$	$2.21^{+0.18}_{-0.24}$	$2.37^{+0.08}_{-0.08}$	$-2.32^{+0.61}_{-0.65}$	$43.15^{+0.02}_{-0.02}$	$0.29^{+0.09}_{-0.09}$	$58794.31^{+2.40}_{-3.54}$
AT2020pj	$1.04^{+0.05}_{-0.05}$	$1.57^{+0.02}_{-0.02}$	$4.10^{+0.01}_{-0.01}$	$43.26^{+0.06}_{-0.05}$	$1.46^{+0.19}_{-0.18}$	$1.50^{+0.05}_{-0.04}$	$-1.56^{+0.24}_{-0.35}$	$43.07^{+0.03}_{-0.02}$	$-0.02^{+0.17}_{-0.11}$	$58866.68^{+1.10}_{-1.07}$
AT2019vcb	$1.18^{+0.04}_{-0.03}$	$1.56^{+0.01}_{-0.01}$	$4.21^{+0.03}_{-0.03}$	$43.85^{+0.09}_{-0.06}$	$1.59^{+0.14}_{-0.15}$	$1.83^{+0.09}_{-0.09}$	$-2.14^{+0.36}_{-0.44}$	$43.59^{+0.04}_{-0.04}$	$0.63^{+0.23}_{-0.20}$	$58825.55^{+2.27}_{-1.53}$
AT2020ddv	$1.19^{+0.03}_{-0.03}$	$1.79^{+0.02}_{-0.02}$	$4.56^{+0.02}_{-0.02}$	$44.86^{+0.06}_{-0.03}$	$1.60^{+0.17}_{-0.19}$	$1.85^{+0.06}_{-0.05}$	$-1.80^{+0.40}_{-0.40}$	$43.86^{+0.01}_{-0.01}$	$-0.44^{+0.27}_{-0.17}$	$58919.26^{+2.51}_{-2.36}$
AT2020ocn	$1.20^{+0.04}_{-0.04}$	$1.88^{+0.03}_{-0.03}$	$4.47^{+0.02}_{-0.02}$	$43.69^{+0.05}_{-0.03}$	$1.90^{+0.11}_{-0.13}$	$1.99^{+0.07}_{-0.06}$	$-2.27^{+0.36}_{-0.36}$	$42.94^{+0.01}_{-0.01}$	$-0.01^{+0.25}_{-0.19}$	$58989.56^{+2.25}_{-3.16}$
AT2020opy	$1.20^{+0.01}_{-0.01}$	$1.80^{+0.02}_{-0.02}$	$4.30^{+0.01}_{-0.01}$	$44.30^{+0.00}_{-0.00}$	$1.14^{+0.17}_{-0.15}$	$1.83^{+0.02}_{-0.02}$	$-0.83^{+0.14}_{-0.17}$	$43.95^{+0.01}_{-0.01}$	$-0.21^{+0.07}_{-0.07}$	$59088.79^{+0.62}_{-2.51}$
AT2020mot	$1.50^{+0.00}_{-0.00}$	$1.83^{+0.01}_{-0.01}$	$4.27^{+0.01}_{-0.00}$	$43.96^{+0.05}_{-0.05}$	$1.87^{+0.08}_{-0.09}$	$1.83^{+0.02}_{-0.02}$	$-1.86^{+0.21}_{-0.22}$	$43.60^{+0.01}_{-0.01}$	$-0.22^{+0.04}_{-0.03}$	$59072.20^{+4.96}_{-2.86}$
AT2020mbq	$1.01^{+0.02}_{-0.02}$	$1.63^{+0.02}_{-0.01}$	$4.12^{+0.02}_{-0.02}$	$43.47^{+0.05}_{-0.04}$	$1.80^{+0.13}_{-0.16}$	$1.80^{+0.05}_{-0.05}$	$-1.96^{+0.35}_{-0.35}$	$43.36^{+0.03}_{-0.03}$	$0.29^{+0.18}_{-0.19}$	$59023.53^{+0.81}_{-0.80}$
AT2020qhs	$1.45^{+0.04}_{-0.07}$	$1.93^{+0.02}_{-0.02}$	$4.48^{+0.01}_{-0.01}$	$45.36^{+0.08}_{-0.04}$	$1.78^{+0.15}_{-0.13}$	$1.92^{+0.02}_{-0.02}$	$-1.65^{+0.28}_{-0.33}$	$44.56^{+0.01}_{-0.01}$	$-0.55^{+0.08}_{-0.07}$	$59063.64^{+2.52}_{-6.85}$
AT2020riz	$0.97^{+0.04}_{-0.04}$	$1.44^{+0.02}_{-0.02}$	$4.52^{+0.04}_{-0.04}$	$45.74^{+0.13}_{-0.12}$	$1.69^{+0.12}_{-0.16}$	$1.46^{+0.07}_{-0.07}$	$-3.82^{+0.89}_{-0.82}$	$44.68^{+0.01}_{-0.01}$	$-1.36^{+0.33}_{-0.38}$	$59082.56^{+0.62}_{-0.68}$
AT2020wey	$1.09^{+0.02}_{-0.02}$	$1.14^{+0.02}_{-0.02}$	$4.36^{+0.02}_{-0.02}$	$43.29^{+0.02}_{-0.01}$	$0.93^{+0.13}_{-0.12}$	$0.93^{+0.03}_{-0.02}$	$-1.71^{+0.23}_{-0.31}$	$42.81^{+0.02}_{-0.02}$	$-1.54^{+0.31}_{-0.17}$	$59156.58^{+0.43}_{-0.51}$
AT2020zso	$0.84^{+0.05}_{-0.05}$	$1.44^{+0.03}_{-0.03}$	$4.23^{+0.01}_{-0.01}$	$43.76^{+0.02}_{-0.02}$	$1.41^{+0.13}_{-0.12}$	$1.39^{+0.05}_{-0.05}$	$-2.12^{+0.28}_{-0.41}$	$43.53^{+0.02}_{-0.02}$	$-1.75^{+0.20}_{-0.16}$	$59188.04^{+1.37}_{-1.35}$
AT2020ysg	$1.49^{+0.00}_{-0.01}$	$2.02^{+0.02}_{-0.02}$	$4.41^{+0.05}_{-0.04}$	$45.34^{+0.16}_{-0.12}$	$1.53^{+0.15}_{-0.19}$	$2.01^{+0.03}_{-0.03}$	$-1.24^{+0.22}_{-0.26}$	$44.59^{+0.03}_{-0.03}$	$-0.24^{+0.08}_{-0.07}$	$59122.64^{+2.35}_{-2.20}$

Table A.2: The light curve fitting parameters from the 3 different light curve models used.

IAU Name	$\log M_{\rm BH}/M_\odot$ (TDEmass)	$\log M_{\rm BH}$ (MOSFiT)	$M_\star/M_\odot$ (TDEmass)	$M_\star/M_\odot$ (MOSFiT)
AT2018zr	$6.97^{+0.09}_{-0.05}$	$6.53^{+0.11}_{-0.17}$	$1.20^{+0.22}_{-0.06}$	$3.52^{+2.20}_{-1.60}$
AT2018bsi	$6.51^{+0.10}_{-0.07}$	$6.65^{+0.52}_{-0.36}$	$1.20^{+1.30}_{-0.20}$	$0.75^{+1.69}_{-0.44}$
AT2018hco	$6.60^{+0.02}_{-0.02}$	$6.50^{+0.36}_{-0.15}$	$2.40^{+0.75}_{-0.39}$	$1.54^{+0.84}_{-0.63}$
AT2018iih	$6.84^{+0.08}_{-0.08}$	$6.34^{+0.05}_{-0.04}$	$63.00^{+59220.00}_{-31.00}$	$3.98^{+1.51}_{-0.88}$
AT2018hyz	$6.77^{+0.02}_{-0.02}$	$6.58^{+0.05}_{-0.06}$	$4.60^{+13.00}_{-1.80}$	$0.99^{+0.05}_{-0.06}$
AT2018lni	$6.45^{+0.01}_{-0.02}$	$6.60^{+0.12}_{-0.17}$	$5.10^{+2.20}_{-1.10}$	$0.79^{+0.31}_{-0.23}$
AT2018lna	$6.11^{+0.01}_{-0.01}$	$6.83^{+0.19}_{-0.13}$	$5.50^{+3.00}_{-1.40}$	$2.85^{+2.82}_{-1.76}$
AT2018jbv	–	$7.55^{+0.10}_{-0.14}$	–	$4.61^{+2.18}_{-1.63}$
AT2019cho	$7.00^{+0.12}_{-0.13}$	$6.41^{+0.10}_{-0.10}$	$1.50^{+0.63}_{-0.25}$	$2.77^{+1.96}_{-0.92}$
AT2019bhf	$6.77^{+0.03}_{-0.07}$	$6.80^{+0.19}_{-0.21}$	$1.80^{+0.94}_{-0.40}$	$0.83^{+0.86}_{-0.49}$
AT2019azh	$6.34^{+0.01}_{-0.00}$	$7.43^{+0.11}_{-0.31}$	$3.60^{+0.70}_{-0.39}$	$3.59^{+2.55}_{-0.95}$
AT2019dsg	$6.30^{+0.01}_{-0.03}$	$6.86^{+0.09}_{-0.08}$	$2.10^{+1.60}_{-0.67}$	$8.71^{+3.04}_{-6.46}$
AT2019ehz	$6.51^{+0.03}_{-0.03}$	$6.78^{+0.08}_{-0.07}$	$1.20^{+0.14}_{-0.08}$	$9.81^{+2.89}_{-3.41}$
AT2019mha	$6.68^{+0.08}_{-0.08}$	$6.64^{+0.12}_{-0.12}$	$1.10^{+0.20}_{-0.11}$	$5.09^{+2.51}_{-1.89}$
AT2019meg	$6.54^{+0.00}_{-0.01}$	$6.68^{+0.47}_{-0.14}$	$3.10^{+0.34}_{-0.20}$	$0.96^{+1.48}_{-0.54}$
AT2019lwu	$6.79^{+0.20}_{-0.15}$	$6.37^{+0.21}_{-0.20}$	$1.10^{+0.35}_{-0.17}$	$1.10^{+2.17}_{-0.22}$
AT2019qiz	$6.20^{+0.02}_{-0.02}$	$6.31^{+1.06}_{-0.29}$	$0.64^{+0.03}_{-0.03}$	$3.00^{+0.57}_{-0.76}$
AT2019teq	$6.30^{+0.05}_{-0.04}$	$6.05^{+0.37}_{-0.40}$	$0.62^{+0.06}_{-0.06}$	$0.49^{+0.34}_{-0.20}$
AT2020pj	$6.46^{+0.05}_{-0.05}$	$7.98^{+0.02}_{-0.03}$	$0.59^{+0.05}_{-0.05}$	$10.37^{+3.78}_{-4.77}$
AT2019vcb	$6.81^{+0.14}_{-0.12}$	$7.92^{+0.04}_{-0.04}$	$1.20^{+0.52}_{-0.17}$	$12.21^{+2.36}_{-3.33}$
AT2020ddv	$5.96^{+0.00}_{-0.01}$	$7.93^{+0.05}_{-0.13}$	$22.00^{+9.90}_{-4.50}$	$13.08^{+3.88}_{-5.34}$
AT2020ocn	$5.65^{+0.01}_{-0.00}$	$7.06^{+0.16}_{-0.35}$	$0.68^{+0.04}_{-0.03}$	$18.12^{+6.53}_{-6.03}$
AT2020opy	$6.46^{+0.00}_{-0.00}$	$6.85^{+0.16}_{-0.15}$	$3.50^{+0.09}_{-0.02}$	$2.69^{+1.64}_{-0.82}$
AT2020mot	$6.51^{+0.06}_{-0.04}$	$6.67^{+0.17}_{-0.19}$	$1.10^{+0.17}_{-0.10}$	$1.01^{+1.50}_{-0.12}$
AT2020mbq	$6.67^{+0.09}_{-0.08}$	$6.82^{+0.33}_{-0.30}$	$0.79^{+0.07}_{-0.05}$	$2.39^{+2.25}_{-1.20}$
AT2020qhs	–	$7.22^{+0.07}_{-0.07}$	–	$1.01^{+0.42}_{-0.28}$
AT2020riz	–	$7.37^{+0.14}_{-0.10}$	–	$4.99^{+2.89}_{-1.51}$
AT2020wey	$5.63^{+0.00}_{-0.00}$	$7.36^{+0.04}_{-0.03}$	$0.48^{+0.02}_{-0.01}$	$4.34^{+1.96}_{-1.53}$
AT2020zso	$6.72^{+0.03}_{-0.03}$	$6.25^{+0.79}_{-0.16}$	$1.00^{+0.04}_{-0.04}$	$0.97^{+0.06}_{-0.71}$
AT2020ysg	–	$7.02^{+0.08}_{-0.08}$	–	$1.26^{+0.87}_{-0.40}$

Table A.3: The black hole mass and the mass of the disrupted star from `TDEmass` and `MOSFiT`.

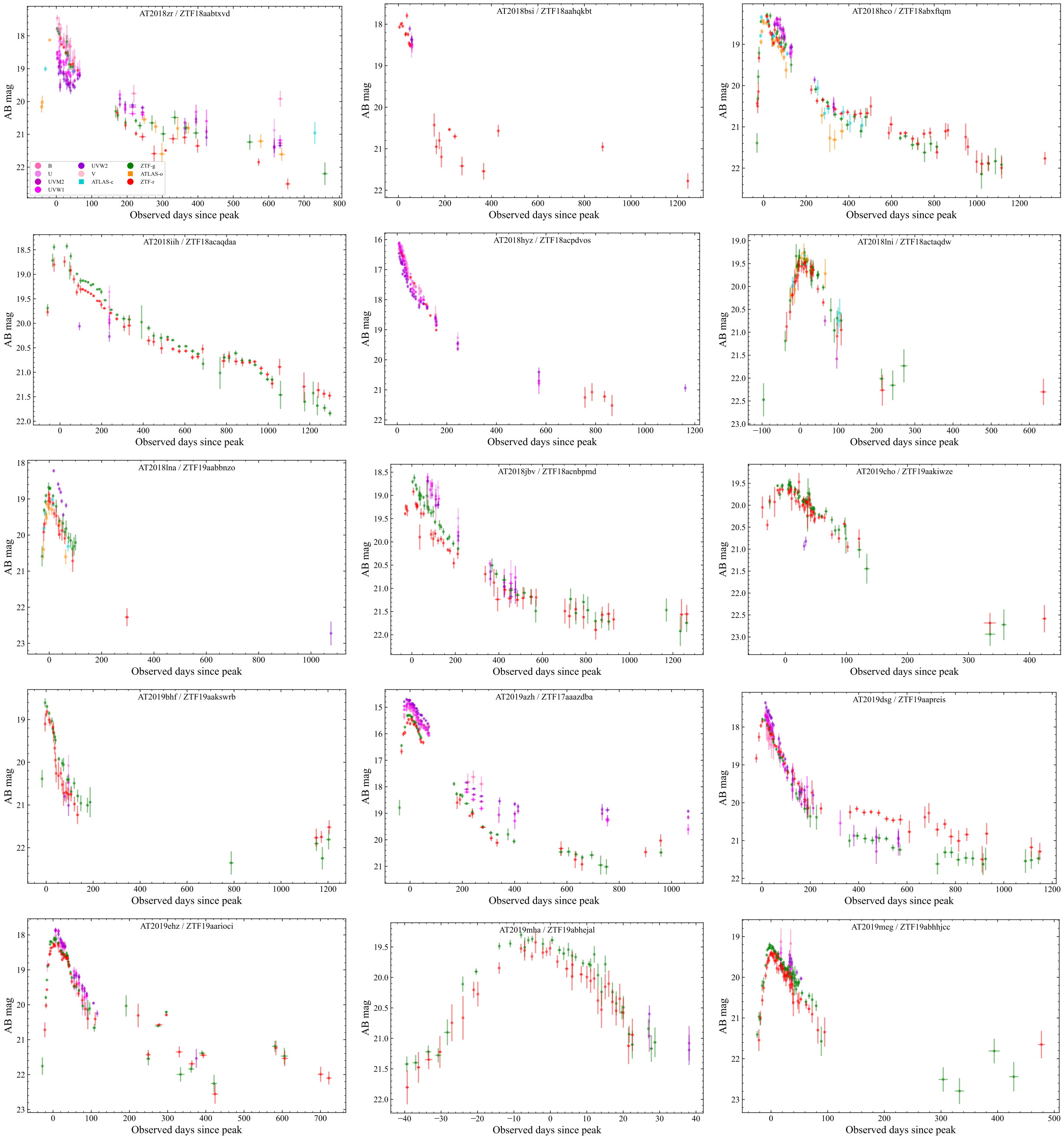

Figure A.4: Optical/UV light curves from ZTF, *Swift*/UVOT, and ATLAS photometry. The light curves are 3-σ detections binned based on time relative to peak, with observations >200 days post-peak binned by 30 days. The legend for the individual bands can be seen in the top left panel.

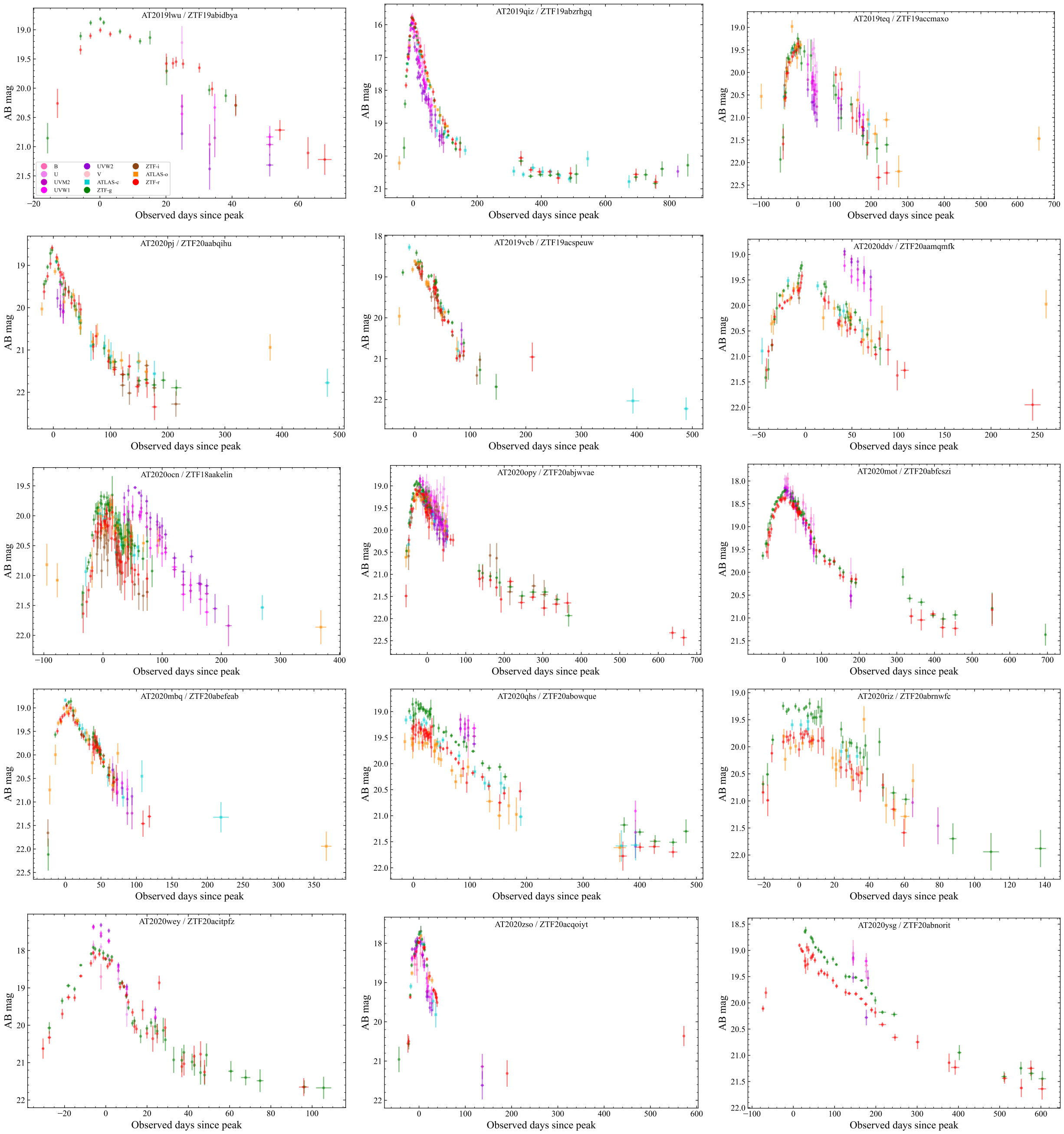

Figure A.5: Optical/UV light curves from ZTF, *Swift*/UVOT, and ATLAS photometry. The light curves are 3-σ detections binned based on time relative to peak, with observations >200 days post-peak binned by 30 days. The legend for the individual bands can be seen in the top left panel.

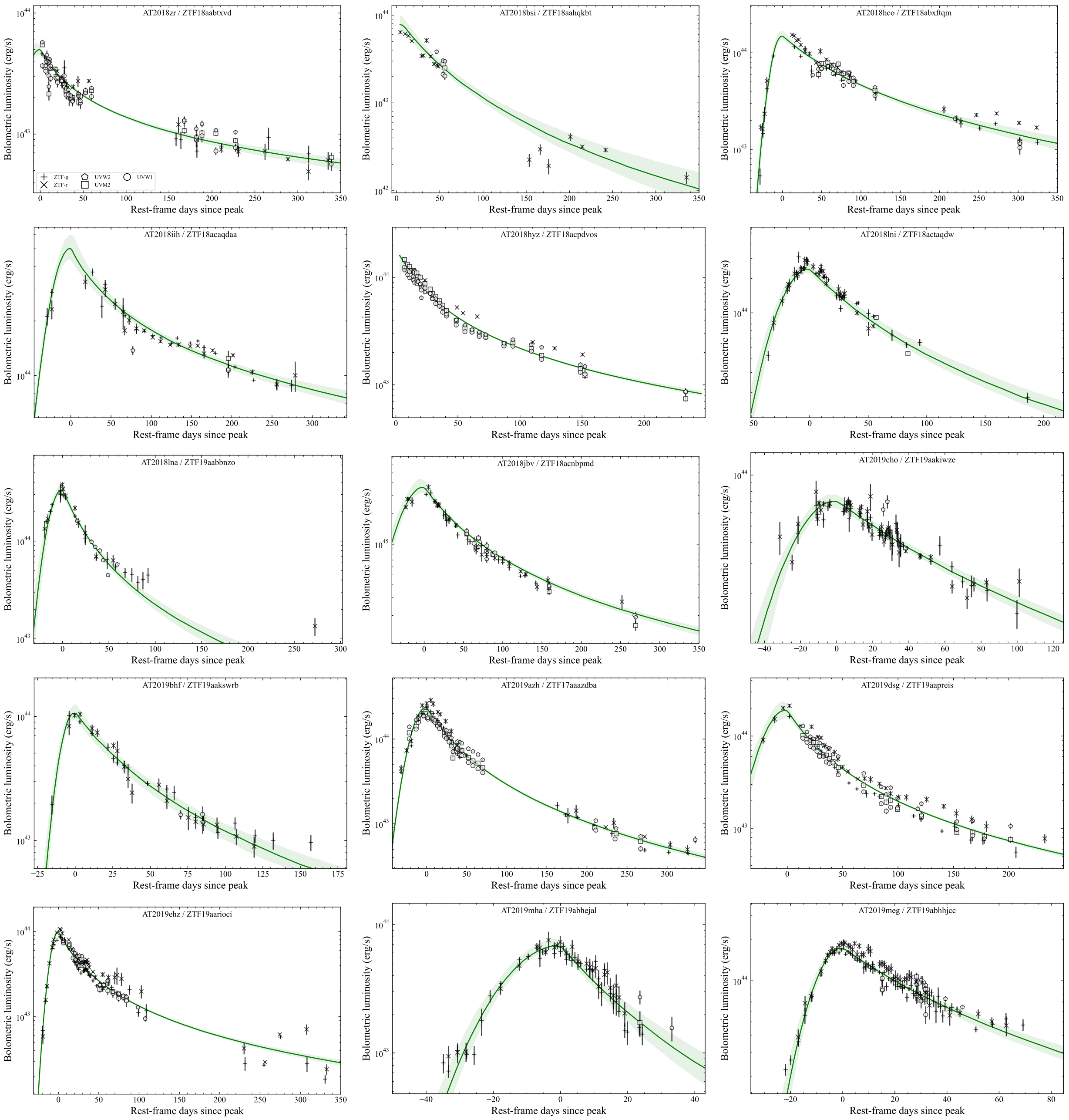

Figure A.6: Gaussian rise and power-law decay fits with flexible temperature fitting, shown with the optical and UV 3-σ detections binned as in Figure A.4. We also show the 1-σ spread in uncertainty of the fit. The legend can be seen in the top left panel.

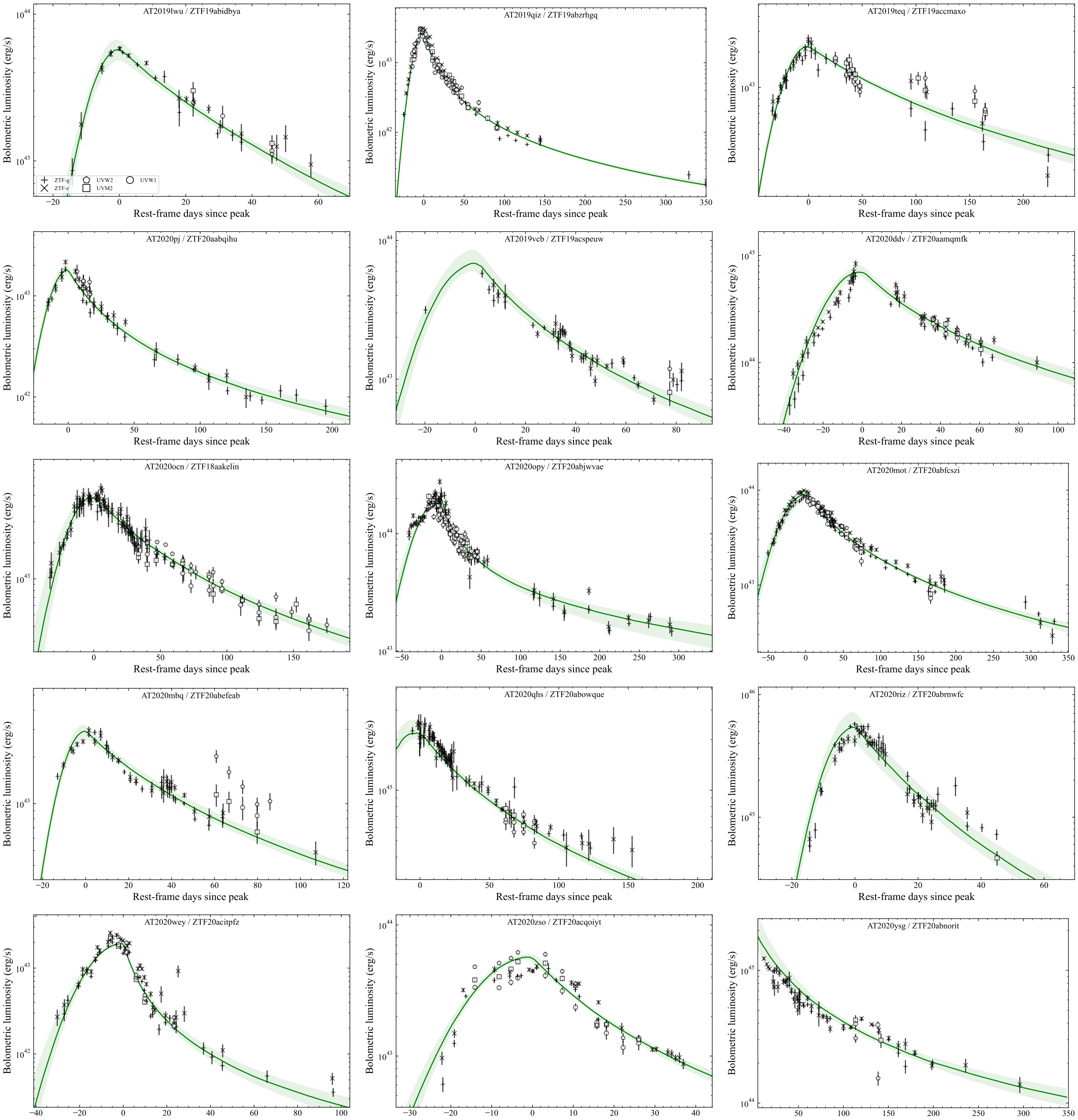

Figure A.7: Gaussian rise and power-law decay fits with flexible temperature fitting, shown with the optical and UV 3-σ detections binned as in Figure A.4. We also show the 1-σ spread in uncertainty of the fit. The legend can be seen in the top left panel.

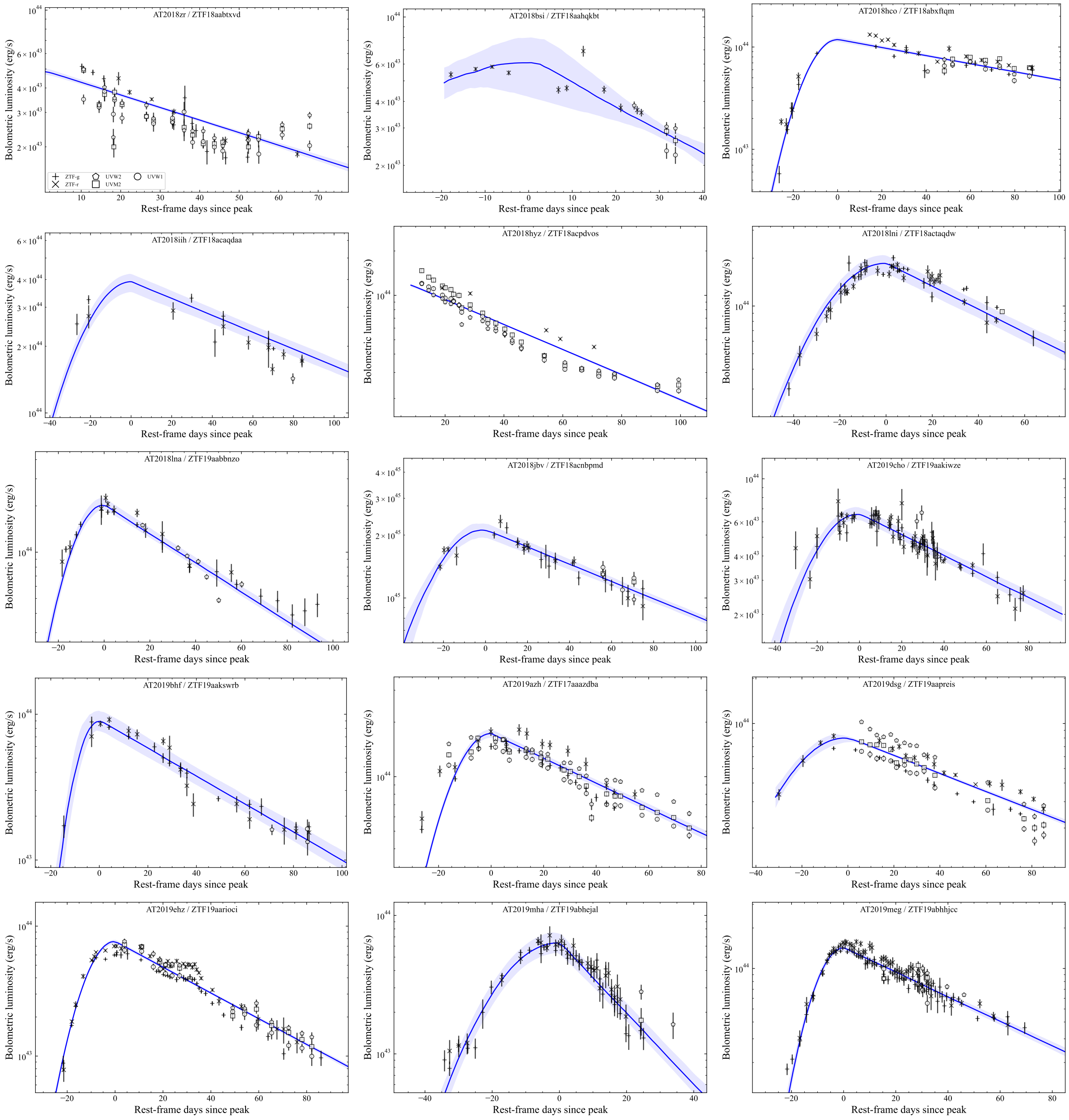

Figure A.8: Gaussian rise and exponential decay fits with fixed temperature, shown with the optical and UV 3-σ detections binned as in Figure A.4. We also show the 1-σ spread in uncertainty of the fit. The legend can be seen in the top left panel.

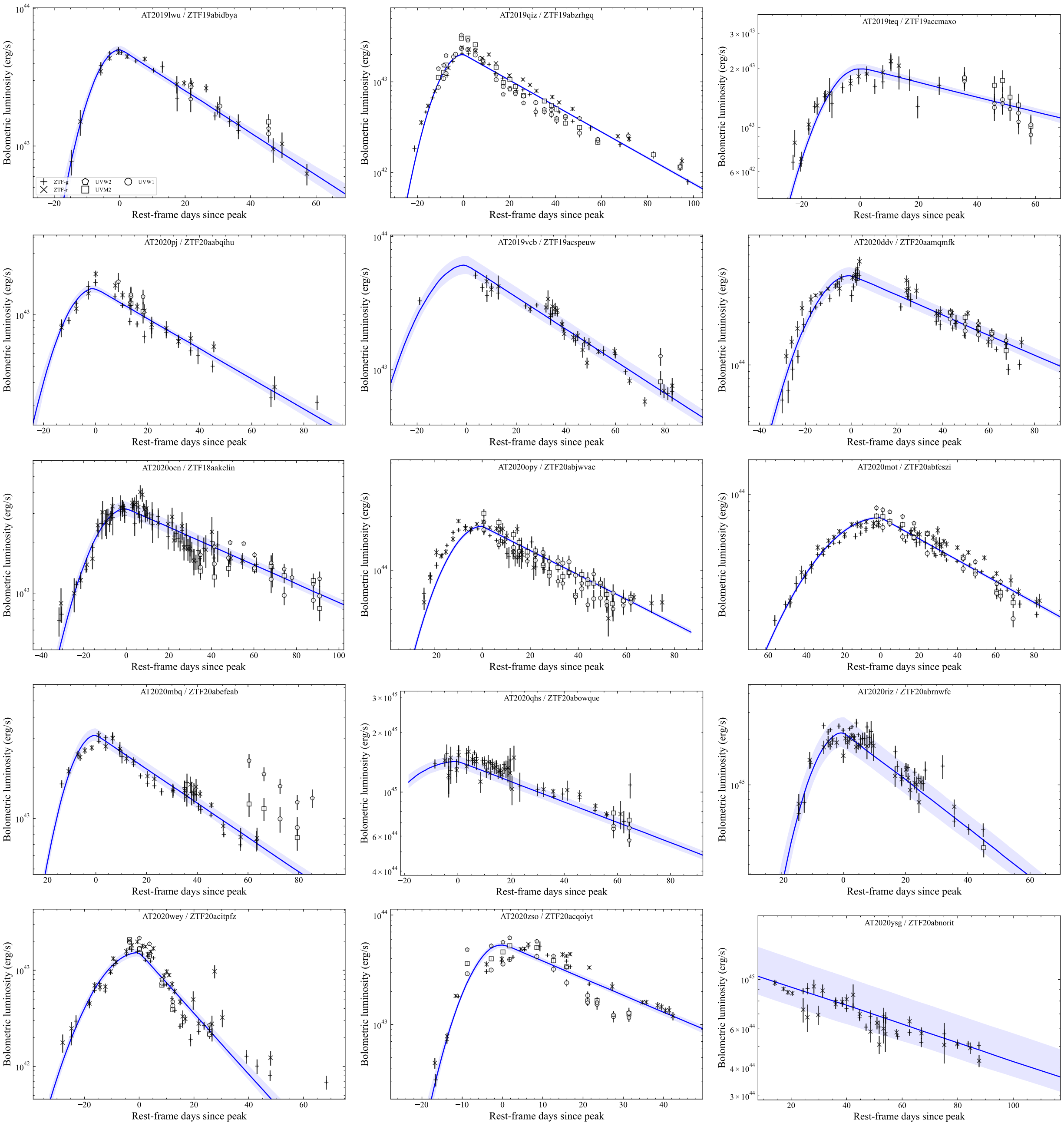

Figure A.9: Gaussian rise and exponential decay fits with fixed temperature, shown with the optical and UV 3-σ detections binned as in Figure A.4. We also show the 1-σ spread in uncertainty of the fit. The legend can be seen in the top left panel.

A.3 Results from Statistical Tests

	$u-r$	$M_{\rm gal}$	p	t_0 ($p=-5/3$)	$L_{\rm peak}$	$R_{\rm peak}$	$T_{\rm peak}$	σ	τ
$u-r$		**0.462 (<0.001)**	0.085 (0.524)	0.149 (0.256)	0.154 (0.241)	0.099 (0.457)	0.209 (0.109)	**0.26 (0.045)**	0.159 (0.227)
$M_{\rm gal}$	**0.462 (<0.001)**		0.007 (0.972)	0.154 (0.241)	**0.361 (0.005)**	0.195 (0.135)	**0.278 (0.031)**	**0.301 (0.019)**	**0.31 (0.016)**
p	0.085 (0.524)	0.007 (0.972)		0.136 (0.304)	0.067 (0.62)	0.067 (0.62)	-0.044 (0.75)	0.172 (0.188)	0.228 (0.08)
t_0 ($p=-5/3$)	0.149 (0.256)	0.154 (0.241)	0.136 (0.304)		0.177 (0.177)	0.214 (0.101)	0.048 (0.724)	**0.421 (<0.001)**	**0.706 (<0.001)**
$L_{\rm peak}$	0.154 (0.241)	**0.361 (0.005)**	0.067 (0.62)	0.177 (0.177)		**0.32 (0.013)**	**0.605 (<0.001)**	0.168 (0.201)	**0.278 (0.031)**
$R_{\rm peak}$	0.099 (0.457)	0.195 (0.135)	0.067 (0.62)	0.214 (0.101)	**0.32 (0.013)**		-0.076 (0.571)	0.094 (0.479)	0.186 (0.155)
$T_{\rm peak}$	0.209 (0.109)	**0.278 (0.031)**	-0.044 (0.75)	0.048 (0.724)	**0.605 (<0.001)**	-0.076 (0.571)		0.131 (0.321)	0.122 (0.357)
σ	**0.26 (0.045)**	**0.301 (0.019)**	0.172 (0.188)	**0.421 (<0.001)**	0.168 (0.201)	0.094 (0.479)	0.131 (0.321)		**0.439 (<0.001)**
τ	0.159 (0.227)	**0.31 (0.016)**	0.228 (0.08)	**0.706 (<0.001)**	**0.278 (0.031)**	0.186 (0.155)	0.122 (0.357)	**0.439 (<0.001)**	

Table A.4: Listed are the Kendall's tau coefficient and associated p-value in parentheses for measured light curve and host galaxy properties. The comparisons which constitute statistically significant ($p < 0.05$) correlations are boldfaced. These correlations and the implications are discussed in Sections 2.6 and 2.8.

	H vs. H+He	H vs. He	H vs. Featureless	H+He vs. He	H+He vs. Featureless	He vs. Featureless	X-ray vs. non-X-ray
τ	> 0.25	0.146	> 0.25	0.118	0.082	> 0.25	0.062
σ	0.082	0.064	0.086	> 0.25	0.114	0.215	> 0.25
$T_{\rm peak}$	> 0.25	0.105	**0.005**	0.102	**0.002**	> 0.25	> 0.25
$R_{\rm peak}$	0.157	0.127	**0.005**	0.134	**0.001**	0.223	> 0.25
$L_{\rm peak}$	> 0.25	0.105	**0.005**	0.054	**0.001**	**0.017**	**0.049**
$M_{\rm gal}$	0.079	**0.009**	**0.005**	0.057	**0.002**	0.163	> 0.25
$u - r$	> 0.25	0.098	**0.025**	**0.003**	**0.001**	0.215	> 0.25
t_0 $(p = -5/3)$	> 0.25	0.219	> 0.25	**0.046**	> 0.25	> 0.25	0.098
p	> 0.25	> 0.25	> 0.25	> 0.25	> 0.25	> 0.25	> 0.25
L_g	> 0.25	0.127	**0.005**	> 0.25	**0.001**	**0.017**	**0.045**

Table A.5: Listed are the p-values from an Anderson-Darling test which tests the null hypothesis that the two samples are drawn from the same parent population. Cases where the null hypothesis can be rejected with $p < 0.05$ are boldfaced.

Appendix B: Supplementary Materials for Chapter 4

B.1 Fits with `GALFIT`

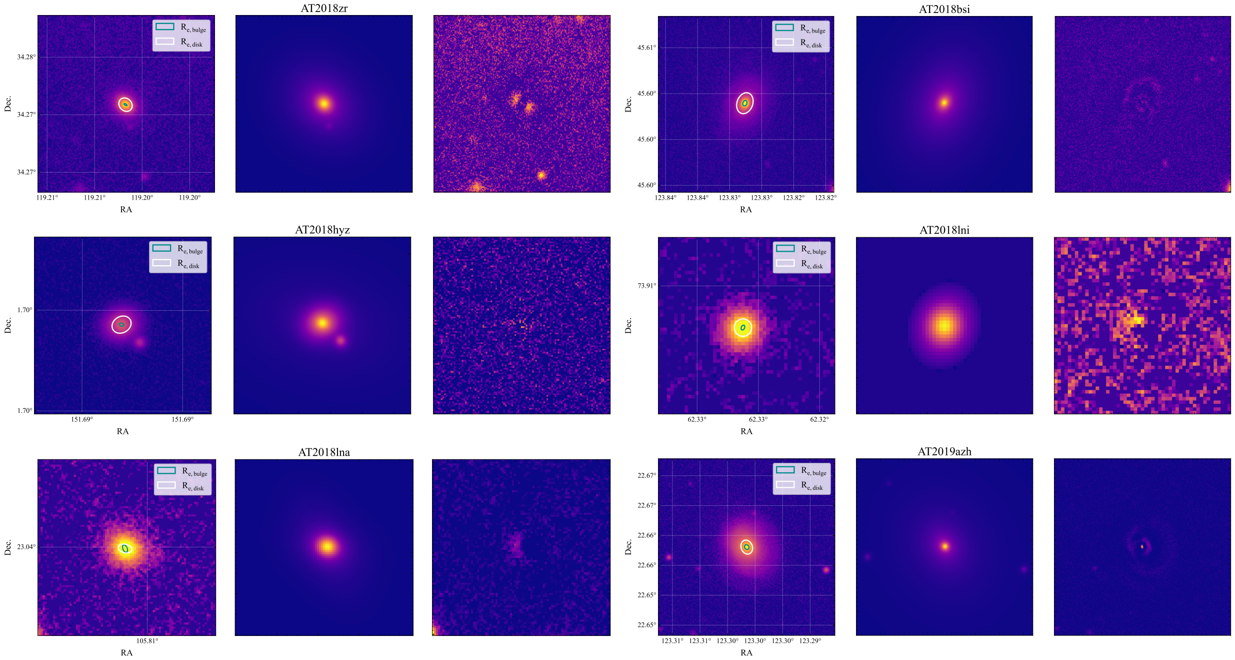
AT2018zr

AT2018bsi

AT2018hyz

AT2018lni

AT2018lna

AT2019azh

Figure B.1: Host galaxy morphological fit to the LMI imaging using `GALFIT`. The fit shown is the bulge+disk fit discussed in Section 4.2.1. `GALFIT` is able to model the host galaxies reasonably well with some residuals showing residual dust lane or spiral arm features which are not as straightforward to model and for the purposes of the study presented in this thesis, are unimportant. In the left panels we show two ellipses representing the fitted bulge effective radius ($R_{\mathrm{e,bulge}}$, cyan) and the disk effective radius (where the relationship between the effective radius and the scale length of the disk is $R_{\mathrm{e,disk}} = 1.678 R_{\mathrm{s,disk}}$, white). The middle panel is the `GALFIT` model and the right panel is the residual.

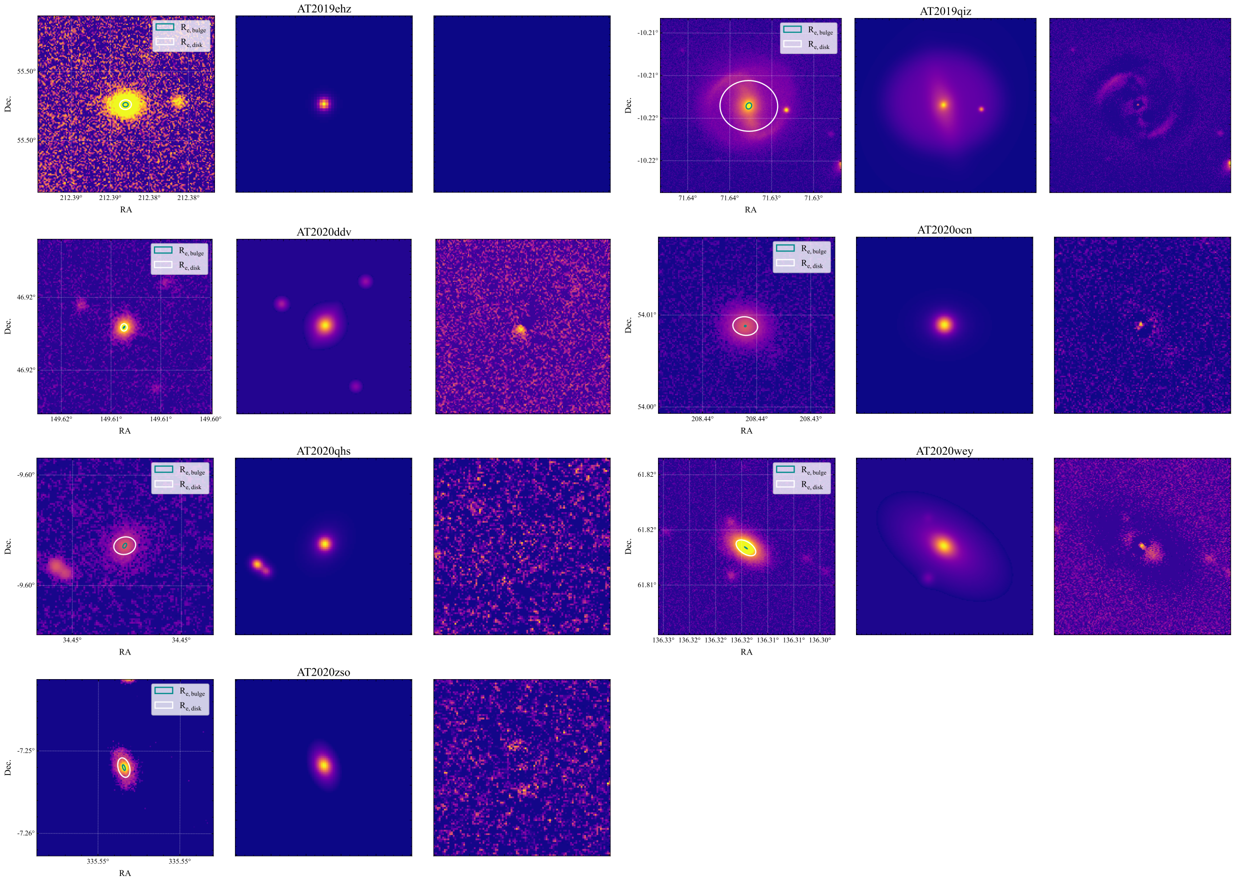

Figure B.2: Host galaxy morphological fit to the LMI imaging using `GALFIT`. The fit shown is the bulge+disk fit discussed in Section 4.2.1. `GALFIT` is able to model the host galaxies reasonably well with some residuals showing residual dust lane or spiral arm features which are not as straightforward to model and for the purposes of the study presented in this thesis, are unimportant. In the left panels we show two ellipses representing the fitted bulge effective radius ($R_{\mathrm{e,bulge}}$, cyan) and the disk effective radius (where the relationship between the effective radius and the scale length of the disk is $R_{\mathrm{e,disk}} = 1.678 R_{\mathrm{s,disk}}$, white). The middle panel is the `GALFIT` model and the right panel is the residual.

B.2 Bulge Spectrum Fits from `ppxf`

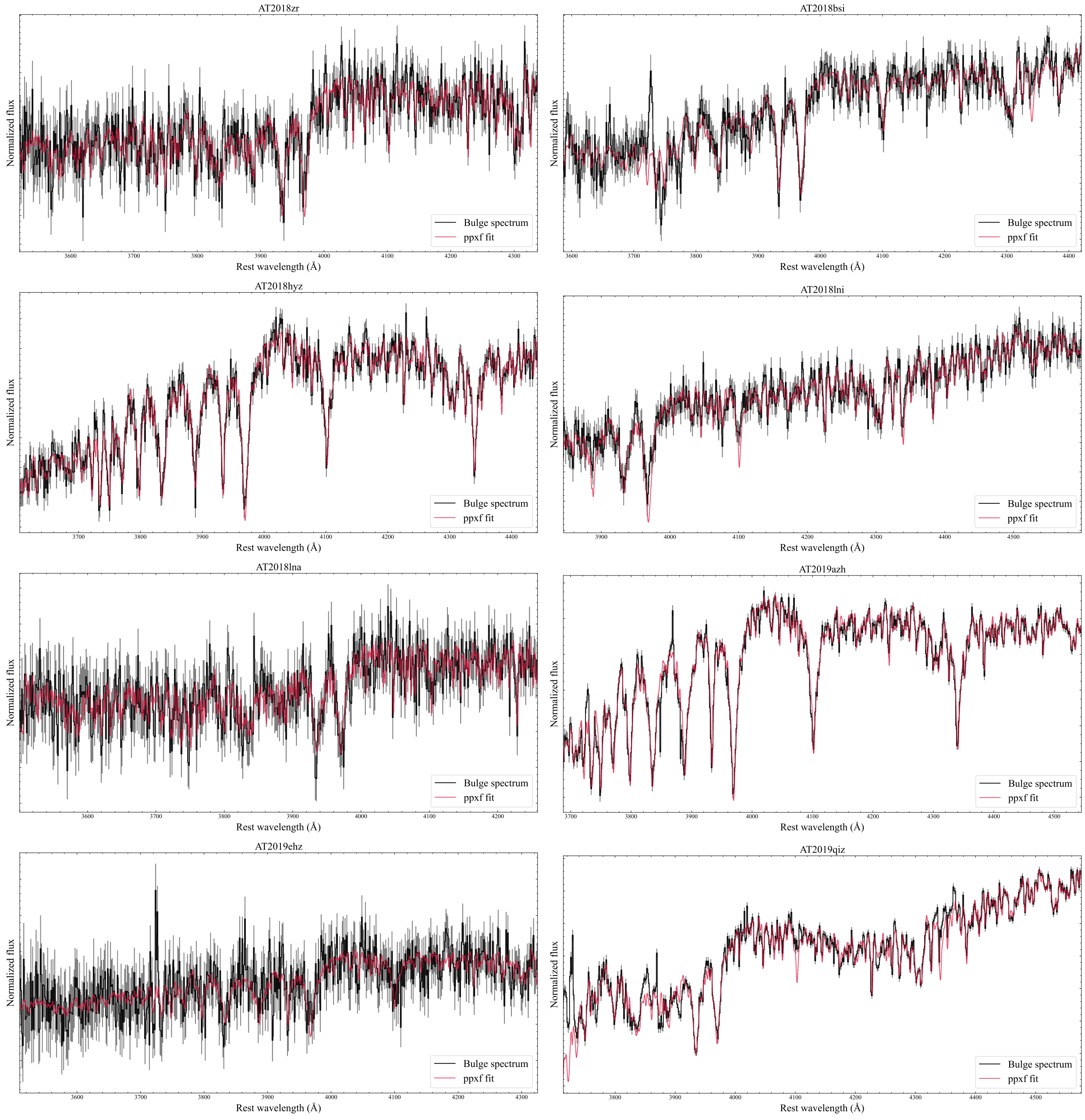
AT2018zr

AT2018bsi

AT2018hyz

AT2018lni

AT2018lna

AT2019azh

AT2019ehz

AT2019qiz

Figure B.3: `ppxf` fits to the bulge spectrum for objects in Chapter 4. The black line is the KCWI spectrum, gray fill is the uncertainty in the spectrum, and red line is the `ppxf` fit.

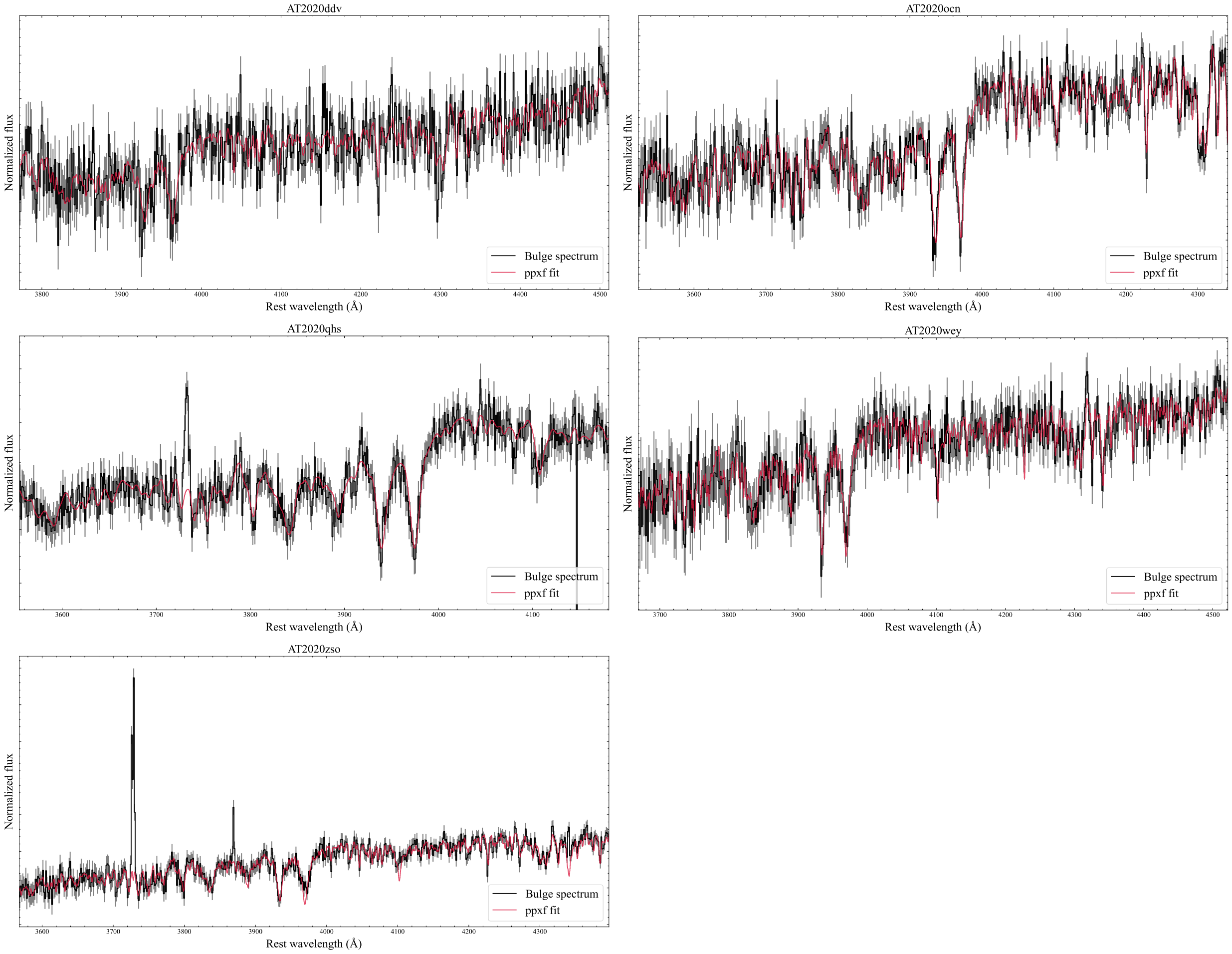

Figure B.4: `ppxf` fits to the bulge spectrum for objects in Chapter 4. The black line is the KCWI spectrum, gray fill is the uncertainty in the spectrum, and red line is the `ppxf` fit.

Appendix C: New Observations of AT2022cmc

MJD	Filter	Mag	eMag	Instrument
59669.87	*r*	22.04	0.11	GITCamera
59676.79	*r*	22.21	0.1	GITCamera
59676.87	*g*	22.02	0.11	GITCamera
59677.1	*g*	22.11	0.06	ALFOSC
59677.11	*r*	22.12	0.06	ALFOSC
59677.13	*i*	22.22	0.07	ALFOSC
59689.98	*r*	22.28	0.16	IO:O
59699.95	*g*	22.51	0.17	IO:O
59703.96	*g*	22.58	0.07	ALFOSC
59703.97	*r*	22.5	0.08	ALFOSC
59703.99	*i*	22.53	0.1	ALFOSC
59721.99	*g*	23.09	0.1	ALFOSC
59722.0	*r*	23.03	0.11	ALFOSC
59722.02	*i*	22.94	0.12	ALFOSC
59732.22	*g*	23.18	0.06	LMI

Continued on next page

MJD	Filter	Mag	eMag	Instrument
59732.22	*r*	23.06	0.06	LMI
59732.22	*i*	22.88	0.06	LMI
59752.98	*g*	23.82	0.14	ALFOSC
59753.0	*r*	23.48	0.12	ALFOSC
59753.01	*i*	23.46	0.14	ALFOSC
59767.91	*r*	25.8	0.58	ALFOSC
59767.91	*g*	26.77	99.0	ALFOSC
59767.92	*i*	25.41	0.48	ALFOSC
59769.0	*i*	23.2	0.2	LMI
59778.9	*r*	25.05	0.26	ALFOSC
59780.93	*i*	24.44	0.26	ALFOSC
59674.0	*u*	22.14	0.02	LBC
59674.0	*g*	22.15	0.02	LBC
59674.0	*r*	22.08	0.03	LBC
59674.0	*i*	22.1	0.04	LBC
59674.0	*z*	22.2	0.07	LBC
59690.0	*u*	22.59	0.07	LBC
59690.0	*g*	22.36	0.06	LBC
59690.0	*r*	22.36	0.06	LBC
59690.0	*i*	22.35	0.08	LBC

Continued on next page

MJD	Filter	Mag	eMag	Instrument
59690.0	z	22.51	0.15	LBC
59729.0	u	23.36	0.05	LBC
59729.0	g	23.16	0.04	LBC
59729.0	r	22.94	0.04	LBC
59729.0	i	22.94	0.08	LBC
59729.0	z	22.82	0.16	LBC
59768.0	u	24.71	0.35	LBC
59768.0	g	24.2	0.19	LBC
59768.0	r	23.79	0.15	LBC
59768.0	i	23.61	0.16	LBC
59768.0	z	23.21	0.21	LBC
59732.2	g	23.18	0.06	LMI
59732.21	r	23.06	0.06	LMI
59732.22	i	22.88	0.06	LMI
59769.23	i	23.19	0.14	LMI

Table C.1: New observations of AT2022cmc since its discovery in Andreoni et al. (2022). These observations are presented in Chapter 5.

Appendix D: Facilities and Software Used in this Thesis

D.1 Facilities

The data analysis in Chapter 4 was performed on the Yorp and Astra clusters administered by the Center for Theory and Computation, part of the Department of Astronomy at the University of Maryland. The data presented here were obtained in part with ALFOSC, which is provided by the Instituto de Astrofisica de Andalucia (IAA) under a joint agreement with the University of Copenhagen and NOT. This thesis made use of the Lowell Discovery Telescope (LDT) at Lowell Observatory. Lowell is a private, non-profit institution dedicated to astrophysical research and public appreciation of astronomy and operates the LDT in partnership with Boston University, the University of Maryland, the University of Toledo, Northern Arizona University and Yale University. The Large Monolithic Imager was built by Lowell Observatory using funds provided by the National Science Foundation (AST-1005313). The upgrade of the DeVeny optical spectrograph has been funded by a generous grant from John and Ginger Giovale and by a grant from the Mt. Cuba Astronomical Foundation.

1. ATLAS
2. ZTF
3. Gemini: GMOS

4. GIT
5. LBT: LBC
6. Lick Observatory: Kast
7. LDT: LMI, DeVeny
8. LT: IO:O
9. Keck-II: KCWI, LRIS, DEIMOS
10. NOT: ALFOSC
11. Swift: XRT, UVOT
12. VLT: Xshooter

D.2 Software

1. Astroplan (Morris et al., 2018)
2. Astropy (Astropy Collaboration et al., 2013, 2018, 2022)
3. astroquery (Ginsburg et al., 2019)
4. corner (Foreman-Mackey, 2016)
5. cwitools (O'Sullivan & Chen, 2020)
6. emcee (Foreman-Mackey et al., 2013)
7. FSPS (Conroy et al., 2009)

8. GALFIT (Peng et al., 2002)
9. GIM2D (Simard, 2010)
10. GIST (Bittner et al., 2019)
11. KCWI-DRP (Neill et al., 2023)
12. matplotlib (Hunter, 2007)
13. MOSFiT (Guillochon et al., 2017)
14. NumPy (Harris et al., 2020)
15. Pandas (pandas development team, 2020)
16. PypeIt (Prochaska et al., 2020)
17. ppxf (Cappellari, 2023; Cappellari & Copin, 2003)
18. Prospector (Johnson et al., 2021)
19. PSFEx (Bertin, 2011)
20. SciPy (Virtanen et al., 2020)
21. SciServer (Taghizadeh-Popp et al., 2020)
22. Source-Extractor (Bertin & Arnouts, 1996)
23. specitils (Astropy-Specutils Development Team, 2019)
24. TDEmass (Ryu et al., 2020)
25. ztfquery (Rigault, 2018)

Bibliography

Anderson, T. W., & Darling, D. A. 1954, Journal of the American Statistical Association, 49, 765

Andreoni, I., Coughlin, M. W., Perley, D. A., et al. 2022, Nature, 612, 430, doi: `10.1038/s41586-022-05465-8`

Arcavi, I. 2018, Transient Name Server Classification Report, 2018-1764, 1

Arcavi, I., Burke, J., Nyiha, I., et al. 2020, Transient Name Server Classification Report, 2020-3228, 1

Arcavi, I., Gal-Yam, A., Sullivan, M., et al. 2014, The Astrophysical Journal, 793, 38, doi: `10.1088/0004-637X/793/1/38`

Arnaud, K. A. 1996, in Astronomical Society of the Pacific Conference Series, Vol. 101, Astronomical Data Analysis Software and Systems V, ed. G. H. Jacoby & J. Barnes, 17

Astropy Collaboration, Robitaille, T. P., Tollerud, E. J., et al. 2013, Astronomy and Astrophysics, 558, A33, doi: `10.1051/0004-6361/201322068`

Astropy Collaboration, Price-Whelan, A. M., Sipőcz, B. M., et al. 2018, The Astronomical Journal, 156, 123, doi: `10.3847/1538-3881/aabc4f`

Astropy Collaboration, Price-Whelan, A. M., Lim, P. L., et al. 2022, The Astrophysical Journal, 935, 167, doi: `10.3847/1538-4357/ac7c74`

Astropy-Specutils Development Team. 2019, Specutils: Spectroscopic analysis and reduction, Astrophysics Source Code Library, record ascl:1902.012

Auchettl, K., Guillochon, J., & Ramirez-Ruiz, E. 2017, The Astrophysical Journal, 838, 149, doi: `10.3847/1538-4357/aa633b`

Bade, N., Komossa, S., & Dahlem, M. 1996, Astronomy and Astrophysics, 309, L35

Baldwin, J. A., Phillips, M. M., & Terlevich, R. 1981, Publications of the Astronomical Society of the Pacific, 93, 5, doi: `10.1086/130766`

Bellm, E. C., Kulkarni, S. R., Graham, M. J., et al. 2019a, Publications of the Astronomical Society of the Pacific, 131, 018002, doi: `10.1088/1538-3873/aaecbe`

Bellm, E. C., Kulkarni, S. R., Barlow, T., et al. 2019b, Publications of the Astronomical Society of the Pacific, 131, 068003, doi: `10.1088/1538-3873/ab0c2a`

Berger, E., Zauderer, A., Pooley, G. G., et al. 2012, The Astrophysical Journal, 748, 36, doi: `10.1088/0004-637X/748/1/36`

Bertin, E. 2011, Astronomical Society of the Pacific Conference Series, Vol. 442, Automated Morphometry with SExtractor and PSFEx, 435

Bertin, E., & Arnouts, S. 1996, Astronomy and Astrophysics, Supplement, 117, 393, doi: `10.1051/aas:1996164`

Bittner, A., Falcón-Barroso, J., Nedelchev, B., et al. 2019, Astronomy and Astrophysics, 628, A117, doi: `10.1051/0004-6361/201935829`

Blagorodnova, N., Gezari, S., Hung, T., et al. 2017, The Astrophysical Journal, 844, 46, doi: `10.3847/1538-4357/aa7579`

Blagorodnova, N., Neill, J. D., Walters, R., et al. 2018, Publications of the Astronomical Society of the Pacific, 130, 035003, doi: `10.1088/1538-3873/aaa53f`

Blagorodnova, N., Cenko, S. B., Kulkarni, S. R., et al. 2019, The Astrophysical Journal, 873, 92, doi: `10.3847/1538-4357/ab04b0`

Bloom, J. S., Giannios, D., Metzger, B. D., et al. 2011, Science, 333, 203, doi: `10.1126/science.1207150`

Bressan, A., Marigo, P., Girardi, L., et al. 2012, Monthly Notices of the Royal Astronomical Society, 427, 127, doi: `10.1111/j.1365-2966.2012.21948.x`

Brinchmann, J., Charlot, S., White, S. D. M., et al. 2004, Monthly Notices of the Royal Astronomical Society, 351, 1151, doi: `10.1111/j.1365-2966.2004.07881.x`

Brown, G. C., Levan, A. J., Stanway, E. R., et al. 2015, Monthly Notices of the Royal Astronomical Society, 452, 4297, doi: `10.1093/mnras/stv1520`

—. 2017, Monthly Notices of the Royal Astronomical Society, 472, 4469, doi: `10.1093/mnras/stx2193`

Bryant, J. J., Owers, M. S., Robotham, A. S. G., et al. 2015, Monthly Notices of the Royal Astronomical Society, 447, 2857, doi: `10.1093/mnras/stu2635`

Burrows, D. N., Hill, J. E., Nousek, J. A., et al. 2005, Space Science Reviews, 120, 165, doi: `10.1007/s11214-005-5097-2`

Burrows, D. N., Kennea, J. A., Ghisellini, G., et al. 2011, Nature, 476, 421, doi: `10.1038/nature10374`

Calzetti, D., Armus, L., Bohlin, R. C., et al. 2000, The Astrophysical Journal, 533, 682, doi: `10.1086/308692`

Cappellari, M. 2017, Monthly Notices of the Royal Astronomical Society, 466, 798, doi: `10.1093/mnras/stw3020`

—. 2023, Monthly Notices of the Royal Astronomical Society, 526, 3273, doi: `10.1093/mnras/stad2597`

Cappellari, M., & Copin, Y. 2003, Monthly Notices of the Royal Astronomical Society, 342, 345, doi: `10.1046/j.1365-8711.2003.06541.x`

Cappellari, M., Emsellem, E., Bacon, R., et al. 2007, Monthly Notices of the Royal Astronomical Society, 379, 418, doi: `10.1111/j.1365-2966.2007.11963.x`

Cendes, Y., Eftekhari, T., Berger, E., & Polisensky, E. 2021, The Astrophysical Journal, 908, 125, doi: `10.3847/1538-4357/abd323`

Cendes, Y., Berger, E., Alexander, K. D., et al. 2023, arXiv e-prints, arXiv:2308.13595, doi: `10.48550/arXiv.2308.13595`

Cenko, S. B., Krimm, H. A., Horesh, A., et al. 2012, The Astrophysical Journal, 753, 77, doi: `10.1088/0004-637X/753/1/77`

Charalampopoulos, P., Leloudas, G., Malesani, D. B., et al. 2022, Astronomy and Astrophysics, 659, A34, doi: `10.1051/0004-6361/202142122`

Chornock, R., Berger, E., Gezari, S., et al. 2014, The Astrophysical Journal, 780, 44, doi: `10.1088/0004-637X/780/1/44`

Conroy, C., Gunn, J. E., & White, M. 2009, The Astrophysical Journal, 699, 486, doi: `10.1088/0004-637X/699/1/486`

Croom, S. M., Owers, M. S., Scott, N., et al. 2021, Monthly Notices of the Royal Astronomical Society, 505, 991, doi: `10.1093/mnras/stab229`

Crumley, P., Lu, W., Santana, R., et al. 2016, Monthly Notices of the Royal Astronomical Society, 460, 396, doi: `10.1093/mnras/stw967`

Dai, L., McKinney, J. C., & Miller, M. C. 2015, The Astrophysical Journal Letters, 812, L39, doi: `10.1088/2041-8205/812/2/L39`

Dai, L., McKinney, J. C., Roth, N., Ramirez-Ruiz, E., & Miller, M. C. 2018, The Astrophysical Journal Letters, 859, L20, doi: `10.3847/2041-8213/aab429`

De Colle, F., Guillochon, J., Naiman, J., & Ramirez-Ruiz, E. 2012, The Astrophysical Journal, 760, 103, doi: `10.1088/0004-637X/760/2/103`

De Colle, F., & Lu, W. 2020, New Astronomy Review, 89, 101538, doi: `10.1016/j.newar.2020.101538`

de Vaucouleurs, G. 1948, Annales d'Astrophysique, 11, 247

Dong, S., Bose, S., Chen, P., et al. 2018, The Astronomer's Telegram, 12198, 1

Dressler, A. 1989, in Active Galactic Nuclei, ed. D. E. Osterbrock & J. S. Miller, Vol. 134, 217

Dressler, A., & Gunn, J. E. 1983, The Astrophysical Journal, 270, 7, doi: `10.1086/161093`

Duev, D. A., Mahabal, A., Masci, F. J., et al. 2019, Monthly Notices of the Royal Astronomical Society, 489, 3582, doi: `10.1093/mnras/stz2357`

Eftekhari, T., Berger, E., Zauderer, B. A., Margutti, R., & Alexander, K. D. 2018, The Astrophysical Journal, 854, 86, doi: `10.3847/1538-4357/aaa8e0`

Evans, C. R., & Kochanek, C. S. 1989, The Astrophysical Journal Letters, 346, L13, doi: `10.1086/185567`

Evans, P. A., Beardmore, A. P., Page, K. L., et al. 2009, Monthly Notices of the Royal Astronomical Society, 397, 1177, doi: `10.1111/j.1365-2966.2009.14913.x`

Fabian, A. C. 2012, Annual Review of Astronomy and Astrophysics, 50, 455, doi: `10.1146/annurev-astro-081811-125521`

Ferrarese, L., & Merritt, D. 2000, The Astrophysical Journal Letters, 539, L9, doi: `10.1086/312838`

Flesch, E. W. 2015, Publications of the Astronomical Society of Australia, 32, e010, doi: `10.1017/pasa.2015.10`

Foreman-Mackey, D. 2016, The Journal of Open Source Software, 1, 24, doi: `10.21105/joss.00024`

Foreman-Mackey, D., Hogg, D. W., Lang, D., & Goodman, J. 2013, Publications of the Astronomical Society of the Pacific, 125, 306, doi: `10.1086/670067`

Frank, J., & Rees, M. J. 1976, Monthly Notices of the Royal Astronomical Society, 176, 633, doi: `10.1093/mnras/176.3.633`

Frederick, S., Gezari, S., Cenko, S. B., et al. 2019, The Astronomer's Telegram, 12543, 1

French, K. D., Arcavi, I., & Zabludoff, A. 2016, The Astrophysical Journal Letters, 818, L21, doi: `10.3847/2041-8205/818/1/L21`

—. 2017, The Astrophysical Journal, 835, 176, doi: `10.3847/1538-4357/835/2/176`

French, K. D., Arcavi, I., Zabludoff, A. I., et al. 2020a, The Astrophysical Journal, 891, 93, doi: `10.3847/1538-4357/ab7450`

French, K. D., Wevers, T., Law-Smith, J., Graur, O., & Zabludoff, A. I. 2020b, Space Science Reviews, 216, 32, doi: `10.1007/s11214-020-00657-y`

French, K. D., & Zabludoff, A. I. 2018, The Astrophysical Journal, 868, 99, doi: `10.3847/1538-4357/aaea64`

Gal-Yam, A. 2012, Science, 337, 927, doi: `10.1126/science.1203601`

Gaskell, C. M., & Rojas Lobos, P. A. 2014, Monthly Notices of the Royal Astronomical Society, 438, L36, doi: `10.1093/mnrasl/slt154`

Gebhardt, K., Bender, R., Bower, G., et al. 2000, The Astrophysical Journal Letters, 539, L13, doi: `10.1086/312840`

Gehrels, N., Chincarini, G., Giommi, P., et al. 2004, The Astrophysical Journal, 611, 1005, doi: `10.1086/422091`

Generozov, A., Mimica, P., Metzger, B. D., et al. 2017, Monthly Notices of the Royal Astronomical Society, 464, 2481, doi: `10.1093/mnras/stw2439`

Gezari, S. 2021, Annual Review of Astronomy and Astrophysics, 59, 21, doi: `10.1146/annurev-astro-111720-030029`

Gezari, S., Cenko, S. B., & Arcavi, I. 2017, The Astrophysical Journal Letters, 851, L47, doi: `10.3847/2041-8213/aaa0c2`

Gezari, S., van Velzen, S., Cenko, S. B., et al. 2018, The Astronomer's Telegram, 12035, 1

Gezari, S., van Velzen, S., Perley, D. A., et al. 2019, The Astronomer's Telegram, 12789, 1

Gezari, S., Velzen, S. v., Stern, D., et al. 2020a, The Astronomer's Telegram, 13859, 1

Gezari, S., Chornock, R., Rest, A., et al. 2012, Nature, 485, 217, doi: `10.1038/nature10990`

Gezari, S., van Velzen, S., Goldstein, D., et al. 2020b, The Astronomer's Telegram, 13655, 1

Gezari, S., Hammerstein, E., Yao, Y., et al. 2021, Transient Name Server AstroNote, 103, 1

Giannios, D., & Metzger, B. D. 2011, Monthly Notices of the Royal Astronomical Society, 416, 2102, doi: `10.1111/j.1365-2966.2011.19188.x`

Ginsburg, A., Sipőcz, B. M., Brasseur, C. E., et al. 2019, The Astronomical Journal, 157, 98, doi: `10.3847/1538-3881/aafc33`

Girardi, L., Bressan, A., Bertelli, G., & Chiosi, C. 2000, Astronomy and Astrophysics, Supplement, 141, 371, doi: `10.1051/aas:2000126`

Gomez, S., Villar, V. A., Berger, E., et al. 2023, The Astrophysical Journal, 949, 113, doi: `10.3847/1538-4357/acc535`

Graham, M. J., Kulkarni, S. R., Bellm, E. C., et al. 2019, Publications of the Astronomical Society of the Pacific, 131, 078001, doi: `10.1088/1538-3873/ab006c`

Graur, O., French, K. D., Zahid, H. J., et al. 2018, The Astrophysical Journal, 853, 39, doi: `10.3847/1538-4357/aaa3fd`

Greene, J. E., Strader, J., & Ho, L. C. 2020, Annual Review of Astronomy and Astrophysics, 58, 257, doi: `10.1146/annurev-astro-032620-021835`

Greiner, J., Schwarz, R., Zharikov, S., & Orio, M. 2000, Astronomy and Astrophysics, 362, L25. `https://arxiv.org/abs/astro-ph/0009430`

Grupe, D., Thomas, H.-C., & Leighly, K. M. 1999, Astronomy and Astrophysics, 350, L31

Guillochon, J., Manukian, H., & Ramirez-Ruiz, E. 2014, The Astrophysical Journal, 783, 23, doi: `10.1088/0004-637X/783/1/23`

Guillochon, J., Nicholl, M., Villar, V. A., et al. 2018, The Astrophysical Journal Supplement, 236, 6, doi: `10.3847/1538-4365/aab761`

Guillochon, J., Parrent, J., Kelley, L. Z., & Margutti, R. 2017, The Astrophysical Journal, 835, 64, doi: `10.3847/1538-4357/835/1/64`

Guillochon, J., & Ramirez-Ruiz, E. 2015, The Astrophysical Journal, 809, 166, doi: `10.1088/0004-637X/809/2/166`

Gültekin, K., Richstone, D. O., Gebhardt, K., et al. 2009, The Astrophysical Journal, 698, 198, doi: `10.1088/0004-637X/698/1/198`

Guolo, M., Gezari, S., Yao, Y., et al. 2023, arXiv e-prints, arXiv:2308.13019, doi: `10.48550/arXiv.2308.13019`

Hammerstein, E. 2020, Transient Name Server Classification Report, 2020-2829, 1

Hammerstein, E., Gezari, S., van Velzen, S., et al. 2021a, The Astrophysical Journal Letters, 908, L20, doi: `10.3847/2041-8213/abdcb4`

Hammerstein, E., Gezari, S., Velzen, S. V., et al. 2021b, Transient Name Server Classification Report, 2021-262, 1

Hammerstein, E., van Velzen, S., Gezari, S., et al. 2023a, The Astrophysical Journal, 942, 9, doi: `10.3847/1538-4357/aca283`

Hammerstein, E., Cenko, S. B., Gezari, S., et al. 2023b, The Astrophysical Journal, 957, 86, doi: `10.3847/1538-4357/acfb84`

Harris, C. R., Millman, K. J., van der Walt, S. J., et al. 2020, Nature, 585, 357, doi: `10.1038/s41586-020-2649-2`

Hatsukade, B., Tominaga, N., Hayashi, M., et al. 2018, The Astrophysical Journal, 857, 72, doi: `10.3847/1538-4357/aab616`

HI4PI Collaboration, Ben Bekhti, N., Flöer, L., et al. 2016, Astronomy and Astrophysics, 594, A116, doi: `10.1051/0004-6361/201629178`

Hill, J. M., Green, R. F., Slagle, J. H., et al. 2008, in Society of Photo-Optical Instrumentation Engineers (SPIE) Conference Series, Vol. 7012, Ground-based and Airborne Telescopes II, ed. L. M. Stepp & R. Gilmozzi, 701203, doi: `10.1117/12.790065`

Hills, J. G. 1975, Nature, 254, 295, doi: `10.1038/254295a0`

Hinkle, J. T., Holoien, T. W. S., Shappee, B. J., et al. 2020, The Astrophysical Journal Letters, 894, L10, doi: `10.3847/2041-8213/ab89a2`

Hinkle, J. T., Holoien, T. W. S., Auchettl, K., et al. 2021, Monthly Notices of the Royal Astronomical Society, 500, 1673, doi: `10.1093/mnras/staa3170`

Ho, L. C. 2008, Annual Review of Astronomy and Astrophysics, 46, 475, doi: `10.1146/annurev.astro.45.051806.110546`

Holoien, T. W. S., Prieto, J. L., Bersier, D., et al. 2014a, Monthly Notices of the Royal Astronomical Society, 445, 3263, doi: `10.1093/mnras/stu1922`

Holoien, T. W.-S., Prieto, J. L., Stanek, K. Z., et al. 2014b, The Astrophysical Journal Letters, 785, L35, doi: `10.1088/2041-8205/785/2/L35`

Holoien, T. W. S., Kochanek, C. S., Prieto, J. L., et al. 2016a, Monthly Notices of the Royal Astronomical Society, 455, 2918, doi: `10.1093/mnras/stv2486`

—. 2016b, Monthly Notices of the Royal Astronomical Society, 463, 3813, doi: `10.1093/mnras/stw2272`

Holoien, T. W. S., Vallely, P. J., Auchettl, K., et al. 2019a, The Astrophysical Journal, 883, 111, doi: `10.3847/1538-4357/ab3c66`

Holoien, T. W. S., Huber, M. E., Shappee, B. J., et al. 2019b, The Astrophysical Journal, 880, 120, doi: `10.3847/1538-4357/ab2ae1`

Hung, T., Gezari, S., Blagorodnova, N., et al. 2017, The Astrophysical Journal, 842, 29, doi: `10.3847/1538-4357/aa7337`

Hung, T., Foley, R. J., Ramirez-Ruiz, E., et al. 2020, The Astrophysical Journal, 903, 31, doi: `10.3847/1538-4357/abb606`

Hunter, J. D. 2007, Computing in Science & Engineering, 9, 90, doi: `10.1109/MCSE.2007.55`

Ihanec, N., Gromadzki, M., Wevers, T., & Irani, I. 2020, Transient Name Server Classification Report, 2020-3486, 1

Jiang, Y.-F., Guillochon, J., & Loeb, A. 2016, The Astrophysical Journal, 830, 125, doi: `10.3847/0004-637X/830/2/125`

Johnson, B. D., Leja, J., Conroy, C., & Speagle, J. S. 2021, The Astrophysical Journal Supplement, 254, 22, doi: `10.3847/1538-4365/abef67`

Kasliwal, M. M., Cannella, C., Bagdasaryan, A., et al. 2019, Publications of the Astronomical Society of the Pacific, 131, 038003, doi: `10.1088/1538-3873/aafbc2`

Kauffmann, G., Heckman, T. M., Tremonti, C., et al. 2003, Monthly Notices of the Royal Astronomical Society, 346, 1055, doi: `10.1111/j.1365-2966.2003.07154.x`

Kendall, M. G. 1938, Biometrika, 30, 81

Kennedy, G. F., Meiron, Y., Shukirgaliyev, B., et al. 2016, Monthly Notices of the Royal Astronomical Society, 460, 240, doi: `10.1093/mnras/stw908`

Kesden, M. 2012, Physical Review D: Particles, Fields, Gravitation and Cosmology, 85, 024037, doi: `10.1103/PhysRevD.85.024037`

Kewley, L. J., Dopita, M. A., Sutherland, R. S., Heisler, C. A., & Trevena, J. 2001, The Astrophysical Journal, 556, 121, doi: `10.1086/321545`

Kochanek, C. S. 2016a, Monthly Notices of the Royal Astronomical Society, 458, 127, doi: `10.1093/mnras/stw267`

—. 2016b, Monthly Notices of the Royal Astronomical Society, 461, 371, doi: `10.1093/mnras/stw1290`

Komossa, S., & Bade, N. 1999, Astronomy and Astrophysics, 343, 775. `https://arxiv.org/abs/astro-ph/9901141`

Komossa, S., & Greiner, J. 1999, Astronomy and Astrophysics, 349, L45

Kormendy, J., & Ho, L. C. 2013, Annual Review of Astronomy and Astrophysics, 51, 511, doi: `10.1146/annurev-astro-082708-101811`

Kormendy, J., & Richstone, D. 1995, Annual Review of Astronomy and Astrophysics, 33, 581, doi: `10.1146/annurev.aa.33.090195.003053`

Krolik, J., Piran, T., Svirski, G., & Cheng, R. M. 2016, The Astrophysical Journal, 827, 127, doi: `10.3847/0004-637X/827/2/127`

Lacy, J. H., Townes, C. H., & Hollenbach, D. J. 1982, The Astrophysical Journal, 262, 120, doi: `10.1086/160402`

Larson, R. L., Finkelstein, S. L., Kocevski, D. D., et al. 2023, The Astrophysical Journal Letters, 953, L29, doi: `10.3847/2041-8213/ace619`

Law-Smith, J., Ramirez-Ruiz, E., Ellison, S. L., & Foley, R. J. 2017, The Astrophysical Journal, 850, 22, doi: `10.3847/1538-4357/aa94c7`

Leloudas, G., Schulze, S., Krühler, T., et al. 2015, Monthly Notices of the Royal Astronomical Society, 449, 917, doi: `10.1093/mnras/stv320`

Leloudas, G., Fraser, M., Stone, N. C., et al. 2016, Nature Astronomy, 1, 0002, doi: `10.1038/s41550-016-0002`

Leloudas, G., Dai, L., Arcavi, I., et al. 2019, The Astrophysical Journal, 887, 218, doi: `10.3847/1538-4357/ab5792`

Levan, A. J., Tanvir, N. R., Cenko, S. B., et al. 2011, Science, 333, 199, doi: `10.1126/science.1207143`

Levan, A. J., Tanvir, N. R., Brown, G. C., et al. 2016, The Astrophysical Journal, 819, 51, doi: `10.3847/0004-637X/819/1/51`

Lidskii, V. V., & Ozernoi, L. M. 1979, Pisma v Astronomicheskii Zhurnal, 5, 28

Lodato, G., & Rossi, E. M. 2011, Monthly Notices of the Royal Astronomical Society, 410, 359, doi: `10.1111/j.1365-2966.2010.17448.x`

Loeb, A., & Ulmer, A. 1997, The Astrophysical Journal, 489, 573

Lu, W., & Bonnerot, C. 2020, Monthly Notices of the Royal Astronomical Society, 492, 686, doi: `10.1093/mnras/stz3405`

Lunnan, R., Chornock, R., Berger, E., et al. 2014, The Astrophysical Journal, 787, 138, doi: `10.1088/0004-637X/787/2/138`

MacLeod, M., Guillochon, J., & Ramirez-Ruiz, E. 2012, The Astrophysical Journal, 757, 134, doi: `10.1088/0004-637X/757/2/134`

Magorrian, J., & Tremaine, S. 1999, Monthly Notices of the Royal Astronomical Society, 309, 447, doi: `10.1046/j.1365-8711.1999.02853.x`

Magorrian, J., Tremaine, S., Richstone, D., et al. 1998, The Astronomical Journal, 115, 2285, doi: `10.1086/300353`

Mainzer, A., Bauer, J., Grav, T., et al. 2011, The Astrophysical Journal, 731, 53, doi: `10.1088/0004-637X/731/1/53`

Maiolino, R., Scholtz, J., Witstok, J., et al. 2023, arXiv e-prints, arXiv:2305.12492, doi: `10.48550/arXiv.2305.12492`

Marigo, P., Bressan, A., Nanni, A., Girardi, L., & Pumo, M. L. 2013, Monthly Notices of the Royal Astronomical Society, 434, 488, doi: `10.1093/mnras/stt1034`

Masci, F. J., Laher, R. R., Rusholme, B., et al. 2019, Publications of the Astronomical Society of the Pacific, 131, 018003, doi: `10.1088/1538-3873/aae8ac`

Masterson, M., De, K., Panagiotou, C., et al. 2024, The Astrophysical Journal, 961, 211, doi: `10.3847/1538-4357/ad18bb`

McConnell, N. J., & Ma, C.-P. 2013, The Astrophysical Journal, 764, 184, doi: `10.1088/0004-637X/764/2/184`

Mendel, J. T., Simard, L., Palmer, M., Ellison, S. L., & Patton, D. R. 2014, The Astrophysical Journal Supplement, 210, 3, doi: `10.1088/0067-0049/210/1/3`

Metzger, B. D., & Stone, N. C. 2016, Monthly Notices of the Royal Astronomical Society, 461, 948, doi: `10.1093/mnras/stw1394`

Miller, J. M., Kaastra, J. S., Miller, M. C., et al. 2015, Nature, 526, 542, doi: `10.1038/nature15708`

Mimica, P., Giannios, D., Metzger, B. D., & Aloy, M. A. 2015, Monthly Notices of the Royal Astronomical Society, 450, 2824, doi: `10.1093/mnras/stv825`

Mockler, B., Guillochon, J., & Ramirez-Ruiz, E. 2019, The Astrophysical Journal, 872, 151, doi: `10.3847/1538-4357/ab010f`

Mockler, B., Twum, A. A., Auchettl, K., et al. 2022, The Astrophysical Journal, 924, 70, doi: `10.3847/1538-4357/ac35d5`

Morris, B. M., Tollerud, E., Sipőcz, B., et al. 2018, The Astronomical Journal, 155, 128, doi: `10.3847/1538-3881/aaa47e`

Morrissey, P., Matuszewski, M., Martin, D. C., et al. 2018, The Astrophysical Journal, 864, 93, doi: `10.3847/1538-4357/aad597`

Mummery, A. 2021, arXiv e-prints, arXiv:2104.06212, doi: `10.48550/arXiv.2104.06212`

Neill, D., Matuszewski, M., Martin, C., Brodheim, M., & Rizzi, L. 2023, KCWI_DRP: Keck Cosmic Web Imager Data Reduction Pipeline in Python, Astrophysics Source Code Library, record ascl:2301.019. `http://ascl.net/2301.019`

Nicholl, M., Lanning, D., Ramsden, P., et al. 2022, Monthly Notices of the Royal Astronomical Society, 515, 5604, doi: `10.1093/mnras/stac2206`

Nicholl, M., Blanchard, P. K., Berger, E., et al. 2019, Monthly Notices of the Royal Astronomical Society, 488, 1878, doi: `10.1093/mnras/stz1837`

Nicholl, M., Wevers, T., Oates, S. R., et al. 2020, Monthly Notices of the Royal Astronomical Society, 499, 482, doi: `10.1093/mnras/staa2824`

Norton, S. A., Gebhardt, K., Zabludoff, A. I., & Zaritsky, D. 2001, The Astrophysical Journal, 557, 150, doi: `10.1086/321668`

O'Connor, B., Troja, E., Dichiara, S., et al. 2022, Monthly Notices of the Royal Astronomical Society, 515, 4890, doi: `10.1093/mnras/stac1982`

Ørum, S. V., Ivens, D. L., Strandberg, P., et al. 2020, Astronomy and Astrophysics, 643, A47, doi: `10.1051/0004-6361/202038176`

O'Sullivan, D., & Chen, Y. 2020, arXiv e-prints, arXiv:2011.05444, doi: `10.48550/arXiv.2011.05444`

pandas development team, T. 2020, pandas-dev/pandas: Pandas, latest, Zenodo, doi: `10.5281/zenodo.3509134`

Pasham, D., Gendreau, K., Arzoumanian, Z., & Cenko, B. 2022, GRB Coordinates Network, 31601, 1

Pasham, D. R., Cenko, S. B., Levan, A. J., et al. 2015, The Astrophysical Journal, 805, 68, doi: `10.1088/0004-637X/805/1/68`

Pasham, D. R., Lucchini, M., Laskar, T., et al. 2023, Nature Astronomy, 7, 88, doi: `10.1038/s41550-022-01820-x`

Patterson, M. T., Bellm, E. C., Rusholme, B., et al. 2019, Publications of the Astronomical Society of the Pacific, 131, 018001, doi: `10.1088/1538-3873/aae904`

Peng, C. Y., Ho, L. C., Impey, C. D., & Rix, H.-W. 2002, The Astronomical Journal, 124, 266, doi: `10.1086/340952`

Perley, D. A. 2022, GRB Coordinates Network, 31592, 1

Perley, D. A., Ho, A. Y. Q., Petitpas, G., & Keating, G. 2022, GRB Coordinates Network, 31627, 1

Perley, D. A., Quimby, R. M., Yan, L., et al. 2016, The Astrophysical Journal, 830, 13, doi: `10.3847/0004-637X/830/1/13`

Pfister, H., Bar-Or, B., Volonteri, M., Dubois, Y., & Capelo, P. R. 2019, Monthly Notices of the Royal Astronomical Society, 488, L29, doi: `10.1093/mnrasl/slz091`

Phinney, E. S. 1989, Nature, 340, 595, doi: `10.1038/340595a0`

Piran, T., Svirski, G., Krolik, J., Cheng, R. M., & Shiokawa, H. 2015, The Astrophysical Journal, 806, 164, doi: `10.1088/0004-637X/806/2/164`

Pracy, M. B., Kuntschner, H., Couch, W. J., et al. 2009, Monthly Notices of the Royal Astronomical Society, 396, 1349, doi: `10.1111/j.1365-2966.2009.14836.x`

Prieto, J. L., Krühler, T., Anderson, J. P., et al. 2016, The Astrophysical Journal Letters, 830, L32, doi: `10.3847/2041-8205/830/2/L32`

Prochaska, J., Hennawi, J., Westfall, K., et al. 2020, The Journal of Open Source Software, 5, 2308, doi: `10.21105/joss.02308`

Ramsden, P., Lanning, D., Nicholl, M., & McGee, S. L. 2022, Monthly Notices of the Royal Astronomical Society, 515, 1146, doi: `10.1093/mnras/stac1810`

Rees, M. J. 1988, Nature, 333, 523, doi: `10.1038/333523a0`

Reines, A. E., & Volonteri, M. 2015, The Astrophysical Journal, 813, 82, doi: `10.1088/0004-637X/813/2/82`

Reynolds, T. M., Arcavi, I., Stone, M. B., et al. 2018, The Astronomer's Telegram, 12281, 1

Rhodes, L., Bright, J. S., Fender, R., et al. 2023, Monthly Notices of the Royal Astronomical Society, 521, 389, doi: `10.1093/mnras/stad344`

Rigault, M. 2018, ztfquery, a python tool to access ZTF data, doi, Zenodo, doi: `10.5281/zenodo.1345222`

Rigault, M., Neill, J. D., Blagorodnova, N., et al. 2019, Astronomy and Astrophysics, 627, A115, doi: `10.1051/0004-6361/201935344`

Roming, P. W. A., Kennedy, T. E., Mason, K. O., et al. 2005, Space Science Reviews, 120, 95, doi: `10.1007/s11214-005-5095-4`

Roth, N., Kasen, D., Guillochon, J., & Ramirez-Ruiz, E. 2016, The Astrophysical Journal, 827, 3, doi: `10.3847/0004-637X/827/1/3`

Roth, N., van Velzen, S., Cenko, S. B., & Mushotzky, R. F. 2021, The Astrophysical Journal, 910, 93, doi: `10.3847/1538-4357/abdf50`

Ryu, T., Krolik, J., & Piran, T. 2020, The Astrophysical Journal, 904, 73, doi: `10.3847/1538-4357/abbf4d`

Salpeter, E. E. 1955, The Astrophysical Journal, 121, 161, doi: `10.1086/145971`

Saxton, R., Komossa, S., Auchettl, K., & Jonker, P. G. 2020, Space Science Reviews, 216, 85, doi: `10.1007/s11214-020-00708-4`

—. 2021, Space Science Reviews, 217, 18, doi: `10.1007/s11214-020-00759-7`

Sazonov, S., Gilfanov, M., Medvedev, P., et al. 2021, Monthly Notices of the Royal Astronomical Society, 508, 3820, doi: `10.1093/mnras/stab2843`

Schawinski, K., Dowlin, N., Thomas, D., Urry, C. M., & Edmondson, E. 2010, The Astrophysical Journal Letters, 714, L108, doi: `10.1088/2041-8205/714/1/L108`

Schawinski, K., Urry, C. M., Simmons, B. D., et al. 2014, Monthly Notices of the Royal Astronomical Society, 440, 889, doi: `10.1093/mnras/stu327`

Schulze, S., Krühler, T., Leloudas, G., et al. 2018, Monthly Notices of the Royal Astronomical Society, 473, 1258, doi: `10.1093/mnras/stx2352`

Schulze, S., Yaron, O., Sollerman, J., et al. 2021, The Astrophysical Journal Supplement, 255, 29, doi: `10.3847/1538-4365/abff5e`

Sérsic, J. L. 1963, Boletin de la Asociacion Argentina de Astronomia La Plata Argentina, 6, 41

Short, P., Nicholl, M., Muller, T., Angus, C., & Yaron, O. 2019, Transient Name Server Classification Report, 2019-772, 1

Short, P., Nicholl, M., Lawrence, A., et al. 2020, Monthly Notices of the Royal Astronomical Society, 498, 4119, doi: `10.1093/mnras/staa2065`

Siebert, M. R., Strasburger, E., Rojas-Bravo, C., & Foley, R. J. 2019, The Astronomer's Telegram, 13131, 1

Simard, L. 2010, GIM2D: Galaxy IMage 2D, Astrophysics Source Code Library, record ascl:1004.001

Simard, L., Mendel, J. T., Patton, D. R., Ellison, S. L., & McConnachie, A. W. 2011, The Astrophysical Journal Supplement, 196, 11, doi: `10.1088/0067-0049/196/1/11`

Simard, L., Willmer, C. N. A., Vogt, N. P., et al. 2002, The Astrophysical Journal Supplement, 142, 1, doi: `10.1086/341399`

Smith, K. W., Smartt, S. J., Young, D. R., et al. 2020, Publications of the Astronomical Society of the Pacific, 132, 085002, doi: `10.1088/1538-3873/ab936e`

Somalwar, J. J., Ravi, V., Dong, D. Z., et al. 2023, arXiv e-prints, arXiv:2310.03791, doi: `10.48550/arXiv.2310.03791`

Speziali, R., Di Paola, A., Giallongo, E., et al. 2008, in Society of Photo-Optical Instrumentation Engineers (SPIE) Conference Series, Vol. 7014, Ground-based and Airborne Instrumentation for Astronomy II, ed. I. S. McLean & M. M. Casali, 70144T, doi: `10.1117/12.790132`

Steele, I. A., Smith, R. J., Rees, P. C., et al. 2004, in Society of Photo-Optical Instrumentation Engineers (SPIE) Conference Series, Vol. 5489, Ground-based Telescopes, ed. J. Oschmann, Jacobus M., 679–692, doi: `10.1117/12.551456`

Stein, R., Mahabal, A., Reusch, S., et al. 2023, arXiv e-prints, arXiv:2312.00139, doi: `10.48550/arXiv.2312.00139`

Stern, D., Assef, R. J., Benford, D. J., et al. 2012, The Astrophysical Journal, 753, 30, doi: `10.1088/0004-637X/753/1/30`

Stone, N., Sari, R., & Loeb, A. 2013, Monthly Notices of the Royal Astronomical Society, 435, 1809, doi: `10.1093/mnras/stt1270`

Stone, N. C., Generozov, A., Vasiliev, E., & Metzger, B. D. 2018, Monthly Notices of the Royal Astronomical Society, 480, 5060, doi: `10.1093/mnras/sty2045`

Stone, N. C., & Metzger, B. D. 2016, Monthly Notices of the Royal Astronomical Society, 455, 859, doi: `10.1093/mnras/stv2281`

Stone, N. C., & van Velzen, S. 2016, The Astrophysical Journal Letters, 825, L14, doi: `10.3847/2041-8205/825/1/L14`

Strauss, M. A., Weinberg, D. H., Lupton, R. H., et al. 2002, The Astronomical Journal, 124, 1810, doi: `10.1086/342343`

Strubbe, L. E., & Quataert, E. 2009, Monthly Notices of the Royal Astronomical Society, 400, 2070, doi: `10.1111/j.1365-2966.2009.15599.x`

—. 2011, Monthly Notices of the Royal Astronomical Society, 415, 168, doi: `10.1111/j.1365-2966.2011.18686.x`

Syer, D., & Ulmer, A. 1999, Monthly Notices of the Royal Astronomical Society, 306, 35, doi: `10.1046/j.1365-8711.1999.02445.x`

Taggart, K., & Perley, D. A. 2021, Monthly Notices of the Royal Astronomical Society, 503, 3931, doi: `10.1093/mnras/stab174`

Taghizadeh-Popp, M., Kim, J. W., Lemson, G., et al. 2020, Astronomy and Computing, 33, 100412, doi: `10.1016/j.ascom.2020.100412`

Tanvir, N. R., de Ugarte Postigo, A., Izzo, L., et al. 2022, GRB Coordinates Network, 31602, 1

Tchekhovskoy, A., Metzger, B. D., Giannios, D., & Kelley, L. Z. 2014, Monthly Notices of the Royal Astronomical Society, 437, 2744, doi: `10.1093/mnras/stt2085`

Tonry, J. L., Denneau, L., Heinze, A. N., et al. 2018, Publications of the Astronomical Society of the Pacific, 130, 064505, doi: `10.1088/1538-3873/aabadf`

Toy, V. L., Cenko, S. B., Silverman, J. M., et al. 2016, The Astrophysical Journal, 818, 79, doi: `10.3847/0004-637X/818/1/79`

Treister, E., Schawinski, K., Urry, C. M., & Simmons, B. D. 2012, The Astrophysical Journal Letters, 758, L39, doi: `10.1088/2041-8205/758/2/L39`

Tucker, M. A., Huber, M., Shappee, B. J., et al. 2018, The Astronomer's Telegram, 11473, 1

Ulmer, A. 1999, The Astrophysical Journal, 514, 180, doi: `10.1086/306909`

van de Sande, J., Scott, N., Bland-Hawthorn, J., et al. 2018, Nature Astronomy, 2, 483, doi: `10.1038/s41550-018-0436-x`

van der Walt, S. J., Crellin-Quick, A., & Bloom, J. S. 2019, Journal of Open Source Software, 4, doi: `10.21105/joss.01247`

van Velzen, S. 2018, The Astrophysical Journal, 852, 72, doi: `10.3847/1538-4357/aa998e`

van Velzen, S., Gezari, S., Hung, T., et al. 2019a, The Astronomer's Telegram, 12568, 1

van Velzen, S., Gezari, S., Ward, C., et al. 2019b, Transient Name Server AstroNote, 88, 1

van Velzen, S., Holoien, T. W. S., Onori, F., Hung, T., & Arcavi, I. 2020, arXiv e-prints, arXiv:2008.05461. `https://arxiv.org/abs/2008.05461`

van Velzen, S., Stone, N. C., Metzger, B. D., et al. 2019c, The Astrophysical Journal, 878, 82, doi: `10.3847/1538-4357/ab1844`

van Velzen, S., Farrar, G. R., Gezari, S., et al. 2011, The Astrophysical Journal, 741, 73, doi: `10.1088/0004-637X/741/2/73` van Velzen, S., Gezari, S., Cenko, S. B., et al. 2018, The Astronomer's Telegram, 12263, 1

—. 2019d, The Astrophysical Journal, 872, 198, doi: 10.3847/1538-4357/aafe0c

van Velzen, S., Gezari, S., Frederick, S., et al. 2019e, The Astronomer's Telegram, 12509, 1

van Velzen, S., Gezari, S., Hammerstein, E., et al. 2021, The Astrophysical Journal, 908, 4, doi: 10.3847/1538-4357/abc258

Vazdekis, A., Coelho, P., Cassisi, S., et al. 2015, Monthly Notices of the Royal Astronomical Society, 449, 1177, doi: 10.1093/mnras/stv151

Veilleux, S., Cecil, G., & Bland-Hawthorn, J. 2005, Annual Review of Astronomy and Astrophysics, 43, 769, doi: 10.1146/annurev.astro.43.072103.150610

Veilleux, S., Maiolino, R., Bolatto, A. D., & Aalto, S. 2020, Astronomy and Astrophysics Reviews, 28, 2, doi: 10.1007/s00159-019-0121-9

Verro, K., Trager, S. C., Peletier, R. F., et al. 2022, Astronomy and Astrophysics, 661, A50, doi: 10.1051/0004-6361/202142387

Virtanen, P., Gommers, R., Oliphant, T. E., et al. 2020, Nature Methods, 17, 261, doi: 10.1038/s41592-019-0686-2

Wang, J., & Merritt, D. 2004, The Astrophysical Journal, 600, 149, doi: 10.1086/379767

Wevers, T., van Velzen, S., Jonker, P. G., et al. 2017, Monthly Notices of the Royal Astronomical Society, 471, 1694, doi: 10.1093/mnras/stx1703

Wevers, T., Pasham, D. R., van Velzen, S., et al. 2019, Monthly Notices of the Royal Astronomical Society, 488, 4816, doi: 10.1093/mnras/stz1976

Wevers, T., Nicholl, M., Guolo, M., et al. 2022, Astronomy and Astrophysics, 666, A6, doi: 10.1051/0004-6361/202142616

Worthey, G., & Ottaviani, D. L. 1997, The Astrophysical Journal Supplement, 111, 377, doi: 10.1086/313021

Xiao, T., Barth, A. J., Greene, J. E., et al. 2011, The Astrophysical Journal, 739, 28, doi: 10.1088/0004-637X/739/1/28

Yang, Y., Zabludoff, A. I., Zaritsky, D., & Mihos, J. C. 2008, The Astrophysical Journal, 688, 945, doi: 10.1086/591656

Yao, Y., Lu, W., Guolo, M., et al. 2022, The Astrophysical Journal, 937, 8, doi: 10.3847/1538-4357/ac898a

Yao, Y., Ravi, V., Gezari, S., et al. 2023, The Astrophysical Journal Letters, 955, L6, doi: 10.3847/2041-8213/acf216

Yuan, W., Komossa, S., Zhang, C., et al. 2016, in Star Clusters and Black Holes in Galaxies across Cosmic Time, ed. Y. Meiron, S. Li, F. K. Liu, & R. Spurzem, Vol. 312, 68–70, doi: `10.1017/S1743921315007516`

Zabludoff, A., Arcavi, I., La Massa, S., et al. 2021, Space Science Reviews, 217, 54, doi: `10.1007/s11214-021-00829-4`

Zabludoff, A. I., Zaritsky, D., Lin, H., et al. 1996, The Astrophysical Journal, 466, 104, doi: `10.1086/177495`

Zauderer, B. A., Berger, E., Margutti, R., et al. 2013, The Astrophysical Journal, 767, 152, doi: `10.1088/0004-637X/767/2/152`

Zauderer, B. A., Berger, E., Soderberg, A. M., et al. 2011, Nature, 476, 425, doi: `10.1038/nature10366`